Effective-diffusion for general nonautonomous systems

by

Phillip Walker

A Dissertation Presented in Partial Fulfillment
of the Requirements for the Degree
Doctor of Philosophy

Approved April 2018 by the
Graduate Supervisory Committee:

Wenbo Tang, Chair
Eric Kostelich
Alex Mahalov
Mohamed Moustaoui
Rodrigo Platte

ARIZONA STATE UNIVERSITY

May 2018

ABSTRACT

The tools developed for the use of investigating dynamical systems have provided critical understanding to a wide range of physical phenomena. Here these tools are used to gain further insight into scalar transport, and how it is affected by mixing. The aim of this research is to investigate the efficiency of several different partitioning methods which demarcate flow fields into dynamically distinct regions, and the correlation of finite-time statistics from the advection-diffusion equation to these regions.

For autonomous systems, invariant manifold theory can be used to separate the system into dynamically distinct regions. Despite there being no equivalent method for nonautonomous systems, a similar analysis can be done. Systems with general time dependencies must resort to using finite-time transport barriers for partitioning; these barriers are the edges of Lagrangian coherent structures (LCS), the analog to the stable and unstable manifolds of invariant manifold theory. Using the coherent structures of a flow to analyze the statistics of trapping, flight, and residence times, the signature of anomalous diffusion are obtained.

This research also investigates the use of linear models for approximating the elements of the covariance matrix of nonlinear flows, and then applying the covariance matrix approximation over coherent regions. The first and second-order moments can be used to fully describe an ensemble evolution in linear systems, however there is no direct method for nonlinear systems. The problem is only compounded by the fact that the moments for nonlinear flows typically don't have analytic representations, therefore direct numerical simulations would be needed to obtain the moments throughout the domain. To circumvent these many computations, the nonlinear system is approximated as many linear systems for which analytic expressions for the moments exist. The parameters introduced in the linear models are obtained locally from the nonlinear deformation tensor.

For my mother,

who unceasingly inspires me to grow and challenge myself in the face of hardship,

and my grandfather Phillip N. Walker,

who's wit, humor, and character enriched the lives of all that knew him.

“The chaos of the waves, gravid with encrypted information, mocks him.”

- Neal Stephenson, *Cryptonomicon*

I am grateful to all of those with whom I have had the pleasure to work during this and any other project. Each of the members of my Dissertation Committee have provided comments and suggestions that have elevated not only the quality of this work, but also my appreciation of the utility mathematics provides. My understanding and appreciation of the numerics necessary for this work were fostered from the initial conversations with Professor Platte in his spectral methods class, and the lessons absorbed from Professor Kostelich’s high-performance computing class. I am grateful to Professors Mohamed Moustaoui and Alex Mahalov who engaged me to think critically of my results, and to explore their implications for 3D systems.

I am indebted to Prof. Nicholas Ouellette for hosting me in his lab, the experience of designing and executing an experiment was unforgettable. As my teacher, mentor, and committee chair, I am most thankful to Professor Wenbo Tang for the extensive discussions, knowledge, and guidance that he has provided during the tenure of this research. Without his suggestions, and valueable insights, I would have not been able to have completed this work.

I am profoundly thankful to Elise Leutwyler, Logan Scholz, and Dr. Alex Farrell for their assistance in shaping the original versions of this work. Their collective grammatical insights have led to a much more readible, coherent, and complete work than I could have done alone. I would also like to acknowledge and thank my family and friends that have provided necessary moral support throughout the years. The long discussions, unwaivering optimism, and innumerable other ways you have been there for me are the reasons for my success – thank you.

TABLE OF CONTENTS

APPENDIX

LIST OF TABLES

LIST OF FIGURES

Figure Page

Figure Page

Chapter 1

MOTIVATION

Mathematical tools and methods from dynamical systems are used to facilitate a more comprehensive understanding of how passive scalar transport processes are affected by coherent structures. This will be done by: using several coherent structure detection diagnostics to investigate their impact on scalar statistics, creating linear strain-shear flow models to recover scalar moments of nonlinear flows for finite-time, and combining these two aspects to create an effective-transport operator, capable of approximating conditional transport processes in nonautonomous dynamical systems.

The standard diffusion model can be used to analytically describe how passive scalars[1] are transported in the absence of forcing. However, when forcing is present, transport barriers can form, thus mitigating transport and leading to anomalous diffusion. These finite-time transport barriers could highlight coherent structures - trajectories of the dynamic system that have major influence over nearby trajectories. Since coherent structures are ubiquitous in environmental and geophysical flows, obtaining models to describe their impacts on transport processes is of great importance not only to the mathematical and physics communities, but also to conservational research.

In Peacock and Haller (2013), this importance was discussed from the viewpoint of determining where contaminants spread in geophysical flows. These examples are varied in scale, and come from volcano eruptions, oil spills, nuclear disasters and even cloud formation. The basic structures in these cases are related back to the ideas of invariant manifold theory and stretching within the flow. Further, in Douglass *et al.*

---

[1] Passive scalars are diffusive contaminants that have no dynamical impact on the fluid motion.

(2014) it was stressed that understanding chlorofluorocarbons transport is necessary for understanding the ozone hole; describing how stronger Brewer-Dobson circulation leads to greater transport in the Arctic lower stratosphere. Moreover, this greater circulation leads to polar stratospheric clouds (PSCs) dissipating from the polar vortex before late April, whereas in the Antarctic vortex, the PSCs can remain until after October. The presence of the PSCs leads to the large depletion of ozone, since heterogeneous chemical reactions are occurring within them to create chlorine gas. The chloroflourocarbons that comprise the PSCs are inertial particles that are carried by the wind patterns, and subject to body forces. In studies with inertial particles viscous drag and other body forces must be accounted for.

In another model using inertial particles, Tang *et al.* (2012) investigated the transport of pollution in an urban setting. It is seen that transport around the buildings is strongly correlated to the stretching field, revealed using the finite-time Lyapunov exponent (FTLE). The results show a strong correlation between the building placements and pathways of pollutant transport, suggesting the presence of concentrated pollutant transport. Such areas of pollution transport should be further investigated and incorporated into city planning processes[2] .

The Fukushima Daiichi nuclear disaster and Deepwater Horizon oil spill, despite providing very rich datasets, illuminated how woefully unprepared and ineffective current methods are at contaminant containment in the ocean. It was seen that the size and impact from these disasters was heavily influenced by their locations and the surrounding flow fields; with the oil spread in the Atlantic mitigated by a Northward circulating flow, and the nuclear contaminants spread dramatically throughout the Pacific due to strong currents along the Fukushima coast. With a better understand-

---

[2] For instance, CiteTree and similar projects could be place based on pollution pathways instead of some other metric.

ing of the role coherent structures play in the transport of such harmful scalars as those released in the aforementioned disasters, better containment strategies can be devised through analytics. For all of these examples, it is vital to understand how transport is affected by stirring, regardless of scale.

Since the primary concern is how a passive scalar's release position affects the scalars evolution, either the standard diffusion model can be solved for every initial condition in the domain – a computationally intensive exercise – or a fractional diffusion model can be used. The fractional diffusion model is a transport model that uses fractional derivatives in space and time; these derivatives are integro-differential operators that extend the notion of the derivative to fractional orders. The fractional diffusion model is appropriate for investigating anomalous diffusion. Experimental and theoretical works on scalar intermittency indicate that the existence of transport barriers and coherent structures leads to non-Gaussian statistics and anomalous diffusion (see Castaing *et al.* (2006); Yakhot *et al.* (1990); Pumir *et al.* (1991); McLaughlin and Majda (1996)).

In Gollub *et al.* (1991) the probability density functions of temperature fluctuations are investigated for a flow stirred with a mean gradient. It is seen that these pdfs depend on some critical Reynolds number (R), a dimensionless parameter given by the ratio between the advective and diffusive time scales. The Reynolds number can be written as $R = uL/\nu$, where u is the characteristic velocity, L is the characteristic length, and ν is the kinematic viscocity. In Gollub *et al.* (1991) Gaussian fits are observed for the case $R = 600$, but with an exponential fit for $R = 3700$. This is expected since low R indicates the system is dominated by molecular diffusion, where a large R suggests that transport is dominated by the advective component, leading to the tails of the pdf being more broad. This change of behavior of the system highlights the change in the dynamics. Solomon *et al.* (1993) study transport in a time-periodic flow composed of a cirrcular chain of vortices in a rapidly rotating annulus. This system has chaotic trajectories, where intermittently trajectories stick near vortices before moving large distances, in avalanche-like motion. The variance of the chaotic trajectories in the azimuthal direction is seen to scale anomalously as $\sigma^2(t) \sim t^\gamma$ with $\gamma = 1.65 \pm .15$. The histograms of the sticking times and flight times follow power law distributions and are seen to correspond very well with theoretical relations.

Anomalous diffusion was observed in the experimental setting for a quasi-two-dimensional turbulent flow in Cardoso *et al.* (1996). The onset of subdiffusion ($\gamma < 1$), which is slower spreading than regular diffusion, was caused by "sticky" or trapping type regions, and superdiffusion ($\gamma > 1$), which spreads faster than regular diffusion, was observed as Lévy flights in the particle trajectories. The probability density function of the flight times had an exponential scaling, where the pdf of the waiting times had algebraic decay. The subdiffusion was observed as the trapping of dye in vortex cores in a lattice of counter-rotating vortices; this lattice is similar to Rayleigh-Bénard convection cells. Although, since this system was given stationary forcing, the results might not hold for turbulent flows that exhibit an inverse energy cascade.

In Elhmaidi *et al.* (1993) the problem of 2-dimensional turbulence is once again addressed, this time where an inverse energy cascade is present. The flow is parameterized based on the dominance of the relative deformation or rotation, leading to a separation into hyperbolic or elliptic classification, respectively. It was noted that surrounding strongly elliptic regions (vorticies) was the presence of strongly hyperbolic regions (circulation cells). The background turbulence is a combination of regions with little deformation and regions of little vorticity. This binary partition of the flow allows for the investigation of the single-particle dispersion conditioned of region. Anamolous scalings were obtained for both the ellpitic and hyperbolic regions.

The scaling for the hyperbolic region was found to be robust, due to the tendency of the particles to concentrate in these regions.

In Tang and Walker (2012), the FTLE was used to highlight transport barriers, which were used to separate coherent regions in a strongly-chaotic periodic flow. Analysis showed that passive scalar variances were multimodal when taken over the entire domain, but when the statistics were conditioned amongst their respective coherent regions, unimodal structures were observed. This unimodal property of the conditional statistics suggests that the isolated regions considered coherent are nearly dynamically homogeneous. It was also noted that the scaling-law parameters varied amoungst the regions, suggesting that the separate coherent regions are dynamically distinct. This, in turn, verifies the presence of anomalous diffusion. Since the scaling-law parameters and the conditional statistics are so intimately dependent on the classification of these coherent regions, the accuracy of finding Lagrangian coherent structures (LCSs) is of critical importance.

In Walker *et al.* (2018), several LCS detection methods (geometric and probabilistic) are used to partition a turbulent flow into coherent regions; these regions were then used to compute scalar statistics. Unlike the previous investigation which was concerned with dispersion statistics, the interest is now in resident-time statistics. It is seen that the scaling type (algebraic or exponential) of the statistics could change based off of which method was used, further supporting that when the coherent regions are incorrectly identified the conditional statistics will be affected.

Along a similar vein, in Jones *et al.* (2018) the FTLE and geodesic methods were used to analyze a 2-bacteria competition model, where the background flow used was the 2D turbulent flow seen in Walker *et al.* (2018). The bacteria species differ in their motility – one species is passive in the flow, while the other species is able to swim, driven via a chemotactic mechanism. The uptake advantage between the species was computed as a function of time and initial release position of the nutrient patch. Areas of high stretching (as indicated by the FTLE) had a maximum in this advantage at earlier times; correlating to the nutrient patch quickly filamenting and being more accessible to the motile and non-motile bacteria. By using geodesic theory the elliptic regions were detected, for which later peaks were seen in the uptake advantage. This is due to the elliptic regions' coherence, it acts to trap the nutrient, only making it available to the bacteria inside. Further, the motile species will be able to enter the elliptic regions, while the non-motile bacteria will not be able to. With the stretching and elliptic regions considered, 3 stages leading to peaks in nutrient consumption were uncovered for this chemotactic model.

With an accurate classification of the coherent regions for general nonautonomous systems, the focus shifts to approximating the covariance matrix for these flows using linear models; this was seen in Walker and Tang (2018). For linear incompressible flows, a closed-form solution for the scalar concentration exists, whereas for nonlinear flows no closed-form solution exists. Because of this, the general nonautonomous system is treated as a sequence of constant-valued linear systems and local approximations to the deformation gradient are obtained. This linearization allows for an accurate approximation to long-time behavior in autonomous and nonautonomous 2D systems.

For 3D systems, the breaking of symmetry of the eigenvectors leads to further modeling concerns. For a fully 3-dimensional linear flow the elements of the covariance matrices are seen to become unwieldy. However, geophysical flows have aspect ratios such that the vertical component plays a minor role, giving quasi-3D flows. Quasi-3d, or weakly 3D, systems are used to understand the importance of surface mixing and how it is affected by vertical advection. It is seen that the GLM3D method is capable of generating approximations to the covariance matrices of the quasi-3D flows from a decoupled 3D linear flow approximation. The major shortcoming of this method, besides being restricted to quasi-3D flows, is the approximation of parameters of the method. Further, since a linear approximation is used, as the integration time is increased the accuracy of the method is reduced.

Chapter 2

BACKGROUND

The Advection-Diffusion Equation

The interplay of diffusion and stirring results in nontrivial mixing structures and finite-time transport barriers. Since the presence of transport barriers is ubiquitous in environmental flows, understanding their impact on mixing processes is paramount. In the following the stirring is introduced by the addition of an advective term to the diffusion equation; this results in the advection-diffusion or transport equation:

$$\partial_t \theta + \nabla \cdot (\mathbf{u}\theta) = \frac{1}{2}\left(\nabla \cdot (\mathbf{D}\nabla\theta)\right), \quad \theta(\mathbf{x}, t_0) = \theta_0(\mathbf{x}), \tag{2.1.1}$$

where $\mathbf{u}$ is the velocity field, θ represents some scalar quantatiy, $\mathbf{D}$ is the diffusivity tensor, and θ_0 is some initial distribution at t_0. In the following the velocity field is incompressible ($\nabla \cdot \mathbf{u} = 0$), and the diffusivity tensor is given by $\mathbf{D} = 2\kappa\mathbf{I}$, for some constant κ, where $\mathbf{I}$ is the identity matrix. This choice of $\mathbf{D}$ corresponds to homogeneous isotropic diffusion. With these assumptions in mind the standard advection-diffusion equation is reduced to:

$$\partial_t \theta + \mathbf{u} \cdot \nabla\theta = \kappa\nabla^2\theta. \tag{2.1.2}$$

Note here that for generic $\mathbf{u}$, (2.1.2) does not have a Green's function, thus the equation will need to be solved for each initial concentration separately.

The Diffusion Equation

When there is no flow present ($\mathbf{u} = \mathbf{0}$), the advection-diffusion equation reduces to the standard diffusion equation. The standard diffusion equation can be used to describe the evolution of an initial distribution within a domain, subject only to uncorrelated microscopic perturbations. The effect of these microscopic perturbations is the softening of concentration gradient; the equation is given as,

$$\partial_t \theta = \frac{1}{2}\left(\nabla \cdot (\mathbf{D}\nabla\theta)\right), \quad \theta(\mathbf{x}, t_0) = \theta_0(\mathbf{x}). \tag{2.1.3}$$

For the homogeneous isotropic case ($D = 2\kappa$), the solution to the standard diffusion equation can be written as:

$$\theta(\mathbf{x}, t) = \int_{-\infty}^{\infty} G(\mathbf{x}, \mathbf{x}'; t, t_0)\theta(\mathbf{x}, t_0)d\mathbf{x}', \tag{2.1.4}$$

where G is the Green's function given by the following,

$$G(\mathbf{x}, \mathbf{x}'; t, t') = \left(\frac{1}{4\pi\kappa(t-t')}\right)^{d/2} e^{-(\mathbf{x}-\mathbf{x}')^2/4\pi\kappa(t-t')}. \tag{2.1.5}$$

From the Green's function it is possible to accurately obtain the evolution of any scalar concentration at time t. However, when a flow is introduced ($\mathbf{u} \neq \mathbf{0}$) an analytic description for θ becomes much more difficult (if not impossible) to obtain due to the formation of transport barriers.

The Effective-Diffusion Equation

As a means of providing an approximate Green's function to (2.1.2), the effective-diffusion model and subsequent Dispersion Diffusion Theory (DDT) were introduced. In Lin *et al.* (2010) an effective-diffusion operator is defined that replaces $\kappa\nabla^2\theta - \mathbf{u}\cdot\nabla\theta$ with $\nabla \cdot \left(\mathbf{K}^{eff} \cdot \nabla\theta\right)$, where $\mathbf{K}^{eff}$ represents the effective diffusivity tensor, which describes transient passive particle dispersion due to the nonlinearity of the flow. The elements of $\mathbf{K}^{eff}$ are of the form:

$$K_{ij}^{eff}(t; \mathbf{x}_0) = \frac{1}{2}\frac{d}{dt}\mathbb{E}[(X_i(t) - X_i(0))(X_j(t) - X_j(0))], \quad i, j = 1, \cdots, d \tag{2.1.6}$$

where $\mathbf{X}(t) = \big(X_1(t), \cdots, X_d(t)\big)^T$ is the trajectory of the passive tracers, and $\mathbf{X}(0) = \mathbf{x_0}$. Once the effective diffusivity tensor is obtained, then without sources or sinks, the probability density of a single passive tracer, denoted as $\rho(\mathbf{x}, t; \mathbf{x_0}, t_0)$, may be approximated by solving:

$$\frac{\partial \rho(\mathbf{x}, t; \mathbf{x_0}, t_0)}{\partial t} = \frac{\partial}{\partial x_i} K_{ij}^{eff}(t - t_0; \mathbf{x_0}) \frac{\partial \rho(\mathbf{x}, t; \mathbf{x_0})}{\partial x_j}, \tag{2.1.7}$$

where the initial distribution $\rho(\mathbf{x}, t_0; \mathbf{x_0}) = \delta(\mathbf{x} - \mathbf{x_0})$. The solution to (2.1.7) is given for spatially periodic problems, with period L, as:

$$\rho(\mathbf{x}, t; \mathbf{x_0}, t_0) = \frac{1}{L^d} \sum_{\frac{L\vec{k}}{2\pi} \in \mathbb{Z}^d} \mathrm{e}^{i\vec{k}\cdot(\mathbf{x}-\mathbf{x_0}) - \frac{1}{2}\vec{k}\cdot M(t-t_0;\mathbf{x_0})\cdot\vec{k}}, \tag{2.1.8}$$

where $M(t - t_0; \mathbf{x_0})$ is the covariance matrix ($\mathbf{K}^{eff} = \frac{1}{2}\frac{d}{dt}\mathbf{M}$). From this, the solution to (2.1.2) with the addition of a general source sink distribution $s(\mathbf{x}, t)$, can be approximated with:

$$\theta_{DDT}(\mathbf{x}, t) = \int_0^t \int_{[0,L]^d} \rho(\mathbf{x}, t; \mathbf{x_0}) s(\mathbf{x_0}, t_0) d\mathbf{x_0} dt_0. \tag{2.1.9}$$

This is the scalar distribution given by Dispersion Diffusion Theory (Lin *et al.*, 2010). Since DDT retains the dependence on initial position in the effective diffusivity, it is viewed as a generalization of Batchelor's inital theory for stirring by homogeneous turbulence. For the flow used in Lin *et al.* (2010) an analytic expression for $\mathbf{K}^{eff}$ is found, however if the flow is too complex then obtaining an analytic representation for $\mathbf{K}^{eff}$ for arbitrary location and time is not possible. The difficulty of obtaining analytic representations for the moments is understood easily with the infinitesimal generator approach, where lower order moments are constructed from higher order moments. Thus, if there isn't some form of a closure condition then the moment approximations cannot be obtained.

Instead of looking for a global operator, the methodology calls for searching for a local operator that takes flow structures into account. Since this effective-diffusion operator can vary with location, this would naturally be describing an anamolous diffusion/transport process. The standard diffusion process is recovered if the local operators are the same. As such, these constrained effective-diffusion operators should be viewed as a generalization of the work in Lin *et al.* (2010).

The Fractional Diffusion Equation

To properly account for transport barriers, the presence of "trapping" and large "jump" events need to be included in the model. Let the "jump" probability distribution function (pdf) be given as $\lambda(\xi)$, and the waiting-time pdf be given as $\phi(\tau)$. For the waiting-time pdf, instead of jump events occuring at regular intervals, the time between jumps, $\tau_i = t_i - t_{i-1}$, is a random variable drawn from the pdf $\phi(\tau)$. The probability of finding a particle at position $\mathbf{x}$ and time t is determined by the Montroll-Weiss equation:

$$P(\mathbf{x}, t) = \delta(\mathbf{x}) \int_t^{\infty} \phi(t')dt' + \int_0^t \phi(t-t') \int_{-\infty}^{\infty} \lambda(\mathbf{x}-\mathbf{x}')p(\mathbf{x}', t')d\mathbf{x}'dt'. \tag{2.1.10}$$

Here the first term corresponds to tracers that haven't moved during the interval $\big[0, t\big]$. The second term corresponds to tracers moving from $\mathbf{x}'$ to $\mathbf{x}$. For the standard diffusion process $\lambda(\xi)$ is a Gaussian (corresponding to Fickian transport), and $\phi(\tau)$ is exponentially decaying (corresponding to a Markovian process). However, a wide range of waiting-times (due to trapping eddy regions) and broad jump distributions (due to avalanche-like transport) have been seen in problems of interest.

It was noted in del Castillo-Negrete *et al.* (2004) that the standard diffusion model was not sufficient for describing the anomalous transport experienced by tracer particles advected in a turbulent plasma. Although this seems like a niche shortcoming, the underlying problem is of great interest. The problem comes from nonlocal effects in space and time. In order to correctly capture the non-Fickian and non-Markovian transport aspects a fractional diffusion model was introduced. This model can be obtained from applying Fourier and Laplace transforms to (2.1.10), which provides:

$$\hat{\tilde{P}}_{rh}(\mathbf{k}, s) = \frac{1-\tilde{\psi}(rs)}{s}\frac{1}{1-\tilde{\psi}(rs)\hat{\lambda}(h\mathbf{k})}, \tag{2.1.11}$$

where r and h are scaling parameters and the Fourier and Laplace transforms are denoted by the hat($\hat{\cdot}$) and tilde($\tilde{\cdot}$), respectively. In the standard diffusion model, the Markovian-Fickian case, the waiting-time and jump pdfs are assumed to be of the following forms:

$$\psi_M(\tau) = \mu e^{-\mu\tau}, \qquad \lambda_F(\zeta) = \frac{1}{\sqrt{2\pi\sigma}}e^{-\zeta^2/(2\sigma)}, \tag{2.1.12}$$

where $\langle\tau\rangle = 1/\mu$ is the characteristic waiting-time, and σ is the characteristic mean-square jump. From taking the transforms, expanding the resulting expressions, and substituting the results back into (2.1.11) the Laplace-Fourier formulation of the standard diffusion model is obtained; as $r, h \to 0$ this is given as:

$$s\hat{\tilde{P}}(k, s) - 1 = -\chi k^2 \hat{\tilde{P}}(k, s), \tag{2.1.13}$$

where $\chi = h^2\sigma\mu/(2r)$. However, if the Markovian or Fickian assumptions are not valid, such a simple model is not obtained. In del Castillo-Negrete *et al.* (2004) jump and waiting-time pdfs are assumed to have asymptotic algebraic decay, these are given as, $\phi \sim \tau^{-(\beta+1)}$ and $\lambda \sim |\xi|^{-(\alpha+1)}$, where α and β are bound. The resulting Laplace-Fourier formulation is thus given as:

$$s^\beta\hat{\tilde{P}}(k, s) - s^{\beta-1} = -\chi|k|^\alpha\hat{\tilde{P}}(k, s), \tag{2.1.14}$$

where $\chi = c_2h^\alpha/(c_1r^\beta)$ is a finite constant, with c_1 and c_2 coming from the expansion of the waiting-time and jump pdfs, respectively. It is noted that (2.1.14) is not obtainable from the Laplace-Fourier transforms of simple derivative operators, but instead fractional derivative operators must be used. The Caputo definition of the fractional derivative operator is given here,

$$ {}_0^cD_t^\beta \phi = \frac{1}{\Gamma(1-\beta)} \int_0^t \frac{\partial_\tau \phi(x,\tau)}{(t-\tau)^\beta} d\tau, \tag{2.1.15} $$

and has the necessary Laplace-Fourier transforms to replace the time derivative. This definition also has the added benefit that it reduces to the standard derivative operator for integer values of β. For the spatial derivatives the definitions for the left and right Riemann-Liouville derivatives are used:

$$ \begin{aligned} {}_0D_x^\alpha \phi &= \frac{1}{\Gamma(m-\alpha)} \frac{\partial^m}{\partial x^m} \int_a^x \frac{\phi(y,\tau)}{(x-y)^{\alpha+1-m}} dy, \\ {}_xD_b^\alpha \phi &= \frac{1}{\Gamma(m-\alpha)} \frac{\partial^m}{\partial x^m} \int_x^b \frac{\phi(y,\tau)}{(y-x)^{\alpha+1-m}} dy, \end{aligned} \tag{2.1.16} $$

where m is the smallest positive integer that is greater than α. It is noted that due to issues at the boundaries the Caputo definition might be used for space as well; owing to the fact that the regularized definitions absorb boundary conditions.

With these definitions the fractional diffusion equation is given as,

$$ {}_0^cD_t^\beta P = \chi \left(\frac{1+\varsigma}{2} {}_0D_x^\alpha P + \frac{1-\varsigma}{2} {}_xD_b^\alpha P \right), \tag{2.1.17} $$

where ς is a skewness parameter that accounts for jumps having a preferential direction in heterogeneous systems. This model provides a direct relation between the scalings of the jump and waiting-time pdfs and the differential operators. Using the rates of decay from the pdfs, (2.1.17) can be used to model the evolution of tracer particles. Further, it was noted in del Castillo-Negrete *et al.* (2004) that for the symmetric case ($\varsigma = 0$), the Green's function is obtained as,

$$ G(x,t) = \frac{1}{2\pi} \int_{-\infty}^{\infty} e^{ikx} \mathcal{E}_\beta \left(-\chi |k|^\alpha t^\beta \right) dk, \tag{2.1.18} $$

where $\mathcal{E}_\beta(z)$ is the Mittag-Leffler function, given as:

$$ \mathcal{E}_\beta(z) = \sum_{n=0}^{\infty} \frac{z^n}{\Gamma(\beta n + 1)}. \tag{2.1.19} $$

For $\alpha = 2$ and $\beta = 1$ (parameters consistent with the standard diffusion model), the Green's function given in (2.1.5) is recovered.

Random Displacement Model

The partial differential equation (PDE) given by (2.1.2) is the Fokker-Planck equation to be solved, which can be accomplished by direct numerical simulations (DNS). However, since the investigation is on how the release position of a tracer patch — the initial condition to (2.1.2) — affects the solution, DNS would have to be computed for a large number of ICs; this method quickly becomes computationally expensive. Further, (2.1.2) corresponds to viewing the problem in the Eulerian prespective, where values at fixed points are measured as a function of time. The mixing process can also be modeled in the Lagrangian perspective, where trajectories are computed as a function of time, defining a dynamical system.

In using this Lagrangian perspective, the Fokker-Planck equation is approximated as a system of stochastic differential equations (SDEs) – one possible form of a random displacement model (RDM). Random displacement models are defined as the evolution of a large ensemble of passive tracers with stochastic trajectories. Since the trajectories of passive tracers are independent, they can be computed in parallel which allows the method to experience a reduction in the computational time.

The RDM that corresponds to (2.1.2) is given by:

$$d\mathbf{X}(t) = \mathbf{u}\left(\mathbf{X}(t), t\right) dt + \sqrt{2\kappa} d\mathbf{W}(t), \tag{2.2.1}$$

where $\mathbf{X}(t)$ represents the location of the passive tracers at time t, and $\mathbf{W}$ is canonical d-dimensional Brownian motion; thus $d\mathbf{W}$ is Gaussian white-noise. Since the noise comes from a Gaussian distribution, (2.2.1) models the standard diffusion process.

The diffusion model, when viewed at the microscopic level, is the work of an uncorrelated Gaussian stochastic process, whereas anomalous diffusion is related to continuous-time random walk (CTRW) processes. Thus the RDM must be able to handle non-Gaussian diffusion as well. This can be done by changing the stochastic perturbation to come from a more general distribution. The RDM used in this work varies only slightly from (2.2.1), as seen here:

$$d\mathbf{X}(t) = \mathbf{u}\left(\mathbf{X}(t), t\right) dt + D d\mathbf{L}(t), \tag{2.2.2}$$

where D represents the magnitude of the stochastic perturbation (previously $\sqrt{2\kappa}$), and the noise vector is $\mathbf{L} = R\mathcal{B}_d$, where R is an α-stable random variable, and $\mathcal{B}_d$ is the d-dimensional unit sphere. In the 3D setting, $\mathbf{L} = \left[R\sqrt{1-S^2}\cos\theta, R\sqrt{1-S^2}\sin\theta, RS\right]$, where θ is a uniformly distributed random variable taking values in $[0, 2\pi]$, and S comes from a uniform distribution for $[-1, 1]$. For the 2D cases, $S = 0$ ($\mathbf{L} = \left[R\cos\theta, R\sin\theta\right]$). R is symmetric, mean-zero, unit-scale with the characteristic exponent α. The flexibility in this model allows for the modeling of Gaussian noise ($\alpha = 2$), as well as super($\alpha < 2$) and sub($\alpha > 2$) diffusive cases. In the following analysis two values for α were used: $\alpha = 2$ and $\alpha = 1.5$ (Lévy noise). When investigating the evolution of deterministic trajectories, $D = 0$.

Dynamical Systems and Coherent Structures

As alluded to earlier, the Lagrangian trajectories of passive tracers define a dynamical system. As such the discussion naturally begins with the classification of dynamical system types. For the systems considered herein two classifications are possible: autonomous and nonautonomous. Autonomous dynamical systems are noted by their lack of dependence on time. Time-periodic flows can be viewed as autonomous systems by looking at maps corresponding to the period of the flow (shown later). The other types of systems, nonautonomous systems, have a general time dependence, which make coherent structure identification not as well defined, since there is no characteristic timescale.

Let $\Phi : X \to Y$ denote a general *autonomous system*, with $X, Y \subseteq \mathbb{R}^d$. For the flow fields investigated herein either periodic or no-slip boundary conditions are used; this reduces the autonomous system to $\Phi : X \to X$. For autonomous systems, the manifolds connecting fixed points can be used to analyze the system behavior. These invariant manifolds are impenetrable to deterministic trajectories and therefore demarcates the dynamics of the system. This is beautifully discussed and depicted in Ottino (1989).

Let $\Phi : X \times \mathbb{R} \to Y$ denote a general *nonautonomous system*. Due to the boundary conditions, the system reduces to $\Phi : X \times \mathbb{R} \to X$. For a periodic flow with period T, the time-T map of the ODE can be used to describe the system in continuous time. The advantage to time-periodic systems is that although the ability to use manifolds is lost over time, with Poincaré sections the precise underlying skeleton of the mixing process can be uncovered. For flows with general time dependence neither invariant manifold theory nor Poincaré sections are suited for the analysis.

As the methods and theories of nonlinear dynamical systems have evolved over previous decades, the objective extraction of coherent structures in nonautonomous systems has also gained popularity. The term "coherent structures" is used to refer to trajectories of dynamic systems that have major influence over nearby trajectories. The term "Lagrangian coherent structures" (LCSs) is used to refer to coherent structures that maintain this property under the action of the dynamic system for some finite-time. Due to their characteristic of inhibiting transport normal to themselves, the presence of these structures naturally lead to anomalous transport and thus they should be viewed as finite-time transport barriers. Generally speaking, in the context of the deterministic advection of a passive tracer, if the tracer is in a coherent region (a region bounded by LCSs) at *some* time then it will remain in that coherent region for the *lifespan*[1] of that coherent region. Since the passive tracer has a deterministic trajectory it will not be able to cross the boundaries of these coherent regions.

As forcing is introduced into the system, transport barriers can start to form. These transport barriers typically present themselves as regions of high strain, large vorticity, or some combination of the two, and could describe physical flow features such as the boundaries of a jet or an eddy region (which correspond to hyperbolic points and KAM regions in the dynamical systems context, respectively). Regardless of the properties of the regions bound by LCSs, LCSs themselves have an inherent property of limiting exchange across themselves. If a LCS forms a closed "curve", it encloses a coherent region. These regions can correspond to persistent KAM curves or the temporary boundary of an eddy region that will be destroyed over time.

Probabilistic LCS Detection Methods

There are two main families of LCS detection methods: geometric and probabilistic. Various methods from both families will be discussed in greater detail in Sections 4.2 and 7.2, while the initial steps for the probabilistic methods are introduced here. The family of probabilistic methods ignore the local transport barrier structures, but instead divide the *phase space* into minimally dispersive sets. These are classified as invariant sets, almost invariant sets, or finite-time coherent sets (dependent on the particular method used and the type of system). Invariant sets and almost-invariant sets are appropriate for autonomous systems, while finite-time coherent sets should be used for nonautonomous systems. The reasoning for this distinction will be clear after the following discussion.

---

[1] The lifespan of a coherent feature is simply the time until the feature becomes decorrelated.

Let $Y \subseteq X \subseteq \mathbb{R}^d$ be closed, it is invariant under the map F if $Y = F^{-1}(Y)$. Almost invariant sets (AISs) are those that approximately satisfy the previous condition, i.e. Y is almost invariant under the mapping F if $Y \approx F^{-1}(Y)$, with respect to the appropriate measure. A finite-time coherent set (FTCS) is inherently different in the fact that the previous two set types (invariant and almost-invariant) were both fixed in phase space. FTCS are sets that come in pairs and are free to move in phase space. They can be defined as follows: Y_{t_0} and $Y_{t_0+\tau}$ are finite-time coherent pairs if $Y_{t_0} \approx F^{-1}\left(Y_{t_0+\tau}\right)$. The probabilistic methods rely on the Perron-Forbenius (or transfer) operator, which is commonly approximated by the Ulam-Galerkin matrix.

Before being able to construct the Ulam-Galerkin matrix, or its' approximation, further definitions are needed. Let $X \subseteq \mathbb{R}^d$ and $Y \subseteq \Phi\left(X\right)$, where Φ defines a general nonautonomous system, define the collection of sets (B_i) and (C_j) to be mutually exclusive covers of X and Y, respectively. This is more clearly written and understood as:

$$X = \bigcup_{i=1}^{n} B_i, \quad \text{and} \quad Y = \bigcup_{j=1}^{m} C_j, \tag{2.4.1}$$

where n and m denote the number of elements in the cover of X and Y, respectively. Note here that in general both (n, m) and (X, Y) need not be the same. Due to the boundary conditions applied, X and Y will be taken as the same. Even with this, it is possible for n and m to be varied, i.e. two different covers. However, in the following they are conveniently taken to be the same.

With the above in mind, the approximation to the Ulam-Galerkin matrix can be written as:

$$P(t)_{ij} = \frac{\#\{x_k | x_k \in B_i \text{ and } \Phi(x_k) \in B_j\}}{\#\{x_k | x_k \in B_i\}} \tag{2.4.2}$$

where the sequence $\{x_k\}$ is an ensemble of passive tracers, B_i is the set the tracers are in at time t_0, B_j is the set that the image of the tracers (that were originally in

B_i) are in at time t, and # denotes the tracer count – number of members from the ensemle satisfying the conditions. Note that since the covers are the same $C_j := B_j$. From here on, the explicit time dependence will be suppressed.

Moment Approximation

Instead of advection via a general flow, if the advection is linear in the coordinates then (2.1.3) can be rewritten as:

$$\partial_t \theta + \mathbf{A}(t) \cdot \mathbf{x} \cdot \nabla \theta = \frac{1}{2} \nabla \cdot (\mathbf{D} \nabla \theta)\,, \quad \theta(\mathbf{x}, t_0) = \theta_0(\mathbf{x}), \tag{2.5.1}$$

where $\mathbf{A}$ and $\mathbf{D}$ are constant matrices; specifically, the Jacobian and the diffusivity tensor, respectively. The advantage to approximating the transport process as a series of linear systems (in d dimensions) is that for an initial condition of $\theta\left(\mathbf{x}, t_0\right) = \delta^d(\mathbf{x} - \mathbf{x}_0)$, a spiked initial concentration at the centroid defined by $\mathbf{x}_0$, the problem in (2.5.1) has a closed-form solution. This solution is dependent on the first and second-order moments, and is found in Van Kampen (1992) as:

$$\theta\left(\mathbf{x}, t\right) = (2\pi)^{-d/2} \left(\det \mathbf{M}(t)\right)^{-1/2} \exp(-\frac{1}{2}(\mathbf{x}^T - \langle \mathbf{x}^T \rangle) \mathbf{M}^{-1}(t)(\mathbf{x} - \langle \mathbf{x} \rangle)), \tag{2.5.2}$$

where $\mathbf{M}(t)$ is the covariance matrix and $\langle \cdot \rangle$ indicates spatial average. The moments can be computed as:

$$\begin{aligned} \langle \mathbf{x} \rangle &= \mathrm{e}^{t\mathbf{A}} \mathbf{x_0}, & (2.5.3) \\ \mathbf{M}(t) &= \int_0^t \mathrm{e}^{(t-s)\mathbf{A}} \mathbf{D} \mathrm{e}^{(t-s)\mathbf{A}^T} ds. & (2.5.4) \end{aligned}$$

From the above: given $\mathbf{A}$ and $\mathbf{D}$, or being able to compute them, provides the time evolution of the moments, which can be used to compute the scalar distribution. Further, it is seen that with our choice of $\mathbf{D}$ that (2.5.4) reduces to the following:

$$\mathbf{M}(t) = 2\kappa \int_0^t \mathrm{e}^{(t-s)\left(\mathbf{A} + \mathbf{A}^T\right)} ds. \tag{2.5.5}$$

With this reduction, it is easy to see that the moment evolution given by (2.5.5) is based on a symmetrized flow: the rotational component is lost. Therefore, this equation is only capable of describing the evolution of the elements of the covariance matrix, and not its orientation. Later other methods for obtaining these covariance matrices that retain the orientation will be investigated.

Given the scalar concentration as defined in (2.5.2), an analytic representation can be obtained for the scalar variance as well. Setting $\langle \theta \rangle = 0$, the variance simplifies to $Var(t) = \langle \theta^2 \rangle$. For θ given by (2.5.2), the vairance is:

$$Var_K(t) = \frac{1}{(2\pi)^d V} \int \left(\det \mathbf{M}(t) \right)^{-1} \exp(-(\mathbf{x}^T - \langle \mathbf{x}^T \rangle)\mathbf{M}^{-1}(t)(\mathbf{x} - \langle \mathbf{x} \rangle))d\mathbf{x}, \quad (2.5.6)$$

where V represents the volume of the domain.

Further, for linear systems of the form (2.5.1) it was shown in Zeldovich *et al.* (1984) and similarly in Thiffeault (2008) that the resulting scalar concentration can be analytically computed using Fourier transforms. In Thiffeault (2008) this is shown as:

$$\theta(\mathbf{x}, t) = \int \hat{\theta}_0(\mathbf{k}_0) \exp\left(-i\mathbf{x} \cdot T_t \cdot \mathbf{k}_0 - \kappa \int_0^t (T_s \cdot \mathbf{k}_0)^2 \, ds \right) d^d k_0, \quad (2.5.7)$$

where $\hat{\theta}_0(\mathbf{k}_0)$ is the Fourier transform of the initial distribution with $\mathbf{k}_0$ as the initial wavevector (multidimensional set of wavenumbers), and T_t is the fundemental solution. The most general expression defining T_t is given as follows:

$$T_t = \exp\left(-\int_0^t A(s) ds \right), \quad T_0 = \mathbf{I}, \quad (2.5.8)$$

where $A(t)$ is the matrix defining the linear system at time t. Recall that this expression is only for linear flows, and further, that (2.5.8) can be reduced for systems independent of time. An analytic representation for the variance is also given in Thiffeault (2008) as:

$$Var_T(t) = \int |\hat{\theta}_0(\mathbf{k}_0)|^2 \exp\left(-2\kappa \int_0^t (T_s \cdot \mathbf{k}_0)^2 \, ds \right) d^d k_0. \quad (2.5.9)$$

Being able to provide an accurate approximation to the scalar variance, it can be incorporated into an effective-diffusion model that is conditional on structure.

PART 1 -

THE 1D CASE

Chapter 3

ONE-DIMENSIONAL ANALYSIS

A one-dimensional setting provides a useful framework for introducing the analysis methodology, and is the natural starting point. In Taylor's seminal work (Taylor, 1920) in order to simplify the analysis for his interests, concerned himself only in the transmission of heat in one direction. With considering a uniform flow, he found that the rate of heat transfer was determined by the mean-value of the traversed distance squared; giving a relation that connected the flow to the scalar moments. Given the flow as $\dot{x} = u$, then the mean value of heat transfer is given by $[u(x-a)]$. Letting $X = x - a$ the heat transfer is given by:

$$[u(x-a)] = \left[X\frac{dX}{dt}\right] = \frac{1}{2}\frac{d}{dt}\left[X^2\right]. \tag{3.0.1}$$

Further, by observing the downwind distribution of smoke from smoke stacks Taylor was able to find rich relations between the moments corresponding to the distributions. It is with his understanding of how a nonphysical abstraction can still provide deep understanding of a physical case that the one-dimensional case is pursued.

Stability Analysis

In 1D flows the analogue to transport barriers are the fixed points of the system. These points provide clear distinctions of the separation of the different dynamics of the system. Even in higher dimensions the connections between hyperbolic fixed points can still be seen to accurately demarcate the flow.

However, in one dimension fixed points are only distinguished as stable (sink/attractor) or unstable (source/repellor). From finding these fixed points and analyzing their stability predictions to the final state behavior of the system are obtained. Given the

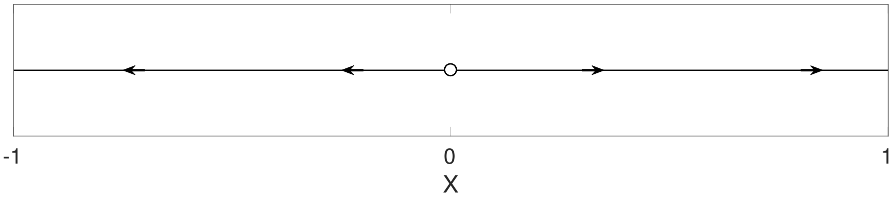

Figure 3.1.1: The phase plot for the exponential growth function shows trajectories moving away from an unstable fixed point at zero, shown as an open circle.

system as $\dot{x} = f(x)$, the 1D phase space is the x-axis, where $x(t)$ represents a trajectory. The only possible outcomes for the trajectories in a vector field on the real line, is that they either approach fixed points or diverge to $\pm\infty$. The fixed points, x^*, of the system correspond to $f(x^*) = 0$. The direction of the transmission of data near a fixed point can be obtained from looking at the sign of $\frac{df}{dx}$ evaluated at that point.

As an example of this method, the simplest linear model will be used, the exponential growth (or decay) function; given by (3.2.1). Due to only having one fixed point the dynamics of the system are very dull: if $\mu > 0$, then $x(0) \in (0, \infty)$ will tend towards infinity, while $x(0) \in (-\infty, 0)$ tends towards $-\infty$. This idea is displayed graphically with the phase plot seen in Fig. 3.1.1, where the arrows indicate the direction of a trajectory, and the circle is the fixed point. The circle is hollow to indicate that the fixed point in unstable. By increasing the number of fixed points, the number of resulting possible final states can also increase. The question then becomes - is it possible, in one of these systems, that the outcome for a trajectory can be changed by perturbations to the trajectory? As will be discussed later, the answer to this question is an uninteresting yes.

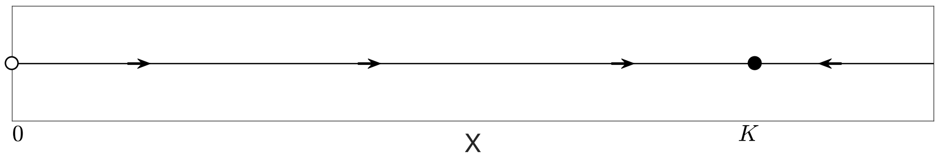

Figure 3.2.1: The phase plot for the logistic equation shows and unstable fixed point at zero and a stable fixed point at K. The stable fixed point is a solid dot, and attracts trajectories from above and below.

Flows and Analysis

The 1D flows investigated were chosen to exhibit a range of behaviors for the trajectories. Below is a list of the different standard one-dimensional cases investigated, along with the fixed points and the type of system represented, where $\mu \in \mathbb{R}$ and $K \in \mathbb{R}^+$.

$$\dot{x} = \mu x, \qquad x^* = 0 \qquad \text{exponential growth} \tag{3.2.1}$$

$$\dot{x} = \mu x(1 - \frac{x}{K}), \qquad x^* = 0, K \qquad \text{logistic growth} \tag{3.2.2}$$

$$\dot{x} = \mu x - x^2, \qquad x^* = 0, \mu \qquad \text{transcritical bifurcation} \tag{3.2.3}$$

$$\dot{x} = \mu x - x^3, \qquad x^* = 0, \pm\sqrt{\mu} \qquad \text{pitchfork bifurcation} \tag{3.2.4}$$

By definition the deterministic trajectories of all the above systems are given by $x(t) = x(0) + \int_0^t \dot{x}(s)ds$. From a perturbation analysis of the trajectories of the exponential model, it is clear that only perturbations around $x = 0$ can result in a change of final states. Given the solution to the exponential model is $x(t) = x(0)e^{\mu t}$, then initially the solution can be approximated by $x(t) \approx x(0)(1 + \mu t)$, for $t << 1$. Thus, for a trajectory initiated near $x = 0$ at some location $b > 0$, a perturbation of magnitude $\epsilon > b(1 + \mu \Delta t)$ could force the trajectory to become negative and diverge to $-\infty$, instead of ∞.

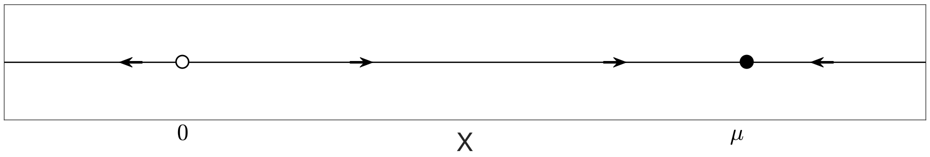

Figure 3.2.2: The phase plot for the transcritical bifurcation is similar to that of the logistic equation. Since trajectories are defined for negative values, values below zero are included.

Having just discussed the growth equation, a system with more interesting dynamics is now analyzed. The logistic equation (3.2.2) admits 2 fixed points: one stable and one unstable. Fig. 3.2.1 gives the phase space plot for the logistic equation. It is first noted that since this equation is intended to model population dynamics, all values of x are non-negative. Further, for $x \in (0, K]$ trajectories tend toward K from below, while if $x \in [K, \infty)$ then the trajectories tend toward K from above; indicating that K is a stable fixed point, and 0 is unstable. The same behavior from the exponential model is essentially seen for the logistic model; any perturbation away from $x = 0$ results in trajectories reaching the final state K.

The transcritical bifurcation is similar to the logistic equation in terms of the type of behavior observed; the phase plot for the transcritical bifurcation is given in Fig. 3.2.2. For the transcritical bifurcation the perturbation around $x = 0$ can either lead trajectories to the fixed point or diverge to $-\infty$. This situation changes slightly for the pitchfork bifurcation – where, on both sides of the unstable fixed point, lie stable fixed points. From the phase plot in Fig. 3.2.3, it is clear that only perturbations around $x = 0$ can result in trajectories approaching either fixed point.

1-dimensional Model of a Limit Cycle

In 2D settings the dynamics are more interesting, and it is possible to have limit cycles around fixed points. These limit cycles are periodic orbits that can either be

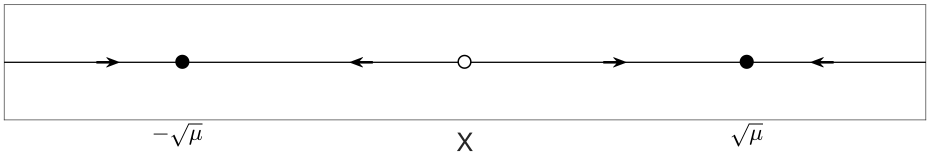

Figure 3.2.3: The phase plot for the pitchfork bifurcation has 3 fixed points: 2 stable, and an unstable fixed point between them. Depending on which side of the unstable fixed point a trajectory starts will predict what fixed point it goes to.

stable or unstable – unstable cycles either expand away from or contract towards a fixed point. For this analysis an unstable repelling limit cycle is presented, and a model is given to describe the return map behavior of trajectories along a fixed axis.

First consider the 1D return map of a 2D trajectory around a limit cycle centered at 0. This model is obtained from only looking at the intersection of the trajectories with the x-axis. An approximation to an unstable limit cycle is obtained from the map $x_{n+1} = -x_n|x_n|$. This model represents decaying spiral trajectories within the bounds of the limit cycle $x \in (-1, 1)$, and expanding spiral trajectories outside of the limit cycle, $x \in (-\infty, -1) \cup (1, \infty)$. While trajectories on the boundary $x \in \{-1, 1\}$ are seen to have periodic orbits, and remain on the boundary. However, it is noted that the accumulation of trajectories to the center of the limit cycle is not physically motivated from the viewpoint of incompressibility. To remedy this a piecewise model is introduced to represent the more realistic return behavior of trajectories inside a vortex (limit cycle). This map is,

$$x_{n+1} = \begin{cases} -x_n, & \text{if } |x_n| \leq 1 \\ -(1+\alpha)\, x_n, & \text{if } |x_n| > 1 \end{cases}, \tag{3.3.1}$$

with the parameter $\alpha > 0$. On the interior of the structure trajectories follow smooth periodic orbits, while on the exterior the trajectories are shed from the edge of the

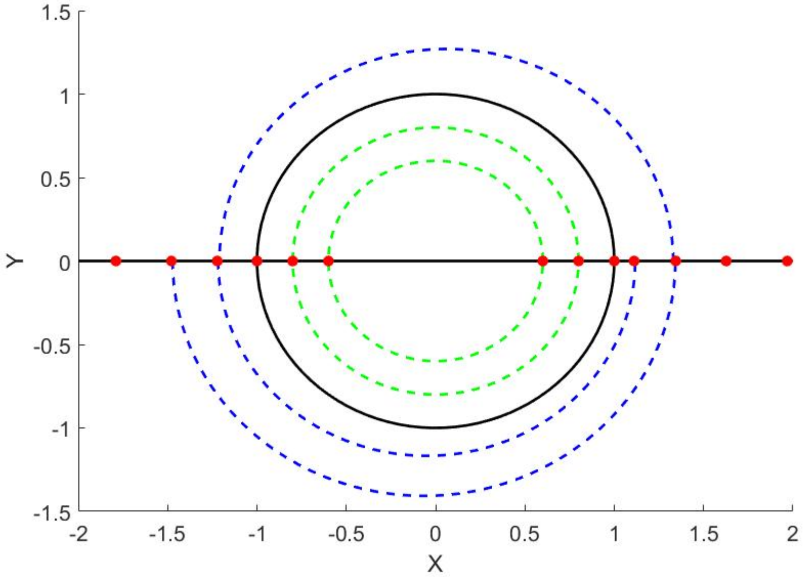

Figure 3.3.1: The return map for the piecewise limit-cycle model shows stable trajectories (in green) inside the bounds of the limit cycle (solid black curve). The blue dashed curve highlights an unstable trajectory, and red dots are used to indicate the return map of the trajectories.

limit cycle; this behavior is seen in Fig. 3.3.1 as the dashed green line (stable periodic orbits) and the dashed blue line (an unstable spiral). The separatrix is seen as the solid black circle with unit radius centered around zero – it is this curve that distinguishes between the behavior seen in the system. The red dots in Fig. 3.3.1 along the $Y = 0$ axis indicate the intersection of the trajectories with that axis.

When the trajectories are deterministic then all trajectories initiated within the structure will be contained within it, and all trajectories initiated outside will spiral away. For the trajectories within the structure this provides simple return maps, where the location is just flipped about the $X = 0$ axis, i.e. $x_{n+1} = -x_n$. If the trajectories are perturbed or slightly stochastic then these behaviors will change. To investigate the impact noise plays in the change of behavior four different perturbation levels are used: $D = \sqrt{.00002}$, $D = \sqrt{.0002}$, $D = \sqrt{.002}$, and $D = \sqrt{.02}$. Trajectories are initiated from $x \in [-1.5, 1.5]$ with $y = 0$; 50000 realizations are used for each initial condition. Since there is a natural competition between D and α, three different α values are used; representing rapid ($\alpha = .1$), moderate ($\alpha = .01$), and slowly ($\alpha = .001$) shedding cases .

Given the mapping as (3.3.1), the deterministic location of tracers initiated outside of the vortex after n iterations is given by, $x_n = (-1)^n(1+\alpha)^n x_0$; where x_0 is the initial tracer location. From this expression the escape time – the time it takes for trajectories outside of the vortex to leave the domain – for the deterministic trajectories can be analytically computed. With the domain arbitrarily taken to be $[-3, 3]$ and the bounds of the vortex having magnitude 1, the escape iteration is given by,

$$n_{escape} = \lceil \frac{\log 3}{\log(1+\alpha)} \rceil, \tag{3.3.2}$$

where $\lceil \cdot \rceil$ denotes the ceiling function, rounding up to the nearest integer. For the systems considered this results in $n_{escape} = [12, 111, 1100]$ for the $\alpha = [.1, .01, .001]$ cases, respectively. By looking at the number of tracers that remain inside the domain after these iterations the impact the noise plays to conteract the shedding can be seen.

In order to look at the retention rate of the original structure, a histogram of tracer locations was computed over the domain $[-3, 3]$ with a resolution of 512 elements; this results in a bin size of $\Delta x_{hist} = .0117$. With this bin spacing, all of the stochastic cases, except for $D = \sqrt{.00002}$, are capable of exhibiting *large* jumping behaviors – where tracers jump over a bin element completely on a single iteration of the map – this behavior is only enhanced in the rapidly shedding case. For the rapidly shedding cases the analytic jump in the map is $\alpha = .1$, thus even in the absence of noise, large jumps can occur in the histogram. Further, for the rapidly shedding cases, three of the four noise levels used are smaller than the magnitude of the shedding, indicating that the advective transport dominates diffusion. This means that even if the stochastic perturbation was *exactly* opposite to the motion of the deterministic portion, the trajectory would still have a net *positive* increase in distance from the center of the domain.

From looking at the time evolution of the histogram the behavior of the system is revealed. In the initial few iterations of the map, the deterministic trajectories that are originally outside the vortex boundary ($x \notin [-1, 1]$) begin to move to the boundary of the system. For $\alpha = .1$, these trajectories are seen as the section of red dots near the boundary at the 50000 level in Fig. 3.3.2. Further, initially right underneath these lines are plateaus (not shown) in the histograms for the three lowest noise levels. These plateaus correspond to a large number of the same initial trajectories as the red lines above them, with the remaining tracers moving further away from or towards the center of the domain. The larger the stochastic perturbation is the more smooth the histograms become, resulting in the features of the curves being lost at large noise levels.

In the case where $D = \sqrt{.02}$, the stochastic perturbation is able to overcome the motion of the deterministic mapping and a few trajectories initially outside of the vortex are able to invade. For a large enough perturbation the short-term behavior is described by two mechanisms: trajectories originally within some δ distance of the boundary (but outside of the structure) are able to cross into the stable region due to the perturbation, and trajectories originally within the structure are able to escape into the unstable region via the perturbation. The long-term behavior of the system is dominated by trajectories finally escaping the structure. In this case, although the perturbation is of a significant size (or perhaps due to this fact), the trajectories that invade the vortex, are expelled before 150 iterations. The quick rate of escape highlights the difficulties of trajectories to *return* to the vortex region after being

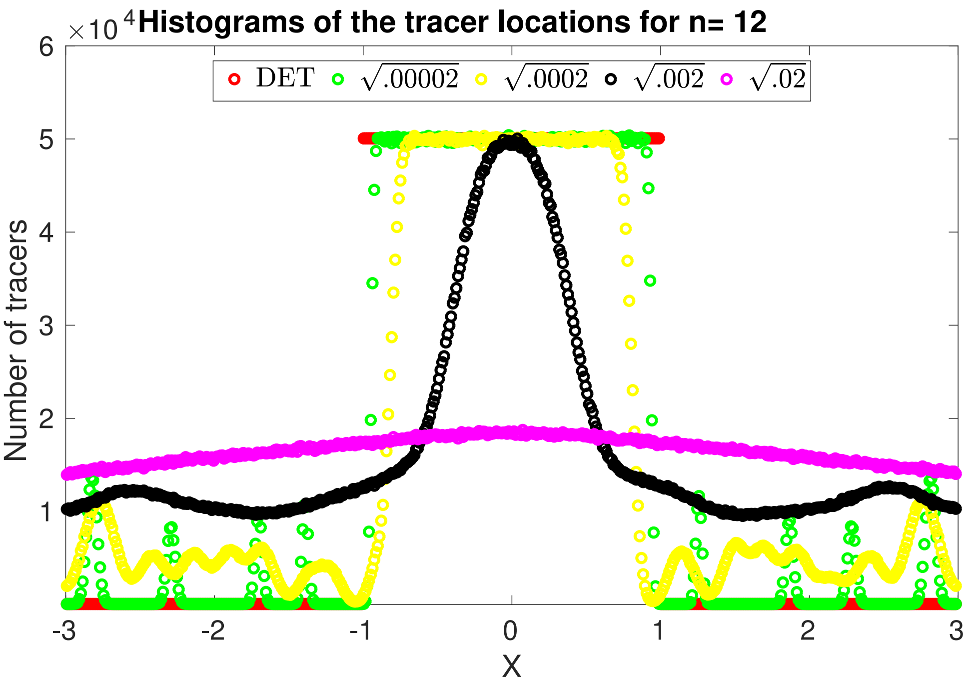

Figure 3.3.2: The histograms of the tracers locations after 12 iterations of the map. The map uses $\alpha = .1$. The red circles correspond to the deterministic trajectories, then in increasing levels of noise intensity are the green($\sqrt{.00002}$), yellow($\sqrt{.0002}$), black($\sqrt{.002}$), and magenta($\sqrt{.02}$) circles.

perturbed outside of it – this will be discussed further alongside the results of the other maps.

To further see the impact of noise on the retention rate of tracers in the vortex region, the ratio of the number of tracers in this region at final time over the number of tracers originally in the region is computed for the various noise levels; listed in Table 3.1. It is seen that, as expected, the ratio of retention for the deterministic cases are all 1, indicating no tracers were perturbed outside of the vortex. When small perturbations are made to the tracers, they are able to escape the vortex and become subject to the strength of the shedding. If the magnitude of the shedding is sufficiently greater than that of the perturbations, the tracers will not be able to return to the vortex. This is observed in the table as the increase of retention

	Deterministic	$\sqrt{.00002}$	$\sqrt{.0002}$	$\sqrt{.002}$	$\sqrt{.02}$
$\alpha = .1$	1	.6207	2×10^{-6}	0	0
$\alpha = .01$	1	.6152	.1186	.0205	.0128
$\alpha = .001$	1	.7725	.6811	.5137	.2184

Table 3.1: The ratio of tracers retained in the vortex region after 400 iterations of the map for various values of α; the different columns corresponding to the different noise levels.

rates as the shedding is lowered. When large perturbations are made to the tracers, the deterministic action is not able to compete, and tracers from throughout the vortex core find their way outside of the vortex region after enough iterations. This is observed as the low retention ratios for the strongest perturbation level.

When $\alpha = .01$, moderate shedding, the structures in the histograms are more well defined and long-lived. Shown in Fig. 3.3.3 are the histograms of the various noise levels for the map with $\alpha = .01$, after 110 iterations. With this α, the stochastic motion will dominate in all except the $D = \sqrt{.00002}$ case. The implications of this are seen in Fig. 3.3.3 as the smoothing out of the dynamics for all except the green curve. Further it is noted that for all the noise levels except $D = \sqrt{.00002}$, considerable amount of trajectories entered the vortex within the first 20 iterations. These trajectories then proceeded to diffuse out of the vortex and towards the domain boundaries. When $\alpha = .001$, slow shedding, the structures in the histograms are extremely long-lived since the dynamics are dominated by the perturbations. In this case, since the shedding is so weak, all of the perturbations are able to counteract the advective component of transport.

To look at the role of noise in the system, the decay rate of the maximum values in the histograms are computed. In Fig. 3.3.4 the maximum values of the histogram

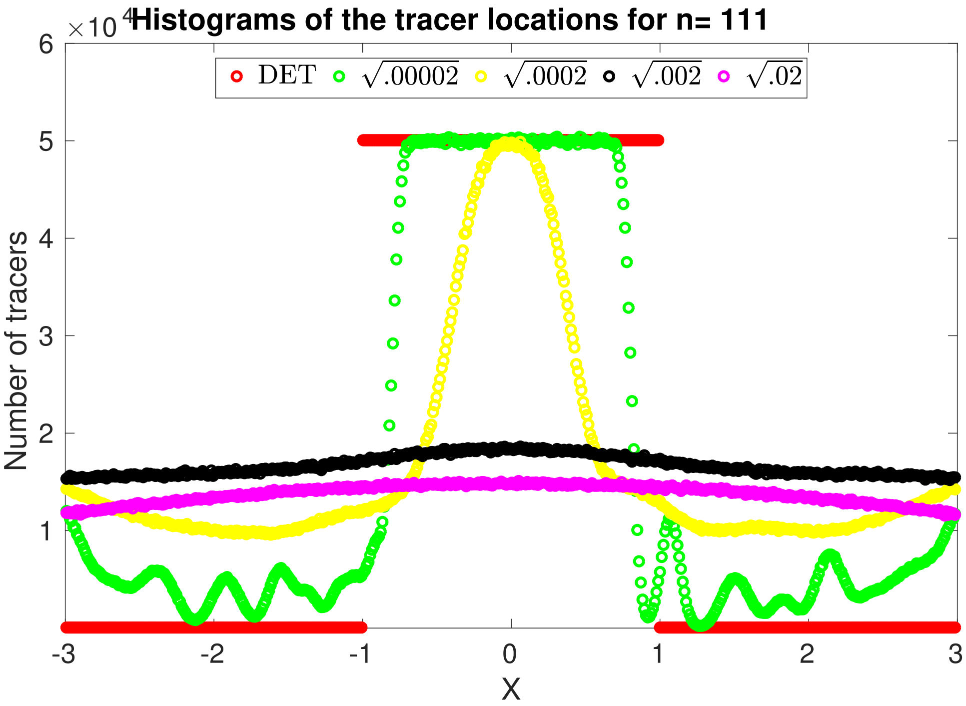

Figure 3.3.3: The histograms of the tracers locations after 111 iterations of the map. The map uses $\alpha = .01$. The red circles correspond to the deterministic trajectories, then in increasing levels of noise intensity are the green($\sqrt{.00002}$), yellow($\sqrt{.0002}$), black($\sqrt{.002}$), and magenta($\sqrt{.02}$) circles.

curves, that are inside the domain, are plotted as a function of time for the various α values. The different line styles are used to reflect the three α values, with solid lines for $\alpha = .001$, hollow circles for $\alpha = .01$, and dots for $\alpha = .1$. Black dashed curves are used to fit exponential functions of the form $e^{\gamma t}$ to the data. From Fig. 3.3.4 it is easy to see that for the $\alpha = .1$ map the decay rates are nearly identical for three of the noise levels, with $D = \sqrt{.00002}$ showing no decay. This result suggests that for $D = \sqrt{.00002}$, very few trajectories inside the vortex region have been expelled by diffusion. The results are similar for the $\alpha = .01$ cases: $D = \sqrt{.00002}$ shows no decay, while the other three curves are seen to follow the same exponential decay rate, $\gamma = -.01$. In the slowly shedding case the decay is very slow with γ taking values between $-.001$ and $-.002$.

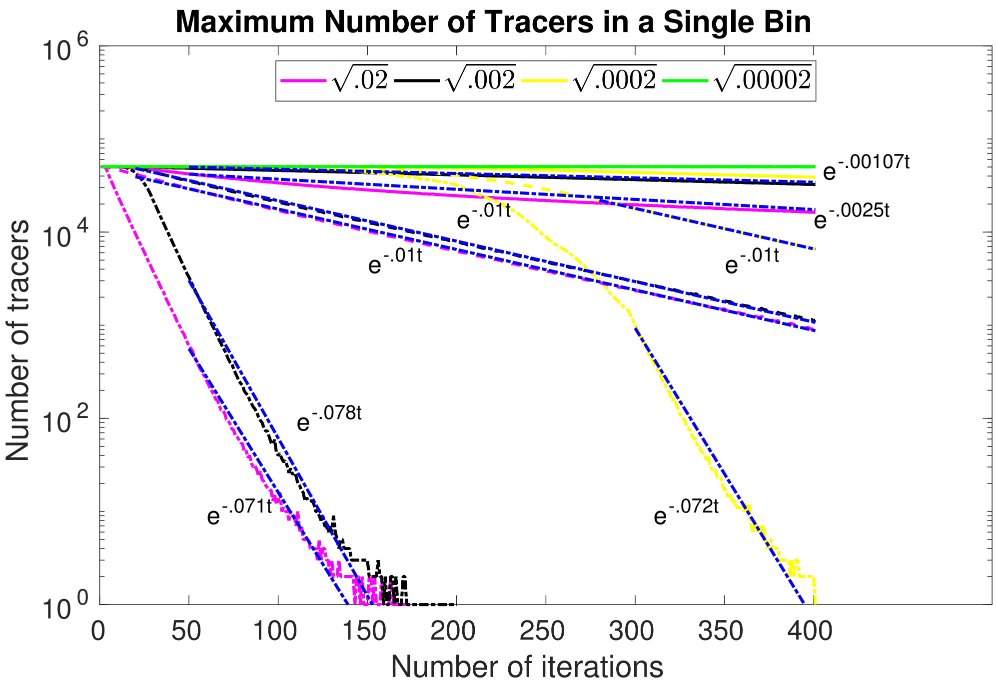

Figure 3.3.4: Time history of the maximum values inside the domain for the various maps and noise levels. The map that uses $\alpha = .1$ are shown as dash-dots, with the $\alpha = .01$ results shown with dash-dash, and $\alpha = .001$ with solid lines. The colors of the curves are used to distinguish the noise level used; green($\sqrt{.00002}$), yellow($\sqrt{.0002}$), black($\sqrt{.002}$), and magenta($\sqrt{.02}$) circles; blue dashed lines are used to show the scalings.

By tracking the number of tracers that originated outside of the vortex and have found their way inside via perturbations, the strength of the shedding can be observed. These time histories are plotted in Fig. 3.3.5 for the various α and D values. It is seen that for larger α values fewer trajectories are able to enter the vortex, and that for some of the noise levels no tracers are seen. This is expected as the deterministic motion expells trajectories too quickly from the vortex barrier for the stochastic perturbations to have a noticeable impact. In the $\alpha = .1$ case only one noise level is able to compete with the deterministic transport. For the moderate shedding case ($\alpha = .01$) three of the noise levels are seen to cause trajectories to enter the vortex region. A quick exponential decay is seen for the $D = \sqrt{.0002}$ case, with $\gamma = -.21$.

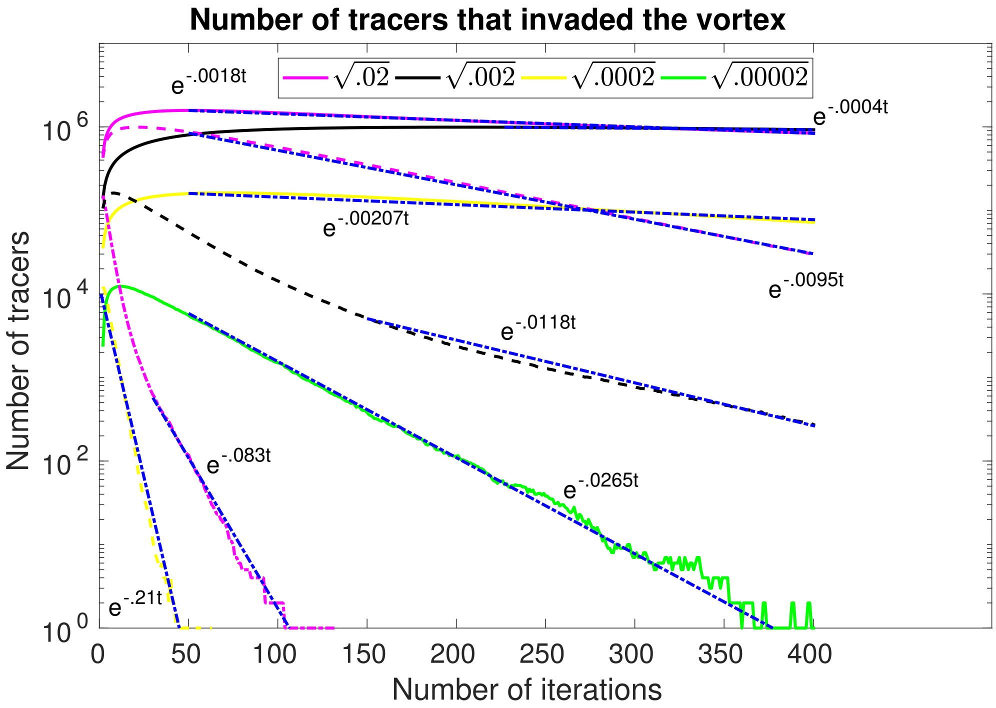

Figure 3.3.5: Time history of trajectories initiated outside the vortex that have invaded for the various α and D values. The line styles designate which α value is used: dash-dot ($\alpha = .1$), dash-dash ($\alpha = .01$), and solid lines ($\alpha = .001$). Colors are used to distinguish what noise level is used: green ($\sqrt{.00002}$), yellow ($\sqrt{.0002}$), black ($\sqrt{.002}$), and magenta ($\sqrt{.02}$); blue dashed lines are used to show the scalings.

The decay in this case is quick since the deterministic transport is in close competition with the stochastic perturbations. For the noise levels $D = \sqrt{.002}$ and $D = \sqrt{.02}$ the decay rates are lower because the perturbations dominate the transport. When $\alpha = .001$ only $D = \sqrt{.00002}$ provides results that are not completely dominated by the perturbations; this curve has a decay rate of $\gamma = -.0265$.

Solomon Experiment

To introduce the framework for the fractional diffusion model, the experiments of Solomon *et al.* (1993, 1994) are discussed, along with the model provided in del

Castillo-Negrete (1997). The experiments studied the dispersion of particles advected by a flow inside an annular tank; the bottom of the tank is slightly conical, to simulate the Coriolis effect seen in geophysical flows. The annulus is set to rotate at a constant rate, approximately $1-2$ Hertz; with such a rapid rotation the flow is quasi two-dimensional. Forcing is added to the system by pumping fluid through holes in the bottom of the tank, seen in Fig. 3 of Solomon *et al.* (1994); with other holes in the system to allow water to exit. When the forcing is sufficiently large the azimuthal flow becomes unstable, resulting in the formation of a vortex chain. When particles are inside a vortex they remain trapped for a very long time – this is referred to as *sticking* – while particles in the jet experience *flights* around the tank. In the experiments particles were seen to alternate between moving in the azimuthal direction and being trapped in vortices. The nearly neutrally bouyant particles in the experiment, made with fluorescent crayons and concrete powder, are tracked using automated image processing techniques.

In del Castillo-Negrete (1997) the following model was proposed to provide an analytic model to approximate the experimental setup:

$$\psi = -\log\left(\cosh y\right) + \zeta\left(x,t\right)\phi(y)\cos mx + cy, \tag{3.4.1}$$

with,

$$\begin{aligned} \zeta\left(x,t\right) &= a - \epsilon\cos^2\big(\left(x+\omega t\right)/2\big) \\ \phi(y) &= \left[1+\tanh y\right]^{\frac{1-c}{2}}\left[1-\tanh y\right]^{\frac{1+c}{2}}, \end{aligned} \tag{3.4.2}$$

where m is the number of vortices, c is the non-dimensional speed of the vortex chain, and ω is the frequency of the perturbation. The perturbation (3.4.2) is further defined with the parameters a and $\epsilon := \epsilon_0 + g$, where ϵ_0 is a constant and g is a random number from a Gaussian distribution.

The contour plot of the unperturbed model ($\epsilon = 0$) is reproduced here, Fig. 3.4.1. From the plot several distinct dynamic regions are observed. Shear bands near the core of the annulus are separated from the shear region on the outer edge

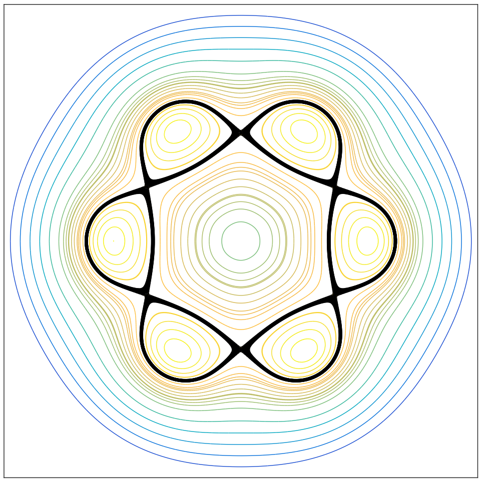

Figure 3.4.1: The contour plot for the unpreturbed annulus flow is shown with the separatrix noted with a solid black curve. Shear regions are seen on either side of the separatrix.

by the vortex chain. The vortices are seen to lie nested between hyperbolic fixed points. The connections between these fixed points forms the separatrix – the barrier distinguishing the different dynamic regions (shown as the thick black lines in the figure).

Since the trajectories of tracers are bound in the radial direction, either by the walls of the annulus or the separatrix, a one-dimensional analysis is able to be done on the azimuthal displacements. From investigating only the azimuthal displacement in this model, del Castillo-Negrete (1997) was able to obtain the same decay exponents for the statistics as obtained in the experiments in Solomon *et al.* (1993). Given the decay exponents of the flight and trapping time statistics, a fractional diffusion model can be implemented, as outlined in del Castillo-Negrete *et al.* (2004). In the hopes of expanding this methodology to higher dimensions, the analysis is reviewed here first for the 1D setting.

Due to the inhomogeneities in the flow, caused by the presence of vortices and shear flow, anomalous diffusion is expected. The distinction between normal and anomalous diffusion can be made by examining the decay rate of the velocity correlation, or similarly, by looking at the rate of growth of the displacement distribution of an ensemble of particles. The variance in the azimuthal direction is given by:

$$\sigma^2(t) = \left\langle \Big(\Delta\theta(t,\tau) - \big\langle \Delta\theta(t,\tau) \big\rangle \Big)^2 \right\rangle, \tag{3.4.3}$$

where $\Delta\theta(t,\tau) = \theta(\tau + t) - \theta(\tau)$ is the azimuthal displacement. The variance is seen to grow as $\sigma^2 \sim t^\gamma$, for $\gamma > 0$. Recalling that the normal diffusion process corresponds to a linear growth of the variance ($\gamma = 1$), anomalous diffusion is seen for this model. In Solomon *et al.* (1993), $\gamma = 1.65 \pm .15$ was obtained from the experimental setup; while values of $\gamma = 1.57$ and $\gamma = 1.9$ were obtained in del Castillo-Negrete (1997). Further, in Solomon *et al.* (1993) the following two relations are given for γ:

$$\gamma = 4 - \mu, \qquad \gamma = \frac{2\nu}{\mu - 1}, \tag{3.4.4}$$

where μ is exponent of decay for the flight-time pdf, and ν is the exponent of decay for the sticking-time pdf. The flight pdf, $P_F(a)$ gives the distribution of a flight event being of a certain length a, and τ_F is the average flight duration. The sticking time pdf, $P_S(a)$, and average sticking time, τ_S, are defined analogously. These pdfs are taken to scale as follows:

$$P_F(a) \sim a^{-\mu} \qquad P_S(a) \sim a^{-\nu}. \tag{3.4.5}$$

In Fig. 3.4.2 the azimuthal displacement of typical trajectories are shown. It is seen that trajectories tend to display both sticking and flight events, with the sticking events presenting themselves as small oscillations around horizontal lines, while the flight events are seen as steep diagonal lines. In del Castillo-Negrete (1997) and

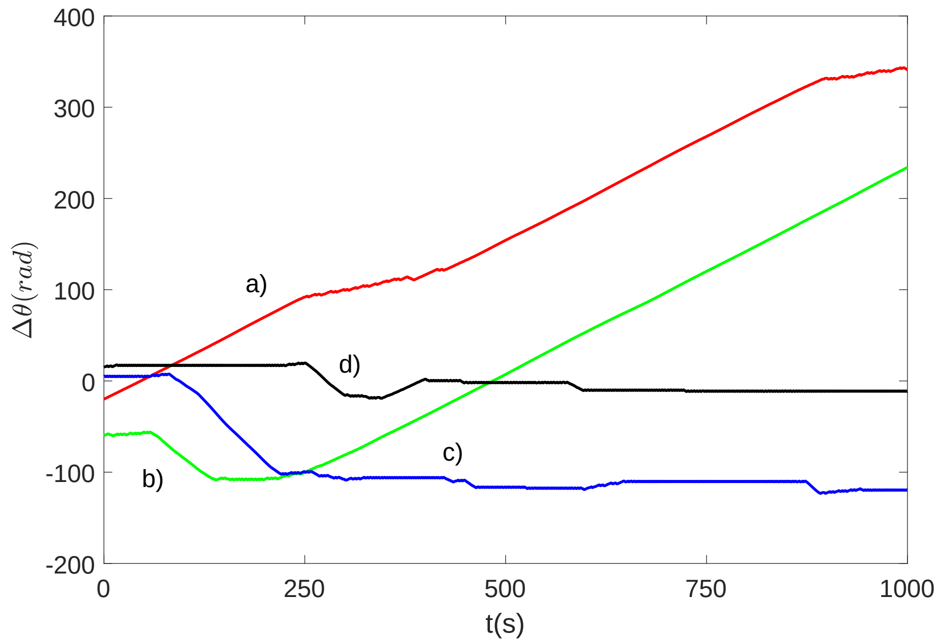

Figure 3.4.2: The azimuthal displacements as a function of time for various trajectories are shown. Sticking events are seen as oscillations about horizonatal lines (beginnings of c and d). Flight events are seen as diagonal lines separating sticking events (end of d). The initial angle $\theta(t = 0)$ is arbitrary for plotting purposes.

Solomon *et al.* (1993, 1994) flight events are classified by $\Delta\theta > \pi/3$ between successive extrema; approximately the angular width of a single vortex. The flight segments are seen to have approximately constant slopes, indicating a steady azimuthal velocity. The sticking times are simply taken as the intervals between flights, and are seen to range from as short as a couple seconds to over 300s. Further, the chaotic trajectories associated to the previous azimuthal displacements are seen in Fig. 3.4.3. In the figure the green dots represent the starting position, while the red dots show the final location. From the figure it is clear that the perturbations in the model allow trajectories to alternate between sticking and flight events.

In using the pdfs of the sticking and flight-times to obtain γ, (3.4.4) provides two possible relations. If the system is dominated by flight events, then the first

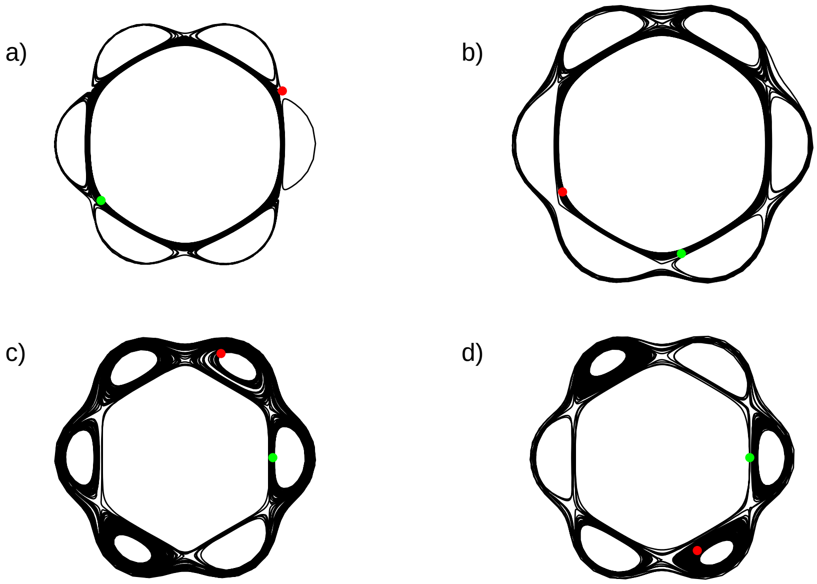

Figure 3.4.3: Chaotic trajectories in the perturbed annulus flow. The beginning of each trajectory is marked with a green dot, with red dots used to mark the end of each trajectory. Long sticking events are seen in each case, with long flight events seen in a) and b).

relation should be used, while the second relation is used when sticking events are vital to the dynamics. From exponents of the pdfs of the sticking and flight-times in Solomon *et al.* (1993); del Castillo-Negrete (1997) ($\nu = 1.6 \pm .3$ and $\mu = 2.3 \pm .2$, and $\nu = \{1.7, 1.85\}$, $\mu = \{2.1, 2.4\}$, respectively), it is observed that the CTRW model prediction-based relation is valid for representing the growth rate of the variance, $\gamma = 4 - \mu$.

As an extension of this study, the affect of noise on trajectories of the unperturbed model is now analyzed in this dissertation. The benefit of looking at the unperturbed model, where $\epsilon = 0$, is that the classification of trapping and non-trapping events is immediate. As discussed earlier, the separatrix provides a natural separation of the different dynamic regions within the system. Trapping events are then simply given by the presence of a particle in the area bound by the upper and lower branches of the

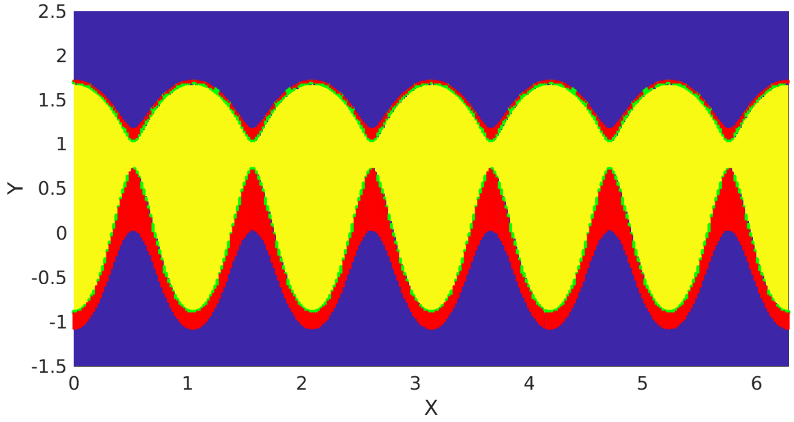

Figure 3.4.4: The partition of the unperturbed annulus model shows the trapping region (yellow), nontrapping region (blue), and tracers that exit the trapping region (green), along with tracers that enter the trapping region (red).

separatrix. The statistics are then conditioned based on residence time of trajectories inside the trapping regions.

It is noted that for deterministic trajectories, these conditional statistics would exhibit flat pdfs with peaks at the terminal time. However, as seen in Fig. 3.4.4 – where the trapping region is shown in yellow, and the nontrapping/flight region is in blue – some of the tracers initiated along the partition boundary exhibit at least one exit event, these tracers are plotted as green dots. Similarly, some tracers initiated outside of the trapping region also exhibited at least one trapping event, and are plotted as red dots. The retention rates of deterministic trajectories in the trapping and flight regions, i.e. the percent of tracers that spend the entire simulation in the trapping region, are 96.92 and 91.68 for the trapping and flight regions, respectively. The lower retention rate for the flight region indicates that the classification can be improved. However, since the partition is obtained from the separatrices it will be used for this autonomous system; investigating the impact and ability of other classification techniques will be done in later sections.

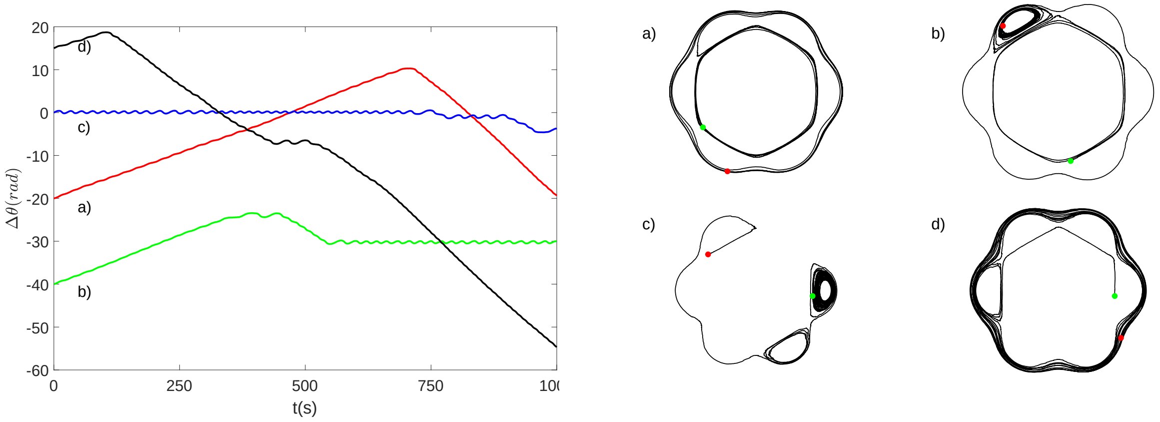

Figure 3.4.5: [left] The azimuthal displacements as a function of time for various trajectories are shown. Sticking events are seen as oscillations about horizonatal lines (beginning of c and the end of b). Flight events are seen as diagonal lines separating sticking events (end of d). The initial angle $\theta(t = 0)$ is arbitrary for plotting purposes. [right] Chaotic trajectories in the perturbed annulus flow, $D = .0225$. The beginning of each trajectory is marked with a green dot, with red dots used to mark the end of each trajectory. Long sticking events are seen in each case, with long flight events seen in a), b) and d).

With the addition of a perturbation on the trajectories, chaotic behavior is observed. The noise amplitude of $D = .0225$ was used so that typical trajectories exhibit at least one trapping event. Fig. 3.4.5 shows the azimuthal displacements (left) and trajectories (right) of typical tracers in the flow. These results compare well with what is seen in Fig. 3.4.2 and Fig. 3.4.3. The retention rates for the trapping and flight regions are now 0.56% and 52.27% respectively. The reduction in retention is naturally expected as now tracers beyond the periphery of the trapping region are able to traverse the boundary.

The pdfs of the trapping and flight-times of the stochastic trajectories are seen in Fig. 3.4.6. The trapping time pdf is in blue, while the flight-time pdf is shown in black. The power-law scalings that fit the data are seen as dashed lines in Fig. 3.4.6. The scales, $\nu = 1.5$ and $\mu = 1.6$, deviate from the experimental and numerical

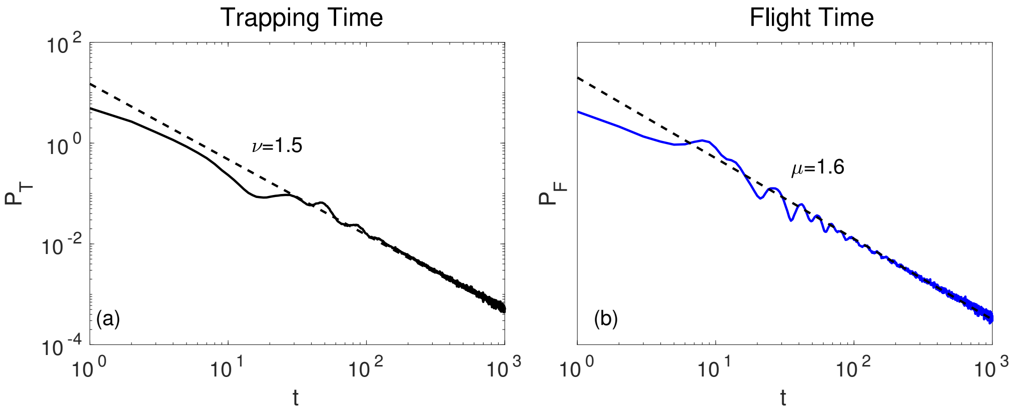

Figure 3.4.6: Pdfs of the (a) trapping and (b) flight-times, for particles in the annulus flow, with noise level $D = .0225$. The dashed black curves show the power-law fit to the data.

results of previous studies. This could be due in part to the large noise component, the statistics are also affected by tracers that don't experience trapping events, but also nontrapping events are defined less strictly here than in the literature. The scales obtained indicate that variance of the azimuthal displacement is dominated by flight events, following the relation $\gamma_{pred} = 4 - \mu$. In Fig. 3.4.7 the variance of the azimuthal displacement is shown along with a curve highlighting the power-law growth. The directly computed growth rate of $\gamma = 1.9$ is within the bounds of the experimental uncertainty, but disagrees with the predicted value of $\gamma_{pred} = 2.4$; $\gamma = 1.9$ is also the value obtained in del Castillo-Negrete (1997) for the model with noise.

Using a smaller perturbation of $D = .0025$ results in retention rates of 82% and 88.26% for the trapping and nontrapping regions, respectively. The pdfs of the trapping and flight-times, as seen in Fig. 3.4.8, follow decay rates of $\nu = 1.4$ and $\mu = 2.1$; these match well with the scales obtained in previous studies. Further, the predicted γ_{pred} value now matches the directly computed value of 1.9.

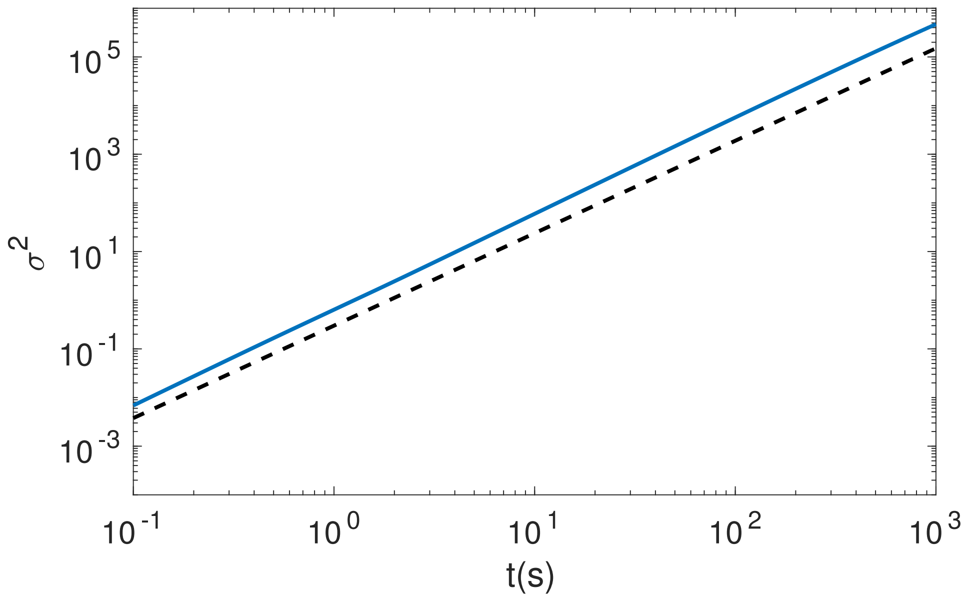

Figure 3.4.7: Variance of the azimuthal displacements of tracers in the steady annulus flow, subject to Gaussian perturbations. The black-dashed curve shows the power-law growth, with an exponent of $\gamma = 1.9$.

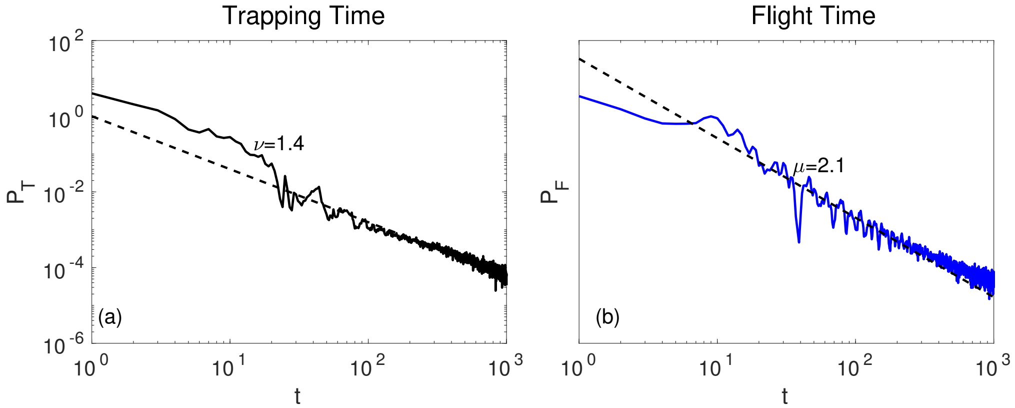

Figure 3.4.8: Pdfs of the (a) trapping and (b) flight-times, for particles in the annulus flow, with noise level $D = .0025$. The dashed black curves show the power-law fit to the data.

In del Castillo-Negrete *et al.* (2004) the parameter scales of the waiting-time and jump statistics, α and β respectively, were used to reproduce the radial displacement pdf. By defining the moments by $\left\langle \left[x - \langle x \rangle\right]^n \right\rangle \sim t^{n\nu}$, the parameters α and β are seen to provide the following relation, $\nu = \frac{\beta}{\alpha}$.

Recalling the Green's function of the fractional diffusion model from (2.1.18), by using the variable $\eta = x(\chi^{1/\beta}t)^{-\beta/\alpha}$ the function can be re-expressed as:

$$G(x,t) = \left(\chi^{1/\beta}t\right)^{-\beta/\alpha} K(\eta), \tag{3.4.6}$$

where

$$K(\eta) = \frac{1}{\pi}\int_0^\infty \cos{(\eta z)} E_\beta(-z^\alpha) dz. \tag{3.4.7}$$

Based on a localized initial conditions $|x| \leq \epsilon/2$ with $\epsilon \ll 1$, the PDF of particle displacements is written as:

$$P(x,t) = \frac{(\chi^{1/\beta}t)^{-\beta/\alpha}}{2\delta}\left(\int_0^{\delta-\eta} K(z)dz + \int_0^{\delta+\eta} K(z)dz\right), \tag{3.4.8}$$

where $\delta = \frac{\epsilon}{2}(\chi^{1/\beta}t)^{-\beta/\alpha}$. The above solution is further approximated as

$$\begin{aligned} P(x,t) &\sim C\chi\frac{t^\beta}{x^{1+\alpha}}\left(1 + \epsilon^2\frac{(\alpha+1)(\alpha+2)}{4!x^2}\cdots\right), \quad |x| > \epsilon/2 \\ P(x,t) &\sim \frac{A}{\alpha\chi t^\beta}\left(\frac{2}{\epsilon}\right)^{1-\alpha}\left(1 - 2\alpha(1-\alpha)\left(\frac{x}{\epsilon}\right)^2\right) + \frac{B}{(\chi^{1/\beta}t)^{\beta/\alpha}}, \quad |x| < \epsilon/2, \end{aligned} \tag{3.4.9}$$

where

$$A = \frac{1}{\pi}\frac{\Gamma(1-\alpha)}{\Gamma(1-\beta)}\sin\left(\frac{\pi\alpha}{2}\right) \quad B = \frac{1}{\pi}\frac{\Gamma(1-1/\alpha)\Gamma(1+1/\alpha)}{\Gamma(1-\beta/\alpha)} \quad C = \frac{1}{\pi}\frac{\Gamma(1+\alpha)}{\Gamma(1+\beta)}\sin\left(\frac{\pi\alpha}{2}\right). \tag{3.4.10}$$

Here the histogram of the radial displacements are compared between the actual model and the curve generated from (3.4.9).

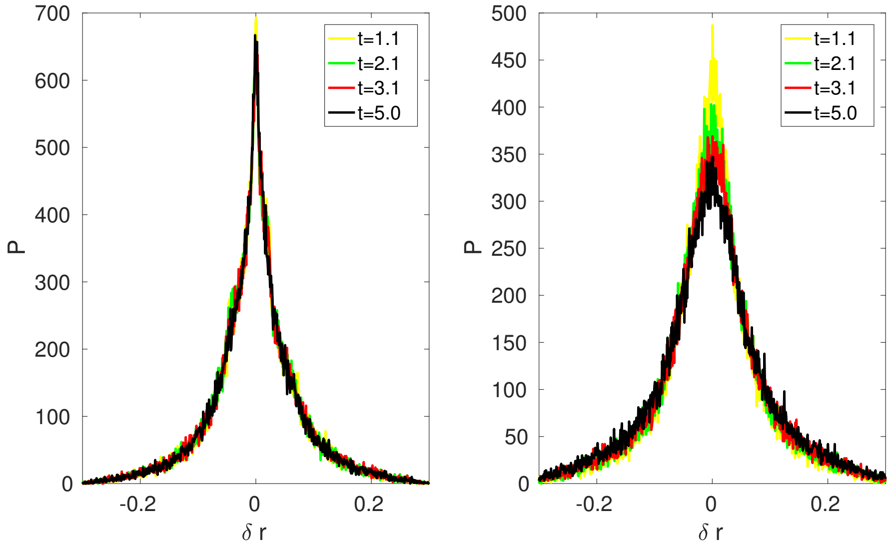

Figure 3.4.9: Long-term radial displacement pdfs for the annulus flow, for $D = .0025$ (left) and $D = .0225$ (right).

Results

From comparing the pdfs of radial displacements for the small noise and large noise cases many interesting features are observed. In Fig. 3.4.9 the long-term behavior is seen for the small noise case (left), and the larger noise case (right). The steep peak seen at the final time ($t = 5$) pdf for the small noise highlights the anomalous transport of the system; indicating a inhibition of dispersion in the radial direction. The large noise case on the other hand has a distribution more reminiscient of a standard Gaussian distribution, this shows the impact noise had smoothing the statistics. For both cases, the pdfs of radial displacemenets have been plotted without scaling, and are seen to be self-similar profiles. For the small noise case the long-term pdfs fall onto the same curve without rescaling, while a scale of $\nu = .4$ can be used for the larger noise case.

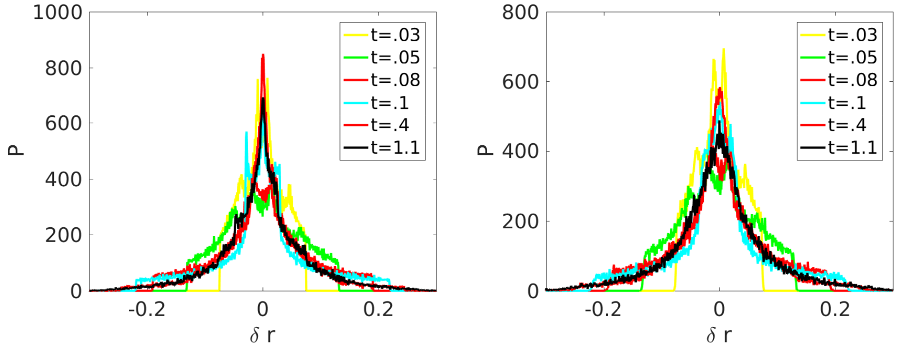

Figure 3.4.10: Short-term radial displacement pdfs for the annulus flow, for $D = .0025$ (left) and $D = .0225$ (right).

In Fig. 3.4.6 the short-term behaviors are compared for the two noise cases. In both plots the initial pdfs are almost indistinguishable until around $t = .1$. For the small noise, $t = .1$ is when the center of the pdf start become more peaked, while the center of the pdf for the large noise becomes more broad and the maximum value starts to decay. The decay of the maximum value is not seen for the small noise, suggesting a clustering of trajectories that is not able to be broken apart from the perturbations; the decay of the maximum, or lack thereof, was also seen in Fig. 3.4.9.

The semilog plot of the scaled radial displacements is shown in Fig. 3.4.11 for both the small and large noise cases. The form of the scalings used are Pt^{ν} and $x/t^{-\nu_2}$; where values of $\nu = .5$ and $\nu_2 = .25$ for the small noise case, and $\nu = .6$ and $\nu_2 = .25$ for the large noise. The use of a two parameter fit indicates that the azimuthal flow is inhibiting dispersion, causing a slow decay in the radial direction. Further, the vortex chain acts to trap tracers, especially for the small noise, thus the statistics are driven by 3 regions: the outer shear flow, inside the vortex chain, and the inner shear flow (near the core of the annulus). Both the outer and inner shear regions utilize the strong shear forces to keep tracers from escaping. With a larger noise amplitude it is possible for these tracers to traverse these boundaries and venture into other dynamic

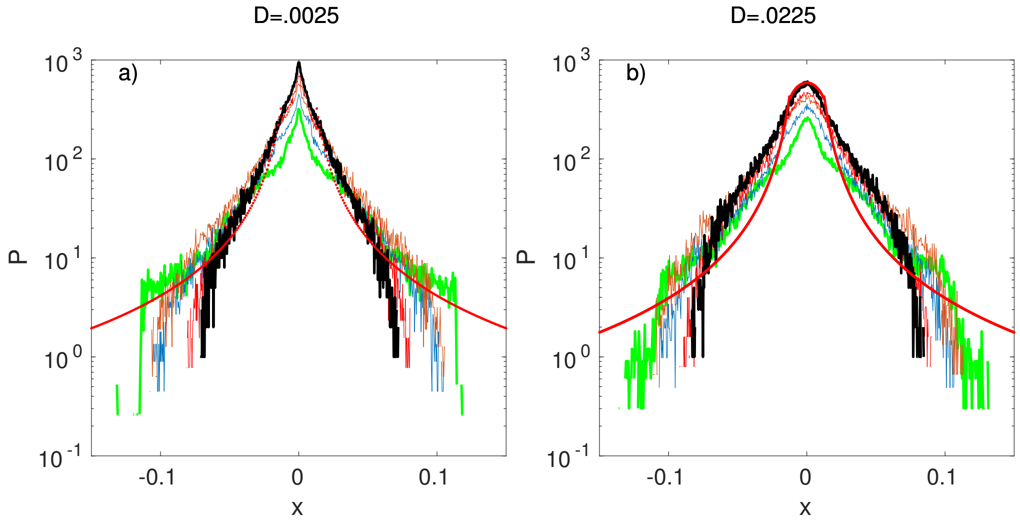

Figure 3.4.11: Scaled radial displacements for the annulus flow with small (left) and large (right) noises. The red curve shows the solution to the fractional diffusion equation given $\alpha = .85$ and $\beta = .5$.

regions. The ability of the tracers to traverse boundaries is seen in Fig. 3.4.11 as the broadening of the tails of the pdf. Also in the figure is the red curve coming from (3.4.9), with $\alpha = .85$, $\beta = .5$ and $\chi = \sqrt{.0025}$.

The parameter α comes from looking at the pdf of radial displacements on a log-log plot, and noticing the decay exponent. In Fig. 3.4.12 the log-log plot of radial displacements is shown with the curve showing the decay rate of $\alpha + 1 = 1.85$. From Fig. 3.4.11 it is seen that the pdf of radial displacements is obtainable from the kernel of the fractional diffusion equation, further highlighting the anomalous characteristics of the system.

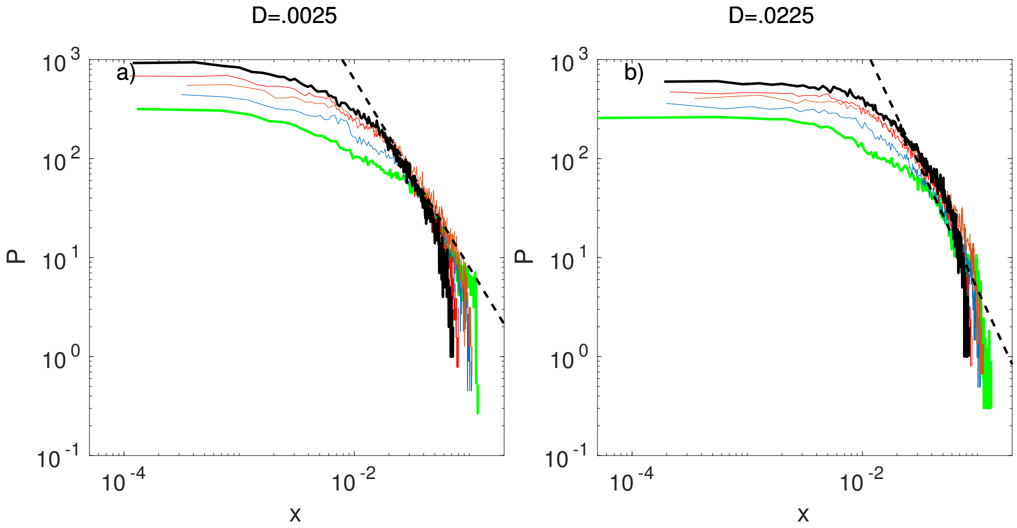

Figure 3.4.12: Scaled radial displacements for the annulus flow with small and large noises. The black-dashed line shows the power-law decay, with an exponent of $\alpha + 1 = 1.85$.

PART 2 -

THE 2D CASE

Chapter 4

2D LCS DETECTION METHODS

In this chapter the various two-dimensional methods for partitioning the flow topology are introduced. As seen later, some of the methods discussed here have natural extensions to 3D, while others are not suitable.

Poincaré Sections

For periodically forced systems, such that $F(\vec{x}, t) = F(\vec{x}, t+T)$, where T is the period of the system, there is an objective method for identifying the different kinematic regions; Poincaré return maps or sections. Poincaré sections (PS) are obtained from looking at the period-T return maps for tracers – this is just a record of the tracer location under the periodic action of the flow. Region boundaries are revealed from tracer locations taken from looking at a large number of applications of the periodic map. There are two main drawbacks with this method. The first being, since PS are constructed from these return maps, a large number of iterations will be needed to reveal them, and further, these structures represent the infinite-time state of the system and therefore don't depict the transient dynamics. The other shortcoming is that PS can only be done for periodic flows, so this method is not valid for nonautonomous systems with general time dependence. Despite these drawbacks, PS will be used to gauge the accuracy of other methods when looking at periodic flows.

LCS Detection Methods

Having no shortage of LCS detection methods to choose from, here the attempt is to offer a broad sampling of these, but the list of methods used is in no way exhaustive. Numerous methods were compared while working towards the goal of finding an accurate but computationally inexpensive method that was suited to work on autonomous and nonautonomous dynamical systems. As stated earlier, when discussing LCS detection there are two families of methods, the geometric methods and the probabilistic methods. The geometric methods use geometric information, such as strain and vorticity, from the map to highlight transport barriers or invariant manifolds. The probabilistic methods, however, use tracer trajectories to determine invariant sets, almost invariant sets, or finite-time coherent sets in phase space.

Geometric Methods

Early studies on flow topology identification were based on Eulerian quantities, specifically the Okubo-Weiss (OW) parameter; as in Elhmaidi *et al.* (1993). Since then, the development of Lagrangian descriptors for coherent structure identification has progressed. It has been noted that Lagrangian diagnostics lead to identifying regions that tend to remain coherent more so than from Eulerian diagnostics. However, in Kadoch *et al.* (2011), the Lagrangian history of the Eulerian OW parameter was used successfully to study the relationship between Lagrangian statistics and flow topology for a 2D turbulent flow. The OW measure is included here to contrast against the Lagrangian measures for turbulent and non-turbulent flows.

The OW parameter is the difference between the norms of the instantaneous strain and vorticity, and is given by:

$$Q(\mathbf{x},t) = s(\mathbf{x},t)^2 - \omega(\mathbf{x},t)^2, \tag{4.2.1}$$

where $s^2 = \big(\partial_x u - \partial_y v\big)^2 + \big(\partial_x v + \partial_y u\big)^2$ and $\omega = \big(\partial_x v - \partial_y u\big)$. So, roughly speaking, regions with high Q value are highly strained, while low Q values indicate regions dominated by rotation. In the following, strain-dominated regions will be classified

Types	Condition
• Elliptic (trapping)	$Q(\mathbf{x},t) \leq -Q_0$
• Hyperbolic (jumping)	$Q(\mathbf{x},t) \geq Q_0$
• Intermediate (both)	$\lvert Q(\mathbf{x},t) \rvert < Q_0$

Table 4.1: Classification of Coherent Regions Given by the OW Measure

as hyperbolic (jumping type regions), rotation-dominated regions will be classified as elliptic (trapping/sticking type regions), and all else is considered part of the intermediate region. This is summarized in Table 4.1. Q_0 is chosen arbitrarily as the standard deviation of the field ($Q_0 = \sqrt{\langle Q(\mathbf{x},t)^2 \rangle}$), and thus the bounds obtained do not correspond to actual transport barriers.

Finite-Time Lyapunov Exponent

LCSs are historically extracted from the finite-time Lyapunov exponent (FTLE) field, Shadden *et al.* (2005). The FTLE is a finite-time analogue of the traditional Lyapunov exponent, which quantifies the *asymptotic* behavior of infinitesimally nearby tracers. The FTLE quantifies the relative rate of separation of infinitesimally nearby tracers over a *finite-time* interval. Roughly speaking, in forward-time, regions of high FTLE value are highly separating, whereas regions of low value tend to be more steady. Since the FTLE highlights regions of large separation, shearing and stretching are not distinguished, and it was noted in Haller (2011) that FTLE ridges can give false positives and negatives, with regards to material transport barriers.

The FTLE is computed from the deformation gradient tensor, $J(t;\mathbf{x_0},t_0) = \partial\mathbf{x}(t;\mathbf{x_0},t_0)/\partial\mathbf{x_0}$, where $\mathbf{x}(t;\mathbf{x_0},t_0)$ denotes the current position of a trajectory that initiated from $(\mathbf{x_0}, t_0)$. The FTLE field, $\Lambda_{t_0}^t(\mathbf{x_0})$, is then defined as the scalar field that associates the maximal rate of stretching with *each* initial position $\mathbf{x_0}$:

$$\Lambda_{t_0}^t(\mathbf{x_0}) = \frac{1}{|t - t_0|} \ln \lambda_{max}\left(J\right), \tag{4.2.2}$$

with $\lambda_{max}(J)$ denoting the maximum singular value from the singular value decomposition of $J(t; \mathbf{x_0}, t_0)$.

Since the FTLE is computed from the rate of separation of infinitesimally nearby trajectories, it seems that a dense mesh would be needed to obtain a valid representation. As discussed in Farazmand and Haller (2012) it is possible to obtain a high resolution FTLE field without resorting to a dense mesh. This is done by using the auxiliary grid method, where small perturbations are taken to the computational grid and they are used to compute the components of the deformation gradient tensor. This is shown schematically in Fig. 4.2.1. Letting $x_j^l(t_0)$ designate an initial aux-grid location, and $x_j^l(t)$ denote its location at time t, then the elements of the Jacobian are given as:

$$J(t; x_j, t_0) = \begin{bmatrix} \frac{x_j^r(t) - x_j^l(t)}{x_j^r(t_0) - x_j^l(t_0)} & \frac{x_j^r(t) - x_j^l(t)}{x_j^u(t_0) - x_j^d(t_0)} \\ \frac{x_j^u(t) - x_j^d(t)}{x_j^r(t_0) - x_j^l(t_0)} & \frac{x_j^u(t) - x_j^d(t)}{x_j^u(t_0) - x_j^d(t_0)} \end{bmatrix} = \begin{bmatrix} \frac{x_j^r(t) - x_j^l(t)}{2\delta x} & \frac{x_j^r(t) - x_j^l(t)}{2\delta y} \\ \frac{x_j^u(t) - x_j^d(t)}{2\delta x} & \frac{x_j^u(t) - x_j^d(t)}{2\delta y} \end{bmatrix}. \tag{4.2.3}$$

All other geometric LCS detection methods used later also use this auxiliary-grid approach.

Instead of giving a cut-off to demarcate the domain, the FTLE simply highlights regions of large deformation. While this gives good characterization of the transport barriers in the Bickley jet and gyre flows, such barriers in the turbulent flow are not easily identified. For the turbulent flow the regions are classified by using one standard deviation away from the mean value; this is analogous to what was done for OW. Letting $\sigma(\mathbf{x}, t) = \Lambda_{t_0}^t(\mathbf{x_0})$ and $\bar{\sigma} = \langle \sigma \rangle$, where $\langle \cdot \rangle$ indicates the spatial average, then Table 4.2 describes the FTLE partition for the turbulent flow. Note that in the

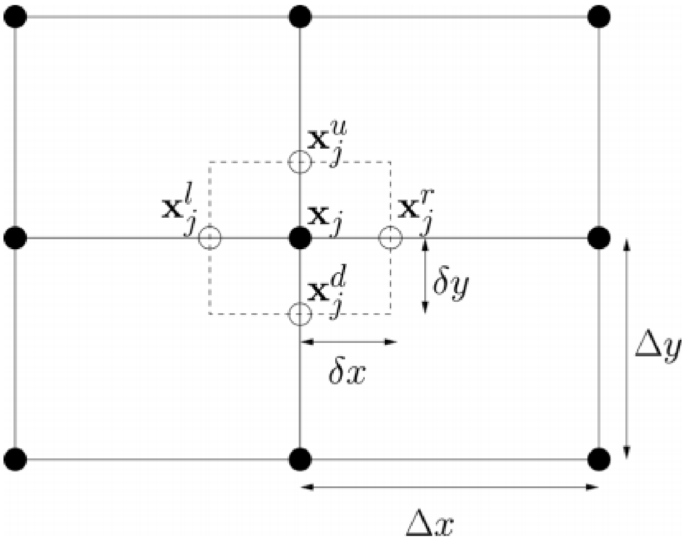

Figure 4.2.1: Hollow circles indicate the auxiliary grid points used for computing the gradient of the flow map, while filled circles represent the original grid.

Types	Condition
• Elliptic (trapping)	$\sigma < \bar{\sigma} - \sqrt{\langle(\sigma - \bar{\sigma})^2\rangle}$
• Hyperbolic (jumping)	$\sigma > \bar{\sigma} + \sqrt{\langle(\sigma - \bar{\sigma})^2\rangle}$
• Intermediate (both)	$\lvert\sigma - \bar{\sigma}\rvert < \sqrt{\langle(\sigma - \bar{\sigma})^2\rangle}$

Table 4.2: Classification of Coherent Regions Given by the FTLE Measure for the Turbulent Flow

other models the FTLE ridges are still used to extract the shear boundaries, while the trapping region condition from Table 4.2 is used to identify the elliptic regions.

Mesochronicity

Mesochronicity (MESO), the diagnostic proposed in Mezić *et al.* (2010), looks at the determinant of the mesochronic Jacobian – the gradient of the Lagrangian average velocity – to partition flows. Similar to OW this method gives clear boundaries for

Types	Condition
• Mesoelliptic (trapping)	$0 < \mathcal{M}_{t_0}^{t+t_0}(\mathbf{x_0}) < \frac{4}{t^2}$
• Mesohyperbolic (jumping)	$\mathcal{M}_{t_0}^{t+t_0}(\mathbf{x_0}) > \frac{4}{t^2}$
• Mesohelical (both)	$\mathcal{M}_{t_0}^{t+t_0}(\mathbf{x_0}) < 0$

Table 4.3: Classification of Coherent Regions Given by the MESO Measure

vortex motion over strain. The classification of region type is based off of the difference between vorticity and strain, computed from the Lagrangian averages, instead of instantaneous values.

Let $\mathbf{u}^*(t+t_0, \mathbf{x}(t+t_0; \mathbf{x_0}, t_0))$ denote the average Lagrangian veloctiy for a trajectory starting at the point $(\mathbf{x_0}, t_0)$ and being advected for an integration time of t. The mesochronic velocity is computed by taking the difference of the trajectories over t, from time t_0 until $t_0 + t$, obtained by:

$$\mathbf{u}^*(t+t_0, \mathbf{x}(t+t_0; \mathbf{x_0}, t_0)) = (\mathbf{x}(t+t_0; \mathbf{x_0}, t_0) - \mathbf{x}(t_0; \mathbf{x_0}, t_0))/t, \tag{4.2.4}$$

or equally from,

$$\mathbf{u}^*(t+t_0, \mathbf{x}(t+t_0; \mathbf{x_0}, t_0)) = \frac{1}{t}\int_{t_0}^{t_0+t} \mathbf{u}(\tau, \mathbf{x}(\tau; \mathbf{x_0}, t_0))d\tau. \tag{4.2.5}$$

The determinant of $\nabla\mathbf{u}^*(\mathbf{x}(t+t_0; \mathbf{x_0}, t_0))$ is then defined as $\mathcal{M}_{t_0}^{t+t_0}(\mathbf{x_0}) :\equiv u_x^* v_y^* - v_x^* u_y^*$. Subsets of the mesochronicity field are easliy classified and defined as mesohelical, mesohyperoblic, and mesoelliptic. The mesoelliptic regions are rotationally dominant, while strain dominates the mesohyperbolic regions, and a combination is seen in the mesohelical; this is summarized in Table 4.3. Note that as the integration time t goes to zero, the Okubo-Weiss criterion are recovered.

Geodesic Theory

The last geometric method investigated is the recently developed geodesic theory (GEO) presented in Farazmand and Haller (2012). Here coherent structures are identified as minimal stretching curves under the action of the system, and are identified by finding extremals to the functional defining the stretching of such curves. The variational problem differs from the classical one in the sense that the extremal end points are *a priori* unknown – this difference leads to the classification of different types of coherent structures based on the boundary conditions imposed. Hyperbolic barriers are defined as *strainline* segments whose relative stretching is locally minimal. Parabolic and elliptic barriers are defined as open and closed *shearlines*, repsectively. The *strainlines* and *shearlines* are calculated by solving a system of first-order differential equations given by:

$$\begin{aligned} r'_{st} &= \xi_1(r) \qquad (4.2.6)\\ r'_{sh} &= \eta_{\pm}(r), \qquad (4.2.7)\end{aligned}$$

where ξ_1 is the eigenvector corresponding to the smaller eigenvalue of the Cauchy-Green strain tensor (J^TJ), $\eta_{\pm}$ are the Lagrangian shear vector fields, and $r_{st,sh}$ denote the strain and shear lines, respectively. The normalized Lagrangian shear vector fields are:

$$\eta_{\pm} = \sqrt{\frac{\lambda_2 - \lambda^2}{\lambda_2 - \lambda_1}}\xi_1 \pm \sqrt{\frac{\lambda^2 - \lambda_1}{\lambda_2 - \lambda_1}}\xi_2, \qquad (4.2.8)$$

where $\lambda^2 = \lambda_1\lambda_2$, and $\lambda_{1,2}$ are the eigenvalues corresponding to $\xi_{1,2}$, respectively. Note that for incompressible flows $\lambda_1\lambda_2 = 1$, but in practice, a small range of values near 1 is used for λ to allow for some stretching and contraction. This identification method is the most sophisticated and computationally demanding of those discussed so far, due to having to solve the additional ODEs, (4.2.6) and (4.2.7). This expense is justified, as the boundaries of the rigorously defined materially coherent regions can be obtained for nonautonomous flows.

Probabilistic Methods

The probabilistic methods rely on the creation and skillful manipulation of the transfer or transition matrix. Recalling Section 2.4, the matrix element P_{ij} gives the probability of a tracer initiated in $B_i \subset X$ ending up in $C_j \subset Y$ at time t.

Finite-Time Entropy

In Froyland and Padberg-Gehle (2012), as a step towards providing a mathematical link between the geometric and probabilistic approaches, they defined the entropy of a probability measure μ, as $H(\mu) := -\sum_{i=1}^{n} \mu(B_i) \log \mu(B_i)$. Making the substitution $p_i = \mu(B_i)$ leads to the form $H(p) = -\sum_{i=1}^{n} p_i \log p_i$. The discrete finite-time entropy (FTE) on the partition set B_i is then defined as $FTE(B_i, t, \tau) = \frac{1}{|\tau|} H(\delta_i P)$, where δ_i is an n-vector with 1 in the i-th position and 0 everywhere else, and τ is the integration time. It is typically seen that the FTE qualitatively correlates very highly to the FTLE, and as such the partition based on the FTE is done similar to that for the FTLE. More clearly, by letting $\alpha = FTE(B_i, t, \tau)$ and $\bar{\alpha}$ be its mean value ($\bar{\alpha} = \langle \alpha \rangle$), then the FTE partition for the turbulent flow is given by Table 4.4. The partition for the Bickley jet shear boundaries are based on the ridges fo the FTE field, and the condition for trapping regions is used to identify elliptic regions.

Almost-Invariant Sets

As discussed in Froyland *et al.* (2010), relative coherent sets can be determined from the transition matrix by applying a thresholding algorithm on the singular vectors; where the singular vectors highlight coherence and the corresponding phase space

Types	Condition
• Elliptic (trapping)	$\alpha < \bar{\alpha} - \sqrt{\langle(\alpha - \bar{\alpha})^2\rangle}$
• Hyperbolic (jumping)	$\alpha > \bar{\alpha} + \sqrt{\langle(\alpha - \bar{\alpha})^2\rangle}$
• Intermediate (both)	$\lvert\alpha - \bar{\alpha}\rvert < \sqrt{\langle(\alpha - \bar{\alpha})^2\rangle}$

Table 4.4: Classification of Coherent Regions Given by the FTE Measure for the Turbulent Flow

structures. These relatively coherent sets are obtained from executing the following algorithm; this will be referred to as the PF-algorithm or just PF[1] for brevity.

PF-algorithm

1. Calculate the second left and right singular vectors $\{x_i\}, \{y_j\}$ of the transition matrix P.
2. Find values $\{(b_k, c_k)\}$ as pairs, and $\varrho\big(X(b_k), Y(c_k)\big) = \frac{\sum_{i|x_i>b_k \& j|y_j>c_k} p_i P_{ij}}{\sum_{i|x_i>b_k} p_i}$, where $p_i = \mu(B_i)$, $X(b_k) = \cup_{i|x_i>b_k} B_i$ and $Y(c_k) = \cup_{j|y_j>c_k} C_j$.
3. Choose the partition that produces the maximum ϱ.

The partitions are then defined as being $X_1 = \cup_{i|x_i>b^*} B_i$ and $X_2 = \cup_{i|x_i \le b^*} B_i$, where (b^*, c^*) is the pair of parameters that maximize ϱ.

When the PF-algorithm is computed for an autonomous system, the resulting sets are almost-invariant sets (AISs). These sets are fixed regions in phase space that are minimally dispersive. Since the Bickley jet is periodic with period T, looking at the time-T map of the system leads to an autonomous system. Thus, the fixed regions in phase space that are almost-invariant under the dynamics of successive applications of the time-T map are sought after. Motivated by the structures seen in the PS, a q-way

---

[1] PF is for the Perron-Frobenius operator, which is what the transfer matrix approximates

cut approach is used to identify q almost-invariant sets. This technique is outlined in Froyland and Dellnitz (2003), and the clustering algorithm used was presented in Bezdek *et al.* (1987) and modified in Froyland (2005).

Finite-Time Coherent Sets

When PF is computed for nonautonomous systems finite-time coherent sets (FTCSs) are obtained instead. These differ from AIS in that the regions defined by FTCS are not fixed in phase space. Since the FTCS partition is binary (results in 2 distinct sets), a recursive calculation is done in order to detect multiple regions that remain coherent. The procedure defining this recursive calculation is given in Ma and Bollt (2013), and briefly reviewed here.

This process starts with the computation of the PF-algorithm to obtain the coherent pairs (X_1, Y_1) and (X_2, Y_2), where Y_1 can be considered as the image of X_1 under the action of the flow, for the specified integration time. Relative measures are then defined for these sets as:

$$\mu_{X_i}(S) = \frac{\mu(S)}{\mu(X_i)}, \quad \text{and} \quad v_{Y_i}(T) = \frac{v(T)}{v(T_i)}, \tag{4.2.9}$$

for all $S \subset X_i$ and $T \subset Y_i$. With these relative measures it is now possible to perform the same thresholding operation (i.e. PF) on X_1 and Y_1, with using μ_{X_1} instead of μ. This leads to coherent pairs (X_{11}, Y_{11}) and (X_{12}, Y_{12}). Relative measures can now be computed for these sets, and so forth. This process can be repeated until the desired amount of sets are found, or the stopping criterion is met. Since the number of coherent regions is usually *a priori* unknown, the relative coherence (ϱ) is used as an indication of when to stop. The procedure should terminate if, for some coherent pair (X_n, Y_n), $\max_k \Big(\varrho\left(X_n(b_k), Y_n(c_k)\right)\Big) < \varrho_0$, where $\varrho_0 \in (0, 1)$.

For a more indepth and complete discussion of almost-invariant and coherent sets, the reader is referred to Bahsoun *et al.* (2014).

Chapter 5

THE FLOWS AND ANOMALOUS TRANSPORT ANALYSES

In this chapter the 2D flows that will be used in later analyses are introduced.

Flows

The 2D flows investigated were chosen to exhibit integrable, chaotic, and turbulent trajectories. Analysis will begin with autonomous or time-periodic systems, where precise partitions are available, via invariant manifold theory and Poincaré sections, respectively.

Quadruple-Gyre Flow

The quadruple-gyre flow, or quad-gyre flow, is a two-dimensional kinematic model of the Rayleigh-Bénard convection cells, with periodic boundary conditions in both directions instead of material boundaries in y. The quasiperiodic version of this system is seen in Lekien and Ross (2010), and a similar system was studied by Shadden *et al.* (2005). The streamfunction is given by:

$$\psi(x, y, t) = \sin\Big(\pi\left(x - g(t)\right)\Big)\sin(\pi y), \tag{5.1.1}$$

where $g(t) = \epsilon_1 \sin(4\pi t) + \epsilon_2 \sin(2t)$. The physical domain of the flow is given by the 2-torus, $[0, 2]^2$.

The system type (i.e. autonomous or nonautonomous) is seen to be dependent on the two parameters ϵ_1 and ϵ_2. When both parameters are equal to zero the steady cell flow is recovered. This system is autonomous, and invariant manifold theory can be used to analyze the dynamics. The flow has families of periodic orbits around elliptic

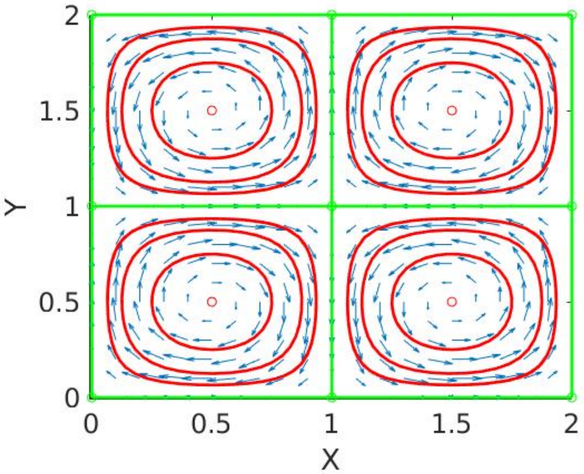

Figure 5.1.1: The invariant manifold analysis for the steady-cell flow. Hyperbolic fixed points of the steady-cell flow are shown as green circles, while elliptic fixed points are red circles. The hyperbolic boundaries that divide the cells are shown as green lines. Red lines highlight some of the periodic orbits.

fixed points, bounded by the heteroclinic orbits that connect the hyperbolic fixed points. The periodic orbits are seen as counter-rotating vortices contained within cells; these orbits are seen in Fig. 5.1.1 as red curves. Further, due to the manifolds connecting the hyperbolic points, no (deterministic) transport is possible between the cells.

However if only one of the ϵ's is nonzero then the streamfunction is periodic. In the periodic case it is possible for KAM regions, closed invariant curves with the period T, to exist within the chaotic sea, whereas in the quasiperiodic case (where both ϵ's are nonzero) these structures are typically destroyed. Using 500 periods of the steady-cell and quad-gyre (periodic) flows, the obtained Poincaré sections are shown in Fig. 5.1.2.

In Fig. 5.1.2a the structures uncovered from the invariant manifold analysis are clearly seen; even the elliptic fixed points are clearly obtained. However, for the

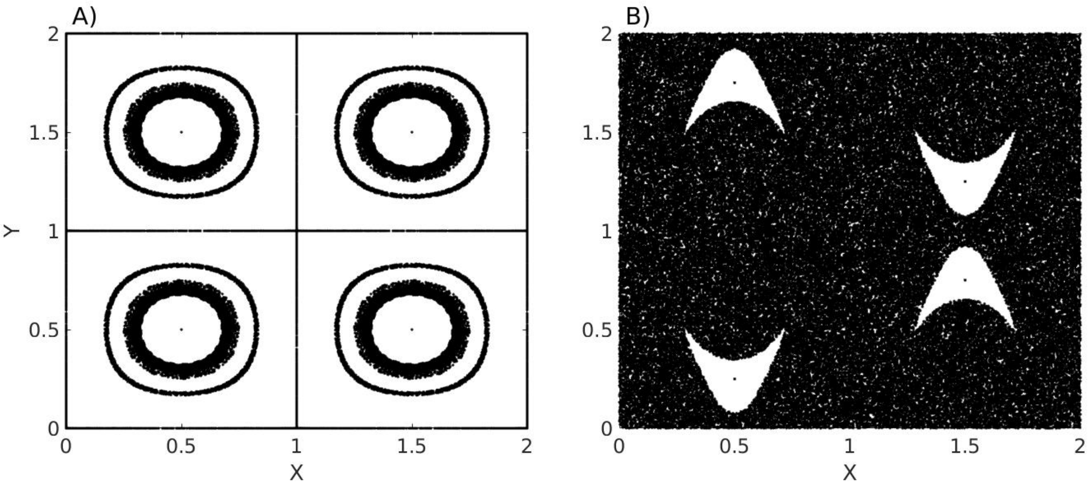

Figure 5.1.2: The Poincaré sections obtained from 500 iterations of the periodic maps for a) the steady-cell flow, and b) the quad-gyre flow.

periodic case (Fig. 5.1.2b), a lot of structure is lost to the chaotic sea, which is only interrupted by the 4 KAM regions. The middle of these KAM regions also contains elliptic points. Writing the parameters ϵ_1 and ϵ_2 as (ϵ_1, ϵ_2), the following cases are investigated: $(0, 0)$, $(.3, 0)$, and $(.3, .1)$.

Bickley Jet

A natural extension from the annulus flow discussed in Section3.4 is the Bickley jet model. It comes from the studies of the stability of a zonal shear flow, where the zonal velocity $u \propto \text{sech}^2 y$ (see Bickley (1937)), and can exhibit two vortex chains separated by a shear jet. The introduction of a second vortex chain allows for more complex dynamics – this is further stressed by the bulk motion of the two chains. The northern chain tends to propagate trajectories westward, while the southern vortices show trajectories heading east. This break in symmetry will present itself later in the tails of the PDFs for the x statistics. The streamfunction of the Bickley jet is given by:

$$\psi(x,y,t) = \tanh y + \operatorname{sech} y \sum_{i=1}^{2} \epsilon_i \cos k_i \left(x - c_i t\right) \tag{5.1.2}$$

where ϵ_i, k_i, c_i are the amplitude, wave number and phase speed of the waves, respectively. Parameters are chosen to be dynamically consistent with the governing equations:

$$\Delta = \sqrt{1 - \frac{3}{2}\beta}, \beta \in \left(0, \frac{2}{3}\right); c_{1,2} = \frac{1}{3}\left(1 \pm \Delta\right), k_{1,2}^2 = 6c_{1,2}, \tag{5.1.3}$$

hence the dynamics are given in a three-parameter family $(\beta, \epsilon_{1,2})$. β is chosen such that the streamfunction is spatially-periodic in the zonal direction with period 5π; $\beta = 0.6144$. A reference frame co-moving with one of the waves, c_2, is adopted. The streamfunction is then time-periodic with period $T = 2\pi/k_1(c_1 - c_2)$. Given the co-moving frame and the choice of β, the period is $T = 21.04$. Further, since the Bickley jet is time periodic it is possible to frame it as an autonomous system. The physical domain for the Bickley jet is given by $[-2.5\pi, 2.5\pi] \times [-3, 3]$, with periodic boundary conditions in x and free-slip boundaries in y.

It has been noted in del Castillo-Negrete and Morrison (1993), that dependent on choice of parameters the phase portrait may transition between homoclinic and heteroclinic connections, as well as transition between a persistent zonal jet and the breaking up of this central barrier. The parameters used in this work were chosen such that for one case the integrable jet coexists with chaotic zones, and for the other case, along with the previous features there also exists persistent eddies. These cases represent a strongly-chaotic Bickley jet with $\epsilon_1 = .1$ and $\epsilon_2 = .3$, and a weakly-chaotic Bickley jet with $\epsilon_1 = .002, \epsilon_2 = .3$.

Turbulent Flow

The two-dimensional turbulent flow is obtained from using the streamfunction-vorticity formulation (below) in a direct numerical simulation (DNS):

$$\omega_t + J\left[\psi, \omega\right] = d + f, \tag{5.1.4}$$

where ψ is the streamfunction, $\omega = \nabla^2\psi$ is the vorticity, $J\left[\psi, \omega\right]$ is the Jacobian operator acting on ψ and ω, d is the dissapation mechanism and f is the forcing to enforce conservation of enstrophy. The dissipation mechanism is given more specifically as, $d = \nabla^2\omega/Re + \psi$. The first term is the standard dissipation mechanism and acts to removes energy at the small scales, whereas the second term, the inverse Laplacian of ω, provides damping at the large scale, limiting the inverse cascade of energy. The forcing f is applied to ensure the conservation of enstrophy at the $(2, 2)$ mode. A random phase on the forcing is used so that coherent structures are not permanent features. From using a length scale of $100km$, a velocity scale of $0.01m/s$ and an eddy viscosity of $1m^2/s$, the Reynolds number Re is given as, $Re = 1000$. The non-dimensional physical domain of the turbulent flow is given by the 2-torus, $[0, 2\pi]^2$.

Anomalous Transport Analyses

The analyses discussed in this chapter focus on using Lagrangian coherent structure identification techniques to partition the topology of a flow into dynamically distinct coherent regions, and then looking at the conditional statistics obtained from these partitions. The probability density functions (pdfs) of these statistics will then be used in a fractional diffusion model to approximate the transport process.

Aiming to show that Lagrangian coherent structures (LCSs) are appropriate for the use in anomalous diffusion modeling, as a first step in this direction is verification that LCSs are effective tools for detecting the barriers between dynamically distinct regions of a dynamical system. This will be done by looking at conditional variances of passive tracer ensembles and observing their behavior. From there, conditional jump and waiting-time pdfs are obtained to use as inputs to a fractional diffusion model.

Conditional Variances

First, a brief review on the work of Tang and Walker (2012). A comparison is done between the FTLE field, and fields highlighting the variability in the variances in x and y. For this analysis the strongly-chaotic and weakly-chaotic Bickley jets (as discussed in Section 5.1.2) will be used, while an integration time of $\tau : t - t_0 = 50T$, where T is the period of the flow, was used to compute the FTLE field. The same integration time was used for the advection of the passive tracers. This long integration time gives ample time for structures to develop, as well as for the variances of the tracer ensembles to reach steady-state.

The statistics of interest are those related to diffusion and dispersion, as such the evolution of the variance for each initial condition is tracked. This variance is computed for an ensemble released at $\mathbf{x_0}$, as:

$$var\left(\mathbf{x}\left(t;\mathbf{x_0},t_0\right)\right) = \sum_{r=1}^{K}\left[\mathbf{x_r}(t;\mathbf{x_0},t_0) - \overline{\mathbf{x_r}(t;\mathbf{x_0},t_0)}\right]^2, \tag{5.2.1}$$

where K represents the number of passive tracers used, $\mathbf{x_r}$ is used to signify that the statistics in x and y are taken separately, and the overbar is used to denote the average taken over the tracer ensemble.

The flow topology and variability of scalar variances for the strongly-chaotic and weakly-chaotic Bickley jets are compared in Figs. 5.2.1 and 5.2.2, respectively. The deterministic forward-time FTLE fields (shown in Figs. 5.2.1a and 5.2.2a for the strong

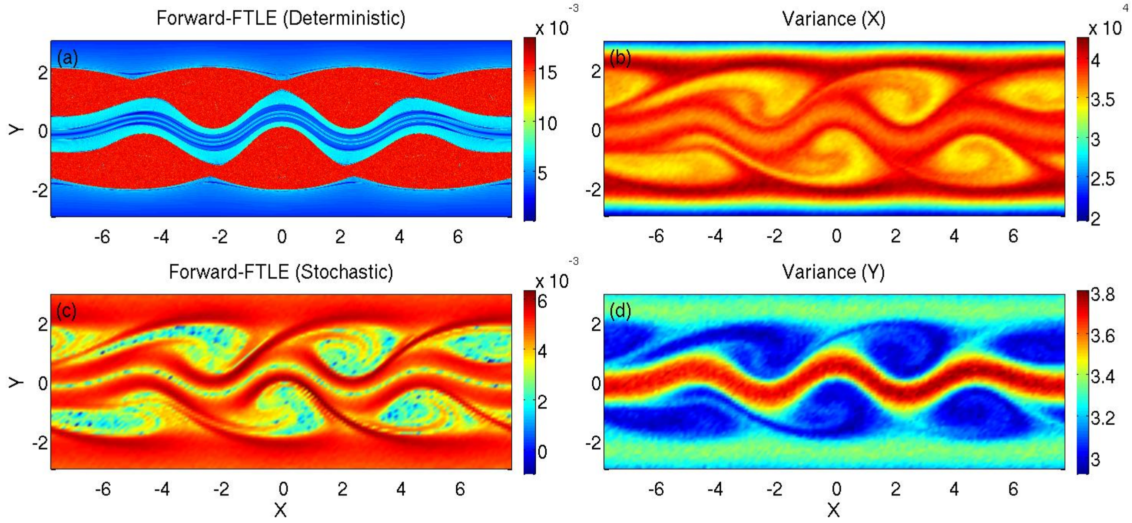

Figure 5.2.1: Comparison among LCS and variances, all dependent on the initial conditions and computed for an integration time of 50 wave periods with the strongly-chaotic Bickley jet. (a) Forward-time FTLE based on deterministic trajectories, (b) forward-time FTLE based on means of stochastic trajectories, (c) variance of x displacements, and (d) variance of y displacements.

and weakly chaotic Bickley jets, respectively) are obtained using an integration time of 50 wave periods, with a resolution of 1152×512. Using the auxiliary grid approach the boundaries of shear regions are highly resolved. With the parameters selected the central barrier is preserved for both flows, depicted as the wavy region of relatively low FTLE values around $Y = 0$.

For the strongly-chaotic Bickley jet(Fig. 5.2.1a), outside of the central jet, jet barriers are seen on both sides. These take the form of a smooth transition of FTLE values, up to highlighting FTLE ridges which separate the jet boundaries from the chaotic zones. The FTLE values inside of the chaotic zones appear to predict large separations, due to the fine structures of the heteroclinic tangles. These tangles are not fully resolved at this resolution, and result is relatively high FTLE values in the chaotic zones. Outside of the chaotic zones are two shear bands, one on the north of the domain, and one on the south.

Figs. 5.2.1b,d show the variability of scalar variances based on initial location in the flow, in the x and y directions, respectively. In order to compute the values seen in the contour maps, an ensemble of tracers is released from every gridcell for a reduced resolution. A reduced resolution of 144×64 was used for the variance plots to reduce computational costs. The ensembles are then evolved forward in time according to (2.2.2) for 50 wave periods. In order to model the normal diffusion process, Gaussian noise was used ($\alpha = 2$), with a noise amplitude of $D = \sqrt{.002}$. The variance in x and y was then computed for each ensemble using (5.2.1), and correlated back to its initial location. Each ensemble was comprised of 50,000 trajectories.

The contour maps indicating the variability of variance correspond well with their respective flow topologies, except for in the chaotic zones. The variance figures display regions of the chaotic zone that have relatively lower variances, indicating low-dispersion. In these regions, although deterministic trajectories are chaotic, an ensemble of stochastic trajectories behave quite regularly after sufficient time. Motivated by this bulk behavior, the stochastic FTLE is computed to see if this behavior is captured.

The stochastic FTLE fields (shown in Figs. 5.2.1c and 5.2.2c, for the strongly and weakly chaotic Bickley jets, respectively) are obtained from the ensemble mean trajectories. The mean trajectories are used to compute the deformation gradient tensor and subsequently the FTLE. The stochatic FTLE (Fig. 5.2.1c) shows regions of relatively low values that correspond very well to the regions of low variance within the chaotic zones (b,d). However, note that the computation of the stochastic FTLE requires the advection of ensembles of trajectories for each cell. Instead the deterministic FTLE is used as the partitioning method, in the hopes of relating the diffusion processes to *a priori* knowledge of coherent structures without having to compute (2.2.2).

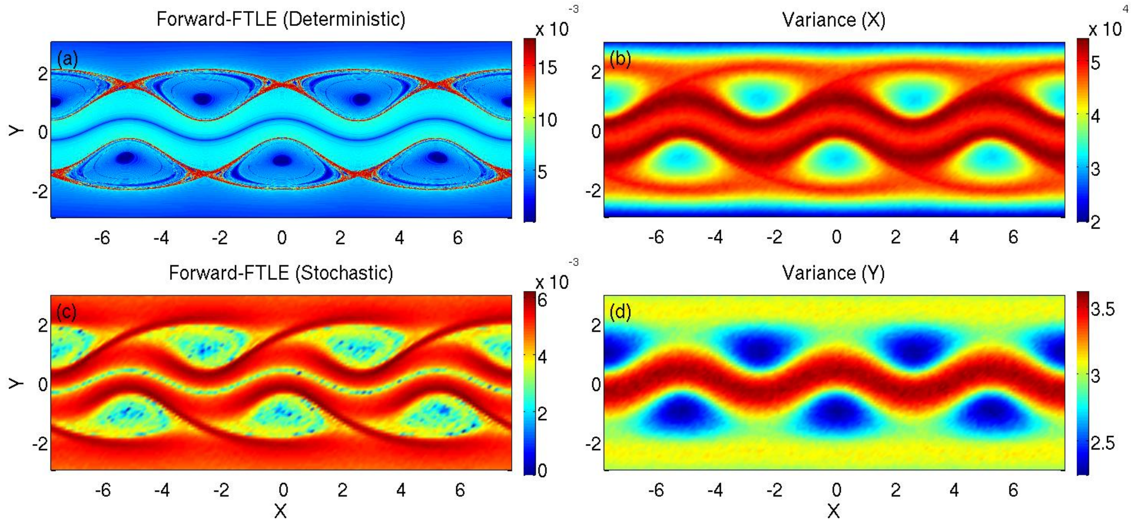

Figure 5.2.2: Comparison among LCS and variances, all dependent on the initial conditions and computed for an integration time of 50 wave periods with the weakly-chaotic Bickley jet. (a) Forward-time FTLE based on deterministic trajectories, (b) forward-time FTLE based on means of stochastic trajectories, (c) variance of x displacements, and (d) variance of y displacements.

For the weakly-chaotic Bickley jet there is less shear in this central jet, thus the jet barriers cover a greater portion of the domain than before; this is seen in Fig. 5.2.2a. Regions of relatively low FTLE values are seen collected together in the chaotic zones, these represent KAM regions. The low values in the center correspond to elliptic cores, where the other low values correspond to resonant islands near the elliptic boundaries. From a direct comparison of the deterministic FTLE to the contour plots of the variance (Figs. 5.2.2b,d) good correlation is seen in the central jet region as well as the vortex chains. The lower values seen in the variance plots confirm that the elliptic structure seen in the FTLE field act to trap the passive tracers. The stochastic FTLE in Fig. 5.2.2c, shows regions of lower FTLE values that correspond to where the lower variances are seen in (b) and (d).

Results

Encouraged by the observation of near-constant variance values within distinct subsets of the flow domain, the probability density functions (pdfs) for the variances conditioned on initial region types are investigated. More explicitly, the flow topology given by Fig. 5.2.1a is separated into 4 distinct regions based on: relative FTLE value, large gradients in the FTLE field, and eliminating spurious results[1] via visual inspection. For the strongly-chaotic Bickley jet, the resulting partition is depicted in Fig. 5.2.3e with colored dots representing members of a given region in their respective locations. This is plotted on top of the FTLE field for further emphasis. Recalling that the variances were computed for all the cells of a 144×64 resolution grid, these initial conditions are used as the representative candidates of the regions.

The initial conditions that belong to the central jet (parabolic region) of the strongly-chaotic Bickley jet, are seen in Fig. 5.2.3e as the collection of white dots that are centered along $Y = 0$. To the north and south of the parabolic region the white dots represent the initial conditions that are in the chaotic zones. The outer most set of black dots represent the initial conditions classified as being in the hyperbolic region, whereas the remaining black dots represent the hyperbolic-shear region. The pdf of the conditional variances for the hyperbolic, hyperbolic-shear, chaotic and parabolic regions are seen in Fig. 5.2.3a-d, respectively. The chaotic and hyperbolic zones represent “jumping” type regions, where tracer trajectories evolve rapidly, exhibiting large displacements, and scalar dispersion is enhanced.

In the plots of the variance pdfs, the solid black curves are used to represent the quantities with respect to the variance in x, and the dashed blue curves are used for

---

[1] These are the false positives and negatives discussed earlier.

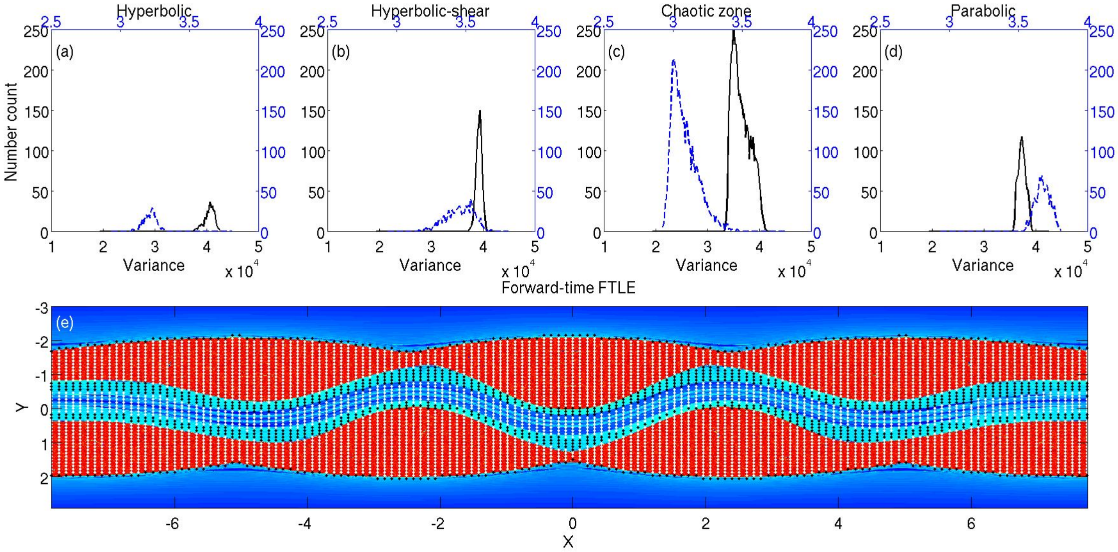

Figure 5.2.3: Conditional statistics of variances and the FTLE based partition of the flow field into different regions; the statistics and FTLE field are obtained from the strongly-chaotic Bickley jet with an integration time of 50 wave periods. (a) Outer barriers that are hyperbolic, (b) inner barriers that transition from hyperbolic to parabolic structures, (c) chaotic zone between the hyperbolic barriers, (d) parabolic central jet, and (e) partitioning of the domain (based on FTLE) superimposed on FTLE.

values obtained from the variance in y. Further, the same color code was used on the axes for those figures.

As expected, in all except for the chaotic zone, the conditional variances show unimodal behavior with relatively narrow width, indicating high probability in a small range of diffusivity. The residence time of trajectories in the center of the chaotic zone is longer than those close to the hyperbolic barriers, due in part to finite-time structures that live on a shorter timescale than the integration time used. The result is a continuous transition of initial conditions from the center towards the edge of the zone – seen as the relatively flat and wide pdf for the variances in Fig. 5.2.3c. From this it is observed that conditional statistics for coherent regions are unimodal — indicating homogeneous dynamics throughout.

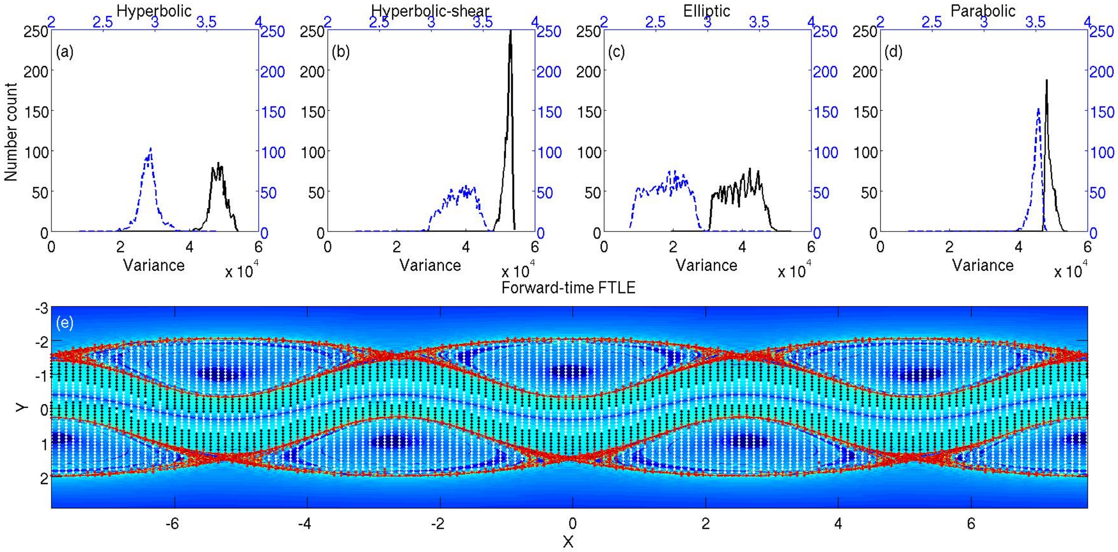

Figure 5.2.4: Conditional statistics of variances and the FTLE based partition of the flow field into different regions; the statistics and FTLE field are obtained from the weakly-chaotic Bickley jet with an integration time of 50 wave periods. (a) Outer barriers that are hyperbolic, (b) inner barriers that transition from hyperbolic to parabolic structures, (c) chaotic zone between the hyperbolic barriers, (d) parabolic central jet, and (e) partitioning of the domain (based on FTLE) superimposed on FTLE.

Having had greater correlation between the FTLE field and the scalar variances of the weakly-chaotic Bickley jet, the results are now contrasted to the previous case. The region detected as chaotic will be represented in Fig. 5.2.4e as red dots, and will be referred to as the hyperbolic region. The white dots along the curve centered around $Y = 0$ represent the parabolic region, while the other white dots now represent the elliptic regions, or “trapping” type regions; in these regions the relative dispersion of scalars is inhibited. The black dots designate the hyperbolic-shear region.

For most of the regions, the pdfs are unimodal with narrow widths. The pdf of the variance in y of the initial conditions that started in the hyperbolic-shear region is seen (in Fig. 5.2.4b) to have a wide and relatively flat peak. The same behavior is seen in the pdfs of the variances for the elliptic region. As before, residence times of trajectories in the center of these elliptic regions is longer than those close to the boundaries. These flat pdfs also suggest that the partition has incorrectly identified several dynamically distinct regions as one; a more refined partition of the field might help distinguish the regions. For instance, the northern and southern elliptic regions are all treated as one region, while in reality the different elliptic regions could have varying dynamics. This rough partition still gives insight to the anomalous transport.

Conditional Dispersion Statistics

Moving from the variances to looking directly at the temporal evolution of the conditional dispersion statistics. The dispersion statistics are obtained from using all of the realizations with the same initial condition, and subtracting their mean value; the relative displacement from the ensemble mean. For each initial condition $\mathbf{x_0}$ in the same LCS (i.e. hyperbolic, chaotic zone, etc.), the pdf of the dispersion is computed as:

$$\delta\mathbf{x_r} = \mathbf{x_r}(t;\mathbf{x_0},t_0) - \overline{\mathbf{x_r}(t;\mathbf{x_0},t_0)}, \tag{5.2.2}$$

where the overline denotes the average at time t of all the realizations originating from $\mathbf{x_0}$. As the statistics reach steady-state it is possible, with a proper rescaling in time, to see the pdfs fall onto self-similar profiles. Here we use the same flows and partitions outlined in Section 5.2.1, for which the variances are seen to reach steady-state within 50 wave periods.

The pdfs for $\delta\mathbf{x_r}$ are shown in Fig. 5.2.5 for the different regions of the strongly-chaotic Bickley jet. The hyperbolic zone in Fig. 5.2.5a corresponds to the combination of the two boundary regions in Fig. 5.2.3(a-b). The chaotic (Fig. 5.2.5b) and parabolic (Fig. 5.2.5c) zones cover the same regions as Fig. 5.2.3c-d, respectively. The results taken over the entire domain are shown in Fig. 5.2.5d. Again, the black curves and axes associate with the x statistics, while blue is used for the y statistics. The lonely

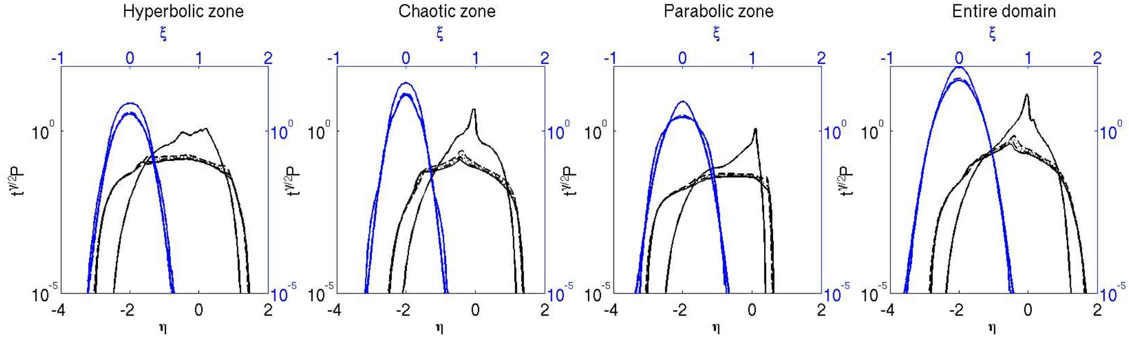

Figure 5.2.5: Conditional statistics on scalar dispersion in different partitions of the flow, for the strongly-chaotic Bickley jet.

solid curves in each panel correspond to $t = 5T$ and those that fall onto the self-similar profile are $t = 35T$ (dashed line), $t = 40T$ (doted line), $t = 45T$ (dashed-dotted line), and $t = 50T$ (solid line), where T is the period. These last four curves (after proper rescaling) are almost indistinguishable in Fig. 5.2.5, with only small variabilities.

In analyzing the δy statistics, simple symmetric structures are noted. With flatter and wider peaks, along with fatter tails, the y statistics at $t = 5T$ appear to be non-Gaussian for all of the regions. The pdfs, with proper rescaling are seen to approach a Gaussian profile as time progresses. The pdf is of the form, $P(\delta y, t) = t^{-\gamma/2} f(\xi)$, $\xi = \delta y / t^{\gamma/2}$, where f is a scaling function, ξ a scaled coordinate, and γ the exponential decay rate. A decay rate of one ($\gamma = 1$) indicates normal diffusion, $\gamma < 1$ indicates subdiffusion, and $\gamma > 1$ indicates superdiffusion. For the strongly-chaotic Bickley jet, the exponent γ is found to be: 0.75, 0.78, 0.72, and 0.7 for Fig. 5.2.5a-d, respectively. The dispersion in y is seen to be consistently subdiffusive. The parabolic region has the least decay, consistent with the fact that the shear barriers inhibit cross-jet transport.

Looking now at the δx statistics, irregular shapes are noted in Fig. 5.2.5. As time progresses the pdfs fall onto self-similar curves, but these are not Gaussian profiles.

In fact, it is seen that the left and right tails scale at different rates. The self-similar profile takes the form, $P(\delta x, t) = t^{-\alpha/2} g(\eta)$, $\eta = \delta x / t^{\beta_{\pm}/2}$, where g is a scaling function, η a scaled coordinate, α is the exponential decay rate, and $\beta_{\pm}$ corresponds to the expansion of the tails in positive and negative branches of δx, respectively.

For the strongly-chaotic Bickley jet, the expansion rates in the positive branch (β_+) are 1.78, 1.78, 1.95, 1.78, while the expansion rates in the negative branch (β_-) are 1.48, 1.52, 1.48, 1.5 and the decay rates α are 1.5, 2, 1.75, 2 for Fig. 5.2.5a-d, respectively. All the scaling parameters are summarized in Table 5.1.

The loss of symmetry in the tails is due to the relative motion of neighboring regions. More explicitly, the parabolic jet moves in the positive x direction, while the chaotic and shear zones move in the negative x direction, resulting in different growth rates in the positive and negative tails. Further, since a significant amount of realizations diffuse into the outer shear regions from the hyperbolic and chaotic zones, a peak is seen in the pdfs at negative values of η in Fig. 5.2.5a-b. Since the parabolic zone has the jet boundaries as effective transport barriers, not a significant amount of realizations leak from the parabolic zone to the chaotic zone; therefore, a similar peak is not seen for negative η values. With the decay rates found for the strongly-chaotic Bickley jet, zonal transport is superdiffusive. Indicating that coherent structures can aid in the mixing/diffusion process.

The pdfs shown in Fig. 5.2.6 are for the different regions of the weakly-chaotic Bickley jet. It is again seen that the y statistics have simple structures compared to their x counterparts. The parameters used for the scaling can be found in Table 5.2. It is seen from the variability of the conditional dispersion statistics that zonal transport in consistently superdiffusive, while dispersion in y is consistently subdiffusive. The conclusion is that even a rough partition (as used here) is able to capture and

Parameter	Zone Type			
	Hyperbolic	Chaotic	Parabolic	Entire
γ	0.75	0.78	0.72	0.7
β_+	1.78	1.78	1.95	1.78
β_-	1.48	1.52	1.48	1.5
α	1.5	2	1.75	2

Table 5.1: Scaling parameters used for the pdfs of the conditional statistics for the strongly-chaotic Bickley jet.

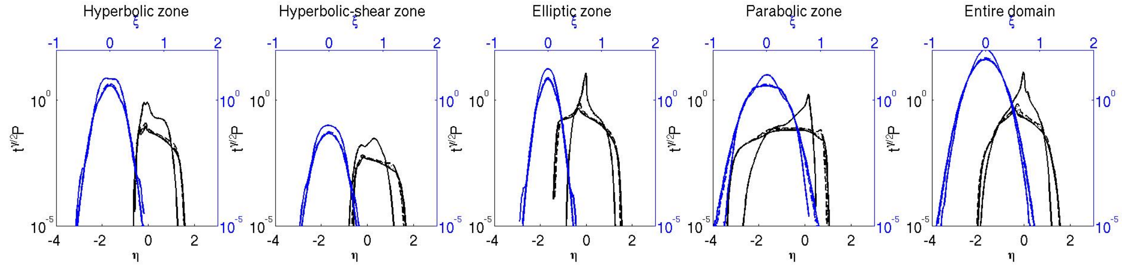

Figure 5.2.6: Conditional statistics on scalar dispersion in different partitions of the flow, for the weakly-chaotic Bickley jet.

characterize some of the aspects of anomalous diffusion, in both weakly and strongly chaotic systems.

Conditional Resident-Time Statistics

In Tang and Walker (2012), it was seen that use of FTLE in studying anomalous diffusion is promising because of its ability to highlight structures. However, it was also noted that poor classification of regions lead to non-unimodal statistics (cf. Fig. 5.2.5d and Fig. 5.2.6d). Here this investigation is expanded upon with a clear objective: a comparison of the effect the partitions obtained from the LCS detection techniques have on the conditional statistics. This is not attempting to make a comparison of the objectivity between the methods, but more simply, the robustness of

Parameter	Zone Type				
	Hyperbolic	Hyperbolic-shear	Elliptic	Parabolic	Entire
γ	0.75	0.75	0.82	0.62	0.66
β_+	1.75	1.7	1.75	1.8	1.8
β_-	1.9	1.93	1.6	1.45	1.6
α	1.7	1.2	1.5	1.6	2

Table 5.2: Scaling parameters used for the pdfs of the conditional statistics for the weakly-chaotic Bickley jet.

the statistics to detection method/tool used for classifying the finite-time coherent *regions*. This section is under review by Physical Review E.

A coherent region is one which retains all of its members under the deterministic action of the flow. When noise is added, passive tracers are able to traverse the transport barriers and escape these regions. The deterministic trajectories are compared with two types of stochastic trajectories; One where the noise is Gaussian ($\alpha = 2$), and the other, with Lévy noise ($\alpha = 1.5$). For both stochastic cases, a noise amplitude of $D = .005$ is used. The trajectories are obtained from solving (2.2.2).

The weakly-chaotic Bickley jet is used as a guide to test the ability of the methods to correctly classify coherent regions. Coherence will be tested by looking at the retention rate for each classified region type. Since the flow is periodic, PS provides a precise partitioning of the flow domain, seen in Fig. 5.2.7a. As such, it is against this partition that the other domain partitions will be compared.

The PS of the model (Fig. 5.2.7a) is obtained by seeding the domain with tracers and integrating their deterministic trajectories for one thousand wave periods. From these, a few special trajectories are used to highlight the partition of the flow topology. Based on the Bickley jet parameter selection, an integrable jet should be present in the

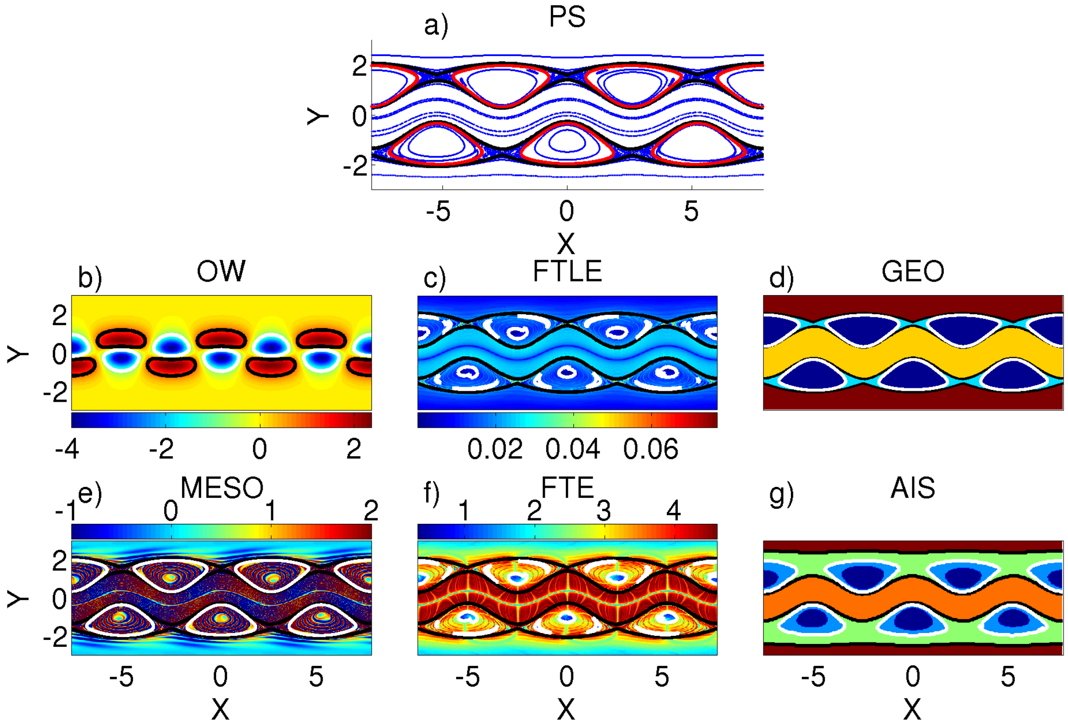

Figure 5.2.7: Comparison of different partitions used for the Bickley jet at $t = 0$. For methods that require an integration time, trajectories were integrated for 10 wave periods, except for PS which used 1000 wave periods. (a) Partition based on PS, (b) based on OW, (c) based on FTLE, (d) based on GEO, (e) based on MESO, (f) based on FTE, and (g) based on AIS. In all panels, the black curves separate the jumping and shear regions and white (red in PS) curves bound trapping regions.

flow – this feature is seen as the white band centered near $Y = 0$. This parabolic jet is bound on either side by black trajectories. Just beyond these black trajectories lie the northern and southern chaotic zones, these regions tend to exhibit large separation of initially nearby trajectories; except for the regions bound by the red curves, these correspond to elliptic regions. The two black trajectories that are furthest from $Y = 0$ indicate the terminal edge of their respective chaotic zones, beyond which lie integrable shear regions.

The partitions for all of the methods are given in Fig. 5.2.7, where the panels are a) Poincare Section (PS), b) Eulerian Okubo-Weiss (OW), c) finite-time Lyapunov exponent (FTLE), d) geodesic method (GEO), e) Mesochronicity (MESO), f) finite-time entropy (FTE), and g) almost-invariant set (AIS) respectively; all corresponding to $t = 0$. Where applicable, the color scales are below the center panels, and above the bottom panels. For the Lagrangian methods, an integration time of 10 wave periods was used. For OW, FTLE, and FTE, the measures are created with a resolution of 576×256. The thresholds for trapping region boundaries are 0.01 for FTLE and 1.75 for FTE. For GEO and MESO, a 1000×1000 resolution grid was used to extract the trapping region boundaries for each KAM structure (roughly corresponding to a subdomain of size $2\pi \times 3$ for each region). As discussed earlier, the auxiliary grid approach is used for computing gradients where appropriate.

For the computation of AIS, the grid resolution is reduced to 288×128 such that the eigenvectors of the transfer matrix can be handled by computer. In order to obtain the transfer matrix used in the FTE computation, 100 initially uniformly distributed trajectories are used for each grid cell. These trajectories are also used for the lower resolution AIS computation – now corresponding to 400 initially uniformly distributed trajectories for each grid cell. A 5-way cut approach/partition has been implemented to provide the relevant flow features for AIS. It is noted that a 4-way cut would have resulted in the exclusion of the resonant islands in the KAM regions.

For all of the partitions, the regions classified as “jumping” regions are bound by black curves, while the “trapping” regions are bound by white curves – except for PS which uses red curves to bound the trapping regions. For the FTLE, MESO, and FTE methods, the boundaries of shear regions are highlighted by a notable change in the measure value and pattern differences. These changes in pattern are used to manually obtain the shear boundaries, resulting in curves that are virtually indistinguishable from those obtained from PS. Further, since the shear boundary extraction for GEO is similar to that for FTLE, the shear and jet regions obtained from GEO are also virtually indistinguishable from those obtained from PS. For AIS, the multi-level partition gives a direct identification of the flow features. Since GEO and AIS are set based approaches – they identify regions instead of boundaries – no color scale is used.

From comparing the partitions, it is evident that the results given by OW are the most different. This is owing to the fact that the OW measure is instantaneous and Eulerian, while the other methods are all Lagrangian. The Lagrangianly integrated OW measure would provide similar images to the other methods, but in order to compare the results to Kadoch *et al.* (2011), which uses the instantaneous OW, the instantaneous OW is used.

From comparing the Lagrangian based methods further, note that the trapping regions as identified via the thresholding for FTLE and FTE provide the least resemblance to PS. The two methods do, however, give very similar results to each other. This is expected since, for the chosen systems the FTE is viewed as a nonlinear generalization of the FTLE, that operates on ϵ-scales instead of infinitesimal; Froyland and Padberg-Gehle (2012). At the center of the KAM regions, as identified by PS, an eddy core can be identified from FTLE/FTE. In addition to the eddy core, some smaller regions of low FTLE/FTE value can be identified around the KAM tori. These smaller regions correspond to resonant islands found in PS (cf. Fig. 5.2.8). The trapping region boundaries identified from GEO and MESO are both close to those obtained in PS, with small differences on the edge. The chaotic zones identified by AIS are slightly larger than the results from PS. The chaotic zones given by AIS include portions of the outer shear regions and the inner jet, as identified by PS.

To highlight the differences in the trapping region detection between the Lagrangian methods, a higher resolution analysis is done around one of the KAM regions, as identified in PS. The comparison is seen in Fig. 5.2.8, where the scattered

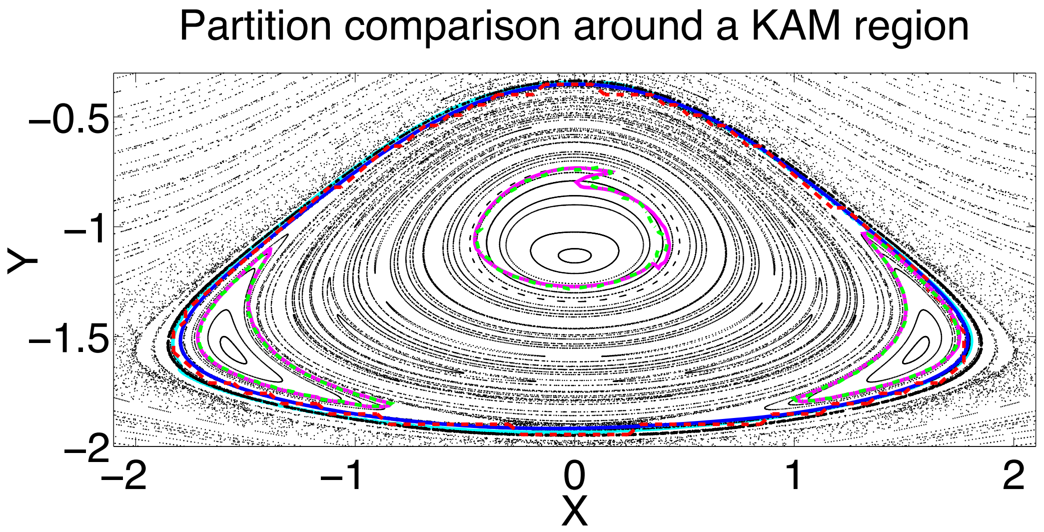

Figure 5.2.8: Comparison of trapping region boundaries among the Lagrangian methods for the Bickley jet. The Ponicaré section is shown as the objective depiction of the KAM. The extracted curves are: black curve –boundary of trapping region from PS; solid blue curve – transport barrier from GEO; dashed red curve – boundary of elliptic coherent sets from AIS; solid magenta curve –isocontour of FTLE at $\sigma = 0.01$; dashed green curve–isocontour of FTE at $\alpha = 1.75$; solid cyan curve – largest smooth ring from MESO.

black points are from PS and highlight the elliptic KAM region, the chaotic zones surrounding it, and portions of the integrable jet and outer shear region to the north and south, respectively. Two resonant islands are clearly visible at the lower left and right of the KAM core. The black curve is the trapping region boundary obtained from trajectories which last for four thousand wave periods without entering the chaotic zone. The solid blue curve is the trapping boundary from GEO. This curve closely approximates the bounding black curve, and also tightly bounds the resonant islands. The red dashed curve is the boundary given by AIS. Although the AIS results suffer from being computed at a lower resolution, they still closely approximate the bounding curve given by PS. The boundary given by MESO is obtained by extracting the largest smooth ring of elliptic motion, and is shown as a solid cyan curve. The partitions given by FTLE (solid magenta curve) and FTE (dashed green curve) are seen to only extract the KAM core and the resonant islands.

Essentially, although there are slight differences, PS, GEO, AIS, and MESO can be grouped together – for this simple model – as a type of approach that emphasizes extraction of elliptic type motion and offer similar results. In the same manner, the FTLE and FTE methods can be grouped as a type of approach that emphasizes hyperbolicity. The thresholding used for FTLE and FTE is not expected to objectively extract the vortices, as the choice of threshold is arbitrarily taken. However, given that only portions of the KAM regions are extracted in these methods, it is interesting to see what affect there will be on the statistics. This is further motivated by the fact that the computation of FTLE is cheaper than GEO, and similarly, computing FTE is cheaper than AIS.

Coherence

If the partition is completely coherent, then the *deterministic* trajectories should return to the same regions – due to the periodicity in time and space for the flow. This is shown in Fig. 5.2.9 for the *four* types of partition methods used. As discussed earlier, the results for PS, GEO, and MESO are all grouped together, but since the chaotic zone was larger for AIS it is considered separately. In all the panels, the initial partition boundaries are shown by black curves. The red and blue dots are used to indicate the terminal position of trajectories that were initiated in jumping and trapping regions, respectively. For the Lagrangian methods, the black dots correspond to the terminal location of trajectories initiated in the shear regions. While black dots correspond to trajectories initiated in the intermediate region for OW. The trajectories were deterministically advected for an integration time of ten wave periods, the same integration time used to obtain the Lagrangian partitions. Since the integration time is an integer multiple of the period, good correlation between the colored dots and the black bounding curves is expected for the Lagrangian methods (i.e. trajectories of the same color should stay in the same region separated by the black curves).

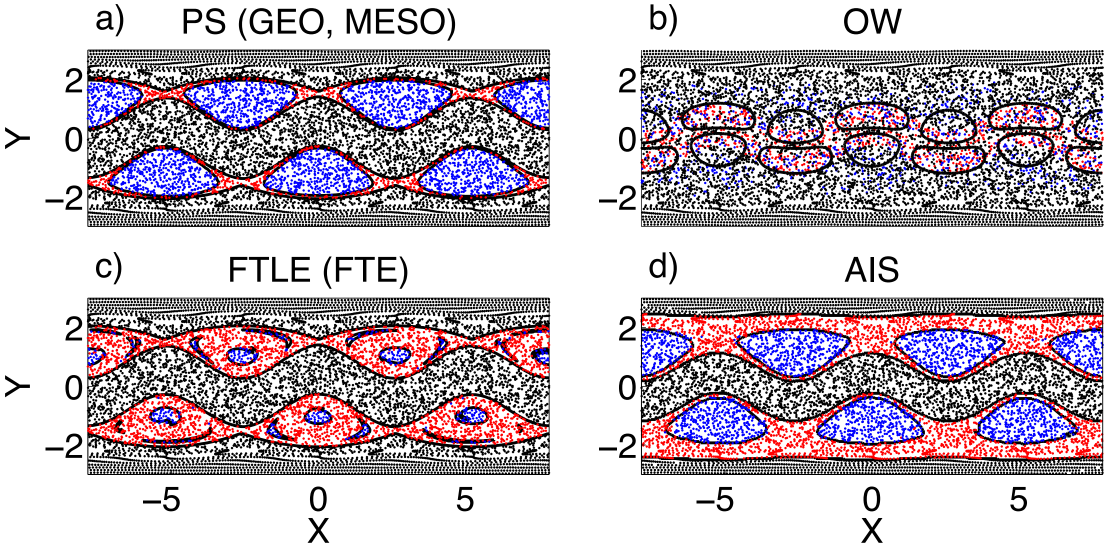

Figure 5.2.9: Comparison between trajectory initial and terminal conditions for various partitions, for trajectories integrated for 10 wave periods with the Bickley jet model. The black curves in each panel show the initial partition of the flow domain, and the color-coded points correspond to the current locations of trajectories and the colors indicate the original partition. The blue indicates tracers that are classified as being in trapping regions at $t = 0$, red indicates tracers classified as being in the jumping region, and the black dots correspond to the remaining tracers. The methods used are (a) PS. (b) OW, (c) FTLE, and (d) AIS.

Fig. 5.2.9a shows the PS results, the OW results are shown in Fig. 5.2.9b, the FTLE and FTE results are grouped together and the FTLE results are shown in Fig. 5.2.9c, and AIS is shown in Fig. 5.2.9d. Despite there still being minor leaks in the Lagrangian partitions, the trapping regions hold up nicely. Bearing in mind the fact that the OW partition is based on an instantaneous quantity, it is not expected that trajectories would return to their original partitions, which is indeed the case.

It is seen for OW that the red and blue dots do not remain bounded by the black contours. As discussed earlier, the chaotic zone given by AIS invades into the northern and southern shear zones as identified by PS, and based on the scattered dots, these boundaries seem to separate high and low shear within the shear regions – instead of separating the integrable and non-integrable trajectories as defined by PS.

Although this qualitative comparison of the coherence is insightful, a quantitative comparison would be more beneficial. To this end, the retention rate for the different region types are computed for each method. Passive tracers are uniformly seeded throughout the computational domain, with 5000 trajectories per grid cell ($20,000$ per cell for AIS due to the larger cell size). The tracers are then advected deterministically in forward-time for ten wave periods, and the percentage of tracers that were in a given region type at $t = 0$ that are still in that partition type at the terminal time (trajectories may leave and return during the interval) is given in Table 5.3.

Region type	Partition method						
	PS	OW	FTLE	MESO	GEO	FTE	AIS
Trapping	99.93	22.1	77.7	98.1	99.1	79.4	93.6
Jet	100	—	100	100	100	100	97.7
Jumping	99.6	46.5	99.91	96.2	97.2	99.93	93.2
Shear	100	88.2	100	100	100	100	96.8

Table 5.3: Comparison of percentage of tracers that remain in their classified region type at the end of ten periods, for various partition methods. The central shear band is labeled as “Jet”, while the shear zones located outside of the hyperbolic regions are collectively labeled as “Shear”.

Note that since OW only identifies trapping and jumping regions, and considers everything else to be in an intermediate region, the intermediate regions are listed under “Shear” in the table above.

It is expected that PS is completely coherent, this appears however to be not the case as indicated by Table 5.3. First, since PS is used to reveal the infinite-time dynamics, it might not accurately reflect the finite-time dynamics. Further, the partition curves are only discrete approximations of the actual partition boundaries, and given a dense coverage of trajectories, there is minor leakage. As such, PS does not have complete coherence in some regions. It does, however, still have the highest mean retention rate of all the methods.

Since the OW partiton is based on an instantaneous measure, it is not expected that strong coherence will be observed (cf. Fig. 5.2.9b). In fact, low coherence is seen in both the trapping and jumping regions. The relatively high coherence in the intermediate region is purely due to the fact that this region corresponds to a majority of the domain, but this region does not necessarily correspond to coherent features of the flow. In fact, parts of the integrable central jet and outer shear regions, as well as some portions of the trapping regions (as identified by PS) are all in the intermediate region based on the OW partition. Since several region types (as identified by PS) are being considered as one (by OW), the statistics obtained from OW should show a marked distinction from the statistics obtained from the Lagrangian measures.

The retention rates for the "Jet" and "Shear" regions are the same amoungst the Lagrangian partition methods, since the shear boundaries extracted for these methods were virtually identical. There is however a notable difference in the retention rates for the trapping and jumping regions. The FTLE and FTE partitions both have lower coherence in the trapping region (slightly less than 80%). This is partly attributed to the thresholding used to obtain these partitions – the isocontours of FTLE/FTE are not material barriers and are chosen arbitrarily. AIS gives much better coherence in the trapping region, as it more closely approximates the PS. However, AIS still gives lower results than MESO or GEO. AIS suffers partly from a lower resolution, each entire grid cell is considered to be within a given region type, where the actual region boundaries might pass through the grid cells. It was seen earlier that MESO and GEO gave the closest approximation to PS, but that GEO was slightly more precise. As such, GEO is seen to have a higher retention rate than MESO. In the jumping regions, the FTE and FTLE methods provide the largest retention rates. The higher retention rate for FTLE and FTE is due to more trajectories being classified as in the jumping regions, but they are actually in the KAM regions (as identified by PS). The jumping regions obtained by PS, MESO, GEO, and AIS show some variability, with PS being the most coherent.

Resident-time Results

To capture the time evolution of the coherent structures the partitions are generated at successive times using a sliding time interval. For the Bickley jet, the time interval between two successive "instances" (time instance related to the partition) is 1/20 of a wave period. The integration time used for the Lagrangian measures is 10 wave periods, and the trajectories are integrated for 50 wave periods. In order to classify the Lagrangian histories of the trajectories to compute the resident events, 1000 instances are necessary – but due to periodicity only 20 partitions need to be computed.

Comparison amoung residence time statistics for the deterministic and stochastic trajectories in the kinematic model of the Bickley jet is summarized in Fig. 5.2.10. In each panel, the resident time statistics for a particular type of partition is contrasted amoung the different methods used for partitioning. The top row shows statistics for deterministic trajectories, the center row for trajectories with Gaussian noise added, and the bottom row is for trajectories with Lévy noise. The columns, from left to right, represent the statistics for the jumping, trapping, jet and shear regions, as classified in Section 4.2. Because of the similarities amoung PS, GEO, and MESO, as well as those between FTLE and FTE, for clarity of the figure only PS, OW, FTLE, and AIS are shown. In each panel, the thick black curve is for PS, the blue curve is from FTLE, the magenta curve is from OW, and the cyan curve is from AIS. The thin black curves are fittings to scaling law behaviors.

Due to the persistence of coherent structures in this model, the resident-time statistics of the deterministic trajectories give valuable insight into the accuracy of the partition. In an ideal situation where the partition boundary is exact, all trajectories would be bound to their partitions, leading to flat statistics with a spiked tail at terminal time. In reality, because the partition boundaries are numerical approximations, and the dynamics within a grid cell need not be homogeneous, leaks are inevitable.

In the jumping region Fig. 5.2.10a, the yellow PS curve indicates that exit events exist for any time duration. The FTLE and AIS curves follow a similar rate of decay, with the AIS curve having a periodic structure. This periodic structure suggests that at certain phases of the flow, it is more likely for trajectories to cross the approximated transport barriers. While the curves obtained from Lagrangian methods showed events at all time scales, the Eulerian OW results show no residence events longer than a period.

Similar decays are also seen in the trapping regions Fig. 5.2.10b, except for the PS curve which shows an exponential decay rate in its tail, followed by a sharp peak. The exponential decay at larger time scales indicates the majority of events happening at small time scales, and the initial decay being due to the partition. The final peak highlights the coherence of the trapping region, in that a portion of tracers never experienced an exit event. The curves for FTLE and AIS are seen to decay at essentially the same rate as in the jumping regions, t^{-2}, however both now reveal more of a periodic structure. This structure is due to leakage around the elliptic

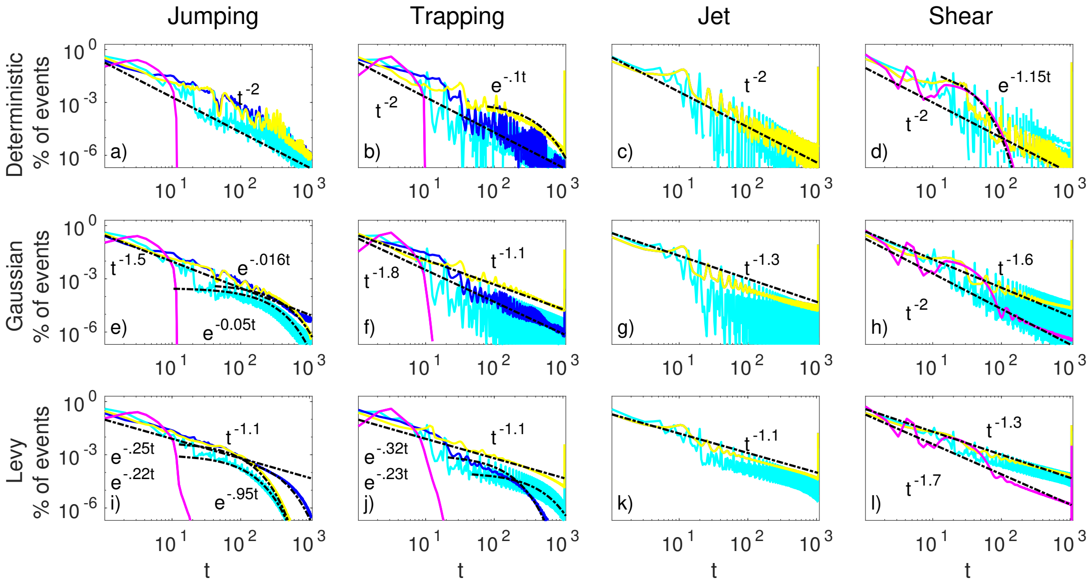

Figure 5.2.10: Each panel corresponds to the comparison of statistics among different partition methods for the same region. The top row correspond to the statistics from deterministic trajectories, the center row from Gaussian noise, and the bottomw row from Lévy noise. The partitions, from left to right, are jumping, trapping, jet and outer shear regions, respectively. In each panel, the thick yellow curve is computed from the partition based on PS, the blue curve from FTLE, magenta curve from OW, and the cyan curve from AIS. The dashed black curves are scalings fit to the different curves.

regions, and the resolution of the partitions. The OW curve is again seen to fall off quickly, with no events longer than a period.

Since the instantaneous Eulerian OW doesn't identify a central jet, and only distinguishes an "intermediate" region (which is contrasted with the shear region), only the statistics corresponding to Lagrangian measures will be used for the jet regions Fig. 5.2.10c. Further, since the partition for the parabolic jet and outer shear regions are the same for the PS and FTLE (or at least indistinguishable), the FTLE curve will be omitted from these figures. The jet region Fig. 5.2.10c shows the PS and AIS curve decaying at the same rate. While both curves show varying degrees of periodicity in their structures, the PS curve has a larger peak in the tail.

In the final deterministic panel Fig. 5.2.10d, the decay rates of the resident-time statistics in the shear regions are shown. The PS and AIS curves are seen to follow a similar decay rate, and show periodicity in their structures; in all cases, more variability is seen in the AIS statistics due to the difference in resolution. The OW curve shows a distinct exponential scaling decay rate, indicating that the majority of trajectories will be predominantly in regions classified as "intermediate" with short (less than half a period intervals) visits into other classified region types, before returning.

In each of the panels discussed, dashed black curves have been used to highlight the various scaling behaviors. In all regions, a t^{-2} algebraic scaling is found for the Lagrangian partitions. The statistics of OW in the jumping and trapping regions drop to zero too quickly for any fit, but the statistics for OW in its intermediate region falls off by $e^{-1.15t}$. This is clearly distinct from the sclaing seen in PS. The tail of the PS curve in the trapping region Fig. 5.2.10c has an exponential decay of $e^{-.1t}$.

Now consider the case where the trajectories were subject to Gaussian noise (center row of Fig. 5.2.10). In all the regions, the curves are seen to follow different algebraic scalings. In the jumping regions Fig. 5.2.10e, the Lagrangian methods follow a scaling of $t^{-1.5}$ for intermediate times (between 1 and 10 periods), but at longer times PS and AIS change behavior. At longer times, the PS and AIS curves follow exponential scalings, given by $e^{-0.016t}$ and $e^{-0.05t}$, respectively. The algebraic decay being lower than the deterministic case suggests more exit events, while the exponential decay at the tails suggest more small scale exit events.

The pdfs of the resident-time statistics conditioned on trapping regions vary between the deterministic and Gaussian cases. In Fig. 5.2.10f the AIS and FTLE curves follow a $t^{-1.8}$ scale of decay, this is slightly less than before, indicating more exit events at the larger times. The PS curve obeys the algebraic decay rate of $t^{-1.1}$, in contrast to the deterministic case where there was an exponential scaling for the tail. This difference is a direct contribution of the noise; the Gaussian noise has increased the number of exit events at all time scales, smoothing out the tails. In the jet and shear regions (Fig. 5.2.10g and h) only algebraic decay rates are seen. Overall the decay rates are lesser than their deterministic counterparts. It is interesting to note that with the introduction of Gaussian noise, the OW curve has changed from exponential scaling to an algebraic scaling of t^{-2}. This change of scaling type is indicative of the impact of noise on events at all length scales.

In analyzing the Lévy case in the bottom row of Fig. 5.2.10, note the similarities to the Gaussian case. From first looking at the jet and shear regions (Fig. 5.2.10k and l) the scaling types are the same as found in the Gaussian case; the scales themselves have just been lessened, indicating an increased number of exit events. The short-time decay rate for the jumping region for the Lévy case (Fig. 5.2.10i) is $t^{-1.1}$, while the Lagrangian methods all show different long term scalings. The long-term behavior is seen as exponential tails, the scalings for the PS, AIS, and FTLE curves are $e^{-.25t}$, $e^{-.22t}$, and $e^{-.95t}$, respectively. The PS curve in the trapping region follows the same scaling in the Gaussian and Lévy cases. The AIS and FTLE curves now have exponential decaying tails; AIS follows a scale of $e^{-.23t}$, while FTLE follows a slightly different scale of $e^{-.32t}$. Now to contrast these findings to those for the turbulent flow.

Turbulent Flow

It is seen from Fig. 5.2.11 that the turbulent flow exhibits well defined trapping regions. However, by construction these are not permanent features of the flow and are therefore referred to as vanishing eddies. In the simulated non-dimensional flow, the typical velocity magnitude around an eddy was 3, with a typical eddy diameter of about 1, giving an eddy turnover time of 1 time unit. Since the interest is in looking at how trapping regions impact the statistics, a moderate integration time of 2 time units is used. This choice provides trajectories in eddy regions enough time to revolve around, while not excluding shorter lived trapping events. Long term trapping and jumping events of trajectories is reflected by the sliding window analyses of evolving coherent structures.

The methods contrasted for the turbulent flow are a) OW, b) FTLE, c) GEO, d) MESO, e) FTE, and f) FTCS. For each pair in Fig. 5.2.11 the top panel shows the extraction at time $t = 0$ and the bottom panel shows the extraction at $t = 2$. More explicitly, for the Lagrangian methods, the top panels contain information from $t \in [0, 2]$, and the bottom panels contain information from $t \in [2, 4]$. Note that PS and AIS were not used; these methods are not suitable for analysis on nonautonomous systems, instead FTCS is the appropriate equivalent for AIS. Further, since the FTCS partition is binary, the heirarchial technique for recursively finding sets that have a relative coherence greater than a threshold is employed. This technique was developed in Ma and Bollt (2013). A relative coherence threshold of $\varrho_0 = .955$ was used.

The grid resolution for the Lagrangian analyses and the flow simulation is 256×256. For the FTLE, GEO, and MESO methods, the auxiliary grid approach was implemented. For the probabilistic measures, FTE and FTCS, a lower resolution of 128×128 is used and 400 trajectories are uniformly released in each grid cell. For OW, FTLE, and FTE, the regions are identified by Tables 4.1, 4.2, and 4.4, respectively. The trapping regions in MESO are identified as the outermost mesoelliptic rings for the coherent regions. Regions where the MESO measure is between 0 and 1 but outside the rings are excluded. This extension of MESO is to properly account for the outermost boundary of the coherent vortices. For GEO, 9 equally spaced λ values between 0.8 and 1.2 are used to find the largest λ-curves [2] . A compromise is made on the number of λ values investigated due to the need to extract these coherent regions for many frames (400) of turbulent data to obtain the resident time statistics.

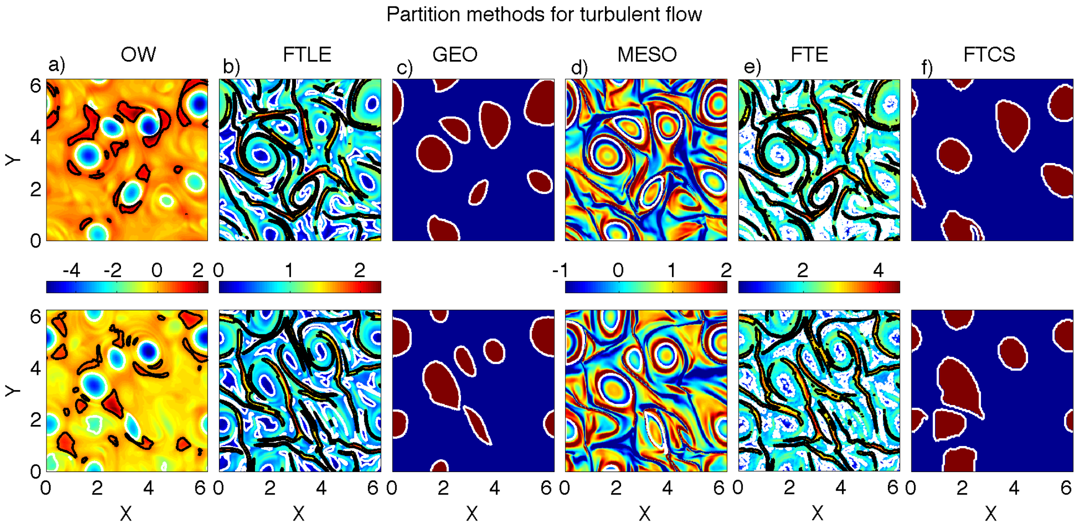

Figure 5.2.11: Comparison of different partitions used for the turbulent flow at $t = 0$ (top row) and $t = 2$ (bottom row). For methods that require an integration time, trajectories were integrated for 2 time units. (a) Partition based on OW, (b) based on FTLE, (c) based on GEO, (d) based on MESO, (e) based on FTE, and (f) based on FTCS. In all panels, the trapping regions are given by the white contours. Black curves give the jumping regions for OW, FTLE, and FTE. Note that the partitions at $t = 2$ are not from advection of the identified boundaries at $t = 0$.

In all except for panels c), d), and f) of Fig. 5.2.11, the black curves enclose regions that are considered to be jumping regions, and the white curves enclose regions that are considered trapping. In between them is the intermediate region, characterized by a combination of stretching and rotation. For GEO, MESO, and FTCS, the flow is only partitioned into trapping and non-trapping domains, and the contours indicating the boundaries are shown in white. This is because the hyperbolic structures as defined in GEO are line segments and do not have measures of area, whereas a fine

---

[2] The λ-curves give the boundaries to the elliptic regions, as defined by GEO.

partition of MESO into mesohyperbolic and meoshelical regions results in jumping trajectories for both of them, and finally FTCS can only partition the domain into two sets. Only three types of regions are considered here because of the complexity of the flow and the lack of easily identifiable jet regions across all partition methods.

In the top row of Fig. 5.2.11, the regions identified at $t = 0$ are seen, based on the flow field data from $t \in [0, 2]$, except for in panel a) since OW is an instantaneous measure. Recall that for the Bickley jet model, the OW measure was not capable of identifying regions similar to those found by the Lagrangian methods. Now however, the trapping regions seen in OW match qualitatively to those identified by GEO. This is quite remarkable due to the difference in computational complexity and cost between the two methods. It is seen that FTLE and FTE methods identify much more of the initial domain to be a trapping region than the other methods. This is due to the arbitrary nature of the partition criteria imposed – the partitions do not correlate to actual material lines.

Coherence

From comparing the top and bottom panels of Fig. 5.2.11 note their similarities. These similarities make it seem possible that the regions obtained at $t = 2$ (from using flow data from $t \in [2, 4]$), coincide with the material advection of the boundaries found at $t = 0$, indicating long lived material transport and containment. To check this, the region classifications at $t = 0$ is used to color-code trajectories based on their initial location, shown in the top row of Fig. 5.2.12. The trajectories are then deterministically advected in forward time for 2 timeunits, and their location is shown.

Fig. 5.2.12 illustrates how the regions identified as coherent are maintained over the integration time. The red dots correspond to tracers initially in regions identified as jump regions, blue dots are used for tracers initially in trapping regions, and black

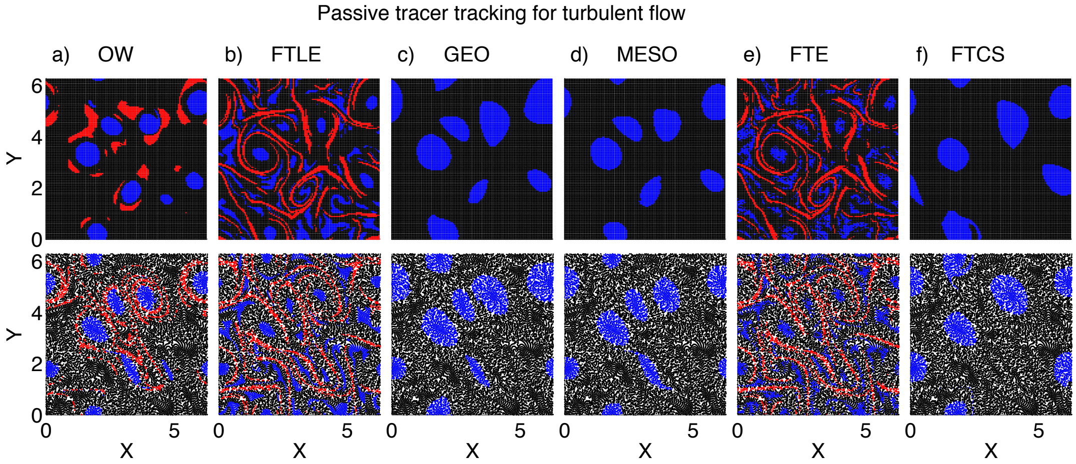

Figure 5.2.12: The top panels for each method show the initial positions of passive tracers, color-coded corresponding to region types as defined by the partition method. The bottom panels for each method are the resultant terminal locations of the passive tracers from being deterministically advected by the flow for 2 time units (the integration time of the methods). The blue indicates tracers that are classified as being in trapping regions at $t = 0$, red indicates tracers classified as being in the jumping region, and the black dots correspond to the remaining tracers.

dots are used for the rest. It is seen that for OW, the hyperbolic regions spread dramatically throughout the flow field, whereas the hyperbolic regions identified by FTLE, and FTE remain hyperbolic in jumping regions. These two thresholding-based partitions (FTLE and FTE) also appear to incorrectly identify intermediate regions as trapping. This is not suprising due to the arbitrary thresholding used. From comparing the methods, it is clear that GEO is the most robust method for trapping regions with MESO and FTCS not trailing far behind.

Resident-time Results

For the turbulent flow, the time between two successive "instances" is 1/20 of a timeunit, and the integration time used for the Lagrangian methods is 2 timeunits.

In order to obtain the statistics, the tracer trajectories are integrated for 20 timeunits, resulting in 400 instances used to classify the resident events.

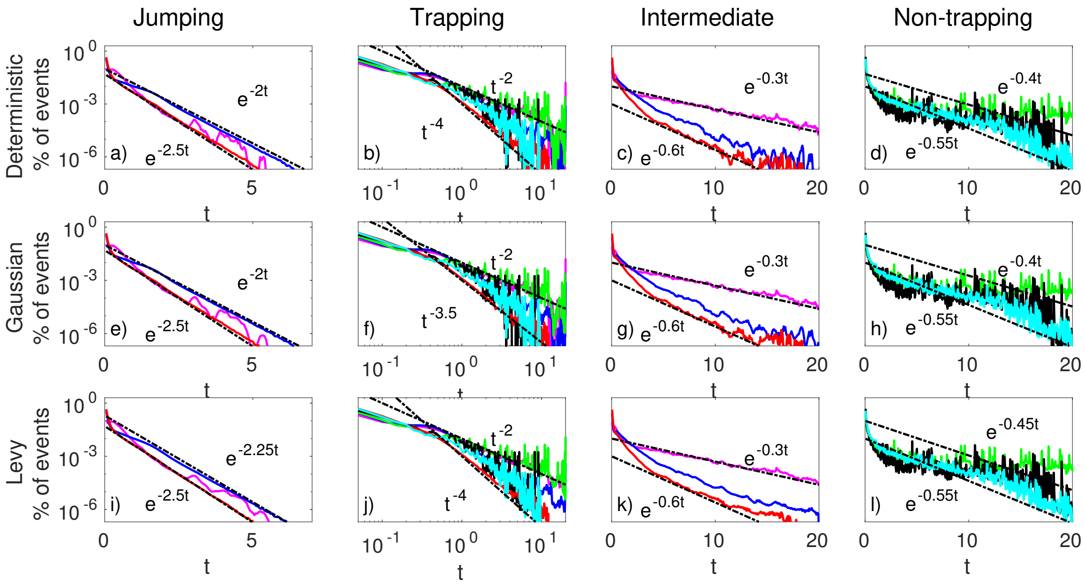

Figure 5.2.13: Each panel corresponds to the comparison of statistics among different partition methods for the same region. The top row correspond to the statistics from deterministic trajectories, the center row from Gaussian noise, and the bottomw row from Lévy noise. The partitions, from left to right, are jumping, trapping, intermediate and nontrapping regions, respectively. In the panels, various methods are represented: FTLE (blue), FTE (red), MESO (green), OW (magenta), FTCS (cyan), and the thick black curve is from GEO. The thin black curves are scalings fit to the different curves.

From comparing each column of Fig. 5.2.13, it is seen that the statistics obtained are robust for the noise level investigated. In the trapping regions, algebraic scalings are seen for the statistics of all of the partitioning methods, and exponential scalings are seen for the intermediate regions. These results are consistent with those found in Kadoch *et al.* (2011). The jumping region however, seems to scale exponentially instead of algebraically, as seen previously. Upon closer inspection of the OW statistics an algebraic scaling is seen in the jumping regions for transient times, for each noise type; the scaling is $t^{-3.75}$, which is consistent with previous results. The results from FTLE, FTE, and OW scale similarly for the jumping regions, where the OW results seem to almost be bound by the other two. In the intermediate region it is seen that the OW method provides the slowest decay, due to a majority of the domain being classified as that region type. Slower decay rates are seen for FTLE and FTE, with FTE decaying slightly more rapidly than FTLE. The FTCS and GEO methods are seen to provide very similar scalings in the non-trapping regions, with FTCS decaying slightly faster. The difference in rates is most likely due to the FTCS using a lower resolution; with a lower resolution trajectories are more easily mis-identified. The MESO statistics do not show any decay with time, suggesting that the non-trapping regions – and by extension, the trapping regions – have exit events at all time scales, and further that few trajectories escaped to other region types. The non-trapping region GEO statistics decay due to poor identification of the trapping regions. Although GEO is the most mathematically rigorous of the methods used, its implementation is also one of the most demanding, and the detection of elliptic structures has been seen to give divergent results.

In conclusion, the conditional resident-time statistics appear robust to noise at low levels, and that different region types display different scaling law behaviors. The most variability between decay rates was seen in the statistics for the Bickley jet model. Since the key features of this flow are naturally Lagrangian (jet and shear regions), it is not surprising that the instantaneous Eulerian OW measure provided such drastically different results to the Lagrangian measures. The inclusion of the OW results is to highlight the methods' dependence on flow characteristics.

It was also seen for the turbulent flow, that in terms of decay rates of the statistics, the OW method provides comparable results to GEO; an instantenous Eulerian measure gives comparable results to a computationally expensive, mathematically rigorous Lagrangian measure. This is partly due to the short integration time implemented to identify all trajectories that have experienced one turn-over rotation. Had the integration time be chosen longer, the results will be very different, however, a longer integration time will also lose the weakly rotating regions. Since the interests are in usability and coherence detection, MESO appears to be the appropriate measure to use.

Chapter 6

SECOND-ORDER MOMENTS OF NONLINEAR FLOWS FROM LINEAR MODELS

Almost a century ago in Taylor (1920) a correlation between different statistical properties of a system were sought after in order to explain the spreading of scalar distributions. In his fundamental work, Taylor looked at a highly idealized case of a 1-dimensional heat transfer problem. Regardless of the simplicity of the model this work provided a theoretical basis for turbulent diffusion. Further, it suggests a first step towards modeling via the moments: obtaining a curve of the variance as a function of time will provide insights to the nature of the flow.

This was followed by the work of Townsend (1951) that looked to further the link between analytic solutions and experimental measurements of diffusion in turbulence. In this work heat spots are created inside a 3-dimensional turbulent flow, and their downstream distribution is measured. The flow field used to advect the heat spots was modeled as an uncoupled linear flow, for which the analytic solution of the scalar distribution can be computed. Since the interests were only in the decay of the peak temperature, the model was reduced further by assuming a simple dependence on time for the flow parameters. Excellent agreement was seen between experimental and analytic results for intermediate values for the Reynolds number. For very high Reynolds numbers the rapid rate of cooling in flows prohibited accurate analysis in their work.

Here it is shown that for nonlinear flows, the second-order moments can be accurately approximated for some finite-time by using local linear-flow approximations (LFAs). The utility of the LFA allows one to reconstruct a density evolving under the action of the nonlinear flow via only linear transformations. This sections is under review by Physical Review E.

Linear Flow Approximations

As discussed earlier the interest is in solving scalar mixing processes of the following form:

$$\partial_t \theta + \mathbf{u} \cdot \nabla \theta = \kappa \nabla^2 \theta, \qquad \theta(\mathbf{x}, t_0) = \theta_0(\mathbf{x}), \tag{6.1.1}$$

where $\mathbf{u}$ is some (possibly nonlinear) flow. In Van Kampen (1992) a closed form solution of (6.1.1) is given, but only for the case of a linear flow, $\mathbf{u} = \sigma \mathbf{x}$ where σ is a constant matrix; which is the form of the LFAs. Note that σ could be dependent on time, but in the following it is taken as constant over an interval.

The closed form solution that Kampen gives is for the d-dimensional problem and is given as follows:

$$\theta(\mathbf{x}, t) = (2\pi)^{-d/2} (\det M(t))^{-1/2} \exp\left(-\frac{1}{2} \left(\mathbf{x} - \langle \mathbf{x} \rangle_t\right)^T M^{-1}(t) \left(\mathbf{x} - \langle \mathbf{x} \rangle_t\right) \right), \tag{6.1.2}$$

where $\langle \mathbf{x} \rangle_t$ and $M(t)$ denotes the mean and the covariance matrix at time t, respectively. Thus, by approximating the first and second-order moments, equation (6.1.2) can be used to approximate the concentration. Moreover, by imposing $\langle \theta(\mathbf{x}, 0) \rangle = 0$, the scalar variance can be computed via the following:

$$Var(t) = (2\pi V)^{-1} \int (\det M(t))^{-1} \exp\left(- \left(\mathbf{x} - \langle \mathbf{x} \rangle_t\right)^T M^{-1}(t) \left(\mathbf{x} - \langle \mathbf{x} \rangle_t\right) \right) d\mathbf{x}, \tag{6.1.3}$$

where V is the domain volume. In the 2-dimensional case, this is just the area of the domain.

With the goal of obtaining an approximation to the covariance matrix, several methods were explored, all of which use strain field information from the nonlinear flow. The nonlinear flow field will be replaced locally with a constant-valued linear systems. The linear approximation has the following form: $\mathbf{u} = \sigma \mathbf{x}$, where the condition trace$(\sigma) = 0$ is imposed to preserve incompressibility.

The first two LFAs investigated are motivated by decoupling the covariance matrix into separate rotational and stretching components. The decomposition is of the form:

$$\mathbf{M}_{t_0}^{t}(\mathbf{x}_0) = \left(\mathbf{R}\bar{\mathbf{M}}_{t_0}^{t}(\mathbf{x}_0) + \left(\mathbf{R}\bar{\mathbf{M}}_{t_0}^{t}(\mathbf{x}_0)\right)^T\right)/2, \tag{6.1.4}$$

where $\mathbf{R}$ is a rotation tensor, and $\bar{\mathbf{M}}_{t_0}^{t}(\mathbf{x}_0)$ is the local principal covariance matrix. This covariance matrix is computed from locally approximating the flow field with the purely straining flow, given by the following system:

$$\sigma_{t_0}^{t}(\mathbf{x}_0) = \begin{bmatrix} \lambda & 0 \\ 0 & -\lambda \end{bmatrix}. \tag{6.1.5}$$

For (6.1.5), it is quickly determined that λ is equal to the finite-time Lyapunov exponent (FTLE) for $\mathbf{x}_0$. Further, from (6.1.5) and with infinitesimal generators (cf. Appendix A), it is easy to determine the principal covariance matrix as:

$$\bar{\mathbf{M}}_{t_0}^{t}(\mathbf{x}_0) = \begin{bmatrix} \frac{\kappa}{\lambda}\left(e^{2\lambda\tau} - 1\right) & 0 \\ 0 & \frac{\kappa}{\lambda}\left(1 - e^{-2\lambda\tau}\right) \end{bmatrix}, \tag{6.1.6}$$

where κ is the diffusivity constant, λ is the FTLE value, and τ is the integration time ($\tau := t - t_0$) used to obtain the strainfield data. Since (6.1.6) is symmetric the expression in (6.1.4) is given as:

$$\mathbf{M}_{t_0}^{t}(\mathbf{x}_0) = \left(\mathbf{R}\bar{\mathbf{M}}_{t_0}^{t}(\mathbf{x}_0) + \bar{\mathbf{M}}_{t_0}^{t}(\mathbf{x}_0)\mathbf{R}^T\right)/2. \tag{6.1.7}$$

Polar Rotation Angle + FTLE

Having accounted for the stretching and compression, the overall rigid-body rotation of material elements needs to be computed. In Farazmand and Haller (2016), a unique decomposition to the deformation gradient is discussed, and the polar rotation angle (PRA) is introduced as $\theta_{t_0}^{t}(\mathbf{x}_0)$.

More specifically, the PRAs are related to the eigenvalues/vectors of the Cauchy-Green strain tensor, by the following relations:

$$\begin{aligned} \cos\theta_{t_0}^{t} &= \langle \xi_i, \nabla F_{t_0}^{t}\xi_i\rangle/\sqrt{\lambda_i}, && \text{i=1 or 2} \\ \sin\theta_{t_0}^{t} &= (-1)^j \langle \xi_i, \nabla F_{t_0}^{t}\xi_j\rangle/\sqrt{\lambda_j}, && \text{(i,j)=(1,2) or (2,1)} \end{aligned}, \tag{6.1.8}$$

where $\lambda_{1,2}$ are the eigenvalues of the 2D Cauchy-Green strain tensor, and $\xi_{1,2}$ are their corresponding eigenvectors. From the above, the actual PRA is found as:

$$\theta_{t_0}^{t} = \left[1 - \operatorname{sign}\left(\sin\theta_{t_0}^{t}\right)\right]\pi + \operatorname{sign}\left(\sin\theta_{t_0}^{t}\right)\arccos\cos\theta_{t_0}^{t}, \tag{6.1.9}$$

where the "sign" function returns 1 if the input is non-negative, and returns -1 otherwise.

Since the computation of the PRA requires the computation of the Cauchy-Green strain tensor's eigenvalues and vectors, the FTLE field can be computed essentially for free. With this, it would be computationally advantageous to use the PRA to compute the rotation tensor in (6.1.4). Using the polar rotation angle $\theta_{t_0}^{t}(\mathbf{x}_0)$ in the rotation tensor gives:

$$\begin{aligned} {}_{PRA}\mathbf{M}_{t_0}^{t}(\mathbf{x}_0) &= \left(\mathbf{R}_{t_0}^{t}(\mathbf{x}_0)\bar{\mathbf{M}}_{t_0}^{t}(\mathbf{x}_0) + \bar{\mathbf{M}}_{t_0}^{t}(\mathbf{x}_0)\mathbf{R}_{t_0}^{t}(\mathbf{x}_0)^T\right)/2 \\ &= \begin{bmatrix} \frac{\kappa}{\lambda}\left(e^{2\lambda\tau}-1\right)\cos\theta_{t_0}^{t}(\mathbf{x}_0) & \frac{\kappa}{\lambda}\left(\cosh 2\lambda\tau - 1\right)\sin\theta_{t_0}^{t}(\mathbf{x}_0) \\ \frac{\kappa}{\lambda}\left(\cosh 2\lambda\tau - 1\right)\sin\theta_{t_0}^{t}(\mathbf{x}_0) & \frac{\kappa}{\lambda}\left(1-e^{-2\lambda\tau}\right)\cos\theta_{t_0}^{t}(\mathbf{x}_0) \end{bmatrix}. \end{aligned} \tag{6.1.10}$$

Dynamic Rotation Tensor + FTLE

It is noted in Farazmand and Haller (2016) and Haller (2016) that the rotation tensor obtained from the PRA is not dynamically consistent. In Haller (2016) a dynamically consistent rotation tensor (DRT) is introduced. The DRT is given as,

$$\dot{\mathbf{O}}_{t_0}^{t}(\mathbf{x}_0) = \mathbf{W}(\mathbf{x},t)\mathbf{O}_{t_0}^{t}(\mathbf{x}_0), \quad \text{with} \quad \mathbf{O}_{t_0}^{t_0}(\mathbf{x}_0) = \mathbf{I}, \tag{6.1.11}$$

where $\mathbf{W}(\mathbf{x},t) = \frac{1}{2}\left(\nabla\mathbf{u} - (\nabla\mathbf{u})^T\right)$. This reduces the computation of the dynamically consistent rotation tensor to:

$$\dot{\mathbf{O}}_{t_0}^t(\mathbf{x}_0) = \begin{bmatrix} 0 & -\frac{\omega(\mathbf{x},t)}{2} \\ \frac{\omega(\mathbf{x},t)}{2} & 0 \end{bmatrix} \mathbf{O}_{t_0}^t(\mathbf{x}_0), \tag{6.1.12}$$

where ω is the vorticity computed from the strainfield of the nonlinear flow. The solution to the system is quickly obtained as,

$$\mathbf{O}_{t_0}^t(\mathbf{x}_0) = \begin{bmatrix} \cos\left(\frac{1}{2}\int_{t_0}^t \omega(\mathbf{x}(s),s)ds\right) & -\sin\left(\frac{1}{2}\int_{t_0}^t \omega(\mathbf{x}(s),s)ds\right) \\ \sin\left(\frac{1}{2}\int_{t_0}^t \omega(\mathbf{x}(s),s)ds\right) & \cos\left(\frac{1}{2}\int_{t_0}^t \omega(\mathbf{x}(s),s)ds\right) \end{bmatrix}, \tag{6.1.13}$$

where $\int_{t_0}^t \omega(\mathbf{x}(s),s)ds =: LAV_{t_0}^t(\mathbf{x}_0)$, is the Lagrangian-averaged vorticity (LAV) as introduced in Haller *et al.* (2016).

Using the dynamic rotation tensor with the principal covariance matrix, the approximation now becomes:

$$\begin{aligned} {}_{DRT}\mathbf{M}_{t_0}^t(\mathbf{x}_0) &= \left(\mathbf{O}_{t_0}^t(\mathbf{x}_0)\bar{\mathbf{M}}_{t_0}^t(\mathbf{x}_0) + \bar{\mathbf{M}}_{t_0}^t(\mathbf{x}_0)\mathbf{O}_{t_0}^t(\mathbf{x}_0)^T\right)/2 \\ &= \begin{bmatrix} \frac{\kappa}{\lambda}\left(e^{2\lambda\tau}-1\right)\cos\left(\frac{1}{2}LAV_{t_0}^t(\mathbf{x}_0)\right) & \frac{\kappa}{\lambda}\left(\cosh 2\lambda\tau - 1\right)\sin\left(\frac{1}{2}LAV_{t_0}^t(\mathbf{x}_0)\right) \\ \frac{\kappa}{\lambda}\left(\cosh 2\lambda\tau - 1\right)\sin\left(\frac{1}{2}LAV_{t_0}^t(\mathbf{x}_0)\right) & \frac{\kappa}{\lambda}\left(1-e^{-2\lambda\tau}\right)\cos\left(\frac{1}{2}LAV_{t_0}^t(\mathbf{x}_0)\right) \end{bmatrix}. \end{aligned} \tag{6.1.14}$$

General Linear Model (GLM)

In this section the moment generation is explored from a different viewpoint. Instead of approximating the flow as purely straining and then applying a rotation, here the most general linear flow with closed form solutions for the elements of the covariance matrix is used, and then the parameters of the linear model are fit to the nonlinear flow. More explicitly, since the focus is 2D nonlinear flows, σ takes the general form of:

$$\sigma_{t_0}^t(\mathbf{x}_0) = \begin{bmatrix} \lambda & \beta \\ \gamma & -\lambda \end{bmatrix}, \tag{6.1.15}$$

where λ, β, and γ are constants. From (6.1.15) and use of infinitesimal generators ([cf. Appendix B]), the elements of the covariance matrix are given as:

$$\begin{aligned}
{}_{GLM}M_{11}(t;\mathbf{x}_0) &= \frac{\kappa}{2\alpha^3}\left(\left(\lambda^2+\alpha^2+\beta^2\right)\sinh(2\alpha\tau)\right) + F\left(\beta,\gamma,\lambda,\kappa,\tau\right)\\
{}_{GLM}M_{12}(t;\mathbf{x}_0) &= \frac{\kappa(\gamma+\beta)}{2\alpha^2}\cosh(2\alpha\tau) + \frac{\kappa\lambda(\gamma-\beta)}{2\alpha^3}\sinh(2\alpha\tau) + \lambda\kappa(\beta-\gamma)\tau/\alpha^2\\
{}_{GLM}M_{22}(t;\mathbf{x}_0) &= \frac{\kappa}{2\alpha^3}\left(\left(\lambda^2+\alpha^2+\gamma^2\right)\sinh(2\alpha\tau)\right) + F\left(\gamma,\beta,-\lambda,\kappa,\tau\right),
\end{aligned} \tag{6.1.16}$$

where $F\left(\beta,\gamma,\lambda,\kappa,\tau\right) = \frac{\kappa}{\alpha^2}\left(\lambda\cosh(2\alpha\tau) - \lambda + \gamma\beta\tau - \beta^2\tau\right)$ and $\alpha := \sqrt{\lambda^2+\beta\gamma}$. In (6.1.15) and (6.1.16) the explicit dependence on time and initial positions are supressed for the GLM parameters for brevity; the full dependence is seen in (6.1.19).

In order to obtain this approximation the values of λ, β, and γ still need to be determined. To do this the deformation tensor is used, given here as:

$$J_{t_0}^{t}(\mathbf{x}_0) = \frac{\partial \mathbf{x}(t;\mathbf{x}_0)}{\partial \mathbf{x}_0}, \tag{6.1.17}$$

where $\mathbf{x}_0$ is the initial location at t_0. The deformation tensor of the general linear model (GLM) is,

$$J_{t_0}^{t}(\mathbf{x}_0) = \begin{bmatrix} \cosh(\alpha\tau) + \frac{\lambda}{\alpha}\sinh(\alpha\tau) & \frac{\beta}{\alpha}\sinh(\alpha\tau) \\ \frac{\gamma}{\alpha}\sinh(\alpha\tau) & \cosh(\alpha\tau) - \frac{\lambda}{\alpha}\sinh(\alpha\tau) \end{bmatrix}. \tag{6.1.18}$$

Thus, the parameters necessary to fit the local linear approximation of the flow – RHS of (6.1.15) – can be obtained directly from manipulating the entries of the deformation tensor of the nonlinear flow. The important parameters of the local approximation are obtained as follows:

$$\begin{aligned}
\alpha(t;\mathbf{x}_0) &= \frac{1}{\tau}\,\mathrm{arcCosh}\left(\frac{J_{11}(t;\mathbf{x}_0)+J_{22}(t;\mathbf{x}_0)}{2}\right), & \beta(t;\mathbf{x}_0) &= \frac{\alpha(t;\mathbf{x}_0)J_{12}(t;\mathbf{x}_0)}{\sinh(\alpha(t;\mathbf{x}_0)\tau)}\\
\lambda(t;\mathbf{x}_0) &= \frac{\alpha(t;\mathbf{x}_0)(J_{11}(t;\mathbf{x}_0)-J_{22}(t;\mathbf{x}_0))}{2\sinh(\alpha(t;\mathbf{x}_0)\tau)}, & \gamma(t;\mathbf{x}_0) &= \frac{\alpha(t;\mathbf{x}_0)J_{21}(t;\mathbf{x}_0)}{\sinh(\alpha(t;\mathbf{x}_0)\tau)}.
\end{aligned} \tag{6.1.19}$$

Note that here $J_{i,j}(t;\mathbf{x}_0)$ are the elements of the deformation tensor for the nonlinear flow. Further, note the form of the linear Jacobian in (6.1.18). By denoting the determinant of the system $\sigma_{t_0}^t(\mathbf{x_0})$ as α_σ^2, the Jacobian comes from the following:

$$J_{t_0}^t(\mathbf{x}_0) = \cosh \alpha_\sigma t \cdot \mathbf{I} + \alpha_\sigma^{-1} \sinh \alpha_\sigma t \cdot \sigma_{t_0}^t(\mathbf{x_0}). \tag{6.1.20}$$

Reconstructions

So far, approximations to the first and second-order moments of the nonlinear flow have been obtained at time t by looking at the strainfield data over the interval $[t_0, t]$. Since the flows considered are nonlinear, the linear flow approximations will become less accurate for longer integration times. However, with shorter integration times more reconstructions are needed to get to t_f (the final time) and this can slow down computations. Therefore, the maximum integration time that still gives accurate results in terms of the components of the covariance matrix is essential to determine.

Since the interest is in $\theta(\mathbf{x}, t_f)$, the case where $t_f \notin [t_0, t]$ must be considered. For the typical case of $t_f > t$, a sequence of reconstructions will have to be done. Here, for simplicity in the computations, it is assumed that t_f is evenly divisible by the integration time – the same time interval corresponding to the approximations. Further, since the moment information is only needed at reconstruction times, the computational cost can be reduced further for autonomous and periodic systems.

For autonomous systems there is no explicit dependence on time, so once an integration time is picked, the strainfield and the subsequent moment information obtained from using it can be reused for each of the reconstruction steps. This provides a way to reconstruct the density for possibly very long times from just one computation of the nonlinear strainfield.

The computational requirements naturally increase when the flow has an explicit time dependence. However, for periodic flows, some of the increased computational necessity can be alleviated by using an integration time that divides the period of the flow, T_p. For example, if the integration time is taken to be $T_p/4$, then only 4 computations of the strainfield are needed (given that t_f is still divisible by the integration time); from $[0, T_p/4]$, $[T_p/4, T_p/2]$, $[T_p/2, 3T_p/4]$, and $[3T_p/4, T_p]$.

Once the strainfields are computed and the moments obtained, the density reconstruction is computed according to one of two methods: the analytic representation and an ensemble approximation. The analytic representation is done by solving (6.1.2) with the moment information. This method, although accurate, can be computational prohibitive; since for each cell of the domain an entire density field has to be computed before all of these fields are composed together. For example, given an N_x by N_y computational domain, the necessary number of computations is on the order of $(N_x N_y)^2$. The ensemble approximation tries to avoid such costly computations by using the covariance matrix approximations to generate new Gaussian distributions with ensemble sizes dependent on density. This method uses an ensemble of tracers that can be quickly sorted through a histogram algorithm to determine the density in each cell and the number of initial conditions to use for the subsequent reconstruction. Now both methods will be discussed in more detail.

Analytic Reconstruction

With the local covariance matrices obtained over the integration time, a Green's function for the system can be constructed over that integration time. This Green's function is given as, $G(\mathbf{x}, \tau | \mathbf{x}_0, t_0)$. The reconstruction steps proceed by convolving this Green's function with the current density field,

$$\theta(\mathbf{x}, t+\tau) = \int_A G(\mathbf{x}, \tau|\mathbf{x}_0, t_0)\theta(\mathbf{x}_0, \tau) d\mathbf{x}_0, \tag{6.2.1}$$

where A represents the computational domain. This process is repeated until final time is reached.

Given the probability density of a single passive tracer by:

$$\rho(\mathbf{x}, t+t_0) = \frac{\left(\det M(t+t_0)\right)^{-1/2}}{2\pi} \exp\left(-\frac{1}{2}\left(\mathbf{x}-\mathbf{x_0}\right) M^{-1}(t+t_0)\left(\mathbf{x}-\mathbf{x_0}\right)\right), \tag{6.2.2}$$

the analytic scalar density reconstruction, from the proposed methods, can be given as:

$$\theta_A(\mathbf{x}, t) = \int_0^t \int_A \rho(\mathbf{x}, t; \mathbf{x_0}, t_0) s(\mathbf{x_0}, t_0) d\mathbf{x_0} dt_0, \tag{6.2.3}$$

where $s(\mathbf{x_0}, t_0)$ defines the source distribution at $(\mathbf{x_0}, t_0)$. Note that in (6.2.2) the dependencies on $\mathbf{x_0}$ and t_0 are suppressed for $M(t; \mathbf{x_0}, t_0)$ and $\rho(\mathbf{x}, t; \mathbf{x_0}, t_0)$ for covenience.

From the start:

First, obtain the strainfield data of the nonlinear flow and pick an initial condition, $\delta(\mathbf{x}_0, t_0)$. For the initial construction, the parameters needed to compute the local approximation are obtained from interpolating the initial condition in the scalar field associated to those parameters. The covariance matrix is then computed as in (6.1.10), (6.1.14) or (6.1.16), and is used to determine the density for every cell in the domain according to (6.2.2). The superposition of all of these densities gives the scalar density for the domain, and is computed by (6.2.3). If $t = t_f$, then the computation is done, otherwise the following steps are repeated until t_f is reached.

Every element of the new density field is now taken as a new initial condition ($s(\mathbf{x}, t) = 1$) and the density given by that element is used to construct the next density field.

From the start:

This approximation starts very similarly to the analytic reconstruction, in that the initial condition $\delta(\mathbf{x}_0, t_0)$ is first used to interpolate the parameter-fields in order to obtain the covariance matrix. However, where the analytic reconstruction uses the moments to compute the density field, the ensemble approximation uses the moment data to create an ensemble distribution of K tracers. The members of the ensemble come from the normal distribution $\mathcal{N}(\mu, M)$, where μ is the mean, and M is the covariance matrix; these values are dependent on the initial condition. Letting $LL^T = M$, the elements of the ensemble, $S(t)$, are given as:

$$S(t) = \{Ly_i + \mu | i = 1, \ldots, K\} \tag{6.2.4}$$

where y_i is a vector with elements picked from a normal random distribution.

The elements of $S(t)$ are then put through a 2D histogram algorithm that returns the number of tracers in each cell. Letting $[\zeta, C] = \texttt{hist}(S)$, then ζ gives the number of tracers in each cell, and C gives the collection of cells that have tracers in them. The tracer count will be used as the density, and more importantly, it informs which cells have tracers in them. This second aspect is where the method gains a computational advantage over the analytic reconstruction; since the subsequent reconstruction step is only going to use non-empty cells as initial conditions. After long enough time, or with a large enough diffusivity, the tracers will homogenize throughout the domain, at which point this method will be on par with the analytic reconstruction, computationally. However, before the homogenization limit is reached, a computational advantage in terms of computational cost is seen.

The number of tracers in C_i is given as ζ_i; if $\zeta_i \neq 0$ then the cell is used as initial condition for the next step of the reconstruction. The set of tracers at $t + \tau$ is then given by,

$$S(t+\tau) = \bigcup_{i|\zeta_i \neq 0} \left(\texttt{randn}\,(\zeta_i, 2)\,\texttt{chol} M_i + \texttt{repmat}\,(\mu_i, \zeta_i, 1) \right), \tag{6.2.5}$$

where μ_i is the mean value and M_i is the covariance matrix, corresponding to C_i. The above equation is similarly written as:

$$\begin{aligned} S_i(t+\tau) &= \{L_i y_j + \mu_i | j = 1, \ldots, \zeta_i\} \quad i|\zeta_i \neq 0 \\ S(t+\tau) &= \bigcup_{i|\zeta_i \neq 0} S_i(t+\tau), \end{aligned} \tag{6.2.6}$$

where L_i is the Cholesky decomposition of the covariance matrix corresponding to C_i. The new collection of tracers is then put through the 2D histogram algorithm and the process is repeated until the final time is reached. At the final time the density field is easily obtained by counting the number of tracers in each cell and dividing it by the original K, for proper scaling. The elements of the density field become $\theta(i,j)(t_f) = \zeta_{i,j}/K$.

Results

In order to obtain the elements of the covariance matrix, for comparison purposes, the Fokker-Planck equation is solved via DNS for every grid in the domain. These initial conditions are evolved with the nonlinear flows and their covariances recorded over time. The elements of the covariance matrices are related back to the initial release position and a field of these elements is constructed. Three different levels of diffusion were investigated: $D = \sqrt{.02}$, $D = \sqrt{.002}$, and $D = \sqrt{.0002}$. Since the covariance matrix approximations are simply scaled by D, looking at various diffusivities can help understand how long the linear approximation is valid.

Moments

In the following, for figures with 4×3 subfigures: the top row of each subfigure are the elements of the covariance matrix approximation ${}_{PRA}\mathbf{M}_{t_0}^{t}(\mathbf{x_0})$, the second row are the elements of the covariance matrix approximation given by ${}_{DRT}\mathbf{M}_{t_0}^{t}(\mathbf{x_0})$, the third row are the elements of the covariance matrix that were computed using the GLM, and the bottom row of each subfigure are the elements of the covariance matrix that were obtained from DNS.

For the figures with 3×3 subfigures: the top row is given by the absolute value of ${}_{PRA}\mathbf{M}_{t_0}^{t}(\mathbf{x_0})$ over the actual values (given by DNS), the middle row is the absolute value of the ratio of ${}_{DRT}\mathbf{M}_{t_0}^{t}(\mathbf{x_0})$ over the actual values, and the bottom row shows the same ratio but for the general linear model (GLM). All the subfigures of a given column use the same color scale: for the 4×3 figures, the scale is given by the DNS results, for the 3×3 figures, the bottom row is used for scaling. The first analysis is with the steady cell flow with $D = \sqrt{.02}$.

It is seen that for the steady cell flow (Fig. 6.3.1) that as the integration time is reduced the agreement between the approximations and the actual variances (bottom rows) becomes greater; which is expected as this is a linear approximation to a nonlinear system. It is also seen that the scale of the cross-covariance terms is about an order of magnitude smaller than the diagonal elements of the covariance. This is a characteristic seen in the other flows as well. For this flow it is seen that the PRA-FTLE and DRT-FTLE methods give similar results. Unfortunately, even for short integration times the cross-covariance elements are poorly represented by these methods. The GLM however is more capable of accurately representing these elements.

From Fig. 6.3.2 the validity of each model is seen as a function of integration time. It is immediately seen that PRA-FTLE and DRT-FTLE given similar results, as is expected. Note that the scale of results given by GLM tend to be more-so centered around 1 than the other methods. For all methods, the largest errors were seen in the cross-covariance terms, due to the scale of the values of the field. After $\tau = .25$ the approximations break down due to nonlinear effects. This puts an upper-bound on the integration time allowable for the steady cell of $\tau = .25$, in order to expect a reliable reconstruction. Although these qualitative comparisons are nice, a quantitative comparison is really needed to see whats going on.

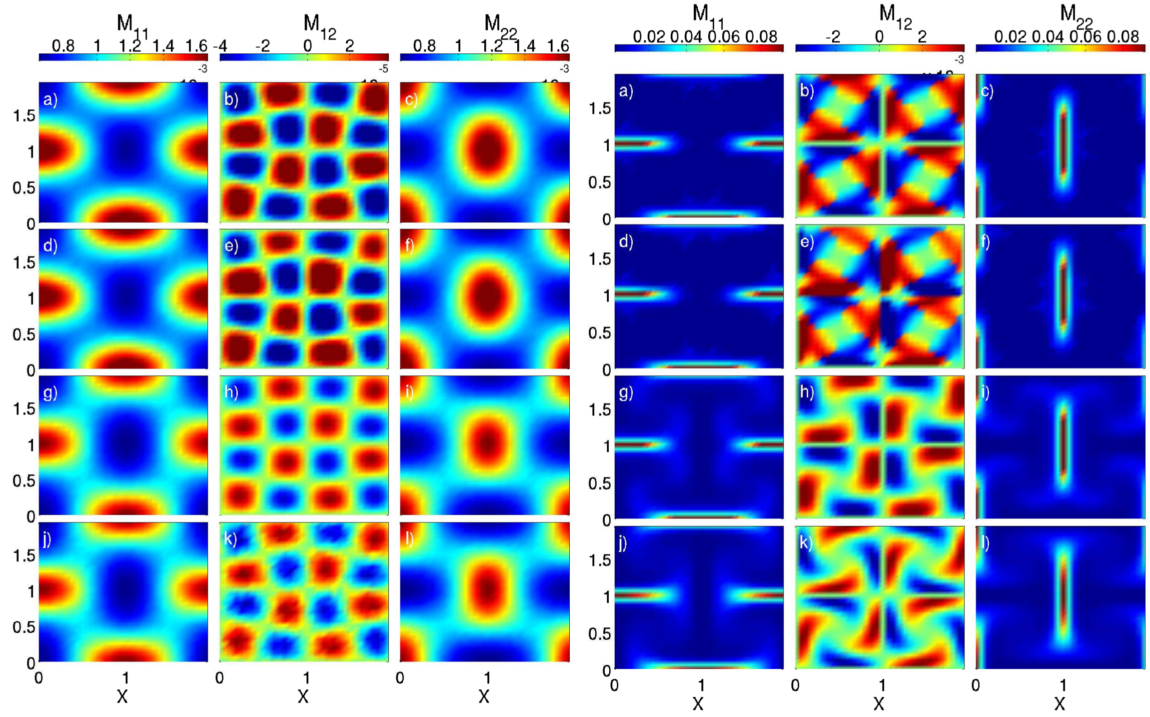

(a)

(b)

Figure 6.3.1: Comparison of the moment approximations obtained from PRA-FTLE (top rows), DRT-FTLE (second rows), and GLM (third rows) to the actual moments (bottom rows) for the steady cell flow with an integration time of (6.3.1a) $\tau = .05$ and (6.3.1b) $\tau = .25$. $D = \sqrt{.02}$.

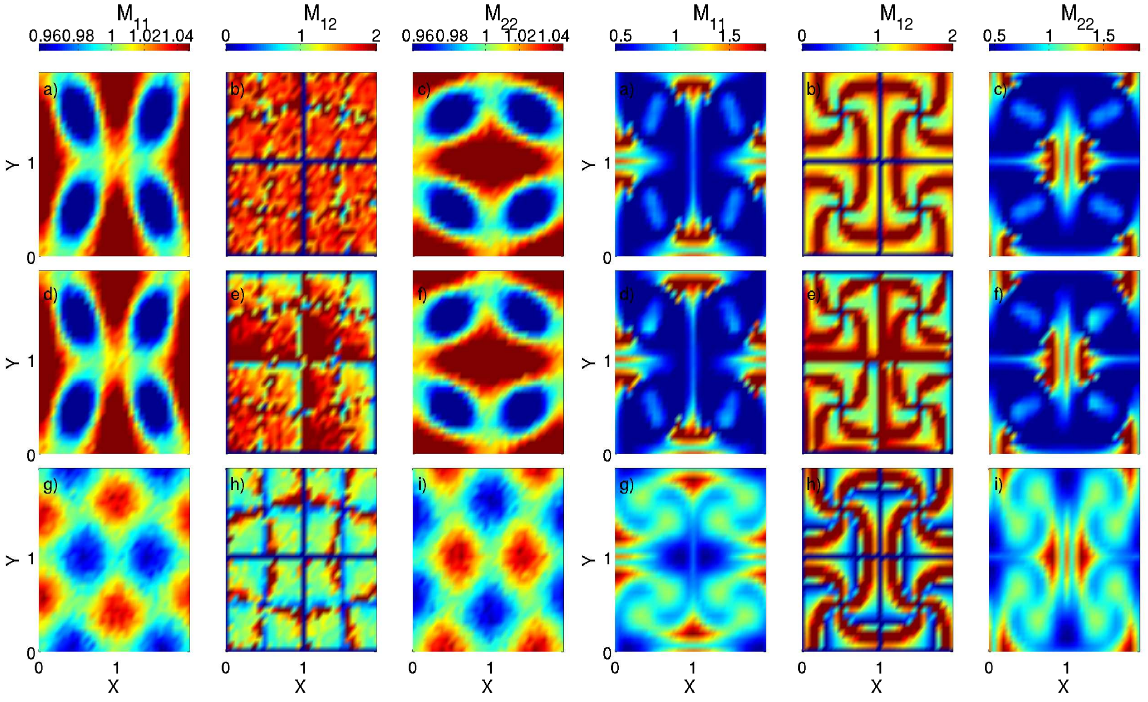

(a) (b)

Figure 6.3.2: Absolute value of the ratio of the approximation given by PRA-FTLE (top rows), DRT-FTLE (middle rows), and GLM (bottom rows) over the actual values for the steady cell flow, with an integration time of (6.3.2a) $\tau = .05$, (6.3.2b) $\tau = .25$. $D = \sqrt{.02}$.

The utility of the methods can be assessed by looking at the histogram of the relative error. The comparisons are for the steady cell flow, the periodic quad-gyre and the aperiodic quad-gyre. In the following figures, the blue lines indicate the results for the case $D = \sqrt{.02}$, the red lines are the results for the $D = \sqrt{.002}$ case, and the green lines are the results when $D = \sqrt{.0002}$. For each 3×3 subfigure: the top row is the histogram given by the absolute value of $_{PRA}\mathbf{M}^t_{t_0}(\mathbf{x_0})$ over the actual values (given by DNS), the middle row is the histogram given by the absolute value of the ratio of $_{DRT}\mathbf{M}^t_{t_0}(\mathbf{x_0})$ over the actual values, and the bottom row shows histograms for the same ratio but for the GLM.

It is first noted, that in each subfigure, little variation is seen between the different diffusivities. However, as the integration time is increased some variation between the curves is seen. This simply suggests that for the integration times investigated, diffusivity has not played much of a role in the transport. Further, for shorter integration times (a)-(b) of Figs 6.3.3-6.3.5, it is seen that the values are peaked around 1 and quite unimodal; suggesting a good approximation. For an integration time of $\tau = .25$ ($125\Delta t$), the peaks of the PRA-FTLE and DRT-FTLE methods start to shift towards 0, while also losing their unimodal shape. For all of the flows, with an integration time of $\tau = .25$ the GLM is able to maintain these peaked unimodal structures centered around one, but only for the diagonal covariance terms. The cross-covariance terms are poorly represented for $\tau \geq .1$. When the integration time exceeds $\tau = .25$ the structures within the histograms are lost. These characteristics are seen for all three gyre flows, with only slight differences in scale; highlighting a characteristic of the short-time variances obtained from convection cells.

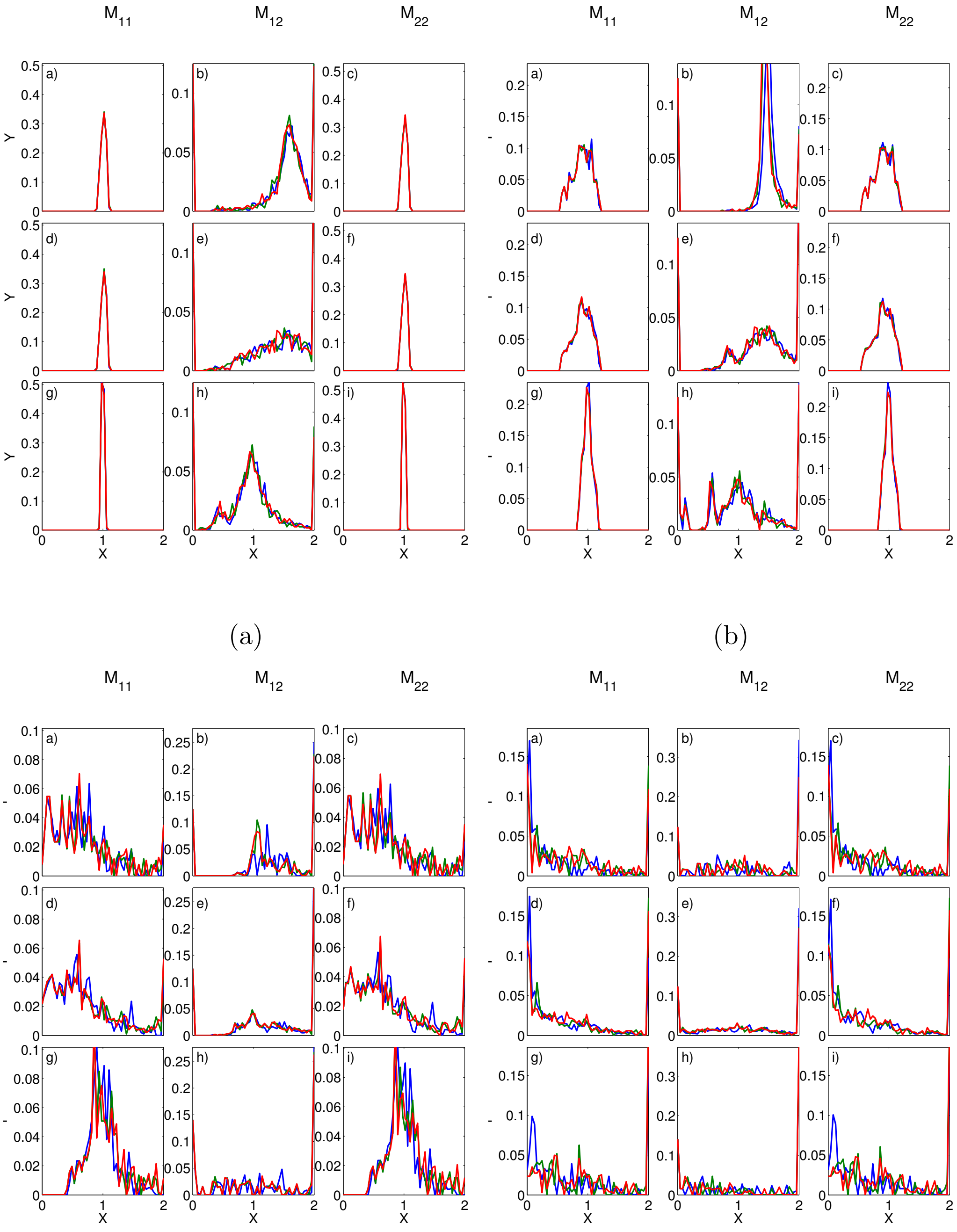

(a) (b)

(c) (d)

Figure 6.3.3: Histograms of the absolute value of the ratio of the approximation given by PRA-FTLE (top rows), DRT-FTLE (middle rows), and GLM (bottom rows) over the actual values for the steady cell flow, for 3 diffusivitives: $\kappa = .01$ (blue), $\kappa = .001$ (red), and $\kappa = .0001$ (green). With an integration times $\tau = .05$ (6.3.3a), $\tau = .1$ (6.3.3b), $\tau = .25$ (6.3.3c), and $\tau = .5$ (6.3.3d).

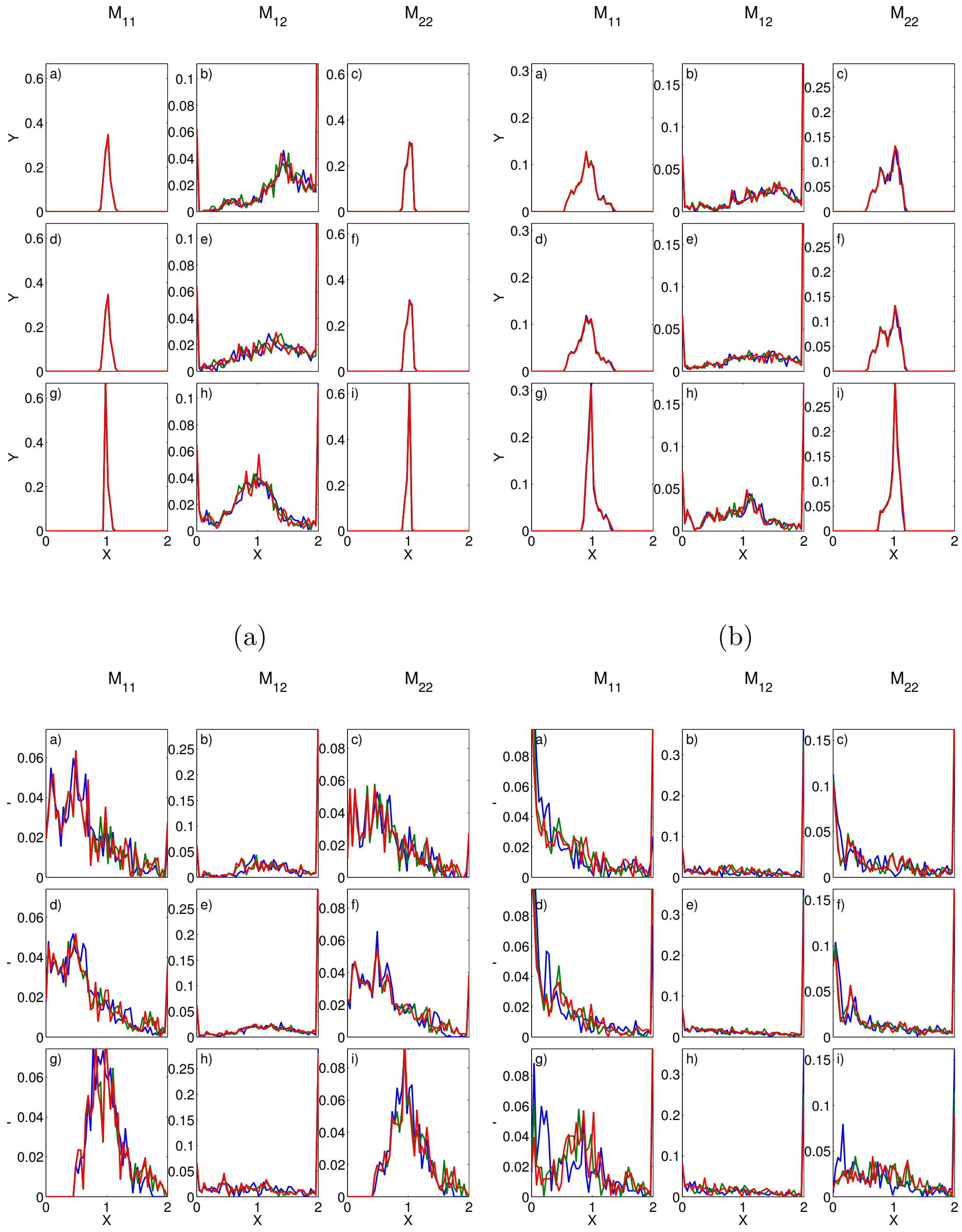

(a)

(b)

(c)

(d)

Figure 6.3.4: Histograms of the absolute value of the ratio of the approximation given by PRA-FTLE (top rows), DRT-FTLE (middle rows), and GLM (bottom rows) over the actual values for the quad-gyre flow, for 3 diffusivitives: $\kappa = .01$ (blue), $\kappa = .001$ (red), and $\kappa = .0001$ (green). With an integration times $\tau = .05$ (6.3.4a), $\tau = .1$ (6.3.4b), $\tau = .25$ (6.3.4c), and $\tau = .5$ (6.3.4d).

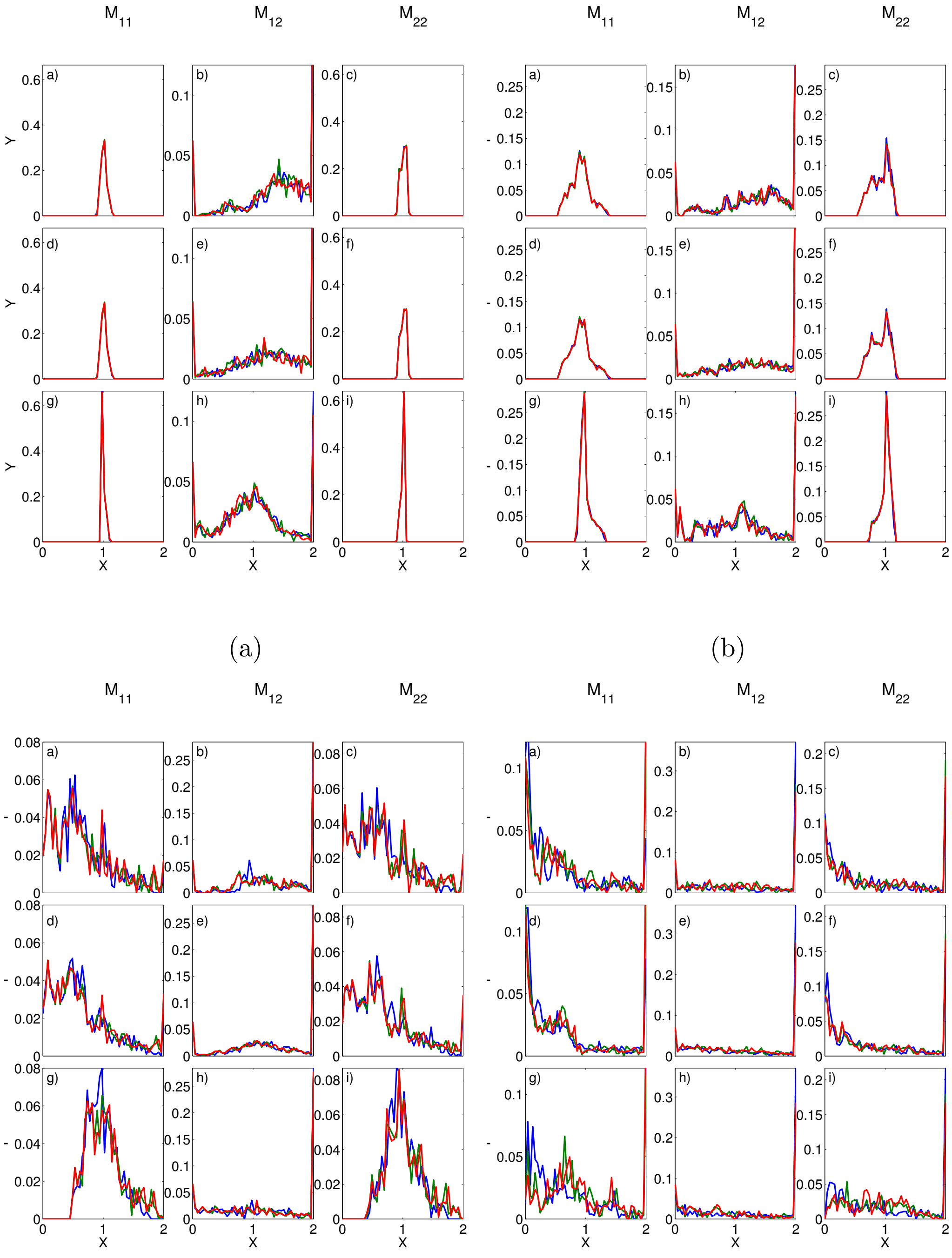

(a) (b)

(c) (d)

Figure 6.3.5: Histograms of the absolute value of the ratio of the approximation given by PRA-FTLE (top rows), DRT-FTLE (middle rows), and GLM (bottom rows) over the actual values for the aperiodic quad-gyre flow, for 3 diffusivitives: $\kappa = .01$ (blue), $\kappa = .001$ (red), and $\kappa = .0001$ (green). With an integration times $\tau = .05$ (6.3.5a), $\tau = .1$ (6.3.5b), $\tau = .25$ (6.3.5c), and $\tau = .5$ (6.3.5d).

From looking at the histogram results, there is high confidence in the ability of the approximation for short times. To see how the differences within the approximations propagate to the final time each approximation was used to try and generate the distribution evolution. An integration time of 125 timesteps ($\tau = .25$) was initially used; this integration time was the largest from earlier whose histograms maintained peaks centered near one (for GLM). Since the validity of the approximation was independent of D at this integration time, the following analysis is only done with $D = \sqrt{.002}$. The initial condition (IC) used in the following analysis was randomly chosen as $[.475, 1.235]$.

Reconstructions for both the periodic and aperiodic quad-gyre flows will be computed. The moment approximations given by both the PRA-FTLE and DRT-FTLE schemes fail to preserve positive definiteness for both flows for the integration time used ($\tau = 125\Delta t$), without this the reconstruction of the density field is not possible. The moment approximations given by GLM preserves the positive definiteness for both flows – allowing a reconstruction to be possible, for the integration time used. For periodic flows, with period T_p, the analytic reconstruction scheme will only have to compute T_p/τ Green's functions; which makes it a viable method to use.

For the quad-gyre flow, in order to check the validity of the final time reconstructions they are compared to the solution obtained from DNS of the Fokker-Planck equation. The DNS solution is seen in Fig. 6.3.6a. The analytic solution for the reconstructions – obtained from (6.1.2) – is seen in Fig. 6.3.6b, while the solution given by the ensemble approximation is seen in Fig. 6.3.6c. To ensure good agreement between the analytic representation and the ensemble approximation, as well as DNS,

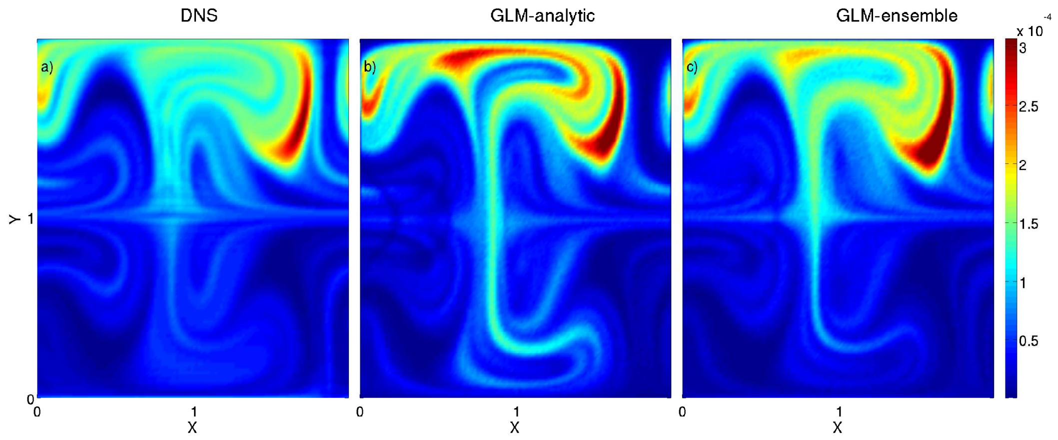

Figure 6.3.6: Comparison of the a) actual solution to the solutions obtained via the b) analytic and c) ensemble approaches, with the GLM; using an integration time of $\tau = .25$, for the quad-gyre flow at $t_f = 5$.

the initial tracer ensemble is taken to have $K = 1000 N_x N_y$ elements, where N_x and N_y are the resolutions of the computational domain.

In Fig. 6.3.6 it is seen that the solution obtained at final time via the GLM (using either method), with an integration time of $\tau = .25$, matches qualitatively very well to the solution given by DNS for $t_f = 5$. The figures use the same color scale, given by DNS. The solution obtained via GLM is seen to have a higher maximum value – evidenced by the dark red regions. These same behaviors are seen in the results for the aperiodic quad-gyre, Fig. 6.3.7. Due to the additional computational cost to compute the analytic solution from (6.1.2), only DNS and the ensemble approaches are used for the aperiodic quad-gyre.

With shorter integration times, better agreement was seen by the approximations (see Fig. 6.3.4(a)-(b)). Further, and arguably more intriguing, is that with a shorter integration time it might be possible for the PRA-FTLE and DRT-FTLE methods to still provide positive definite approximations. Guided by these curiosities, a substantially shorter integration time of 50 timesteps ($\tau = .1$) was used to compute the

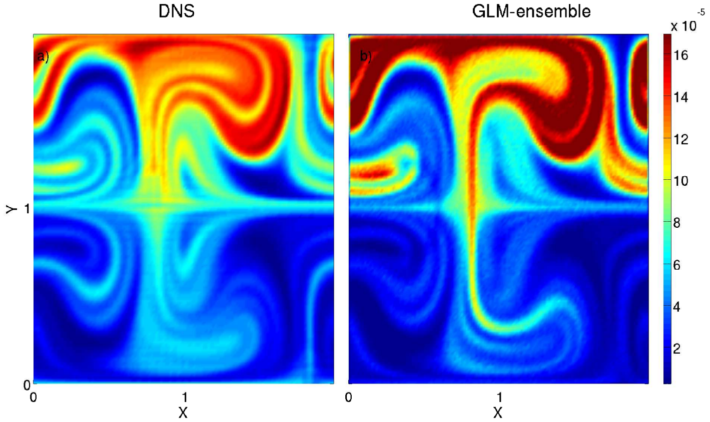

Figure 6.3.7: Comparison of the a) actual solution to the solution obtained via the b) ensemble approach, with the GLM; using an integration time of $\tau = .25$, for the aperiodic quad-gyre flow at $t_f = 5$.

reconstructions. These results are seen in Fig. 6.3.8 for the periodic quad-gyre, and Fig. 6.3.9 for the aperiodic quad-gyre.

Even with this much shorter integration time the moment approximations given by the DRT-FTLE method violated the positive definiteness for these flows, while the PRA-FTLE method was able to provide approximations capable of reconstruction. In interest of time and brevity, the reconstructions for the GLM and the PRA-FTLE approximations are only done using the ensemble approximation.

In Fig. 6.3.8 it is seen that the solutions obtained at final time via the GLM and PRA-FTLE approaches, with an integration time of $\tau = .1$, match qualitatively very well to the solution given by DNS for $t_f = 5$. The solution obtained via GLM is seen to have a higher maximum value than DNS, and is almost indistinguishable from the solution given by PRA-FTLE. These same behaviors are seen in the results for the aperiodic quad-gyre, in Fig. 6.3.9. The two approximations (GLM and PRA-FTLE) give similar results to each other, and are seen to over and underapproximate the

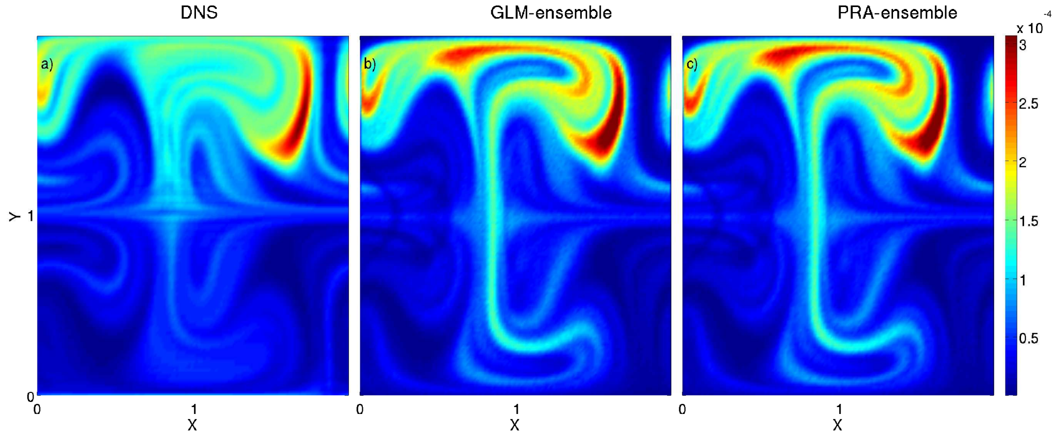

Figure 6.3.8: Comparison of the actual solution (a) to the solution obtained via the ensemble approximation with the GLM (b), and with PRA-FTLE (c) using an integration time of $\tau = .1$, for the quad-gyre flow. $t_f = 5$.

solution in certain regions. More specifically, the density along the $Y = 1$ line is seen to be consistently underestimated by the approximations.

Scalar Variance Decay

Motivated by the qualitative resemblance of the reconstructions, and previous research interests, the focus is now on the scalar variance. The scalar variance is defined as $\theta_{rms}(t) = \sqrt{\langle \theta^2(\mathbf{x}, t)\rangle - \langle \theta(\mathbf{x}, t)\rangle^2}$. This is computed at every timestep in the DNS, and at every reconstruction step for the approximations (GLM and PRA-FTLE). The time history of the scalar variance for the IC is seen in Fig. 6.3.10 for the periodic quad-gyre, and Fig. 6.3.11 for the aperiodic quad-gyre. In Fig. 6.3.10 good agreement between the actual variance and all of the computed variances is seen. Given the "analytic" reconstruction formulation, (6.2.3), the variance is obtained as follows (assuming $\langle \theta(\mathbf{x}, t)\rangle = 0$):

$$\langle \theta^2(\mathbf{x}, t)\rangle = \int_A \left(\int_0^t \int_A \rho(\mathbf{x}, t; \mathbf{x_0}, t_0) s(\mathbf{x_0}, t_0) d\mathbf{x_0} dt_0 \right)^2 d\mathbf{x_0}. \tag{6.3.1}$$

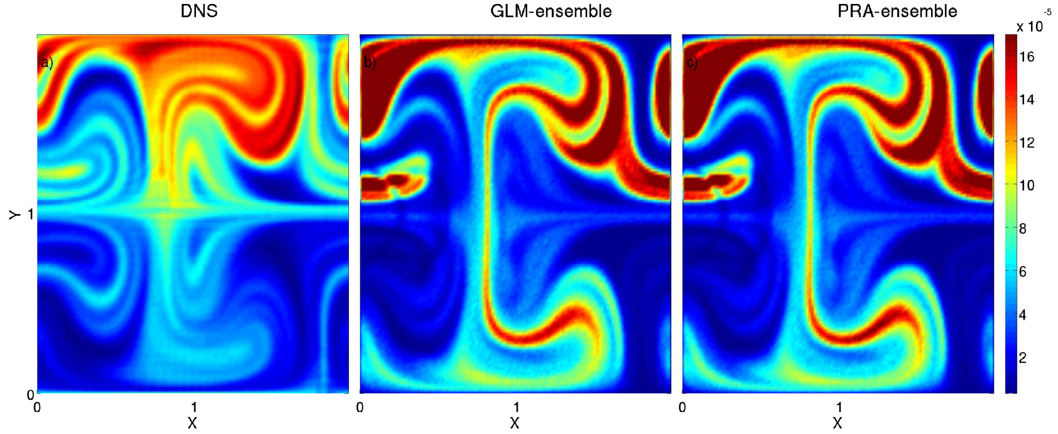

Figure 6.3.9: Comparison of the actual solution (a) to the solution obtained via the ensemble approximation with the GLM (b), and with PRA-FTLE (c) using an integration time of $\tau = .1$, for the aperiodic quad-gyre flow. $t_f = 5$.

This relation simplifies greatly for single source, delta-function type distributions, but not for random source distributions. Given the formulation of the ensemble approximations a closed-form representation of the scalar variance cannot be obtained.

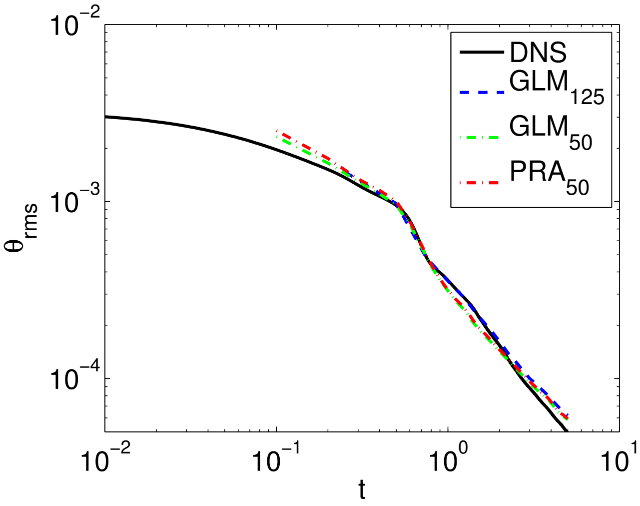

Figure 6.3.10: Time history of the scalar variance for $[.475, 1.235]$, in the periodic quad-gyre flow until $t_f = 5$.

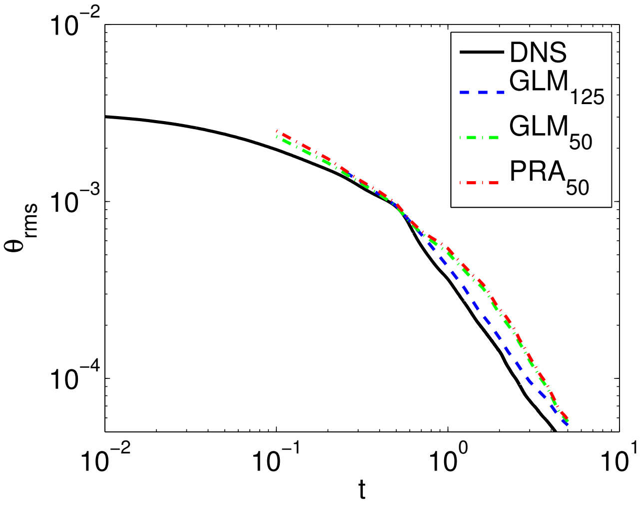

Figure 6.3.11: Time history of the scalar variance for $[.475, 1.235]$, in the aperiodic quad-gyre flow until $t_f = 5$.

PART 3 -

THE 3D CASE

Chapter 7

3D LCS DETECTION METHODS AND GLM

In this chapter the models used for the 3-dimensional cases are discussed, as well as extensions the previously discussed LCS detection methods to 3D. When changing from the 2D to 3D setting the symmetry imposed by the incompressibility condition is lost. This asymmetry, coupled with the difficulties of visualizing the phase space of the system, makes the analysis of 3-dimensional systems more difficult. Previously the incompressibility condition $\Pi_{i=1}^{d}\lambda_i = 1$ led to $\lambda_1 = 1/\lambda_2$. This highlights that expansion in one direction is exactly compensated for by compression in a direction normal to the first. This dichotomy of expansion and contraction could be seen in the 2D straining flow as $\sigma = \begin{bmatrix} \lambda & 0 \\ 0 & -\lambda \end{bmatrix}$. For the 3D cases, the incompressibility condition only gives $\lambda_1\lambda_2\lambda_3 = 1$, from which little can be obtained. As discussed in Zeldovich *et al.* (1984), there are two scenarios of interest: the "rope" ($\lambda_3 > 1$, and $\lambda_1, \lambda_2 \leq 1$), and the "pancake" ($\lambda_3, \lambda_2 \geq 1$, and $\lambda_1 \leq 1$), where, without loss of generality, $\lambda_1 \leq \lambda_2 \leq \lambda_3$. In the rope case, one expansion direction and two compressive directions transform fluid elements into long tube-like structures. The "pancake" is noted by the two expansive directions and single compressive direction, leading to fluid elements evolving into thin sheet-like manifolds. These two fundamental structure types lead to rich dynamics.

Probabilistic Methods

Since the probabilistic methods rely on finding minimally dispersive regions of phase space, the methods naturally extend to higher dimensions. However, the increase in size of the transfer matrix that occurs from moving to the 3D setting makes these methods not computationally viable. Due to the computational cost of these approaches, they will not be pursued in this work. However, it is noted that these approaches have been used previously to investigate various 3-dimensional systems. In Froyland and Padberg-Gehle (2012), the kinematic models of the Lornez flow and ABC flow are analyzed with finite-time entropy (FTE). Moreover, in Froyland *et al.* (2010), 2D and 3D geophysical flows are investigated using finite-time coherent sets (FTCS).

Geometric Methods

As alluded to earlier, while several of the coherent structure identification methods are strictly limited to the 2-dimensional setting, some of the methods are defined for the 3D case as well. The finite-time Lyapunov exponent (FTLE) is an example of a geometric method that is applicable across all (finite) dimensions, as it is computed from the deformation gradient tensor. However, the FTLE field is still subject to false positives and negatives. Thus, while it provides valuable insight about the system, it is not precise in indicating coherent boundaries in the flow. Here a few other methods suited for 3D are briefly discussed, noting that this list is by no means exhaustive. Ease of computation, as well as extension from previous methods were taken into consideration when choosing these methods.

Okubo-Weiss-Chong

In the 2D cases one instantaneous Eulerian measure (OW) was used to compare and contrast to the Lagrangian measures. Although there is no direct extension to 3D, the Okubo-Weiss-Chong (OWC) classification gives an instantaneous Eulerian description of the flow topology; this classification is given in Chong *et al.* (1990).

OWC is based on 3 invariant measures that come from analyzing the stability of critical points in the flow. These invariant measures are the coefficients of the characteristic polynomial of the deformation gradient tensor. Letting A be the deformation gradient tensor, the characteristic polynomial is given as:

$$\lambda^3 + P\lambda^2 + Q\lambda + R = 0, \tag{7.2.1}$$

where $P := -\texttt{trace}(A)$, $Q := .5(P^2 - \texttt{trace}(A^2))$, and $R := -\texttt{det}(A)$. Regions are classified as non-hyperbolic for $R = 0$, and hyperbolic otherwise. Note that further classification of the hyperbolic and non-hyperbolic regions is possible, but unnecessary for the analysis.

Polar Rotation Angle

Another measure with a natural extension to 3D is the polar rotation angle (PRA). Given the eigenvectors of the Cauchy-Green strain tensor and the deformation tensor as ξ_i and $\nabla F_{t_0}^t$, respectively, the 3D form of the PRA satisfies:

$$\begin{aligned}
\cos\theta_{t_0}^t &= \frac{1}{2}\left(\Sigma_{i=1}^{3}\frac{\langle \xi_i, \nabla F_{t_0}^t \xi_i\rangle}{\sqrt{\lambda_i}} - 1\right) && (7.2.2)\\
\sin\theta_{t_0}^t &= \frac{\langle \xi_i, \nabla F_{t_0}^t \xi_j\rangle - \langle \xi_j, \nabla F_{t_0}^t \xi_i\rangle}{\sqrt{2\epsilon_{ijk} e_k}}, \quad i \neq j \in 1,2,3, && (7.2.3)
\end{aligned}$$

where $e = [e_1, e_2, e_3]^T$ is the normalized eigenvector corresponding to the unit eigenvalue of the matrix,

$$[H_{t_0}^t]_{jk} = \frac{\langle \xi_j, \nabla F_{t_0}^t \xi_k\rangle}{\sqrt{\lambda_k}}, \quad j,k \in 1,2,3, \tag{7.2.4}$$

and ϵ_{ijk} is the Levi-Civita symbol. The four-quadrant PRA is then obtained from:

$$\theta_{t_0}^t = (1 - \texttt{sign}(\sin\theta_{t_0}^t))\pi + \texttt{sign}(\sin\theta_{t_0}^t)\cos^{-1}\left(\cos\theta_{t_0}^t\right), \tag{7.2.5}$$

where sign(α) is 1 for non-negative *alpha* ($\alpha \geq 0$), and -1 otherwise.

In Farazmand and Haller (2016) the PRA was not only used to identify elliptic islands in 2D systems, but was also used for the 3D steady ABC flow. The flow is an exact steady solution of Euler's equation of inviscid Newtownian fluids with periodic boundary conditions. Due to the property of coinciding connected level sets[1] , it is possible to obtain the classification corresponding to (7.2.5) without solving for $\sin\theta_{t_0}^t$. The two-quadrant angle is then simply given by:

$$\theta_{t_0}^t = \cos^{-1}\left(\frac{1}{2}\left(\Sigma_{i=1}^3 \frac{\langle \xi_i, \nabla F_{t_0}^t \xi_i \rangle}{\sqrt{\lambda_i}} - 1\right)\right). \tag{7.2.6}$$

Elliptic Lagrangian coherent structures can be approximated as the outermost closed PRA level curves. It was further noted in Farazmand and Haller (2016) that the PRA is not objective in 3D.

Lagrangianly Averaged Vorticity Deviation

Haller *et al.* (2016) introduced a measure for uncovering vortices in nonautonomous systems based on the vorticity. This relatively simple computation gives similar results to the computationally intensive geodesic theory (for 2-dimensional flows). With no direct extension for geodesic theory to 3D, the Lagrangianly averaged vorticity deviation (LAVD) could be used in these settings to obtain elliptic (trapping) regions. The LAVD (for 3D cases) is given as:

$$LAVD_{t_0}^{t_0+t}(\mathbf{x_0}) = \int_{t_0}^{t_0+t} |\boldsymbol{\omega}(\mathbf{x}(s;\mathbf{x_0}), s) - \bar{\omega}(s)| ds, \tag{7.2.7}$$

where ω is the vorticity, and the overbar denotes the field average. From this field, vortex centers are found as local maximums, and level sets around these centers are used to obtain the 3-dimensional vortex tubes. Note that the same type of level set

---

[1] This property ensures that connected level sets of $\cos\theta_{t_0}^t$ and $\sin\theta_{t_0}^t$ correspond to connected level-sets of $\theta_{t_0}^t$.

extraction is used for the PRA fields, and that with the PRA, vortex centers are distinguished by local extrema in the field.

General Linear Model (GLM3D)

Motivated by the results seen in the 2D case, an approximation to the deformation over short intervals is sought for the 3D setting. First, the 2D linear flow-subsystem is simply imbedded in a 3D computational domain, where the third dimension does not contribute to the dynamics. This 3D system is given as:

$$\begin{aligned} \dot{x} &= \lambda x + \beta y \\ \dot{y} &= \gamma x - \lambda y \\ \dot{z} &= 0, \end{aligned} \tag{7.3.1}$$

and referred to as *barely*-3D. Since it is only in name that the dynamics of this system could be classified as 3-dimensional. The barley-3D system inherits its incompressibility from the 2D subsystem, but the determinant is now seen to be 0. The Jacobian is computed with the use of infinitesimal generators (seen in Appendix C), and is given as:

$$J = \begin{bmatrix} \cosh \alpha t + \frac{\lambda}{\alpha} \sinh \alpha t & \frac{\beta}{\alpha} \sinh \alpha t & 0 \\ \frac{\gamma}{\alpha} \sinh \alpha t & \cosh \alpha t - \frac{\lambda}{\alpha} \sinh \alpha t & 0 \\ 0 & 0 & 1 \end{bmatrix}, \tag{7.3.2}$$

where $\alpha := \sqrt{\lambda^2 + \beta\gamma}$ (the determinant of the 2D subsystem) as previously seen. The Jacobian in (7.3.2) is seen to contain the 2D-Jacobian within it, and 1 in the $(3,3)$ component, indicating no variation in z-direction. This is consistent with the method in which (7.3.1) is constructed. Further, from looking at the second-order moments (using infinitesimal generators, in Appendix C), it is seen that the moments matrix also contains its 2D counterpart. However, more than the $(3,3)$ component is nonzero. The z-based generators give the following expressions:

$$\begin{aligned} \mathbb{E}[\dot{XZ}] &= \lambda \mathbb{E}[XZ] + \beta \mathbb{E}[YZ] \\ \mathbb{E}[\dot{YZ}] &= \gamma \mathbb{E}[XZ] - \lambda \mathbb{E}[YZ] \\ \mathbb{E}[\dot{Z^2}] &= 2\kappa. \end{aligned} \tag{7.3.3}$$

It is seen that the (XZ, YZ)-subsystem is of the same form as the first-order moments of the 2D linear system. Thus the z-moments are given as:

$$\begin{aligned} \mathbb{E}[XZ] &= \mathbb{E}[XZ](t_0)\left(\cosh(\alpha\tau) + \frac{\lambda}{\alpha}\sinh(\alpha\tau)\right) + \mathbb{E}[YZ](t_0)\frac{\beta}{\alpha}\sinh(\alpha\tau) \\ \mathbb{E}[YZ] &= \mathbb{E}[YZ](t_0)\left(\cosh(\alpha\tau) - \frac{\lambda}{\alpha}\sinh(\alpha\tau)\right) + \mathbb{E}[XZ](t_0)\frac{\gamma}{\alpha}\sinh(\alpha\tau) \\ \mathbb{E}[Z^2] &= \mathbb{E}[Z^2](t_0) + 2\kappa\tau. \end{aligned} \tag{7.3.4}$$

Assuming an initial distribution of a delta function, all of the initial values of the second-order moments are set to zero ($\mathbb{E}[X^2](t_0) = 0, \mathbb{E}[XY](t_0) = 0, \mathbb{E}[XZ](t_0) = 0$, etc.). The moments are given as:

$$\begin{aligned} \mathbb{E}[X^2] &= \frac{\kappa}{2\alpha^3}\Big(\big(\lambda^2 + \alpha^2 + \beta^2\big)\sinh(2\alpha\tau)\Big) + F(\beta, \gamma, \lambda, \kappa, \tau) \\ \mathbb{E}[XY] &= \frac{\kappa(\gamma+\beta)}{2\alpha^2}\big(\cosh(2\alpha\tau) - 1\big) + \frac{\kappa\lambda(\gamma-\beta)}{2\alpha^3}\sinh(2\alpha\tau) + \lambda\kappa(\beta-\gamma)\tau/\alpha^2 \\ \mathbb{E}[Y^2] &= \frac{\kappa}{2\alpha^3}\Big(\big(\lambda^2 + \alpha^2 + \gamma^2\big)\sinh(2\alpha\tau)\Big) + F(\gamma, \beta, -\lambda, \kappa, \tau) \\ \mathbb{E}[Z^2] &= 2\kappa\tau. \end{aligned} \tag{7.3.5}$$

where $F(\beta, \gamma, \lambda, \kappa, \tau) = \frac{\kappa}{\alpha^2}\big(\lambda\cosh(2\alpha\tau) - \lambda + \gamma\beta\tau - \beta^2\tau\big)$. Schematically the moment matrix appears as:

$$M = \begin{bmatrix} \mathbb{E}[X^2] & \mathbb{E}[XY] & 0 \\ \mathbb{E}[XY] & \mathbb{E}[Y^2] & 0 \\ 0 & 0 & \mathbb{E}[Z^2] \end{bmatrix}. \tag{7.3.6}$$

Moving slightly past the model built up from the 2D case: a *quasi*-3D flow can be obtained from incorporating small perturbations to (7.3.1). The new flow takes the form:

$$\begin{aligned} \dot{x} &= \lambda x + \beta y \\ \dot{y} &= \gamma x - \lambda y \\ \dot{z} &= \eta z, \end{aligned} \tag{7.3.7}$$

where $\eta \ll 1$ is small; to leading order this system is identical to (7.3.1). However, when the contributions of $O(\epsilon)$ terms are considered slight variability in the z-direction is possible. For $\eta \neq 0$ the system is not truly incompressible, but approximately. From the first-order generators (seen in Appendix C) the Jacobian is obtained as:

$$J = \begin{bmatrix} \cosh \alpha t + \frac{\lambda}{\alpha} \sinh \alpha t & \frac{\beta}{\alpha} \sinh \alpha t & 0 \\ \frac{\gamma}{\alpha} \sinh \alpha t & \cosh \alpha t - \frac{\lambda}{\alpha} \sinh \alpha t & 0 \\ 0 & 0 & e^{\eta t} \end{bmatrix}, \tag{7.3.8}$$

where $\alpha := \sqrt{\lambda^2 + \beta\gamma}$. It is noted here that as $\eta \to 0$, (7.3.8) converges to (7.3.2).

For this system, approximations to the elements of the covariance matrices can be explicitly obtained, as shown in Appendix C. It is immediately seen that the elements obtained here are those seen in the 2D case. It is further noted that the $\mathbb{E}[Z^2]$ has changed to the following:

$$\mathbb{E}[Z^2] = E_{z^2} e^{2\eta\tau} + \frac{\kappa}{\eta} \left(e^{2\eta\tau} - 1 \right). \tag{7.3.9}$$

Assuming $\eta \ll 1$, the exponential can be expanded into its series form. The resulting expression would be,

$$\mathbb{E}[Z^2] = E_{z^2} e^{2\eta\tau} + \frac{\kappa}{\eta} \left((2\eta\tau) + \frac{(2\eta\tau)^2}{2} + \frac{(2\eta\tau)^3}{6} + \cdots \right), \tag{7.3.10}$$

and is seen to converge to $\mathbb{E}[Z^2] = E_{z^2} + 2\kappa\tau$; this is the same expression for the barely-3D model.

The parameters necessary to obtain the covariance elements are then obtained in the same fashion as the 2D case, through the expressions in (6.1.19). More specifically, the following expressions are used to determine the parameters of the model:

$$\begin{aligned}
\alpha(t;\mathbf{x}_0) &= \frac{1}{\tau}\operatorname{arcCosh}\left(\frac{J_{11}(t;\mathbf{x}_0)+J_{22}(t;\mathbf{x}_0)}{2}\right), &\quad \beta(t;\mathbf{x}_0) &= \frac{\alpha(t;\mathbf{x}_0)J_{12}(t;\mathbf{x}_0)}{\sinh(\alpha(t;\mathbf{x}_0)\tau)}\\
\lambda(t;\mathbf{x}_0) &= \frac{\alpha(t;\mathbf{x}_0)(J_{11}(t;\mathbf{x}_0)-J_{22}(t;\mathbf{x}_0))}{2\sinh(\alpha(t;\mathbf{x}_0)\tau)}, & \gamma(t;\mathbf{x}_0) &= \frac{\alpha(t;\mathbf{x}_0)J_{21}(t;\mathbf{x}_0)}{\sinh(\alpha(t;\mathbf{x}_0)\tau)}\\
\eta(t;\mathbf{x}_0) &= \frac{1}{\tau}\log J_{33}(t;\mathbf{x}_0).
\end{aligned} \tag{7.3.11}$$

Decoupled-3D Model

To properly analyze 3D-incompressible flows, the following *decoupled*-3D model is introduced:

$$\begin{aligned}
\dot{x} &= \lambda x + \beta y\\
\dot{y} &= \gamma x - (\lambda+\eta)\,y\\
\dot{z} &= \eta z.
\end{aligned} \tag{7.3.12}$$

Although there is no restriction on $\eta \ll 1$, it is seen that as $\eta \to 0$, (7.3.1) is recovered yet again.

Using the same approach as in Appendix E, the first-order moments can be obtained for the x and y terms. By appending the result obtained from $\mathbb{E}[Z]$ to the solutions for $\mathbb{E}[X]$ and $\mathbb{E}[Y]$, the Jacobian matrix is obtained:

$$J = \begin{bmatrix} e^{\frac{-\eta t}{2}}\left(\cosh\theta t/2 + \frac{\eta+2\lambda}{\theta}\sinh\theta t/2\right) & e^{\frac{-\eta t}{2}}\frac{2\beta}{\theta}\sinh\theta t/2 & 0\\ e^{\frac{-\eta t}{2}}\frac{2\gamma}{\theta}\sinh\theta t/2 & e^{\frac{-\eta t}{2}}\left(\cosh\theta t/2 - \frac{2\lambda+\eta}{\theta}\sinh\theta t/2\right) & 0\\ 0 & 0 & e^{\eta t} \end{bmatrix}, \tag{7.3.13}$$

where $\theta := \sqrt{\eta^2 + 4(\lambda^2 + \eta\lambda + \beta\gamma)}$. It is seen that as $\eta \to 0$, the results approach that of the barely-3D flow (Appendix C). However, when η does not tend towards zero the parameters of the model become difficult to recover.

The full second-order moments are given in Appendix D, while here the expressions are given assuming a delta-function as the initial condition. The delta-function initial condition provides that the initial expectations (E_{x^2}, E_{xy}, and E_{y^2}) can be reasonably approximated as 0.

$$\begin{aligned}\mathbb{E}[X^2] = &\frac{\kappa e^{-\eta\tau}\theta\sinh\theta\tau}{\theta^2(\lambda^2+\eta\lambda+\beta\gamma)}\big((\eta+\lambda)(\eta+2\lambda)+\beta\gamma+\beta^2\big)\\ &+\frac{\kappa e^{-\eta\tau}\cosh\theta\tau}{\theta^2(\lambda^2+\eta\lambda+\beta\gamma)}\big(\theta^2(\eta+\lambda)+\beta\eta(\beta-\gamma)\big)\\ &-\frac{\kappa(\eta+\lambda)}{(\lambda^2+\eta\lambda+\beta\gamma)}-\frac{\kappa\beta(\beta-\gamma)\eta}{\theta^2(\lambda^2+\eta\lambda+\beta\gamma)}-\frac{4\kappa\beta(\beta-\gamma)}{\theta^2\eta}\big(1-e^{-\eta\tau}\big)\end{aligned} \tag{7.3.14}$$

$$\begin{aligned}\mathbb{E}[XY] = &\frac{\kappa e^{-\eta\tau}}{\theta^2(\lambda^2+\eta\lambda+\beta\gamma)}\theta\sinh\theta\tau\,\big(\gamma(\eta+\lambda)-\beta\lambda\big)\\ &+\frac{\kappa e^{-\eta\tau}}{\theta^2(\lambda^2+\eta\lambda+\beta\gamma)}\cosh\theta\tau\Big((\beta+\gamma)\big(\theta^2-\lambda(\eta+2\lambda)-2\beta\gamma\big)-2\beta\eta\lambda\Big)\\ &+\frac{\kappa}{\theta^2(\lambda^2+\eta\lambda+\beta\gamma)}\Big(\gamma\big(2\eta^2-\theta^2\big)+\lambda\eta(\beta-\gamma)\Big)-\frac{2\kappa(\beta-\gamma)e^{-\eta\tau}}{\theta^2}\\ &+\frac{4\kappa\lambda(\beta-\gamma)}{\theta^2\eta}\big(1-e^{-\eta\tau}\big)\end{aligned} \tag{7.3.15}$$

$$\begin{aligned}\mathbb{E}[Y^2] = &\frac{\kappa e^{-\eta\tau}\theta\sinh\theta\tau}{\theta^2(\lambda^2+\eta\lambda+\beta\gamma)}\big(\lambda(\eta+2\lambda)+\gamma(\gamma+\beta)\big)\\ &+\frac{\kappa e^{-\eta\tau}\cosh\theta\tau}{\theta^2(\lambda^2+\eta\lambda+\beta\gamma)}\big(\eta\gamma(\gamma-\beta)-\lambda\theta^2\big)\\ &+\frac{\kappa\lambda}{(\lambda^2+\eta\lambda+\beta\gamma)}+\frac{\kappa\gamma(\beta-\gamma)\eta}{\theta^2(\lambda^2+\eta\lambda+\beta\gamma)}+\frac{4\kappa\gamma(\beta-\gamma)}{\theta^2\eta}\big(1-e^{-\eta\tau}\big)\end{aligned} \tag{7.3.16}$$

The parameters necessary for the second-order moments are obtained from the following relations:

$$\begin{aligned} \eta &= \frac{1}{t}\log(J_{33}), &\qquad \theta &= \frac{2}{t}\,\mathrm{arcCosh}\left(\left(\frac{J_{11}+J_{22}}{2}\right)e^{\frac{\eta t}{2}}\right) \\ \gamma &= \frac{\theta J_{21} e^{\frac{\eta t}{2}}}{2\sinh\frac{\theta t}{2}}, &\qquad \beta &= \frac{\theta J_{12} e^{\frac{\eta t}{2}}}{2\sinh\frac{\theta t}{2}} \\ \lambda &= \frac{(J_{11}-J_{22})\,\theta e^{\frac{\eta t}{2}}}{4\sinh\frac{\theta t}{2}} - \frac{\eta}{2} \end{aligned} . \qquad (7.3.17)$$

Fully-3D Model

When a fully-3D linear flow, as such:

$$\begin{aligned} \dot{x} &= \lambda_1 x + \beta_1 y + \beta_2 z \\ \dot{y} &= \gamma_1 x + \lambda_2 y + \beta_3 z \\ \dot{z} &= \gamma_2 x + \gamma_3 y + \lambda_3 z, \end{aligned} \qquad (7.3.18)$$

is considered, the parameters become unwieldy and closed analytic expressions for the moments are difficult to obtain.

Chapter 8

THE FLOWS AND ANALYSIS

Flows

Arnold-Beltrami-Childress Flow

The Arnold-Beltrami-Childress (ABC) flow is a 3D flow with a periodic domain that has been a test-bed for various computational algorithms. The dynamics of the system are governed by the parameters $A, B, C, D \in \mathbb{R}$, and is given as:

$$\begin{aligned} \dot{x} &= A(t)\sin z + C\cos y \\ \dot{y} &= B\sin x + A(t)\cos z \\ \dot{z} &= C\sin y + B\cos x, \end{aligned} \tag{8.1.1}$$

with $A(t) = A + Dt\sin t$. For $D = 0$ the system is autonomous, and further, if any other parameter is also zero then the system will be integrable. In this integrable case, the system can be rephrased as a decoupled second-order system; the solutions of which can be written as polynomials or in terms of elliptic functions. When all of the parameters are non-zero the system is nonautonomous with a general time dependency. The physical domain of the system is given by the 3-torus, on $[0, 2\pi]^3$. Given the flow parameters as (A, B, C, D), the following cases were pursued to provide a direct comparison to previous works: integrable case $(0, \sqrt{2}, 1, 0)$, steady case $(\sqrt{3}, \sqrt{2}, 1, 0)$, and nonautonomous case $(\sqrt{3}, \sqrt{2}, 1, 1)$.

Inertia-Gravity Wave

In Tang *et al.* (2010) the impact of noise on a 3-dimensional inertia-gravity wave (IGW) model is investigated. The IGW model provides a prototypical integrable model for studying the affect of noise on Lagrangian dynamics. With the ubiquity of these waves in the environment understanding how sub-scale perturbations can affect mixing is of vital importance. The non-dimensional IGW model is given as:

$$\begin{aligned}\dot{x} &= U\cos\big(2\pi\,(x+z-t)\big)\\ \dot{y} &= U\sin\big(2\pi\,(x+z-t)\big)\\ \dot{z} &= -U\cos\big(2\pi\,(x+z-t)\big),\end{aligned} \tag{8.1.2}$$

where U is the nondimensional velocity scale, and the nondimensional wave phase is defined as $\Phi := 2\pi\,(x+z-t)$. Due to the cancellation of the x and z terms in the wave phase, the system is integrable. This means that for a deterministic flow no Lagrangian mixing will occur over the flows wave period. This property also makes it possible to obtain closed form solutions for the second-order moments. Since these moments are directly computable, these will be used to directly compare against the moment approximations obtained from the GLM3D method. However, since GLM3D is modeled for a flow where the surface dynamics are mostly decoupled from the vertical component, good agreement between the actual moment values and the approximations obtained by GLM3D is not expected, even for short times.

Ocean Surface Mixing Model: Quasi-3D Flow

The need for anisotropy in the diffusivities of geophysical flows was also discussed in Tang *et al.* (2010). Since vertical fluctuations are suppressed in density stratified environments, the components of diffusivity in the horizontal ($\sigma_h^2 = 2\epsilon_h$) and vertical ($\sigma_v^2 = 2\epsilon_v$) directions are taken at separate scales. Further, in Aharon *et al.* (2012) the impact of vertical convection on surface layer mixing in the ocean was investigated. The vertical convection was modeled as a 3D perturbation to an asymmetric double-gyre flow. This convoluted model is generated from three planar stream functions, $\Psi_{xy}(x, y, t)$, $\Psi_{yz}(y, z, t)$ and $\Psi_{xz}(x, z, t)$, as:

$$\begin{aligned}\dot{x} &= \frac{\partial \Psi_{xy}}{\partial y} - \frac{\partial \Psi_{xz}}{\partial z} \\ \dot{y} &= -\frac{\partial \Psi_{xy}}{\partial x} + \frac{\partial \Psi_{yz}}{\partial z} \\ \dot{z} &= \frac{\partial \Psi_{xz}}{\partial x} - \frac{\partial \Psi_{yz}}{\partial y},\end{aligned} \tag{8.1.3}$$

where the stream functions are given by,

$$\begin{aligned}\Psi_{xy}(x, y, t) &= \frac{u_{double-gyre}}{2\pi}\left(\sin\frac{2\pi y}{L_y} + \sin\frac{\pi y}{L_y}\right)\sin\frac{\pi x}{L_x} \\ &\quad + \frac{\epsilon u_{tide}}{2\pi}\sin\left(\omega_{tide} t + \theta_{tide}\right)\sin\frac{2\pi y}{L_y}\sin\frac{\pi x}{L_x} \\ \Psi_{yz}(y, z, t) &= \frac{\epsilon u_{vert}}{4\pi}\xi(t)\sin\pi z\tanh\frac{\alpha y}{L_y}\tanh\frac{\alpha\left(y_{hz} - y\right)}{L_y}\tanh\frac{\alpha\left(y - L_y\right)}{L_y} \\ \Psi_{xz}(x, z, t) &= 0,\end{aligned} \tag{8.1.4}$$

with the parameter values given as: $L_x = 3/4$, $L_y = 5/4$, $y_{hz} = L_y/2$, $\omega_{tide} = 36\pi/19$, $\omega_{day} = \pi$, $\bar{c_2} = 1$, $\alpha = 10$, and $\xi(t) \coloneqq \left(\bar{c_2} + \frac{4}{\pi}\sin\omega_{day} t\right)$. For the parameters used, $t = 2$ corresponds to a day in dimensional units.

It was observed in Aharon *et al.* (2012) that the strength of the vertical perturbation was capable of changing the dynamics of mixing; where with the decrease in perturbation, the results approach those obtained from the 2D surface layer model. It is noted that for the GLM2D, short integration times (as long as 1/4 of the period of the flow) were necessary such that the linear flow approximation was still valid. Given the additional complexity of another dimension this short time restriction is still seen.

Types	Condition
• Elliptic (trapping)	$\sigma < \bar{\sigma} - \sqrt{\langle(\sigma - \bar{\sigma})^2\rangle}$
• Hyperbolic (jumping)	$\sigma > \bar{\sigma} + \sqrt{\langle(\sigma - \bar{\sigma})^2\rangle}$
• Intermediate (both)	$\lvert\sigma - \bar{\sigma}\rvert < \sqrt{\langle(\sigma - \bar{\sigma})^2\rangle}$

Table 8.1: Classification of Coherent Regions Given by the FTLE Measure for the 3-dimensional Flows

Analysis for 3D Systems

The following sections will be submitted to Physics of Fluids. The first step of the analysis for the 3D systems is obtaining the LCS classification of trapping regions. In Budišić *et al.* (2015) the same ABC systems were analyzed, and it is noted here that the full OWC partitions obtained therein contain no non-hyperbolic regions(i.e. trapping regions). As such, the OWC partition although theoretically interesting is not suited for the following analysis, and will therefore be omitted.

The finite-time Lyapunov exponent (FTLE) field will be used to identify trapping type regions via a threshholding argument, similar to what was done for the 2D turbulent flow. The regions are classified by using one standard deviation away from the mean value. Letting $\sigma(\mathbf{x}, t) = \Lambda_{t_0}^{t}(\mathbf{x_0})$ denote the FTLE field, and $\bar{\sigma} = \langle\sigma\rangle$ be the field average ($\langle\cdot\rangle$ indicates the spatial average), then Table 8.1 describes the FTLE partition for the 3D flows. Note that in the 3D cases only trapping and nontrapping regions are considered, therefore the "Hyperbolic" and "Intermediate" regions are combined.

Further, since the integrable and steady ABC flows are autonomous, only one set of partitions is needed to analyze their dynamics. As such, for these flows level-sets

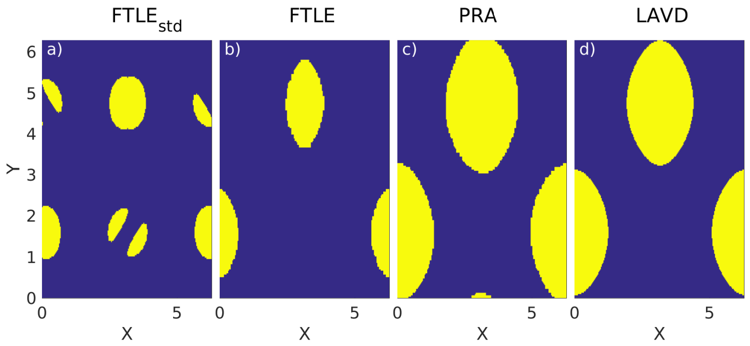

Figure 8.2.1: Comparison of the partitions for the integrable ABC flow, obtained by a) the standard deviation of the FTLE field, b) the FTLE level-sets, c) the PRA level-sets, and d) the LAVD level-sets, using an integration time of $\tau = 5$. The fields are horizontal slices at $z = 0$

extracted from the FTLE fields are also used to partition the domain. However, since this procedure is computationally intensive and requires well defined transport boundaries, the unsteady ABC flow will not use the level-sets extracted from the FTLE field. As discussed earlier, the trapping regions for the PRA and LAVD methods are obtained by extruding level-sets throughout the 3-dimensional domain.

In Fig. 8.2.1 the trapping regions for the integrable ABC flow are shown. It is seen that using the classification based on the standard deviation of FTLE gives false positives for trapping regions. This partition is also the most dissimilar to the others. The partitions obtained from using level-set extraction all give similar results, only differing if the size of the defined trapping regions. It is also noted that for the integrable ABC flow, the boundaries of the trapping regions do not change with z; the partitions obtained at $z = 0$ are the same for all $z \in [0, 2\pi]$.

In a similar manner, the partitions for the steady ABC flow can be seen in Fig. 8.2.2. This figure shows a comparison of the partitions obtained using an integration time of $\tau = 10$, at the $z = 0$ slice. Similar to the integrable flow, the FTLE partition obtained via threshholding is the most dissimilar, and least accurate. The major distinctions between the level-set based partitions appears to be the width of the

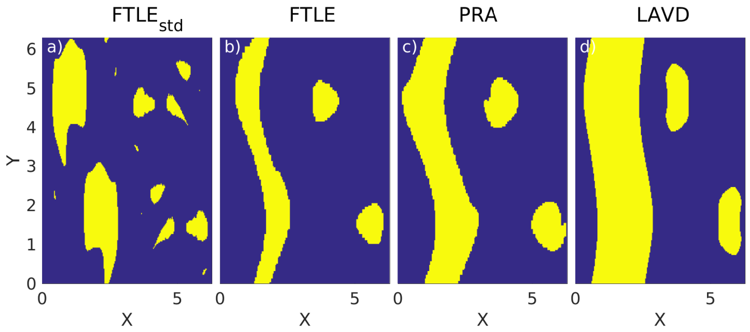

Figure 8.2.2: Comparison of the partitions for the steady ABC flow, obtained by a) the standard deviation of the FTLE field, b) the FTLE level-sets, c) the PRA level-sets, and d) the LAVD level-sets, using an integration time of $\tau = 10$. The fields are horizontal slices at $z = 0$.

vortex-tube on the leftside of the domain; for the FTLE and PRA methods only the vortex core is extracted, while LAVD extracts a much wider region.

Further, unlike the integrable case, the partitions of the steady flow vary along the z-axis. Fig. 8.2.3 depicts the interior of trapping regions with black dots. In this figure the vortex-tubes can clear be inferred. Having seen how poor a partition the FTLE$_{std}$ gave in Fig. 8.2.2, it is no suprise to see many erroneous classifications in the 3D plot.

For the nonautonomous case, the classification of trapping regions at later times is necessary. In order to achieve this a sliding time interval is used (just like what was used in the 2D analysis), with a spacing of 1/20 of a timeunit between partitions and an integration time of $\tau = 5$ time units. In Fig. 8.2.4 the partitions of the unsteady ABC flow are seen, for $t = 0$. Due to the nonlinear temporal terms in the flow, the simple structures that obtained the steady case are lost. With the well defined barriers lost, the level-set approach is not used for the FTLE field. However, since both the PRA and LAVD methods rely on extracting level-sets surrounding local extrema in the fields, extraction is used for these partitions. The ellitpic region, as defined in Table 8.1, is seen as the dark blue regions in Fig. 8.2.4a); these regions

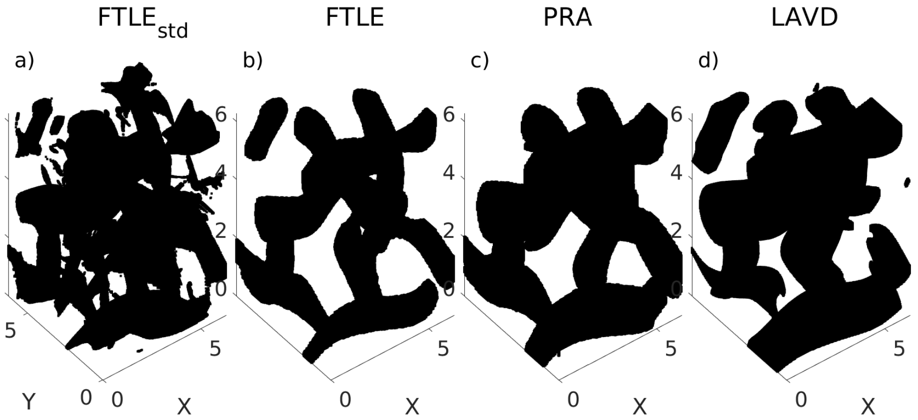

Figure 8.2.3: Comparison of the extracted trapping regions for the steady ABC flow, obtained by a) the standard deviation of the FTLE field, b) the FTLE level-sets, c) the PRA level-sets, and d) the LAVD level-sets, using an integration time of $\tau = 10$.

do not appear to correspond well with the underlying dynamics, this is a result of the arbitrary nature of the threshold used for demarcating the regions. For the PRA and LAVD partitions, the respective fields are first plot, then on top the trapping regions, as obtained from level-set extraction, are distinguished. In Fig. 8.2.4b) the trapping regions are seen as black dots, that correspond well to the structure of the underlying field, with a few random artifacts present. The reason for the spurious results could be due to imaginary components in the PRA. The trapping regions for the LAVD field, presented as red curves in Fig. 8.2.4c), distinguish similar regions to PRA, without the additional artifacts. Further, the LAVD method captures two regions on the left side of the domain, in the region that was a horizontal vortex tube for the steady case. This suggests that when the instability is introduced for the unsteady flow and the vortex tube starts to breakdown, the bulk motion of tracers in this region may not be chaotic over the integration time used for the field.

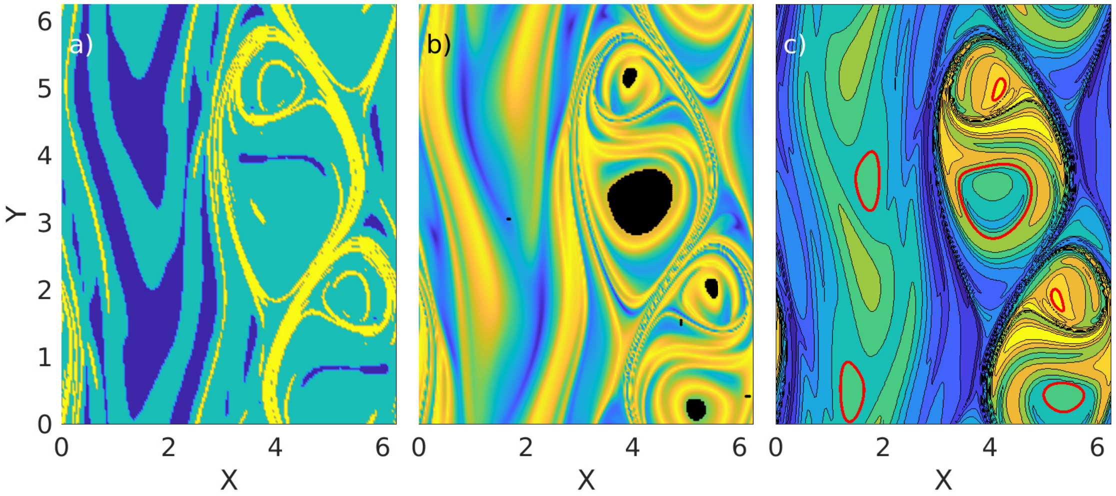

Figure 8.2.4: Comparison of the partitions for the unsteady ABC flow, obtained by a) the standard deviation of the FTLE field, b) the PRA level-sets, and c) the LAVD level-sets, using an integration time of $\tau = 5$. The fields are horizontal slices at $z = 0$

Conditional Jump and Flight-time Statistics

Using the partitions from the previous section, the scalings of the jump and flight-time pdfs are obtained. Two types of trajectories are analyzed for each flow: deterministic (N) and stochastic. The stochastic trajectories use Gaussian noise to simulate the diffusion process. Further, two types of stochastic trajectories are used in order to investigate isotropic (G_1) and anisotropic (G_2) diffusion. The anisotropic diffusion is done by using a horizontal diffusivity κ_h, and vertical diffusivity $\kappa_v \equiv \kappa_h/100$. By looking at how the statistics vary between these two cases, some of the modeling necessities for geophysical flows by toy models can be better understood.

Recalling the simple structures of the partitions for the integrable ABC flow two complimentary analyses are done for it. Since the flow is uniform in the z-direction, a dense sampling of the $x-y$ plane is used to obtain the statistics; the sampling uses 40000 initiation points (corresponding to a 200×200 grid) for tracer ensembles with

4900 members. However, due to data storage issues this dense of a sampling cannot be extended to the third dimension. Instead, for flows that vary in z, a much more sparse initial sampling is used. The sparse sampling uses initiation points corresponding to a $32 \times 32 \times 32$ lattice. To draw a direct comparison of the impact of the sampling types, both are used for the integrable ABC flow.

The dense data is obtained by initiating the tracer ensemble at a single point in the 200×200 grid, while the sparse sampling is done using $17 \times 17 \times 17$ uniformly spaced tracers in each cell of the $32 \times 32 \times 32$ lattice. An integration time of 50 time units is used for computing the trajectories.

In Table 8.2 the relative *coherence* rates for the different partitions and initiation type are seen. These coherence rates are similar to the retention rates, howere where retention rates cares only about the classification of the tracer's initial and final locations, the coherence rates checks if a tracer ever has an exit event – switching from one classification to another. For the deterministic trajectories this number provides a metric for gauging the accuracy of the partition. Further, when noise is added this number indicates the robustness of the coherent structures. From the table it is seen that the the densely and sparsely initiated cases maintained similar levels of coherence (to each other) for the 3 noise cases, suggesting that the sparse sampling is sufficient.

For the deterministic case the largest rates of coherence are expected, as the trajectories are not able to traverse the transport barrier. It is seen that the two types of stochastic trajectories result in the same retention rates approximately, this is expected for this flow since the anisotropic noise limits the perturbation in the z direction. The FTLE_{std} is seen to consistently give the lowest coherence, due to the arbitrary nature in which partitioning is done, while the level-set based approaches have greater coherence. When noise is added the trajectories are able to escape the

Region Type	Partition Type			
	FTLE$_{std}$	FTLE	PRA	LAVD
Trapping (d/s) (N)	.4224 : .3985	.7271 : .7118	.8982 : .9029	.8989 : .8911
Flight (d/s) (N)	.6409 : .6444	.9505 : .9547	.9391 : .9310	.9576 : .9616
Trapping (d/s) (G_1)	.1035 : .1027	.2567 : .2491	.5697 : .5765	.5410 : .5387
Flight (d/s) (G_1)	.3618 : .3617	.8473 : .8510	.7173 : .7139	.7733 : .7758
Trapping (d/s) (G_2)	.1034 : .1024	.2566 : .2491	.5716 : .5765	.5423 : .5388
Flight (d/s) (G_2)	.3612 : .3617	.8473 : .8510	.7169 : .7139	.7737 : .7758

Table 8.2: Coherence rates for the integrable ABC flow using 3 noise types: deterministic (N), isotropic Gaussian noise (G_1), and anisotropic Gaussian noise (G_2); along with 2 initial release configurations: dense (d) and sparse (s). The trajectories are obtained using an integration time of $\tau = 50$.

trapping and flight regions, resulting in lower coherence. However, relatively large coherence is maintained in the flight/nontrapping regions for the level set approaches, due to the size of this region compared to the domain. As expected little difference is seen between the isotropic and anisotropic cases since there is no variability of the flow in the z direction.

The pdfs of trapping and nontrapping events for the sparsely initiated integrable flow are seen in Fig. 8.2.5. It is seen that the PRA and LAVD give similar results, with FTLE and FTLE$_{std}$ being slightly different; this is expected due to the differences in the partitions. Due to the simplicity of this flow, the mixing of tracers is driven by the noise. Further, due to the noise level, a majority of tracers originally in one of the vortex tubes will stay there, with only a few tracers on the boundaries entering and exiting; this is seen as the spikes in the histograms at the final time. Further, the oscillatory behavior seen in the FTLE$_{std}$ and FTLE indicate that the boundaries of the vortex tubes were not correctly classified, resulting in tracers inside the vortex tube to be misidentified as exiting the region. The dashed black lines show the

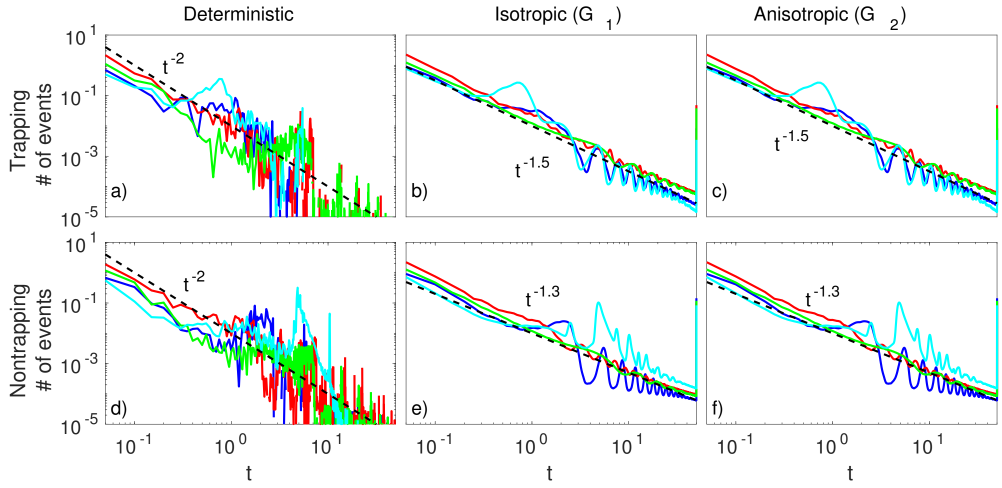

Figure 8.2.5: Pdfs of trapping and nontrapping regions for the integrable ABC flow, as obtained from FTLE$_{std}$ (cyan), FTLE (blue), PRA (red), and LAVD (green), using an integration time of $\tau = 10$. The black dashed lines show the power-law decay rates for the various noises.

power-law decay rates, ranging from $t^{-1.3}$ to t^{-2}. The same decay rates are seen for the isotropic and anisotropic noise, which is expected due to the structure of the flow. The fast decay rate for the deterministic trajectories corresponds to tracers that were originally mislabelled, and from only portions of coherent regions being extracted.

For the steady and unsteady ABC flows it is expected that the isotropic and anisotropic diffusions will lead to differing results; due to the partitions variability in z. In Table 8.3 the coherence rates for the steady and unsteady ABC flows are seen. Since the steady flow is still autonomous, tracers are expected to stay coherent over the integration time of their trajectories. However, for the unsteady case the coherent regions are not permanent features of the flow, and can deform or even disassociate over the integration time of the trajectories. Further, since the coherent regions in which a trajectory is initiated can be destroyed before the end of the simulation, lower coherences are expected. Interestingly greater coherence is seen in the anisotropic noise, than for the isotropic, owing to the fact that the anisotropic perturbation alters the tracer location by a smaller distance. The smaller perturbation offers tracers fewer opportunities to escape their partitions. It is again seen that the FTLE$_{std}$ has the lowest retention for both the steady and unsteady flows, owing to the arbitrary value the partition is based on.

Region Type	Partition Type			
	FTLE$_{std}$	FTLE	PRA	LAVD
Trapping (S/U) (N)	.0727 : 6.66e-4	.1964	.2183 : 0	.5472 : 0
Flight (S/U) (N)	.0976 : .1042	.7277	.3836 : .3433	.6574 : .3417
Trapping (S/U) (G_1)	2.9747e-4 : 6.09e-4	.0048	.0187 : 0	.2224 : 0
Flight (S/U) (G_1)	.0092 : .0625	.2979	.1713 : .3379	.2979 : .3334
Trapping (S/U) (G_2)	.0052 : 2.4692e-5	.0215	.0584 : 0	.3084 : 0
Flight (S/U) (G_2)	.0154 : .0857	.5824	.2287 : .3429	.3916 : .3400

Table 8.3: Conditional coherence rates for the steady (S) and unsteady (U) ABC flows using 3 noise types: deterministic (N), isotropic Gaussian noise (G_1), and anisotropic Gaussian noise (G_2). The trajectories of the steady ABC flows are obtained with an integration time of $\tau = 50$, while the unsteady flow uses an integration time of $\tau = 8$.

Further, from looking at the pdfs of the trapping and nontrapping events the impact of the anisotropy can also be seen. In Fig. 8.2.6, the pdfs of the trapping and nontrapping events are shown along with power-law scales shown in black. It is seen that not only is there much more variability between the results of the different partitions, but that anisotropy has an impact on the curves. Tracers originating in trapping regions are less likely to exit the transversal vortex tubes, and would find it even more difficult to escape a vertical vortex tube.

As discussed earlier (and seen in Fig. 8.2.4) the partitions for the unsteady ABC flow are less well defined, making the presence of coherent regions less noticeable. The difficulty in accurately obtaining the trapping regions leads to misclassified regions, as seen in the partition figure. In Fig. 8.2.7 the pdfs of the trapping and nontrapping

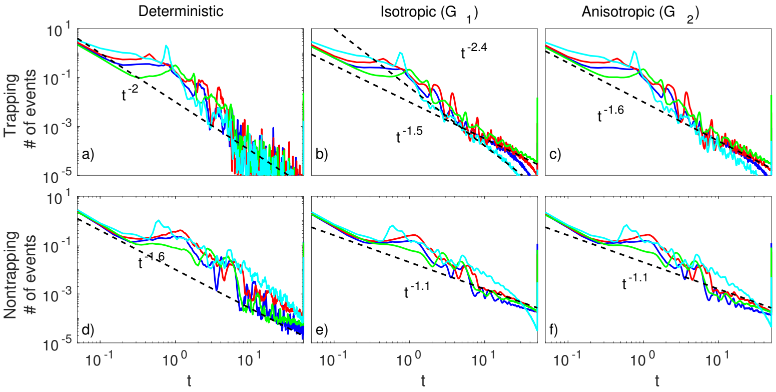

Figure 8.2.6: Pdfs of trapping and nontrapping regions for the steady ABC flow, as obtained from FTLE, FTLE$_{std}$, PRA, and LAVD, using an integration time of $\tau = 10$. The black dashed curves show the power-law decay rates for the various partitions.

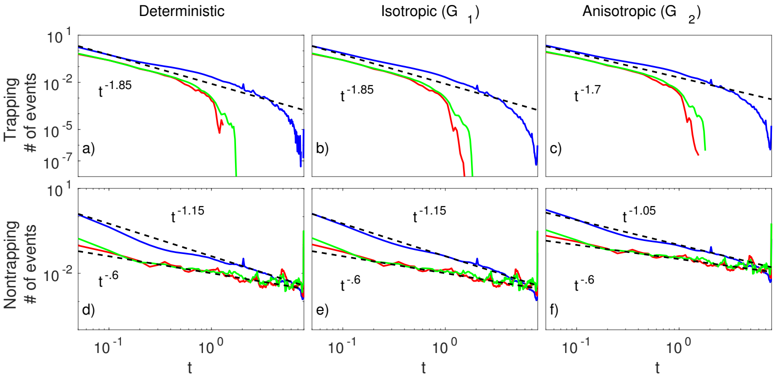

Figure 8.2.7: Pdfs of trapping and nontrapping regions for the unsteady ABC flow, as obtained from FTLE$_{std}$, PRA, and LAVD, using an integration time of $\tau = 10$. The black dashed curves show the power-law decay rates for the various partitions.

regions are seen. The curves are more unsteady and unpredicatable compared to those obtained for the integrable and steady cases. This is due to the misclassification of tracers either at their initial location or along their trajectories. Despite the misclassifications the general shapes of the curves still suggest similar scaling laws as the other flows.

Use Statistics to Model Transport

Having the different scales from the pdfs, they can be used as parameters for modelling the 3D nonlinear transport as a 1D system. Previously the reduction of a higher dimensional system to 1D used the radial displacement of tracers. Since the 3D flows do not offer natural boundaries, like those seen in the annulus case, the *total* displacement is used for the 1D model. The total displacement is simply given as,

$$\Delta_{tot}(t) = \sqrt{\big(x(t) - x_0\big)^2 + \big(y(t) - y_0\big)^2 + \big(z(t) - z_0\big)^2}, \tag{8.2.1}$$

where x_0, y_0, and z_0 indicate the initial tracer location. The total displacement can display many different behaviors depending on where the tracer is located. If a tracer is in a chaotic region the changes in the total displacement can be very rapid, with trapping-like behavior suddenly followed by a large flight event. For tracers in vortex tubes, the total displacement could oscillate if the tracer was initiated near the vortex core, or the total displacement could grow linearly if the tracer travels longitudinally through the tube.

The following scaling models are used in order to obtain self-similar displacement pdfs:

$$P(\Delta_{tot}, t) = t^{-\nu} f(\xi), \qquad \xi = \Delta_{tot}/t^{\beta_\pm}, \tag{8.2.2}$$

where f is a scaling function, ξ a scaled coordinate, and ν and $\beta_\pm$ are the decay rate and expansion rates of the tails.

The impact of transport barriers becomes apparent from the pdfs of the total displacements, shown in Fig. 8.2.8 as the multimodal structures seen in the steady and unsteady cases. The various peaks, along with the tails of the pdf having different scales, are signatures of anomalous transport. For the steady and unsteady flows, the left and right tails of the pdf are seen to take values $\beta_- = -.35 \pm .05$ and

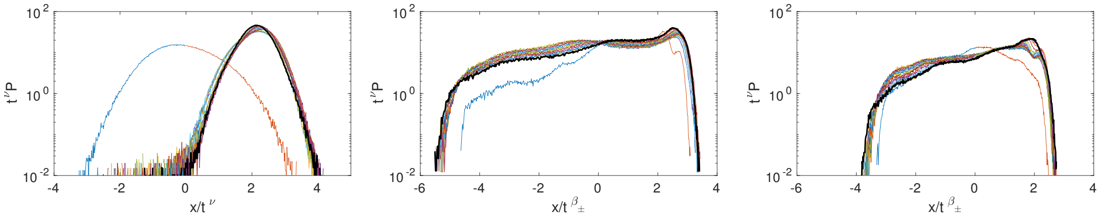

Figure 8.2.8: Pdfs of the total displacements of tracers in the a) integrable, b) steady, and c) unsteady ABC flows for isotropic noise. The black curves indicate the self-similar profile obtained at final time, and the lone curves are for an earlier time.

$\beta_+ = -.55 \pm .05$. The timescale is slightly different between the two flows, with the steady flow having $\nu = .9$ and the unsteady flow $\nu = .7$; implying that the displacement of trajectories is greater in the steady flow. This is understandable since there are long-lasting vortex tubes in which to promote displacement, whereas the chaotic sea of the unsteady flow may cause tracers to rapidly change their direction, inhibiting displacement.

A single well defined Gaussian is obtained in the case of the integrable flow, with scaling parameter $\nu = .5$. The pdfs obtained from the anisotropic noise are seen to use the same parameters.

For the unsteady ABC flow it is less clear what the contributing factors are to the changes seen in the total displacement. Since the coherent structures of this flow can decorrelate over time, tracers initiated in trapping regions can exhibit chaotic trajectories. Further, since coherent structures develop with time, it is also possible that a tracer with a chaotic trajectory can enter into a trapping region and have a smooth (possibly integrable) trajectory. This alternating between trajectory types makes deciphering the statistics more difficult to understand, since it isn't just perturbations that are causing tracers to change their dynamic region. However, with the two stochastic cases, analyzing the impact of anisotropy is possible. It is seen that with the smaller pertrubation in the z direction, the pdf grows more slowly.

For the 2D case, two distinct modeling approaches were used to approximate the elements of the covariance matrix of nonlinear flows; the first was the decomposition approach, where first the fluid element is contorted along its principal axis and then subject to a rotation, and the second was the GLM method. For the 3D case however, only the quasi-3D (Q3D) and decoupled-3D (D3D) versions of the GLM3D method will be used to model the moments.

The analytic expressions for the second-order moments of the IGW model are given in Appendix F. Having these analytic moments the validity of the GLM3D models can be gauged for integrable non-decoupled 3D flows. In order to obtain the parameters of the GLM3D, the Jacobian of the nonlinear flow is computed and the elements of it are manipulated. The Jacobian for the IGW model is given by:

$$J_{t_0}^{t}(\mathbf{x}_0) = \begin{bmatrix} -2\pi U \sin 2\pi\,(x+z-\tau) & 0 & -2\pi U \sin 2\pi\,(x+z-\tau) \\ 2\pi U \cos 2\pi\,(x+z-\tau) & 0 & 2\pi U \cos 2\pi\,(x+z-\tau) \\ 2\pi U \sin 2\pi\,(x+z-\tau) & 0 & 2\pi U \sin 2\pi\,(x+z-\tau) \end{bmatrix}. \tag{8.2.3}$$

Recalling the form of the Jacobian for D3D, given by (7.3.13), it is clear that the parameters obtained from (7.3.17) will be inaccurate, and further that Q3D and D3D are not suited for non-decoupled 3D flows.

The surface mixing flow, which is decoupled, is suited for analysis with D3D. Using the stream-functions, the Jacobian of the decoupled surface mixing model is given by:

$$J_{t_0}^{t}(\mathbf{x}_0) = \begin{bmatrix} \partial_x\partial_y\Psi_{xy} & \partial_y\partial_y\Psi_{xy} & 0 \\ -\partial_x\partial_x\Psi_{xy} & -\partial_y\partial_x\Psi_{xy} + \partial_y\partial_z\Psi_{yz} & \partial_z\partial_z\Psi_{yz} \\ 0 & -\partial_y\partial_y\Psi_{yz} & -\partial_z\partial_y\Psi_{yz} \end{bmatrix}. \tag{8.2.4}$$

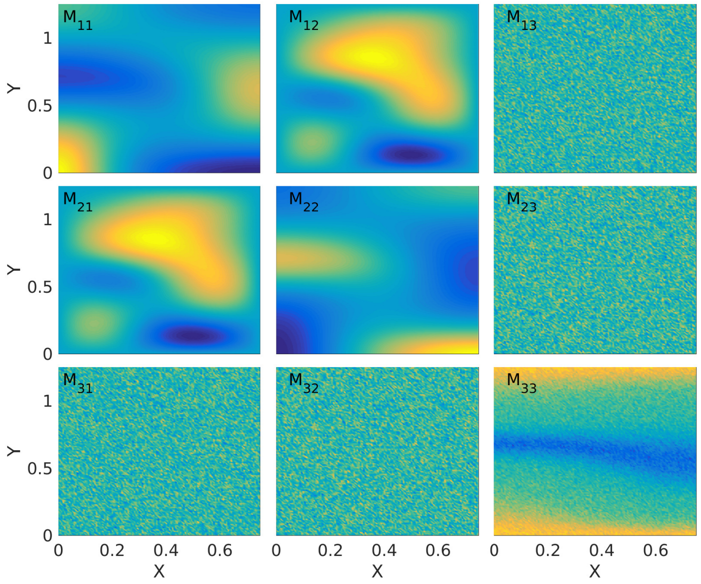

Figure 8.2.9: The second-order moments of the surface mixing model obtained from the RDM with an integration time of $\tau = .05$

Recalling the expression of Ψ_{yz} from (8.1.4) and that the model is concerned with surface mixing, only the $z = 0$ plane is looked at. Further, by looking at this specific z value, it is seen that $\partial_z \partial_z \Psi_{yz} = 0$ and $\partial_z \partial_z \Psi_{yz} = 0$, giving the above Jacobian the same form as the D3D Jacobian.

Results

In order to compare with the moment approximations obtained from Q3D and D3D, the RDM is used to obtain the moments. For each cell of the domain an ensemble of 5 million tracers is used to obtain the moments. It is seen in Fig. 8.2.9 that with such large ensembles of tracers the moments are very smooth, except for the in the bottom row and last column. The M_{13}, M_{23}, M_{31}, and M_{32} elements seem chaotic, however

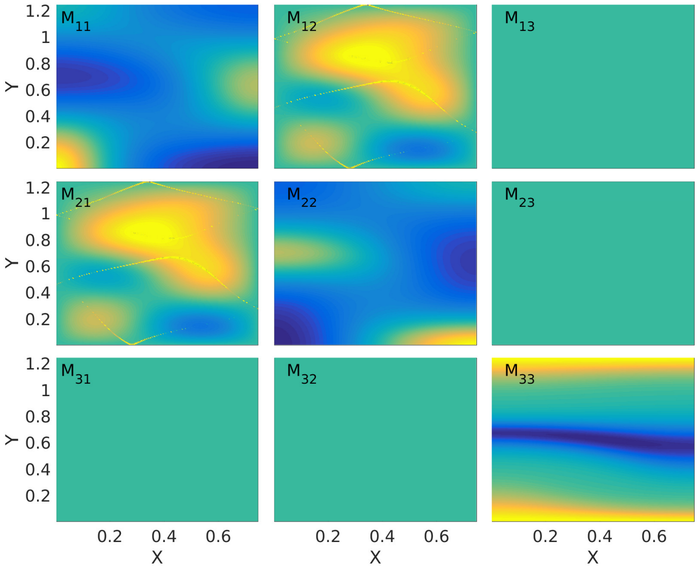

Figure 8.2.10: The second-order moments of the surface mixing model obtained from the D3D with an integration time of $\tau = .05$

since the mean value of these fields are 0, the granularity seen is due to numerical rounding.

As seen in Fig. 8.2.10, the moment approximations obtained from D3D give reasonable qualitative agreement to the actual values. It is also seen that the M_{12} (and M_{21}) elements contain artifacts not seen in the actual moments. These artifacts lie on the boundary of where θ starts to take imaginary values. More accurate moment approximations for this model are obtained from the Q3D formulation; this is seen in Fig. 8.2.11. Since the M_{12} term is computed using α instead of θ the artifacts are not present.

Direct comparisons for the moments of interest are done in Figures 8.2.12 and 8.2.13. These figures show how the approximations vary as the integration time is extended. As the integration time is extended, the moment approximations become less accurate since they are based on a linearization of the nonlinear system. The

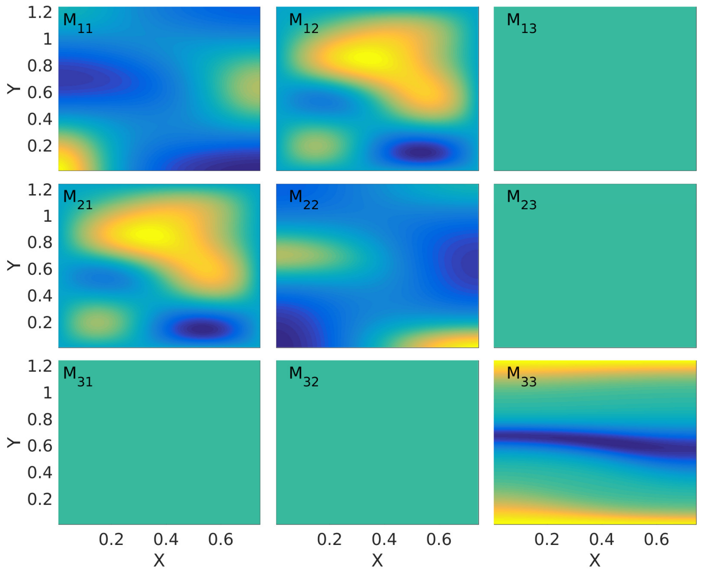

Figure 8.2.11: The second-order moments of the surface mixing model obtained from the Q3D with an integration time of $\tau = .05$

differences between the approximations and the actual moments can already be seen for $\tau = .1$, and is most notable in the M_{12} term. When $\tau = .15$ these differences become even more apparent. With an integration time of $\tau = .2$ the D3D and Q3D methods produce moments that have imaginary components, since this is nonphysical further integration times were not explored.

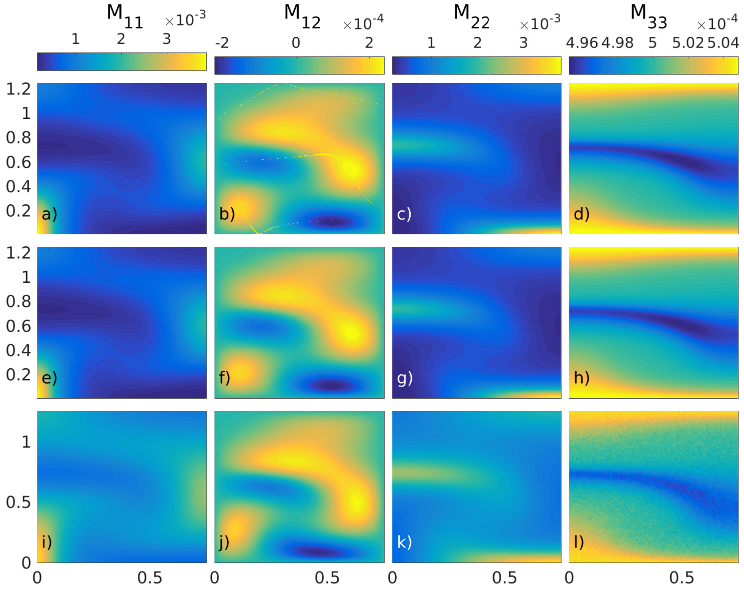

Figure 8.2.12: The second-order moments of the surface mixing model obtained from the (top) D3D, (middle) Q3D, and (bottom) RDM with an integration time of $\tau = .1$

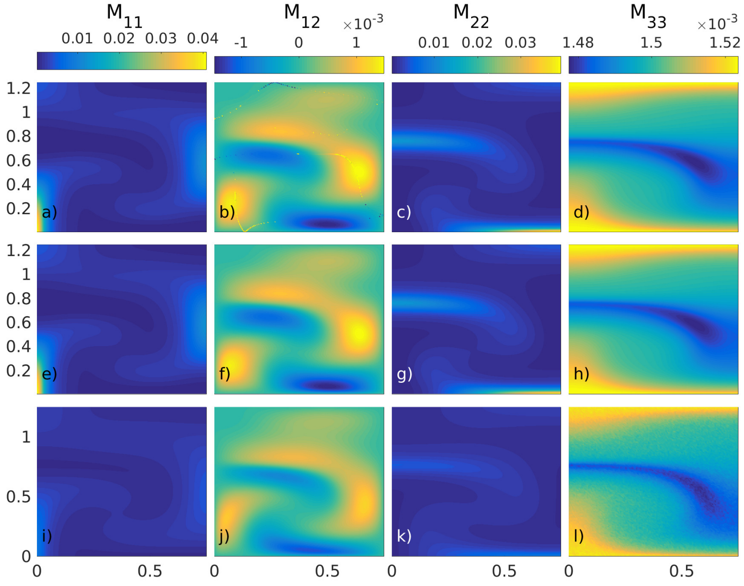

Figure 8.2.13: The second-order moments of the surface mixing model obtained from the (top) D3D, (middle) Q3D, and (bottom) RDM with an integration time of $\tau = .15$

Chapter 9

SUMMARY AND CONCLUSIONS

In order to understand the finite-time, or transient, affects of mixing on scalars, material transport barriers are used. It was observed that Lagrangian coherent structures (LCSs) are the material transport barriers that should be used in nonautonomous systems to distinguish the boundaries of coherent regions. The coherent regions obtained from LCS identification techniques were observed to have unimodal statistics, with different scaling parameters associated with different regions; the implications of which being that the regions are dynamically homogeneous, with possibly different dynamics for each region. It was further seen that for nonturbulent flows Eulerian measures do not correctly distinguish the coherence of regions.

Using the coherent regions extracted using LCS methods, conditional statistics of passive tracers were analyzed. In order to model the advection-diffusion process as a purely diffusive one, the resident-time and dispersion statistics can be used as inputs to a fractional diffusion equation. Here the conditional resident-time and dispersion statistics are obtained for various flow features, and the scales of the statistics are seen to vary by region. The differences of the scales between the varioius regions highlights the anomalous aspect of the diffusion. Previously, the resident-time and dispersion statistics were analyzed using the tracer trajectory information, whereas here trapping and nontrapping behavior is clearly identified using the coherent regions of the flows.

Analytic solutions can be obtained by reframing the advection-diffusion equation as either an effective-diffusion equation or the linear-flow advection-diffusion equation. For both of these equations, the computation of the covariance matrix is needed. Here the elements of the covariance matrix for any nonlinear 2D flow can be estimated using the General Linear Method (GLM). Further, an analytic approximation for the elements of the covariance matrix for nonlinear quasi-3D flows is given. Both of these methods (GLM and GLM3D) rely on the incompressibility of the flows to provide a closure argument when generating the higher order moments.

Geophysical flows can sometimes be viewed as quasi-3D, due to their aspect ratio and the slight influence to the dynamics from the z-direction. For these flows, the proposed GLM3D is capable of accurately approximating the elements of the covariance matrix for finite-time. This provides a means by which to solve for the evolution of a scalar concentration using the linear-flow advection-diffusion equation - a novel modeling approach for geophysical flows. Further, the same covariance approximations can also be used in a conditional effective-diffusion equation to represent the evolution of a scalar based on the type of coherent region the scalar was initiated in.

As natural extensions to this work, future topics of exploration fall into two aspects: using the resident-time and dispersion statistics for modeling, and using the moment approximations for modeling. By utilizing the homogenization of dynamics within coherent regions, the same scaling parameters may be assigned throughout the region. It is noted here that some care would need to be taken on region boundaries to ensure consistent results. Further, the scale parameters of the resident-time and dispersion statistics can be used in higher order fractional diffusion equations, which might reflect the anomalous transport more accurately. In terms of working further with the moment approximations, the GLM3D can be used to approximate the evolution of scalar concentration as well as the decay of scalar variance for geophysical flows. Since GLM3D is a linear flow approximation, the solution to the linear advection-diffusion equation can be used. However, the moment approximations can be directly imployed in an effective-diffusion model.

REFERENCES

Aharon, R., V. Rom-Kedar and H. Gildor, “When complexity leads to simplicity: Ocean surface mixing simplified by vertical convection”, Physics of Fluids **24**, 056603 (2012).

Bahsoun, W., C. Bose and G. Froyland, *Ergodic Theory, Open Dynamics, and Coherent Structures* (Springer, 2014).

Bezdek, J., R. Hathaway, M. Sobin and W. Tucker, “Convergence theory for fuzzy c-means: Counterexamples and repairs”, IEEE Trans. Syst. Man Cybern. **17**, 5, 873–877, URL `http://dl.acm.org/citation.cfm?id=40899.40917` (1987).

Bickley, W., “Lxxiii. the plane jet”, The London, Edinburgh, and Dublin Philosophical Magazine and Journal of Science **23**, 156, 727–731, URL `http://dx.doi.org/10.1080/14786443708561847` (1937).

Budišić, M., S. Siegmund, D. T. Son and I. Mezić, “Mesochronic classification of trajectories in incompressible 3d vector fields over finite times”, arXiv preprint arXiv:1506.05333 (2015).

Cardoso, O., B. Gluckmann, O. Parcollet and P. Tabeling, “Dispersion in a quasi twodimensional turbulent flow: An experimental study”, Physics of Fluids **8**, 1, 209–214, URL `http://scitation.aip.org/content/aip/journal/pof2/8/1/10.1063/1.868828` (1996).

Castaing, B., G. Gunaratne, F. Heslot, L. Kadanoff, A. Libchaber, S. Thomae, X.-Z. Wu, S. Zaleski and G. Zanetti, “Scaling of hard thermal turbulence in rayleigh-bénard convection”, Journal of Fluid Mechanics **204**, 1–30, URL `https://www.cambridge.org/core/article/scaling-of-hard-thermal-turbulence-in-rayleigh-benard-convection/D563428CEF506206916D83DB495AC2D4` (2006).

Chong, M., A. Perry and B. Cantwell, “A general classification of three-dimensional flow fields”, Physics of Fluids A: Fluid Dynamics **2**, 5, 765 (1990).

del Castillo-Negrete, D., “Asymmetric transport and non-gaussian statistics of passive scalars in vortices in shear”, Physics of Fluids (1997).

del Castillo-Negrete, D., B. A. Carreras and V. E. Lynch, “Fractional diffusion in plasma turbulence”, Physics of Plasmas (2004).

del Castillo-Negrete, D. and P. Morrison, “Chaotic transport by rossby waves in shear flow”, Physics of Fluids A: Fluid Dynamics (1989-1993) **5**, 4, 948–965 (1993).

Douglass, A. R., P. A. Newman and S. Solomon, “The antarctic ozone hole: An update”, Physics today **67**, 7, 42–48 (2014).

Elhmaidi, D., A. Provenzale and A. Babiano, “Elementary topology of two-dimensional turbulence from a lagrangian viewpoint and single-particle dispersion”, Journal of Fluid Mechanics **257**, 533–558 (1993).

Farazmand, M. and G. Haller, “Computing lagrangian coherent structures from their variational theory”, Chaos: An Interdisciplinary Journal of Nonlinear Science **22**, 1, 013128 (2012).

Farazmand, M. and G. Haller, “Polar rotation angle identifies elliptic islands in unsteady dynamical systems”, Physica D: Nonlinear Phenomena **315**, 1 – 12, URL `http://www.sciencedirect.com/science/article/pii/S01672789150017` (2016).

Froyland, G., “Statistically optimal almost-invariant sets”, Physica D: Nonlinear Phenomena **200**, 3, 205–219 (2005).

Froyland, G. and M. Dellnitz, “Detecting and locating near-optimal almost-invariant sets and cycles”, SIAM Journal on Scientific Computing **24**, 6, 1839–1863 (2003).

Froyland, G. and K. Padberg-Gehle, “Finite-time entropy: A probabilistic approach for measuring nonlinear stretching”, Physica D: Nonlinear Phenomena **241**, 19, 1612–1628 (2012).

Froyland, G., N. Santitissadeekorn and A. Monahan, “Transport in time-dependent dynamical systems: Finite-time coherent sets”, Chaos **20**, 043116 (2010).

Gollub, J. P., J. Clarke, M. Gharib, B. Lane and O. N. Mesquita, “Fluctuations and transport in a stirred fluid with a mean gradient”, Phys. Rev. Lett. **67**, 3507–3510, URL `http://link.aps.org/doi/10.1103/PhysRevLett.67.3507` (1991).

Haller, G., “A variational theory of hyperbolic lagrangian coherent structures”, Physica D: Nonlinear Phenomena **240**, 7, 574–598 (2011).

Haller, G., “Dynamic rotation and stretch tensors from a dynamic polar decomposition”, Journal of the Mechanics and Physics of Solids **86**, 70 – 93, URL `http://www.sciencedirect.com/science/article/pii/S0022509615301988` (2016).

Haller, G., A. Hadjighasem, M. Farazmand and F. Huhn, “Defining coherent vortices objectively from the vorticity”, Journal of Fluid Mechanics **795**, 136–173, URL `http://journals.cambridge.org/article/pii/S0022112016001518` (2016).

Jones, K., P. Walker and W. Tang, “The domain dependence of chemotaxis in two-dimensional turbulence”, Physical Review E (2018).

Kadoch, B., D. del Castillo-Negrete, W. Bos and K. Schneider, “Lagrangian statistics and flow topology in forced two-dimensional turbulence”, Physical Review E **83**, 3, 036314 (2011).

Lekien, F. and S. D. Ross, “The computation of finite-time lyapunov exponents on unstructured meshes and for non-euclidean manifolds”, Chaos: An Interdisciplinary Journal of Nonlinear Science **20**, 1, 017505, URL `https://doi.org/10.1063/1.3278516` (2010).

Lin, Z., K. Bodová and C. R. Doering, “Models and measures of mixing and effective diffusion”, arXiv preprint arXiv:1011.1320 (2010).

Ma, T. and E. M. Bollt, “Relatively coherent sets as a hierarchical partition method”, International Journal of Bifurcation and Chaos **23**, 07, 1330026 (2013).

McLaughlin, R. M. and A. J. Majda, “An explicit example with nongaussian probability distribution for nontrivial scalar mean and fluctuation”, Physics of Fluids **8**, 2, 536–547, URL `http://scitation.aip.org/content/aip/journal/pof2/8/2/10.1063/1.868806;jsessionid=4Nf-ODOXB2x69vPnyBgWOFTv.x-aip-live-03` (1996).

Mezić, I., S. Loire, V. A. Fonoberov and P. Hogan, “A new mixing diagnostic and gulf oil spill movement”, Science **330**, 6003, 486–489 (2010).

Ottino, J., *The Kinematics of Mixing: Stretching, Chaos, and Transport*, Cambridge Texts in Applied Mathematics (Cambridge University Press, 1989), URL `https://books.google.com/books?id=8OLVcbRoNSgC`.

Peacock, T. and G. Haller, “Lagrangian coherent structures: The hidden skeleton of fluid flows”, Physics today **66**, 2, 41 (2013).

Pumir, A., B. I. Shraiman and E. D. Siggia, “Exponential tails and random advection”, Phys. Rev. Lett. **66**, 2984–2987, URL `http://link.aps.org/doi/10.1103/PhysRevLett.66.2984` (1991).

Shadden, S. C., F. Lekien and J. E. Marsden, “Definition and properties of lagrangian coherent structures from finite-time lyapunov exponents in two-dimensional aperiodic flows”, Physica D (2005).

Solomon, T. H., E. R. Weeks and H. L. Swinney, “Observation of anomalous diffusion and lévy flights in a two-dimensional rotating flow”, Phys. Rev. Lett. **71**, 3975–3978, URL `http://link.aps.org/doi/10.1103/PhysRevLett.71.3975` (1993).

Solomon, T. H., E. R. Weeks and H. L. Swinney, “Chaotic advection in a two-dimensional flow: Lévy flights and anomalous diffusion”, Physica D **76**, 70–84 (1994).

Tang, W., B. Knutson, A. Mahalov and R. Dimitrova, “The geometry of inertial particle mixing in urban flows, from deterministic and random displacement models”, Physics of Fluids **24**, 6, URL `http://scitation.aip.org/content/aip/journal/pof2/24/6/10.1063/1.4729453` (2012).

Tang, W., J. E. Taylor and A. Mahalov, “Lagrangian dynamics in stochastic inertia-gravity waves”, Physics of Fluids (2010).

Tang, W. and P. Walker, “Finite-time statistics of scalar diffusion in lagrangian coherent structures”, Physical Review **E**, 045201 (2012).

Taylor, G. I., “Diffusion by continuous movements”, PT URL `http://archipelago.uma.pt/pdf_library/Taylor_1920_PT.pdf` (1920).

Thiffeault, J.-L., *Scalar Decay in Chaotic Mixing*, vol. 744 of *Lecture Notes in Physics, Berlin Springer Verlag* (2008).

Townsend, A. A., “The diffusion of heat spots in isotropic turbulence”, Proc. Roy. Soc. (1951).

Van Kampen, N. G., *Stochastic processes in physics and chemistry*, vol. 1 (Elsevier, 1992).

Walker, P. and W. Tang, “Obtaining second order moments from first order approximations”, Physical Review E (2018).

Walker, P., W. Tang and D. del Castillo-Negre, “The lagrangian statistics of passive scalar transport dependent on coherent structure identifications”, Physical Review E (2018).

Yakhot, V., S. A. Orszag, S. Balachandar, E. Jackson, Z.-S. She and L. Sirovich, “Phenomenological theory of probability distributions in turbulence”, Journal of Scientific Computing **5**, 3, 199–221, URL `http://dx.doi.org/10.1007/BF01089164` (1990).

Zeldovich, Y., A. Ruzmaikin, S. Molchanov and D. Sokoloff, “Kinematic dynamo problem in a linear veloctu field”, Journal of Fluid Mechanics pp. 1–11 (1984).

APPENDIX A

INFINITESIMAL GENERATORS AND USE FOR SECOND-ORDER MOMENTS

In this appendix infinitesimal generators are introduced and used to compute the principal covariance matrix given by (6.1.6). Given a function $Z\left(X,Y,t\right)$, that is continuous in its arguments, the expectation of $w(t) = \mathbb{E}\big[Z\left(X,Y,t\right)\big]$ solves the following integral equation:

$$w(t) = w(t_0) + \int_{t_0}^{t} \mathbb{E}\left(A[Z(s)]\right) ds, \tag{A.1.1}$$

where $A[Z] = \partial_t Z + u\partial_x Z + v\partial_y Z + \kappa\left(\partial_x^2 Z + \partial_y^2 Z\right)$ is the infinitesimal generator of the diffusion process that solves (2.1.2).

For the decoupled linear system (6.1.5), the generators for the second-order moments are given as:

$$\begin{aligned} A[X^2] &= 2\lambda X^2 + 2\kappa \\ A[XY] &= 0 \\ A[Y^2] &= -2\lambda Y^2 + 2\kappa \end{aligned} \quad . \tag{A.1.2}$$

The above system gives 3 simple linear ODEs to solve, with initial conditions defined as: $\mathbb{E}[X^2](t_0) = \mathbb{E}[X_0^2]$, $\mathbb{E}[XY](t_0) = \mathbb{E}[XY_0]$, and $\mathbb{E}[Y^2](t_0) = \mathbb{E}[Y_0^2]$. Solving these ODEs gives the elements of the covariance matrix as follows.

$$\begin{aligned} \mathbb{E}[X^2] &= \frac{\kappa}{\lambda}\left(e^{2\lambda\tau} - 1\right) + \mathbb{E}[X_0^2]e^{2\lambda\tau} \\ \mathbb{E}[XY] &= \mathbb{E}[XY_0] \\ \mathbb{E}[Y^2] &= \frac{\kappa}{\lambda}\left(1 - e^{-2\lambda\tau}\right) + \mathbb{E}[Y_0^2]e^{-2\lambda\tau} \end{aligned} \quad . \tag{A.1.3}$$

Since the initial distribution is assumed to be a delta function $\mathbb{E}[X_0^2] = 0$, $\mathbb{E}[XY_0] = 0$, $\mathbb{E}[Y_0^2] = 0$, and the expression in (6.1.6) is obtained.

APPENDIX B

MOMENTS FOR THE GENERAL LINEAR MODEL (GLM)

In this appendix it will be shown how to obtain the analytic expression of the moments for the general linear model given by (6.1.15). The generators for the first-order moments are given by:

$$\begin{aligned} A[X] &= \lambda X + \beta Y \\ A[Y] &= \gamma X - \lambda Y \end{aligned} \tag{B.1.1}$$

This reduces to a simple system of equations

$$\begin{aligned} \dot{\mathbb{E}[X]} &= \lambda \mathbb{E}[X] + \beta \mathbb{E}[Y] \\ \dot{\mathbb{E}[Y]} &= \gamma \mathbb{E}[X] - \lambda \mathbb{E}[Y] \end{aligned}, \tag{B.1.2}$$

with solutions given by,

$$\dot{x} = e^{\sigma t} x_0. \tag{B.1.3}$$

The matrix exponential can be obtained from the eigenvalues and eigenvectors of σt. Denoting D as the matrix of eigenvalues along the diagonal and V as the matrix of eigenvectors, for the given system these result in:

$$D = \begin{bmatrix} -\alpha t & 0 \\ 0 & \alpha t \end{bmatrix} \quad V = \begin{bmatrix} (\lambda - \alpha)/\gamma & (\lambda + \alpha)/\gamma \\ 1 & 1 \end{bmatrix}, \tag{B.1.4}$$

where $\alpha := \sqrt{\lambda^2 + \beta\gamma}$. The first-order moments are then obtained via $J := e^{\sigma t}$, where J is the Jacobian and $e^{\sigma t} = V \exp D V^{-1}$.

$$\begin{aligned} J &= \begin{bmatrix} (\lambda - \alpha)/\gamma & (\lambda + \alpha)/\gamma \\ 1 & 1 \end{bmatrix} \begin{bmatrix} e^{-\alpha t} & 0 \\ 0 & e^{\alpha t} \end{bmatrix} \left(\begin{bmatrix} (\lambda - \alpha)/\gamma & (\lambda + \alpha)/\gamma \\ 1 & 1 \end{bmatrix} \right)^{-1} \\ &= \frac{-\gamma}{2\alpha} \begin{bmatrix} (\lambda - \alpha) e^{-\alpha t}/\gamma & (\lambda + \alpha) e^{\alpha t}/\gamma \\ e^{-\alpha t} & e^{\alpha t} \end{bmatrix} \begin{bmatrix} 1 & -(\lambda + \alpha)/\gamma \\ -1 & (\lambda - \alpha)/\gamma \end{bmatrix} \\ &= \frac{-1}{2\alpha} \begin{bmatrix} \lambda \left(e^{-\alpha t} - e^{\alpha t} \right) - \alpha \left(e^{-\alpha t} + e^{\alpha t} \right) & \beta \left(e^{-\alpha t} - e^{\alpha t} \right) \\ \gamma \left(e^{-\alpha t} - e^{\alpha t} \right) & -\lambda \left(e^{-\alpha t} - e^{\alpha t} \right) - \alpha \left(e^{-\alpha t} + e^{\alpha t} \right) \end{bmatrix} \\ &= \begin{bmatrix} \left(\cosh(\alpha\tau) + \frac{\lambda}{\alpha} \sinh(\alpha\tau) \right) & \frac{\beta}{\alpha} \sinh(\alpha\tau) \\ \frac{\gamma}{\alpha} \sinh(\alpha\tau) & \left(\cosh(\alpha\tau) - \frac{\lambda}{\alpha} \sinh(\alpha\tau) \right) \end{bmatrix}. \end{aligned} \tag{B.1.5}$$

The first-order moments are then given as:

$$\begin{aligned} \mathbb{E}[X](t) &= \mathbb{E}[X_0] \left(\cosh(\alpha\tau) + \frac{\lambda}{\alpha} \sinh(\alpha\tau) \right) + \mathbb{E}[Y_0] \frac{\beta}{\alpha} \sinh(\alpha\tau) \\ \mathbb{E}[Y](t) &= \mathbb{E}[Y_0] \left(\cosh(\alpha\tau) - \frac{\lambda}{\alpha} \sinh(\alpha\tau) \right) + \mathbb{E}[X_0] \frac{\gamma}{\alpha} \sinh(\alpha\tau) \end{aligned}. \tag{B.1.6}$$

These solutions give an analytic connection to the deformation tensor, via (6.1.17).

The generators for the second-order moments are given as:

$$\begin{aligned} A[X^2] &= 2\lambda X^2 + 2\beta XY + 2\kappa \\ A[XY] &= \gamma X^2 + \beta Y^2 \qquad\qquad , \\ A[Y^2] &= 2\gamma XY - 2\lambda Y^2 + 2\kappa \end{aligned} \tag{B.1.7}$$

From the above it is seen that the integral equations for second-order moments would give:

$$\begin{aligned} \mathbb{E}[\dot{X}^2] &= 2\lambda \mathbb{E}[X^2] + 2\beta \mathbb{E}[XY] + 2\kappa \\ \mathbb{E}[\dot{X}Y] &= \gamma \mathbb{E}[X^2] + \beta \mathbb{E}[Y^2] \\ \mathbb{E}[\dot{Y}^2] &= 2\gamma \mathbb{E}[XY] - 2\lambda \mathbb{E}[Y^2] + 2\kappa \end{aligned} \tag{B.1.8}$$

By taking the derivative w.r.t. time once again for the top and bottom rows of the above, and subtituting the middle row where appropriate the following two equations are obtained:

$$\begin{aligned} \mathbb{E}[\ddot{X}^2] &= 2\lambda \mathbb{E}[\dot{X}^2] + 2\beta \left(\gamma \mathbb{E}[X^2] + \beta \mathbb{E}[Y^2]\right) \\ \mathbb{E}[\ddot{Y}^2] &= 2\gamma \left(\gamma \mathbb{E}[X^2] + \beta \mathbb{E}[Y^2]\right) - 2\lambda \mathbb{E}[\dot{Y}^2] \end{aligned} \tag{B.1.9}$$

Letting $x_1 = \mathbb{E}[X^2]$, $x_2 = \mathbb{E}[\dot{X}^2]$, $x_3 = \mathbb{E}[Y^2]$, and $x_4 = \mathbb{E}[\dot{Y}^2]$, the above system is rewritten as:

$$\dot{\vec{x}} = \dot{\begin{bmatrix} x_1 \\ x_2 \\ x_3 \\ x_4 \end{bmatrix}} = \begin{bmatrix} 0 & 1 & 0 & 0 \\ 2\beta\gamma & 2\lambda & 2\beta^2 & 0 \\ 0 & 0 & 0 & 1 \\ 2\gamma^2 & 0 & 2\beta\gamma & -2\lambda \end{bmatrix} \begin{bmatrix} x_1 \\ x_2 \\ x_3 \\ x_4 \end{bmatrix}. \tag{B.1.10}$$

When this system is written more compactly as $\dot{\vec{x}} = B\vec{x}$, the solution is immediate as $\vec{x}(t) = e^{B(t-t_0)}\vec{x}(t_0)$. The solutions for the variances and their rates of change are found by using an initial condition of:

$$\vec{x}(t_0) = \begin{bmatrix} \mathbb{E}[X_0^2] \\ 2\lambda \mathbb{E}[X_0^2] + 2\beta \mathbb{E}[XY_0] + 2\kappa \\ \mathbb{E}[Y_0^2] \\ 2\gamma \mathbb{E}[XY_0] - 2\lambda \mathbb{E}[Y_0^2] + 2\kappa \end{bmatrix}. \tag{B.1.11}$$

Letting the initial conditions be represented by E_{x^2} for the x-variance, E_{xy} for the cross-variance term, and E_{y^2} for the y-variance, the solutions are given by the following:

$$\begin{aligned}
\mathbb{E}[X^2] &= \frac{\sinh 2\tau\alpha}{2\alpha^3}\left(\left(E_{xy}\beta + E_{x^2}\lambda\right)\left(\lambda^2+\alpha^2+\beta\gamma\right) + \kappa\left(\lambda^2+\alpha^2+\beta^2\right)\right) \\
&\quad + \frac{\cosh 2\tau\alpha}{\alpha^2}\left(E_{x^2}\left(\lambda^2+\frac{\beta\gamma}{2}\right) + E_{y^2}\frac{\beta^2}{2} + \lambda\beta E_{xy} + \kappa\lambda\right) \\
&\quad + \frac{1}{\alpha^2}\left(E_{x^2}\frac{\beta\gamma}{2} - E_{y^2}\frac{\beta^2}{2} - E_{xy}\beta\lambda + \kappa\left(\beta\tau\left(\gamma-\beta\right)-\lambda\right)\right), \\
\mathbb{E}[Y^2] &= \frac{\sinh 2\tau\alpha}{2\alpha^3}\left(\left(E_{xy}\gamma - E_{y^2}\lambda\right)\left(\lambda^2+\alpha^2+\beta\gamma\right) + \kappa\left(\lambda^2+\alpha^2+\gamma^2\right)\right) \\
&\quad + \frac{\cosh 2\tau\alpha}{\alpha^2}\left(E_{y^2}\left(\lambda^2+\frac{\beta\gamma}{2}\right) + E_{x^2}\frac{\gamma^2}{2} - \lambda\gamma E_{xy} - \kappa\lambda\right) \\
&\quad + \frac{1}{\alpha^2}\left(-E_{x^2}\frac{\gamma^2}{2} + E_{y^2}\frac{\beta\gamma}{2} + E_{xy}\gamma\lambda + \kappa\left(\gamma\tau\left(\beta-\gamma\right)+\lambda\right)\right).
\end{aligned} \tag{B.1.12}$$

The equations for $\mathbb{E}[X^2]$ and $\mathbb{E}[Y^2]$ can now be used in the middle row of (B.1.8) to solve for $\mathbb{E}[XY]$, giving:

$$\begin{aligned}
\mathbb{E}[XY] &= \frac{\sinh 2\tau\alpha}{2\alpha^3}\left(E_{x^2}\gamma\alpha^2 + E_{y^2}\beta\alpha^2 + \lambda\kappa(\gamma-\beta)\right) \\
&\quad + \frac{\cosh\left(2\tau\alpha\right)-1}{2\alpha^2}\left(E_{x^2}\lambda\gamma - E_{y^2}\beta\lambda + 2E_{xy}\beta\gamma + \kappa(\gamma+\beta)\right) \\
&\quad + \frac{\kappa\lambda(\beta-\gamma)\tau}{\alpha^2} + E_{xy}.
\end{aligned} \tag{B.1.13}$$

Since the initial distribution is assumed to be a delta function $E_{x^2} = 0$, $E_{xy} = 0$, and $E_{y^2} = 0$; and (6.1.16) is recovered. Further, it is seen that when $\beta = 0$ and $\gamma = 0$, the above moments converge to those obtained in Appendix A.

APPENDIX C

MOMENTS FOR THE BARELY-3D AND QUASI-3D FLOWS

In this appendix it will be shown how to obtain the analytic expression of the moments for the barely-3D and quasi-3D flows, given by (7.3.1) and (7.3.7), respectively.

Barely-3D Flow Moments

First-order Moments

The generators for the first-order moments are given by:

$$\begin{aligned} A[X] &= \lambda X + \beta Y \\ A[Y] &= \gamma X - \lambda Y \\ A[Z] &= 0, \end{aligned} \tag{C.1.1}$$

where it is apparent that the first-order moments are unchanged from the 2D flow; this and the simple relation for the z-moment make it simple to obtain the moments. Following the same analysis presented in Appendix B, the first-order moments are then given as:

$$\begin{aligned} \mathbb{E}[X](t) &= \mathbb{E}[X_0]\left(\cosh(\alpha\tau) + \frac{\lambda}{\alpha}\sinh(\alpha\tau)\right) + \mathbb{E}[Y_0]\frac{\beta}{\alpha}\sinh(\alpha\tau) \\ \mathbb{E}[Y](t) &= \mathbb{E}[Y_0]\left(\cosh(\alpha\tau) - \frac{\lambda}{\alpha}\sinh(\alpha\tau)\right) + \mathbb{E}[X_0]\frac{\gamma}{\alpha}\sinh(\alpha\tau) \\ \mathbb{E}[Z](t) &= \mathbb{E}[Z_0], \end{aligned} \tag{C.1.2}$$

where $\alpha = \sqrt{\lambda^2 + \beta\gamma}$.

Second-Order Moments

The generators for the second-order moments are given as:

$$\begin{aligned} A[X^2] &= 2\lambda X^2 + 2\beta XY + 2\kappa \\ A[XY] &= \gamma X^2 + \beta Y^2 \\ A[Y^2] &= 2\gamma XY - 2\lambda Y^2 + 2\kappa \\ A[XZ] &= \lambda XZ + \beta YZ \\ A[YZ] &= \gamma XZ - \lambda YZ \\ A[Z^2] &= 2\kappa. \end{aligned} \tag{C.1.3}$$

The integral equations for the second-order moments can then be written as 3 systems:

$$
\begin{aligned}
\mathbb{E}[\dot{X^2}] &= 2\lambda\mathbb{E}[X^2] + 2\beta\mathbb{E}[XY] + 2\kappa \\
\mathbb{E}[\dot{XY}] &= \gamma\mathbb{E}[X^2] + \beta\mathbb{E}[Y^2] \\
\mathbb{E}[\dot{Y^2}] &= 2\gamma\mathbb{E}[XY] - 2\lambda\mathbb{E}[Y^2] + 2\kappa \\
\\
\mathbb{E}[\dot{XZ}] &= \lambda\mathbb{E}[XZ] + \beta\mathbb{E}[YZ] \\
\mathbb{E}[\dot{YZ}] &= \gamma\mathbb{E}[XZ] - \lambda\mathbb{E}[YZ] \\
\\
\mathbb{E}[\dot{Z^2}] &= 2\kappa
\end{aligned}
\tag{C.1.4}
$$

From previous analysis in the 2D case (Appendix B), the solutions to (C.1.4) are immediately known. Letting the initial conditions be represented by E_{x^2} for the x-variance, E_{xy} for the XY cross-variance term, E_{y^2} for the y-variance, etc.; the solutions are given by the following:

$$
\begin{aligned}
\mathbb{E}[X^2] &= \frac{\sinh 2\tau\alpha}{2\alpha^3}\left(\left(E_{xy}\beta + E_{x^2}\lambda\right)\left(\lambda^2 + \alpha^2 + \beta\gamma\right) + \kappa\left(\lambda^2 + \alpha^2 + \beta^2\right)\right) \\
&\quad + \frac{\cosh 2\tau\alpha}{\alpha^2}\left(E_{x^2}\left(\lambda^2 + \frac{\beta\gamma}{2}\right) + E_{y^2}\frac{\beta^2}{2} + \lambda\beta E_{xy} + \kappa\lambda\right) \\
&\quad + \frac{1}{\alpha^2}\left(E_{x^2}\frac{\beta\gamma}{2} - E_{y^2}\frac{\beta^2}{2} - E_{xy}\beta\lambda + \kappa\left(\beta\tau\left(\gamma - \beta\right) - \lambda\right)\right), \\
\mathbb{E}[Y^2] &= \frac{\sinh 2\tau\alpha}{2\alpha^3}\left(\left(E_{xy}\gamma - E_{y^2}\lambda\right)\left(\lambda^2 + \alpha^2 + \beta\gamma\right) + \kappa\left(\lambda^2 + \alpha^2 + \gamma^2\right)\right) \\
&\quad + \frac{\cosh 2\tau\alpha}{\alpha^2}\left(E_{y^2}\left(\lambda^2 + \frac{\beta\gamma}{2}\right) + E_{x^2}\frac{\gamma^2}{2} - \lambda\gamma E_{xy} - \kappa\lambda\right) \\
&\quad + \frac{1}{\alpha^2}\left(-E_{x^2}\frac{\gamma^2}{2} + E_{y^2}\frac{\beta\gamma}{2} + E_{xy}\gamma\lambda + \kappa\left(\gamma\tau\left(\beta - \gamma\right) + \lambda\right)\right) \\
\mathbb{E}[XY] &= \frac{\sinh 2\tau\alpha}{2\alpha^3}\left(E_{x^2}\gamma\alpha^2 + E_{y^2}\beta\alpha^2 + E_{xy}\lambda\beta(\gamma - \beta) + \lambda\kappa(\gamma - \beta)\right) \\
&\quad + \frac{\cosh\left(2\tau\alpha\right) - 1}{2\alpha^2}\left(E_{x^2}\lambda\gamma - E_{y^2}\beta\lambda + 2E_{xy}\beta\gamma + \kappa(\gamma + \beta)\right) \\
&\quad + \frac{\kappa\lambda(\beta - \gamma)\tau}{\alpha^2} + E_{xy}
\end{aligned}
\tag{C.1.5}
$$

$$
\begin{aligned}
\mathbb{E}[XZ] &= E_{xz}\left(\cosh(\alpha\tau) + \frac{\lambda}{\alpha}\sinh(\alpha\tau)\right) + E_{yz}\frac{\beta}{\alpha}\sinh(\alpha\tau) \\
\mathbb{E}[YZ] &= E_{yz}\left(\cosh(\alpha\tau) - \frac{\lambda}{\alpha}\sinh(\alpha\tau)\right) + E_{xz}\frac{\gamma}{\alpha}\sinh(\alpha\tau) \\
\mathbb{E}[Z^2] &= E_{z^2} + 2\kappa\tau.
\end{aligned} \tag{C.1.6}
$$

Quasi-3D Flow Moments

First-order Moments

The generators for the first-order moments are given by:

$$
\begin{aligned}
A[X] &= \lambda X + \beta Y \\
A[Y] &= \gamma X - \lambda Y \\
A[Z] &= \eta Z,
\end{aligned} \tag{C.2.1}
$$

where $\eta \ll 1$. Note that as $\eta \to 0$, (C.2.1) converges to (C.1.1). The first-order moments are obtained as 2 decoupled systems:

$$
\begin{aligned}
\dot{\mathbb{E}[X]} &= \lambda\mathbb{E}[X] + \beta\mathbb{E}[Y] \\
\dot{\mathbb{E}[Y]} &= \gamma\mathbb{E}[X] - \lambda\mathbb{E}[Y] \\
\dot{\mathbb{E}[Z]} &= \eta\mathbb{E}[Z].
\end{aligned} \tag{C.2.2}
$$

The solution to the x and y terms of (C.2.2) are the same as those of the 2D subsystem defined by $\sigma_{t_0}^t(\mathbf{x}_0) = \begin{bmatrix} \lambda & \beta \\ \gamma & -\lambda \end{bmatrix}$. The first-order moments are given as:

$$
\begin{aligned}
\mathbb{E}[X](t) &= \mathbb{E}[X_0]\left(\cosh(\alpha\tau) + \frac{\lambda}{\alpha}\sinh(\alpha\tau)\right) + \mathbb{E}[Y_0]\frac{\beta}{\alpha}\sinh(\alpha\tau) \\
\mathbb{E}[Y](t) &= \mathbb{E}[Y_0]\left(\cosh(\alpha\tau) - \frac{\lambda}{\alpha}\sinh(\alpha\tau)\right) + \mathbb{E}[X_0]\frac{\gamma}{\alpha}\sinh(\alpha\tau) \\
\mathbb{E}[Z](t) &= \mathbb{E}[Z_0]e^{\eta\tau},
\end{aligned} \tag{C.2.3}
$$

where $\alpha = \sqrt{\lambda^2 + \beta\gamma}$.

Second-Order Moments

The generators for the second-order moments are given as:

$$
\begin{aligned}
A[X^2] &= 2\lambda X^2 + 2\beta XY + 2\kappa \\
A[XY] &= \gamma X^2 + \beta Y^2 \\
A[Y^2] &= 2\gamma XY - 2\lambda Y^2 + 2\kappa \\
A[XZ] &= (\eta + \lambda)\, XZ + \beta YZ \\
A[YZ] &= \gamma XZ + (\eta - \lambda)\, YZ \\
A[Z^2] &= 2\eta Z^2 + 2\kappa.
\end{aligned} \tag{C.2.4}
$$

Again the integral equations for second-order moments result in 3 systems. These systems are given by:

$$\begin{aligned}
\mathbb{E}[\dot{X^2}] &= 2\lambda\mathbb{E}[X^2] + 2\beta\mathbb{E}[XY] + 2\kappa \\
\mathbb{E}[\dot{XY}] &= \gamma\mathbb{E}[X^2] + \beta\mathbb{E}[Y^2] \\
\mathbb{E}[\dot{Y^2}] &= 2\gamma\mathbb{E}[XY] - 2\lambda\mathbb{E}[Y^2] + 2\kappa \\
\\
\mathbb{E}[\dot{XZ}] &= (\eta+\lambda)\,\mathbb{E}[XZ] + \beta\mathbb{E}[YZ] \\
\mathbb{E}[\dot{YZ}] &= \gamma\mathbb{E}[XZ] + (\eta-\lambda)\,\mathbb{E}[YZ] \\
\\
\mathbb{E}[\dot{Z^2}] &= 2\eta\mathbb{E}[Z^2] + 2\kappa
\end{aligned} \tag{C.2.5}$$

The first set of equations in (C.2.5) are seen to be the same as the 2D case, and their solutions are given by (B.1.7). The second group of equations in (C.2.5) is solved by virtue of the Cayley-Hamilton theorem (seen in Appendix E), while the solution to the last equation is computed directly. The roots of the characteristic polynomial for the system using the Cayley-Hamilton theorem are obtained as $\sigma_{1,2} = \eta \pm \alpha$, where $\alpha := \sqrt{\lambda^2 + \beta\gamma}$. The matrix exponential takes the following form,

$$e^{tA} = s_0(t)\mathbf{I} + s_1(t)A, \tag{C.2.6}$$

where $s_0(t)$ and $s_1(t)$ are defined as,

$$\begin{aligned}
s_0(t) &= \frac{\sigma_1 e^{\sigma_2 t} - \sigma_2 e^{\sigma_1 t}}{\sigma_1 - \sigma_2} \\
s_1(t) &= \frac{e^{\sigma_1 t} - e^{\sigma_2 t}}{\sigma_1 - \sigma_2}.
\end{aligned} \tag{C.2.7}$$

For the $XZ - YZ$ system, the above result in,

$$\begin{aligned}
s_0(t) &= e^{\eta t}\left(\cosh\alpha t - \frac{\eta}{\alpha}\sinh\alpha t\right) \\
s_1(t) &= \frac{e^{\eta t}}{\alpha}\sinh\alpha t
\end{aligned} \tag{C.2.8}$$

Letting the initial conditions be represented by E_{x^2} for the x-variance, E_{xy} for the XY cross-variance term, E_{y^2} for the y-variance, etc., the solutions are given by the following:

$$\begin{aligned}
\mathbb{E}[XZ] &= E_{xz}e^{\eta t}\left(\cosh(\alpha\tau) + \frac{\lambda}{\alpha}\sinh(\alpha\tau)\right) + E_{yz}e^{\eta t}\frac{\beta}{\alpha}\sinh(\alpha\tau) \\
\mathbb{E}[YZ] &= E_{yz}e^{\eta t}\left(\cosh(\alpha\tau) - \frac{\lambda}{\alpha}\sinh(\alpha\tau)\right) + E_{xz}e^{\eta t}\frac{\gamma}{\alpha}\sinh(\alpha\tau)
\end{aligned} \tag{C.2.9}$$

And the solution for $\mathbb{E}[Z^2]$ is given as:

$$\mathbb{E}[Z^2] = E_{z^2}e^{2\eta\tau} + \frac{\kappa}{\eta}\left(e^{2\eta\tau} - 1\right). \tag{C.2.10}$$

APPENDIX D

MOMENTS FOR THE DECOUPLED-3D FLOW

In this appendix it will be shown how to obtain the analytic expression of the moments for the decoupled-3D flow given by (7.3.12).

First-Order Moments

The generators for the first-order moments are given by:

$$\begin{aligned} A[X] &= \lambda X + \beta Y \\ A[Y] &= \gamma X - (\lambda + \eta) Y \\ A[Z] &= \eta Z. \end{aligned} \tag{D.1.1}$$

Using the same approach as in Appendix E, the first-order moments can be obtained for the x and y terms. The functions $s_k(t)$, from (C.2.7), take the following values:

$$\begin{aligned} s_0(t) &= e^{\frac{-\eta t}{2}} \left(\cosh \theta t/2 + \frac{\eta}{\theta} \sinh \theta t/2 \right) \\ s_1(t) &= \frac{2e^{\frac{-\eta t}{2}}}{\theta} \sinh \theta t/2. \end{aligned} \tag{D.1.2}$$

With these functions, and a little integration, the resulting Jacobian is:

$$J = \begin{bmatrix} e^{\frac{-\eta t}{2}} \left(\cosh \theta t/2 + \frac{\eta + 2\lambda}{\theta} \sinh \theta t/2 \right) & e^{\frac{-\eta t}{2}} \frac{2\beta}{\theta} \sinh \theta t/2 & 0 \\ e^{\frac{-\eta t}{2}} \frac{2\gamma}{\theta} \sinh \theta t/2 & e^{\frac{-\eta t}{2}} \left(\cosh \theta t/2 - \frac{2\lambda + \eta}{\theta} \sinh \theta t/2 \right) & 0 \\ 0 & 0 & e^{\eta t} \end{bmatrix}, \tag{D.1.3}$$

where $\theta := \sqrt{\eta^2 + 4(\lambda^2 + \eta\lambda + \beta\gamma)}$. The first-order moments are obtained via $\mathbb{E}[\mathbf{X}] = J\mathbb{E}[\mathbf{X_0}]$.

Second-Order Moments

The generators for the second-order moments are given as:

$$\begin{aligned} A[X^2] &= 2\lambda X^2 + 2\beta XY + 2\kappa_h \\ A[XY] &= \gamma X^2 - \eta XY + \beta Y^2 \\ A[Y^2] &= 2\gamma XY - 2\left(\lambda + \eta\right) Y^2 + 2\kappa_h \\ A[XZ] &= (\lambda + \eta) XZ + \beta YZ \\ A[YZ] &= \gamma XZ - \lambda YZ \\ A[Z^2] &= 2\eta Z^2 + 2\kappa_v. \end{aligned} \tag{D.2.1}$$

From looking at the leading order terms of the above, it is seen that the integral equations for second-order moments would result in 3 systems:

$$
\begin{aligned}
\mathbb{E}[\dot{X^2}] &= 2\lambda\mathbb{E}[X^2] + 2\beta\mathbb{E}[XY] + 2\kappa_h \\
\mathbb{E}[\dot{XY}] &= \gamma\mathbb{E}[X^2] - \eta\mathbb{E}[XY] + \beta\mathbb{E}[Y^2] \\
\mathbb{E}[\dot{Y^2}] &= 2\gamma\mathbb{E}[XY] - 2\left(\lambda + \eta\right)\mathbb{E}[Y^2] + 2\kappa_h \\
\\
\mathbb{E}[\dot{XZ}] &= \left(\lambda + \eta\right)\mathbb{E}[XZ] + \beta\mathbb{E}[YZ] \\
\mathbb{E}[\dot{YZ}] &= \gamma\mathbb{E}[XZ] - \lambda\mathbb{E}[YZ] \\
\\
\mathbb{E}[\dot{Z^2}] &= 2\eta\mathbb{E}[Z^2] + 2\kappa_v
\end{aligned}
\tag{D.2.2}
$$

From previous analysis in the 2D case (Appendix B and Appendix C), the solutions to two of the above systems are immediately known. Letting the initial conditions be represented by E_{x^2} for the x-variance, E_{xy} for the XY cross-variance term, E_{y^2} for the y-variance, etc., the solutions are given by the following:

$$
\begin{aligned}
\mathbb{E}[XZ] &= E_{xz}\left(\cosh(\theta\tau/2) + \left(\frac{\eta + 2\lambda}{\theta}\right)\sinh(\theta\tau/2)\right)e^{\eta\tau/2} + E_{yz}\frac{2\beta\lambda}{\gamma\theta}\sinh(\theta\tau/2)e^{\eta\tau/2} \\
\mathbb{E}[YZ] &= E_{yz}\left(\cosh(\theta\tau/2) - \left(\frac{\eta + 2\lambda}{\theta}\right)\sinh(\theta\tau/2)\right)e^{\eta\tau/2} + E_{xz}\frac{2\gamma}{\theta}\sinh(\theta\tau/2)e^{\eta\tau/2} \quad . \\
\mathbb{E}[Z^2] &= E_{z^2}e^{2\eta\tau} + \frac{\kappa_v}{\eta}\left(e^{2\eta\tau} - 1\right).
\end{aligned}
\tag{D.2.3}
$$

For the remaining system, the following is system is used to compute the solution:

$$
\dot{z} = \begin{bmatrix}
2\lambda & 2\beta\gamma & 0 & -2\beta\eta & 0 & 2\beta^2 \\
1 & 0 & 0 & 0 & 0 & 0 \\
\gamma & -\gamma\eta & 0 & \eta^2 & \beta & -\beta\eta \\
0 & 0 & 1 & 0 & 0 & 0 \\
0 & 2\gamma^2 & 0 & -2\gamma\eta & -2(\lambda + \eta) & 2\beta\gamma \\
0 & 0 & 0 & 0 & 1 & 0
\end{bmatrix} z, \tag{D.2.4}
$$

where $z = \begin{bmatrix}\mathbb{E}[\dot{X^2}] & \mathbb{E}[X^2] & \mathbb{E}[\dot{XY}] & \mathbb{E}[XY] & \mathbb{E}[\dot{Y^2}] & \mathbb{E}[Y^2]\end{bmatrix}^T$. The solution to the above is given as $z(t) = M(t)z(0)$, where $M(t)$ represents the matrix exponential of the system. Noting that the second-order moments of interest come from multiplying rows 2, 4, and 6 of $M(t)$ with the initial condition vector $z(0)$, the elements of these rows are listed:

$$\begin{aligned}
&M(2,1) = (\eta^5 e^{-\eta\tau}\left(2\sinh\theta\tau\right) + 2\eta^4 e^{-\eta\tau}\theta\left(2\cosh\theta\tau\right) + 16\eta\lambda^4 e^{-\eta\tau}\left(2\sinh\theta\tau\right)\\
&+ 8\eta^4\lambda e^{-\eta\tau}\left(2\sinh\theta\tau\right) + \eta^3 e^{-\eta\tau}\theta^2\left(2\sinh\theta\tau\right)\\
&+ 32\eta^2\lambda^3 e^{-\eta\tau}\left(2\sinh\theta\tau\right) + 24\eta^3\lambda^2 e^{-\eta\tau}\left(2\sinh\theta\tau\right)\\
&+ 2\eta^2\lambda e^{-\eta\tau}\theta^2\left(2\sinh\theta\tau\right) + 8\beta^2\eta\gamma^2 e^{-\eta\tau}\left(2\sinh\theta\tau\right)\\
&+ 8\eta\lambda^3 e^{-\eta\tau}\theta\left(2\cosh\theta\tau\right) + 10\eta^3\lambda e^{-\eta\tau}\theta\left(2\cosh\theta\tau\right)\\
&+ 6\beta\eta^3\gamma e^{-\eta\tau}\left(2\sinh\theta\tau\right) + 16\eta^2\lambda^2 e^{-\eta\tau}\theta\left(2\cosh\theta\tau\right) + 24\beta\eta\gamma\lambda^2 e^{-\eta\tau}\left(2\sinh\theta\tau\right)\\
&+ 24\beta\eta^2\gamma\lambda e^{-\eta\tau}\left(2\sinh\theta\tau\right) + 6\beta\eta^2\gamma e^{-\eta\tau}\theta\left(2\cosh\theta\tau\right)\\
&+ 8\beta\eta\gamma\lambda e^{-\eta\tau}\theta\left(2\cosh\theta\tau\right) - 4\eta^4\theta - 16\eta\lambda^3\theta - 20\eta^3\lambda\theta + 16\beta^2\gamma^2\theta\\
&- 32\eta^2\lambda^2\theta - 16\beta^2\gamma^2 e^{-\eta\tau}\theta - 12\beta\eta^2\gamma\theta + 16\beta\gamma\lambda^2\theta - 16\beta\gamma\lambda^2 e^{-\eta\tau}\theta\\
&- 16\beta\eta\gamma\lambda e^{-\eta\tau}\theta\\
&/(8\eta(\lambda^2 + \eta\lambda + \beta\gamma)\theta^3)
\end{aligned}\tag{D.2.5}$$

$$\begin{aligned}
M(2,2) = {} & \eta^6 e^{\tau\theta-\eta\tau} - 6\eta^5\theta - \eta^6 e^{-\eta\tau-\tau\theta} - 32\eta\lambda^5 e^{\tau\theta-\eta\tau}\\
&+ 6\eta^5\lambda e^{\tau\theta-\eta\tau} + 32\eta\lambda^5 e^{-\eta\tau-\tau\theta} - 6\eta^5\lambda e^{-\eta\tau-\tau\theta}\\
&+ 32\eta\lambda^4\theta - 16\eta^4\lambda\theta - \eta^4 e^{\tau\theta-\eta\tau}\theta^2 + \eta^4 e^{-\eta\tau-\tau\theta}\theta^2\\
&- 48\eta^2\lambda^4 e^{\tau\theta-\eta\tau} - 16\eta^3\lambda^3 e^{\tau\theta-\eta\tau} + 8\eta^4\lambda^2 e^{\tau\theta-\eta\tau}\\
&+ 48\eta^2\lambda^4 e^{-\eta\tau-\tau\theta} + 16\eta^3\lambda^3 e^{-\eta\tau-\tau\theta} - 8\eta^4\lambda^2 e^{-\eta\tau-\tau\theta}\\
&+ 64\eta^2\lambda^3\theta + 16\eta^3\lambda^2\theta + 8\eta\lambda^3 e^{\tau\theta-\eta\tau}\theta^2 - 2\eta^3\lambda e^{\tau\theta-\eta\tau}\theta^2\\
&- 8\eta\lambda^3 e^{-\eta\tau-\tau\theta}\theta^2 + 2\eta^3\lambda e^{-\eta\tau-\tau\theta}\theta^2 + 32\beta^2\eta\gamma^2\theta\\
&+ 4\eta^2\lambda^2 e^{\tau\theta-\eta\tau}\theta^2 - 4\eta^2\lambda^2 e^{-\eta\tau-\tau\theta}\theta^2 + 8\beta^2\eta^2\gamma^2 e^{\tau\theta-\eta\tau}\\
&- 8\beta^2\eta^2\gamma^2 e^{-\eta\tau-\tau\theta} + 6\beta\eta^4\gamma e^{\tau\theta-\eta\tau} - 6\beta\eta^4\gamma e^{-\eta\tau-\tau\theta}\\
&- 16\beta\eta^3\gamma\theta + 8\beta^2\eta\gamma^2 e^{\tau\theta-\eta\tau}\theta + 8\beta^2\eta\gamma^2 e^{-\eta\tau-\tau\theta}\theta\\
&- 48\beta\eta\gamma\lambda^3 e^{\tau\theta-\eta\tau} + 12\beta\eta^3\gamma\lambda e^{\tau\theta-\eta\tau} + 48\beta\eta\gamma\lambda^3 e^{-\eta\tau-\tau\theta}\\
&- 12\beta\eta^3\gamma\lambda e^{-\eta\tau-\tau\theta} + 64\beta\eta\gamma\lambda^2\theta + 64\beta\eta^2\gamma\lambda\theta\\
&+ 4\beta\eta^2\gamma e^{\tau\theta-\eta\tau}\theta^2 - 4\beta\eta^2\gamma e^{-\eta\tau-\tau\theta}\theta^2 - 24\beta\eta^2\gamma\lambda^2 e^{\tau\theta-\eta\tau}\\
&- 16\beta^2\eta\gamma^2\lambda e^{\tau\theta-\eta\tau} + 24\beta\eta^2\gamma\lambda^2 e^{-\eta\tau-\tau\theta} + 16\beta^2\eta\gamma^2\lambda e^{-\eta\tau-\tau\theta}\\
&- 6\beta\eta^3\gamma e^{\eta\tau}\theta - 6\beta\eta^3\gamma e^{-\eta\tau}\theta - 16\beta\gamma\lambda^3 e^{\eta\tau}\theta + 16\beta\gamma\lambda^3 e^{-\eta\tau}\theta\\
&+ 6\beta\eta^3\gamma e^{\tau\theta-\eta\tau}\theta + 6\beta\eta^3\gamma e^{-\eta\tau-\tau\theta}\theta - 24\beta^2\eta\gamma^2 e^{\eta\tau}\theta\\
&+ 8\beta^2\eta\gamma^2 e^{-\eta\tau}\theta - 16\beta^2\gamma^2\lambda e^{\eta\tau}\theta + 16\beta^2\gamma^2\lambda e^{-\eta\tau}\theta - 40\beta\eta\gamma\lambda^2 e^{\eta\tau}\theta\\
&- 28\beta\eta^2\gamma\lambda e^{\eta\tau}\theta + 24\beta\eta\gamma\lambda^2 e^{-\eta\tau}\theta - 4\beta\eta^2\gamma\lambda e^{-\eta\tau}\theta\\
&+ 8\beta\eta\gamma\lambda^2 e^{\tau\theta-\eta\tau}\theta + 16\beta\eta^2\gamma\lambda e^{\tau\theta-\eta\tau}\theta + 8\beta\eta\gamma\lambda^2 e^{-\eta\tau-\tau\theta}\theta\\
&+ 16\beta\eta^2\gamma\lambda e^{-\eta\tau-\tau\theta}\theta + 8\beta\eta\gamma\lambda e^{\tau\theta-\eta\tau}\theta^2\\
&- 8\beta\eta\gamma\lambda e^{-\eta\tau-\tau\theta}\theta^2)/(2\eta(\theta^2 - 4\eta^2)\theta^3)
\end{aligned}\tag{D.2.6}$$

$$
\begin{aligned}
&M(2,3) = -(\eta^7\lambda e^{-\eta\tau-\tau\theta} - \eta^7\lambda e^{\tau\theta-\eta\tau} + 32\eta^2\lambda^6 e^{\tau\theta-\eta\tau} \\
&+ 48\eta^3\lambda^5 e^{\tau\theta-\eta\tau} + 16\eta^4\lambda^4 e^{\tau\theta-\eta\tau} - 8\eta^5\lambda^3 e^{\tau\theta-\eta\tau} - 6\eta^6\lambda^2 e^{\tau\theta-\eta\tau} \\
&- 32\eta^2\lambda^6 e^{-\eta\tau-\tau\theta} - 48\eta^3\lambda^5 e^{-\eta\tau-\tau\theta} - 16\eta^4\lambda^4 e^{-\eta\tau-\tau\theta} \\
&+ 8\eta^5\lambda^3 e^{-\eta\tau-\tau\theta} + 6\eta^6\lambda^2 e^{-\eta\tau-\tau\theta} + \eta^5\lambda e^{\tau\theta-\eta\tau}\theta^2 \\
&- \eta^5\lambda e^{-\eta\tau-\tau\theta}\theta^2 + 64\beta^3\eta\gamma^3\theta + 64\beta^3\gamma^3\lambda\theta - 8\eta^2\lambda^4 e^{\tau\theta-\eta\tau}\theta^2 \\
&- 4\eta^3\lambda^3 e^{\tau\theta-\eta\tau}\theta^2 + 2\eta^4\lambda^2 e^{\tau\theta-\eta\tau}\theta^2 + 8\eta^2\lambda^4 e^{-\eta\tau-\tau\theta}\theta^2 \\
&+ 4\eta^3\lambda^3 e^{-\eta\tau-\tau\theta}\theta^2 - 2\eta^4\lambda^2 e^{-\eta\tau-\tau\theta}\theta^2 + 12\beta^2\eta^4\gamma^2 e^{\tau\theta-\eta\tau} \\
&+ 16\beta^3\eta^2\gamma^3 e^{\tau\theta-\eta\tau} - 12\beta^2\eta^4\gamma^2 e^{-\eta\tau-\tau\theta} - 16\beta^3\eta^2\gamma^3 e^{-\eta\tau-\tau\theta} \\
&- 32\beta^2\eta^3\gamma^2\theta + 128\beta^2\gamma^2\lambda^3\theta + 2\beta\eta^6\gamma e^{\tau\theta-\eta\tau} - 2\beta\eta^6\gamma e^{-\eta\tau-\tau\theta} \\
&- 12\beta\eta^5\gamma\theta + 64\beta\gamma\lambda^5\theta + 256\beta^2\eta\gamma^2\lambda^2\theta + 96\beta^2\eta^2\gamma^2\lambda\theta + 10\beta\eta^5\gamma\lambda e^{\tau\theta-\eta\tau} \\
&- 10\beta\eta^5\gamma\lambda e^{-\eta\tau-\tau\theta} + 64\beta^2\eta^2\gamma^2\lambda^2 e^{\tau\theta-\eta\tau} - 64\beta^2\eta^2\gamma^2\lambda^2 e^{-\eta\tau-\tau\theta} \\
&- 12\beta^2\eta^3\gamma^2 e^{\eta\tau}\theta + 12\beta^2\eta^3\gamma^2 e^{-\eta\tau}\theta - 64\beta^2\gamma^2\lambda^3 e^{\eta\tau}\theta - 64\beta^2\gamma^2\lambda^3 e^{-\eta\tau}\theta \\
&+ 192\beta\eta\gamma\lambda^4\theta - 44\beta\eta^4\gamma\lambda\theta + 4\beta\eta^4\gamma e^{\tau\theta-\eta\tau}\theta^2 - 4\beta\eta^4\gamma e^{-\eta\tau-\tau\theta}\theta^2 \\
&+ 16\beta^2\eta^3\gamma^2 e^{\tau\theta-\eta\tau}\theta + 16\beta^2\eta^3\gamma^2 e^{-\eta\tau-\tau\theta}\theta + 80\beta\eta^2\gamma\lambda^4 e^{\tau\theta-\eta\tau} \\
&+ 88\beta\eta^3\gamma\lambda^3 e^{\tau\theta-\eta\tau} + 36\beta\eta^4\gamma\lambda^2 e^{\tau\theta-\eta\tau} - 80\beta\eta^2\gamma\lambda^4 e^{-\eta\tau-\tau\theta} \\
&- 88\beta\eta^3\gamma\lambda^3 e^{-\eta\tau-\tau\theta} - 36\beta\eta^4\gamma\lambda^2 e^{-\eta\tau-\tau\theta} - 32\beta\gamma\lambda^5 e^{\eta\tau}\theta \\
&- 32\beta\gamma\lambda^5 e^{-\eta\tau}\theta + 160\beta\eta^2\gamma\lambda^3\theta + 6\beta\eta^5\gamma e^{\tau\theta-\eta\tau}\theta + 6\beta\eta^5\gamma e^{-\eta\tau-\tau\theta}\theta \\
&+ 40\beta^2\eta^3\gamma^2\lambda e^{\tau\theta-\eta\tau} - 40\beta^2\eta^3\gamma^2\lambda e^{-\eta\tau-\tau\theta} - 48\beta^3\eta\gamma^3 e^{\eta\tau}\theta \\
&- 16\beta^3\eta\gamma^3 e^{-\eta\tau}\theta - 32\beta^3\gamma^3\lambda e^{\eta\tau}\theta - 32\beta^3\gamma^3\lambda e^{-\eta\tau}\theta - 112\beta\eta\gamma\lambda^4 e^{\eta\tau}\theta \\
&- 12\beta\eta^4\gamma\lambda e^{\eta\tau}\theta - 80\beta\eta\gamma\lambda^4 e^{-\eta\tau}\theta + 12\beta\eta^4\gamma\lambda e^{-\eta\tau}\theta \\
&- 8\beta\eta^2\gamma\lambda^2 e^{\tau\theta-\eta\tau}\theta^2 + 8\beta\eta^2\gamma\lambda^2 e^{-\eta\tau-\tau\theta}\theta^2 + 22\beta\eta^4\gamma\lambda e^{\tau\theta-\eta\tau}\theta \\
&+ 22\beta\eta^4\gamma\lambda e^{-\eta\tau-\tau\theta}\theta - 136\beta\eta^2\gamma\lambda^3 e^{\eta\tau}\theta - 68\beta\eta^3\gamma\lambda^2 e^{\eta\tau}\theta \\
&- 40\beta\eta^2\gamma\lambda^3 e^{-\eta\tau}\theta + 20\beta\eta^3\gamma\lambda^2 e^{-\eta\tau}\theta + 8\beta\eta^2\gamma\lambda^3 e^{\tau\theta-\eta\tau}\theta \\
&+ 24\beta\eta^3\gamma\lambda^2 e^{\tau\theta-\eta\tau}\theta + 8\beta\eta^2\gamma\lambda^3 e^{-\eta\tau-\tau\theta}\theta + 24\beta\eta^3\gamma\lambda^2 e^{-\eta\tau-\tau\theta}\theta \\
&- 160\beta^2\eta\gamma^2\lambda^2 e^{\eta\tau}\theta - 104\beta^2\eta^2\gamma^2\lambda e^{\eta\tau}\theta - 96\beta^2\eta\gamma^2\lambda^2 e^{-\eta\tau}\theta \\
&- 8\beta^2\eta^2\gamma^2\lambda e^{-\eta\tau}\theta + 4\beta\eta^3\gamma\lambda e^{\tau\theta-\eta\tau}\theta^2 - 4\beta\eta^3\gamma\lambda e^{-\eta\tau-\tau\theta}\theta^2 \\
&+ 8\beta^2\eta^2\gamma^2\lambda e^{\tau\theta-\eta\tau}\theta + 8\beta^2\eta^2\gamma^2\lambda e^{-\eta\tau-\tau\theta}\theta) \\
&/(4\eta\gamma(\lambda^2 + \eta\lambda + \beta\gamma)(\theta^2 - 4\eta^2)\theta^3)
\end{aligned}
\tag{D.2.7}
$$

$$\begin{aligned}
&M(2,4) = -(\eta^6 e^{\tau\theta-\eta\tau}\theta - \eta^4 e^{\tau\theta-\eta\tau}\theta^3 + \eta^4 e^{-\eta\tau-\tau\theta}\theta^3 - \eta^6 e^{-\eta\tau-\tau\theta}\theta \\
&- 16\beta^2\eta^3\gamma^2 e^{-\eta\tau} + 128\beta^2\gamma^2\lambda^3 e^{-\eta\tau} + 8\eta\lambda^3 e^{\tau\theta-\eta\tau}\theta^3 - 32\eta\lambda^5 e^{\tau\theta-\eta\tau}\theta \\
&- 2\eta^3\lambda e^{\tau\theta-\eta\tau}\theta^3 + 6\eta^5\lambda e^{\tau\theta-\eta\tau}\theta - 8\eta\lambda^3 e^{-\eta\tau-\tau\theta}\theta^3 + 32\eta\lambda^5 e^{-\eta\tau-\tau\theta}\theta \\
&+ 2\eta^3\lambda e^{-\eta\tau-\tau\theta}\theta^3 - 6\eta^5\lambda e^{-\eta\tau-\tau\theta}\theta - 6\beta\eta^5\gamma e^{-\eta\tau} + 64\beta\gamma\lambda^5 e^{-\eta\tau} \\
&+ 4\eta^2\lambda^2 e^{\tau\theta-\eta\tau}\theta^3 - 48\eta^2\lambda^4 e^{\tau\theta-\eta\tau}\theta - 16\eta^3\lambda^3 e^{\tau\theta-\eta\tau}\theta + 8\eta^4\lambda^2 e^{\tau\theta-\eta\tau}\theta \\
&- 4\eta^2\lambda^2 e^{-\eta\tau-\tau\theta}\theta^3 + 48\eta^2\lambda^4 e^{-\eta\tau-\tau\theta}\theta + 16\eta^3\lambda^3 e^{-\eta\tau-\tau\theta}\theta - 8\eta^4\lambda^2 e^{-\eta\tau-\tau\theta}\theta \\
&+ 32\beta^3\eta\gamma^3 e^{-\eta\tau} + 64\beta^3\gamma^3\lambda e^{-\eta\tau} - 6\beta\eta^3\gamma e^{\eta\tau}\theta^2 - 16\beta\gamma\lambda^3 e^{\eta\tau}\theta^2 + 96\beta\eta^2\gamma\lambda^3 e^{-\eta\tau} \\
&- 16\beta\eta^3\gamma\lambda^2 e^{-\eta\tau} + 6\beta\eta^3\gamma e^{\tau\theta-\eta\tau}\theta^2 + 6\beta\eta^3\gamma e^{-\eta\tau-\tau\theta}\theta^2 \\
&+ 8\beta^2\eta^2\gamma^2 e^{\tau\theta-\eta\tau}\theta - 8\beta^2\eta^2\gamma^2 e^{-\eta\tau-\tau\theta}\theta - 24\beta^2\eta\gamma^2 e^{\eta\tau}\theta^2 - 16\beta^2\gamma^2\lambda e^{\eta\tau}\theta^2 \\
&+ 192\beta^2\eta\gamma^2\lambda^2 e^{-\eta\tau} + 32\beta^2\eta^2\gamma^2\lambda e^{-\eta\tau} + 8\beta^2\eta\gamma^2 e^{\tau\theta-\eta\tau}\theta^2 + 8\beta^2\eta\gamma^2 e^{-\eta\tau-\tau\theta}\theta^2 \\
&+ 4\beta\eta^2\gamma e^{\tau\theta-\eta\tau}\theta^3 + 6\beta\eta^4\gamma e^{\tau\theta-\eta\tau}\theta - 4\beta\eta^2\gamma e^{-\eta\tau-\tau\theta}\theta^3 - 6\beta\eta^4\gamma e^{-\eta\tau-\tau\theta}\theta \\
&+ 160\beta\eta\gamma\lambda^4 e^{-\eta\tau} - 28\beta\eta^4\gamma\lambda e^{-\eta\tau} - 48\beta\eta\gamma\lambda^3 e^{\tau\theta-\eta\tau}\theta + 12\beta\eta^3\gamma\lambda e^{\tau\theta-\eta\tau}\theta \\
&+ 48\beta\eta\gamma\lambda^3 e^{-\eta\tau-\tau\theta}\theta - 12\beta\eta^3\gamma\lambda e^{-\eta\tau-\tau\theta}\theta - 24\beta\eta^2\gamma\lambda^2 e^{\tau\theta-\eta\tau}\theta \\
&- 16\beta^2\eta\gamma^2\lambda e^{\tau\theta-\eta\tau}\theta + 24\beta\eta^2\gamma\lambda^2 e^{-\eta\tau-\tau\theta}\theta + 16\beta^2\eta\gamma^2\lambda e^{-\eta\tau-\tau\theta}\theta - 40\beta\eta\gamma\lambda^2 e^{\eta\tau}\theta^2 \\
&- 28\beta\eta^2\gamma\lambda e^{\eta\tau}\theta^2 + 8\beta\eta\gamma\lambda^2 e^{\tau\theta-\eta\tau}\theta^2 + 16\beta\eta^2\gamma\lambda e^{\tau\theta-\eta\tau}\theta^2 + 8\beta\eta\gamma\lambda^2 e^{-\eta\tau-\tau\theta}\theta^2 \\
&+ 16\beta\eta^2\gamma\lambda e^{-\eta\tau-\tau\theta}\theta^2 + 8\beta\eta\gamma\lambda e^{\tau\theta-\eta\tau}\theta^3 - 8\beta\eta\gamma\lambda e^{-\eta\tau-\tau\theta}\theta^3) \\
&/(2\gamma(-3\theta^2)\big(16\beta^2\gamma^2 + 8\beta\eta^2\gamma + 32\beta\eta\gamma\lambda + 32\beta\gamma\lambda^2 \\
&+\eta^4 + 8\eta^3\lambda + 24\eta^2\lambda^2 + 32\eta\lambda^3 + 16\lambda^4)\big)
\end{aligned} \tag{D.2.8}$$

$$\begin{aligned}
&M(2,5) = (32\eta\lambda^6 e^{-\eta\tau}(2\sinh\theta\tau) + \eta^6\lambda e^{-\eta\tau}(2\sinh\theta\tau) + 80\eta^2\lambda^5 e^{-\eta\tau}(2\sinh\theta\tau) \\
&+ 80\eta^3\lambda^4 e^{-\eta\tau}(2\sinh\theta\tau) + 40\eta^4\lambda^3 e^{-\eta\tau}(2\sinh\theta\tau) + 10\eta^5\lambda^2 e^{-\eta\tau}(2\sinh\theta\tau) \\
&- 8\eta\lambda^4\theta^2 e^{-\eta\tau}(2\sinh\theta\tau) - \eta^4\lambda\theta^2 e^{-\eta\tau}(2\sinh\theta\tau) + 8\beta^3\eta\gamma^3 e^{-\eta\tau}(2\sinh\theta\tau) \\
&- 12\eta^2\lambda^3\theta^2 e^{-\eta\tau}(2\sinh\theta\tau) - 6\eta^3\lambda^2\theta^2 e^{-\eta\tau}(2\sinh\theta\tau) + 6\beta^2\eta^3\gamma^2 e^{-\eta\tau}(2\sinh\theta\tau) \\
&+ \beta\eta^5\gamma e^{-\eta\tau}(2\sinh\theta\tau) + 64\beta\eta\gamma\lambda^4 e^{-\eta\tau}(2\sinh\theta\tau) + 14\beta\eta^4\gamma\lambda e^{-\eta\tau}(2\sinh\theta\tau) \\
&- \beta\eta^3\gamma\theta^2 e^{-\eta\tau}(2\sinh\theta\tau) + 2\beta^2\eta^2\gamma^2\theta e^{-\eta\tau}(2\cosh\theta\tau) + 104\beta\eta^2\gamma\lambda^3 e^{-\eta\tau}(2\sinh\theta\tau) \\
&+ 60\beta\eta^3\gamma\lambda^2 e^{-\eta\tau}(2\sinh\theta\tau) + 40\beta^2\eta\gamma^2\lambda^2 e^{-\eta\tau}(2\sinh\theta\tau) \\
&+ 32\beta^2\eta^2\gamma^2\lambda e^{-\eta\tau}(2\sinh\theta\tau) - 8\beta\eta\gamma\lambda^2\theta^2 e^{-\eta\tau}(2\sinh\theta\tau) \\
&- 6\beta\eta^2\gamma\lambda\theta^2 e^{-\eta\tau}(2\sinh\theta\tau) - 16\beta^3\gamma^3\theta + 16\beta^3\gamma^3\theta e^{-\eta\tau} - 4\beta^2\eta^2\gamma^2\theta - 16\beta^2\gamma^2\lambda^2\theta \\
&+ 16\beta^2\gamma^2\lambda^2\theta e^{-\eta\tau} - 16\beta^2\eta\gamma^2\lambda\theta + 16\beta^2\eta\gamma^2\lambda\theta e^{-\eta\tau})/(8\eta\gamma^2\theta^3(\lambda^2 + \lambda\eta + \beta\gamma))
\end{aligned} \tag{D.2.9}$$

$$
\begin{aligned}
&M(2,6) = (\beta\eta^6 e^{\tau\theta-\eta\tau} - \beta\eta^6 e^{-\eta\tau-\tau\theta} - \beta\eta^4 e^{\tau\theta-\eta\tau}(\theta^2) + \beta\eta^4 e^{-\eta\tau-\tau\theta}\theta^2 + 6\beta^2\eta^4\gamma e^{\tau\theta-\eta\tau} \\
&- 6\beta^2\eta^4\gamma e^{-\eta\tau-\tau\theta} - 48\beta\eta^2\lambda^4 e^{\tau\theta-\eta\tau} - 16\beta\eta^3\lambda^3 e^{\tau\theta-\eta\tau} + 8\beta\eta^4\lambda^2 e^{\tau\theta-\eta\tau} + 48\beta\eta^2\lambda^4 e^{-\eta\tau-\tau\theta} \\
&+ 16\beta\eta^3\lambda^3 e^{-\eta\tau-\tau\theta} - 8\beta\eta^4\lambda^2 e^{-\eta\tau-\tau\theta} + 8\beta^3\eta^2\gamma^2 e^{\tau\theta-\eta\tau} - 8\beta^3\eta^2\gamma^2 e^{-\eta\tau-\tau\theta} - 32\beta\eta\lambda^5 e^{\tau\theta-\eta\tau} \\
&+ 6\beta\eta^5\lambda e^{\tau\theta-\eta\tau} + 32\beta\eta\lambda^5 e^{-\eta\tau-\tau\theta} - 6\beta\eta^5\lambda e^{-\eta\tau-\tau\theta} + 6\beta^2\eta^3\gamma e^{\tau\theta-\eta\tau}\theta + 8\beta^3\eta\gamma^2 e^{\tau\theta-\eta\tau}\theta \\
&+ 6\beta^2\eta^3\gamma e^{-\eta\tau-\tau\theta}\theta + 8\beta^3\eta\gamma^2 e^{-\eta\tau-\tau\theta}\theta + 8\beta\eta\lambda^3 e^{\tau\theta-\eta\tau}\theta^2 - 2\beta\eta^3\lambda e^{\tau\theta-\eta\tau}\theta^2 \\
&- 8\beta\eta\lambda^3 e^{-\eta\tau-\tau\theta}\theta^2 + 2\beta\eta^3\lambda e^{-\eta\tau-\tau\theta}\theta^2 - 48\beta^2\eta\gamma\lambda^3 e^{\tau\theta-\eta\tau} + 12\beta^2\eta^3\gamma\lambda e^{\tau\theta-\eta\tau} \\
&- 16\beta^3\eta\gamma^2\lambda e^{\tau\theta-\eta\tau} + 48\beta^2\eta\gamma\lambda^3 e^{-\eta\tau-\tau\theta} - 12\beta^2\eta^3\gamma\lambda e^{-\eta\tau-\tau\theta} + 16\beta^3\eta\gamma^2\lambda e^{-\eta\tau-\tau\theta} \\
&+ 4\beta^2\eta^2\gamma e^{\tau\theta-\eta\tau}\theta^2 - 4\beta^2\eta^2\gamma e^{-\eta\tau-\tau\theta}\theta^2 + 4\beta\eta^2\lambda^2 e^{\tau\theta-\eta\tau}\theta^2 - 4\beta\eta^2\lambda^2 e^{-\eta\tau-\tau\theta}\theta^2 \\
&- 24\beta^2\eta^2\gamma\lambda^2 e^{\tau\theta-\eta\tau} + 24\beta^2\eta^2\gamma\lambda^2 e^{-\eta\tau-\tau\theta} - 6\beta^2\eta^3\gamma e^{\eta\tau}\theta - 24\beta^3\eta\gamma^2 e^{\eta\tau}\theta - 6\beta^2\eta^3\gamma e^{-\eta\tau}\theta \\
&+ 8\beta^3\eta\gamma^2 e^{-\eta\tau}\theta - 16\beta^2\gamma\lambda^3 e^{\eta\tau}\theta - 16\beta^3\gamma^2\lambda e^{\eta\tau}\theta + 16\beta^2\gamma\lambda^3 e^{-\eta\tau}\theta + 16\beta^3\gamma^2\lambda e^{-\eta\tau}\theta \\
&- 40\beta^2\eta\gamma\lambda^2 e^{\eta\tau}\theta - 28\beta^2\eta^2\gamma\lambda e^{\eta\tau}\theta + 24\beta^2\eta\gamma\lambda^2 e^{-\eta\tau}\theta - 4\beta^2\eta^2\gamma\lambda e^{-\eta\tau}\theta + 8\beta^2\eta\gamma\lambda^2 e^{\tau\theta-\eta\tau}\theta \\
&+ 16\beta^2\eta^2\gamma\lambda e^{\tau\theta-\eta\tau}\theta + 8\beta^2\eta\gamma\lambda^2 e^{-\eta\tau-\tau\theta}\theta + 16\beta^2\eta^2\gamma\lambda e^{-\eta\tau-\tau\theta}\theta + 8\beta^2\eta\gamma\lambda e^{\tau\theta-\eta\tau}\theta^2 \\
&- 8\beta^2\eta\gamma\lambda e^{-\eta\tau-\tau\theta}\theta^2)/(2\eta\gamma(-3\theta^2)(4\beta\gamma + 4\eta\lambda + \eta^2 + 4\lambda^2)^{3/2})
\end{aligned}
\tag{D.2.10}
$$

$$
\begin{aligned}
&M(4,1) = (\eta^4\gamma e^{-\eta\tau}\,(2\sinh\theta\tau) + \eta^2\theta^2\gamma e^{-\eta\tau}\,(2\sinh\theta\tau) + 4\beta\eta^2\gamma^2 e^{-\eta\tau}\,(2\sinh\theta\tau) \\
&+ 12\eta^2\gamma\lambda^2 e^{-\eta\tau}\,(2\sinh\theta\tau) + 2\eta^3\gamma\theta e^{-\eta\tau}\,(2\cosh\theta\tau) + 8\eta\gamma\lambda^3 e^{-\eta\tau}\,(2\sinh\theta\tau) \\
&+ 6\eta^3\gamma\lambda e^{-\eta\tau}\,(2\sinh\theta\tau) + 8\beta\eta\gamma^2\lambda e^{-\eta\tau}\,(2\sinh\theta\tau) + 4\beta\eta\gamma^2\theta e^{-\eta\tau}\,(2\cosh\theta\tau) \\
&+ 4\eta\gamma\lambda^2\theta e^{-\eta\tau}\,(2\cosh\theta\tau) + 6\eta^2\gamma\lambda\theta e^{-\eta\tau}\,(2\cosh\theta\tau) - 4\eta^3\gamma\theta - 16\gamma\lambda^3\theta - 32\eta\gamma\lambda^2\theta \\
&- 20\eta^2\gamma\lambda\theta + 16\gamma\lambda^3 e^{-\eta\tau}\theta - 16\beta\eta\gamma^2\theta - 16\beta\gamma^2\lambda\theta + 8\beta\eta\gamma^2 e^{-\eta\tau}\theta + 16\beta\gamma^2\lambda e^{-\eta\tau}\theta \\
&+ 24\eta\gamma\lambda^2 e^{-\eta\tau}\theta + 8\eta^2\gamma\lambda e^{-\eta\tau}\theta) \\
&/(8\eta\theta^3(\lambda^2 + \eta\lambda + \beta\gamma))
\end{aligned}
\tag{D.2.11}
$$

$$
\begin{aligned}
&M(4,2) = -(\eta^5\gamma e^{-\eta\tau-\tau\theta} - \eta^5\gamma e^{\tau\theta-\eta\tau} + 6\eta^4\gamma\theta - 32\gamma\lambda^4\theta - 32\beta^2\gamma^3\theta - 64\eta\gamma\lambda^3\theta \\
&+ 16\eta^3\gamma\lambda\theta + \eta^3\gamma e^{\tau\theta-\eta\tau}\theta^2 - \eta^3\gamma e^{-\eta\tau-\tau\theta}\theta^2 - 4\beta\eta^3\gamma^2 e^{\tau\theta-\eta\tau} + 4\beta\eta^3\gamma^2 e^{-\eta\tau-\tau\theta} \\
&+ 16\eta^2\gamma\lambda^3 e^{\tau\theta-\eta\tau} - 16\eta^2\gamma\lambda^3 e^{-\eta\tau-\tau\theta} - 3\eta^4\gamma e^{\eta\tau}\theta - 3\eta^4\gamma e^{-\eta\tau}\theta + 16\gamma\lambda^4 e^{\eta\tau}\theta \\
&+ 16\gamma\lambda^4 e^{-\eta\tau}\theta + 16\beta\eta^2\gamma^2\theta - 64\beta\gamma^2\lambda^2\theta - 16\eta^2\gamma\lambda^2\theta + 32\beta^2\gamma^3 e^{\eta\tau}\theta + 16\eta\gamma\lambda^4 e^{\tau\theta-\eta\tau} \\
&- 4\eta^4\gamma\lambda e^{\tau\theta-\eta\tau} - 16\eta\gamma\lambda^4 e^{-\eta\tau-\tau\theta} + 4\eta^4\gamma\lambda e^{-\eta\tau-\tau\theta} - 8\beta\eta^2\gamma^2 e^{\tau\theta-\eta\tau}\theta \\
&- 8\beta\eta^2\gamma^2 e^{-\eta\tau-\tau\theta}\theta - 64\beta\eta\gamma^2\lambda\theta - 4\beta\eta\gamma^2 e^{\tau\theta-\eta\tau}\theta^2 + 4\beta\eta\gamma^2 e^{-\eta\tau-\tau\theta}\theta^2 \\
&- 4\eta\gamma\lambda^2 e^{\tau\theta-\eta\tau}\theta^2 + 4\eta\gamma\lambda^2 e^{-\eta\tau-\tau\theta}\theta^2 + 16\beta\eta\gamma^2\lambda^2 e^{\tau\theta-\eta\tau} - 16\beta\eta\gamma^2\lambda^2 e^{-\eta\tau-\tau\theta} \\
&+ 32\eta\gamma\lambda^3 e^{\eta\tau}\theta - 8\eta^3\gamma\lambda e^{\eta\tau}\theta + 32\eta\gamma\lambda^3 e^{-\eta\tau}\theta - 8\eta^3\gamma\lambda e^{-\eta\tau}\theta - 4\beta\eta^2\gamma^2 e^{\eta\tau}\theta \\
&+ 4\beta\eta^2\gamma^2 e^{-\eta\tau}\theta + 48\beta\gamma^2\lambda^2 e^{\eta\tau}\theta + 16\beta\gamma^2\lambda^2 e^{-\eta\tau}\theta + 8\eta^2\gamma\lambda^2 e^{\eta\tau}\theta + 8\eta^2\gamma\lambda^2 e^{-\eta\tau}\theta \\
&+ 48\beta\eta\gamma^2\lambda e^{\eta\tau}\theta + 16\beta\eta\gamma^2\lambda e^{-\eta\tau}\theta) \\
&/(2\eta * (-3\theta^2) * (4\beta\gamma + 4\eta\lambda + \eta^2 + 4\lambda^2)^{3/2})
\end{aligned}
\tag{D.2.12}
$$

$$
\begin{aligned}
&M(4,3) = -(\eta^6\lambda e^{-\eta\tau-\tau\theta} - \eta^6\lambda e^{\tau\theta-\eta\tau} + 16\eta^2\lambda^5 e^{\tau\theta-\eta\tau} + 16\eta^3\lambda^4 e^{\tau\theta-\eta\tau} \\
&- 4\eta^5\lambda^2 e^{\tau\theta-\eta\tau} - 16\eta^2\lambda^5 e^{-\eta\tau-\tau\theta} - 16\eta^3\lambda^4 e^{-\eta\tau-\tau\theta} + 4\eta^5\lambda^2 e^{-\eta\tau-\tau\theta} \\
&- 32\lambda^6 e^{\eta\tau}\theta + 32\lambda^6 e^{-\eta\tau}\theta + 64\beta^3\gamma^3\theta + \eta^4\lambda e^{\tau\theta-\eta\tau}\theta^2 - \eta^4\lambda e^{-\eta\tau-\tau\theta}\theta^2 \\
&- 96\eta\lambda^5 e^{\eta\tau}\theta + 6\eta^5\lambda e^{\eta\tau}\theta + 96\eta\lambda^5 e^{-\eta\tau}\theta - 6\eta^5\lambda e^{-\eta\tau}\theta - 4\eta^2\lambda^3 e^{\tau\theta-\eta\tau}\theta^2 \\
&+ 4\eta^2\lambda^3 e^{-\eta\tau-\tau\theta}\theta^2 + 8\beta^2\eta^3\gamma^2 e^{\tau\theta-\eta\tau} - 8\beta^2\eta^3\gamma^2 e^{-\eta\tau-\tau\theta} - 64\beta^3\gamma^3 e^{\eta\tau}\theta \\
&- 80\eta^2\lambda^4 e^{\eta\tau}\theta + 22\eta^4\lambda^2 e^{\eta\tau}\theta + 80\eta^2\lambda^4 e^{-\eta\tau}\theta - 22\eta^4\lambda^2 e^{-\eta\tau}\theta - 32\beta^2\eta^2\gamma^2\theta \\
&+ 128\beta^2\gamma^2\lambda^2\theta + 2\beta\eta^5\gamma e^{\tau\theta-\eta\tau} - 2\beta\eta^5\gamma e^{-\eta\tau-\tau\theta} - 12\beta\eta^4\gamma\theta + 64\beta\gamma\lambda^4\theta \\
&+ 8\beta\eta^4\gamma\lambda e^{\tau\theta-\eta\tau} - 8\beta\eta^4\gamma\lambda e^{-\eta\tau-\tau\theta} + 8\beta^2\eta^2\gamma^2 e^{\eta\tau}\theta + 8\beta^2\eta^2\gamma^2 e^{-\eta\tau}\theta \\
&- 160\beta^2\gamma^2\lambda^2 e^{\eta\tau}\theta + 32\beta^2\gamma^2\lambda^2 e^{-\eta\tau}\theta + 128\beta\eta\gamma\lambda^3\theta - 32\beta\eta^3\gamma\lambda\theta + 4\beta\eta^3\gamma e^{\tau\theta-\eta\tau}\theta^2 \\
&- 4\beta\eta^3\gamma e^{-\eta\tau-\tau\theta}\theta^2 + 8\beta^2\eta^2\gamma^2 e^{\tau\theta-\eta\tau}\theta + 8\beta^2\eta^2\gamma^2 e^{-\eta\tau-\tau\theta}\theta \\
&+ 32\beta\eta^2\gamma\lambda^3 e^{\tau\theta-\eta\tau} + 24\beta\eta^3\gamma\lambda^2 e^{\tau\theta-\eta\tau} - 32\beta\eta^2\gamma\lambda^3 e^{-\eta\tau-\tau\theta} - 24\beta\eta^3\gamma\lambda^2 e^{-\eta\tau-\tau\theta} \\
&+ 6\beta\eta^4\gamma e^{\eta\tau}\theta - 6\beta\eta^4\gamma e^{-\eta\tau}\theta - 128\beta\gamma\lambda^4 e^{\eta\tau}\theta + 64\beta\gamma\lambda^4 e^{-\eta\tau}\theta + 32\beta\eta^2\gamma\lambda^2\theta \\
&+ 128\beta^2\eta\gamma^2\lambda\theta + 6\beta\eta^4\gamma e^{\tau\theta-\eta\tau}\theta + 6\beta\eta^4\gamma e^{-\eta\tau-\tau\theta}\theta + 16\beta^2\eta^2\gamma^2\lambda e^{\tau\theta-\eta\tau} \\
&- 16\beta^2\eta^2\gamma^2\lambda e^{-\eta\tau-\tau\theta} - 256\beta\eta\gamma\lambda^3 e^{\eta\tau}\theta + 24\beta\eta^3\gamma\lambda e^{\eta\tau}\theta + 128\beta\eta\gamma\lambda^3 e^{-\eta\tau}\theta \\
&- 8\beta\eta^3\gamma\lambda e^{-\eta\tau}\theta + 8\beta\eta^3\gamma\lambda e^{\tau\theta-\eta\tau}\theta + 8\beta\eta^3\gamma\lambda e^{-\eta\tau-\tau\theta}\theta - 104\beta\eta^2\gamma\lambda^2 e^{\eta\tau}\theta \\
&- 160\beta^2\eta\gamma^2\lambda e^{\eta\tau}\theta + 56\beta\eta^2\gamma\lambda^2 e^{-\eta\tau}\theta + 32\beta^2\eta\gamma^2\lambda e^{-\eta\tau}\theta + 8\beta\eta^2\gamma\lambda^2 e^{\tau\theta-\eta\tau}\theta \\
&+ 8\beta\eta^2\gamma\lambda^2 e^{-\eta\tau-\tau\theta}\theta - 4\beta\eta^2\gamma\lambda e^{\tau\theta-\eta\tau}\theta^2 + 4\beta\eta^2\gamma\lambda e^{-\eta\tau-\tau\theta}\theta^2) \\
&/(4\eta * (\lambda^2 + \eta\lambda + \beta\gamma) * (-3\theta^2) * (4\beta\gamma + 4\eta\lambda + \eta^2 + 4\lambda^2)^{3/2})
\end{aligned}
\tag{D.2.13}
$$

$$\begin{aligned}
&M(4,4) = (64\lambda^6 e^{-\eta\tau} - 3\eta^6 e^{-\eta\tau} + \eta^3 e^{\tau\theta-\eta\tau}\theta^3 - \eta^5 e^{\tau\theta-\eta\tau}\theta - \eta^3 e^{-\eta\tau-\tau\theta}\theta^3 \\
&+ \eta^5 e^{-\eta\tau-\tau\theta}\theta + 192\eta\lambda^5 e^{-\eta\tau} - 20\eta^5\lambda e^{-\eta\tau} - 3\eta^4 e^{\eta\tau}\theta^2 + 16\lambda^4 e^{\eta\tau}\theta^2 + 176\eta^2\lambda^4 e^{-\eta\tau} \\
&+ 32\eta^3\lambda^3 e^{-\eta\tau} - 36\eta^4\lambda^2 e^{-\eta\tau} + 32\beta^2\gamma^2 e^{\eta\tau}\theta^2 + 8\eta^2\lambda^2 e^{\eta\tau}\theta^2 + 16\beta^2\eta^2\gamma^2 e^{-\eta\tau} \\
&+ 64\beta^2\gamma^2\lambda^2 e^{-\eta\tau} - 4\eta\lambda^2 e^{\tau\theta-\eta\tau}\theta^3 + 16\eta\lambda^4 e^{\tau\theta-\eta\tau}\theta - 4\eta^4\lambda e^{\tau\theta-\eta\tau}\theta \\
&+ 4\eta\lambda^2 e^{-\eta\tau-\tau\theta}\theta^3 - 16\eta\lambda^4 e^{-\eta\tau-\tau\theta}\theta + 4\eta^4\lambda e^{-\eta\tau-\tau\theta}\theta - 8\beta\eta^4\gamma e^{-\eta\tau} \\
&+ 128\beta\gamma\lambda^4 e^{-\eta\tau} + 16\eta^2\lambda^3 e^{\tau\theta-\eta\tau}\theta - 16\eta^2\lambda^3 e^{-\eta\tau-\tau\theta}\theta + 32\eta\lambda^3 e^{\eta\tau}\theta^2 \\
&- 8\eta^3\lambda e^{\eta\tau}\theta^2 - 4\beta\eta^2\gamma e^{\eta\tau}\theta^2 + 48\beta\gamma\lambda^2 e^{\eta\tau}\theta^2 + 128\beta\eta^2\gamma\lambda^2 e^{-\eta\tau} + 64\beta^2\eta\gamma^2\lambda e^{-\eta\tau} \\
&- 8\beta\eta^2\gamma e^{\tau\theta-\eta\tau}\theta^2 - 8\beta\eta^2\gamma e^{-\eta\tau-\tau\theta}\theta^2 - 4\beta\eta\gamma e^{\tau\theta-\eta\tau}\theta^3 + 4\beta\eta\gamma e^{-\eta\tau-\tau\theta}\theta^3 \\
&- 4\beta\eta^3\gamma e^{\tau\theta-\eta\tau}\theta + 4\beta\eta^3\gamma e^{-\eta\tau-\tau\theta}\theta + 256\beta\eta\gamma\lambda^3 e^{-\eta\tau} + 16\beta\eta\gamma\lambda^2 e^{\tau\theta-\eta\tau}\theta \\
&- 16\beta\eta\gamma\lambda^2 e^{-\eta\tau-\tau\theta}\theta + 48\beta\eta\gamma\lambda e^{\eta\tau}\theta^2)/\bigl(2(-3\theta^2)(16\beta^2\gamma^2 + 8\beta\eta^2\gamma \\
&+32\beta\eta\gamma\lambda + 32\beta\gamma\lambda^2 + \eta^4 + 8\eta^3\lambda + 24\eta^2\lambda^2 + 32\eta\lambda^3 + 16\lambda^4)\bigr)
\end{aligned} \tag{D.2.14}$$

$$\begin{aligned}
&M(4,5) = (16\eta\lambda^5 e^{-\eta\tau}(2\sinh\theta\tau) + \eta^5\lambda e^{-\eta\tau}(2\sinh\theta\tau) + 32\eta^2\lambda^4 e^{-\eta\tau}(2\sinh\theta\tau) \\
&+ 24\eta^3\lambda^3 e^{-\eta\tau}(2\sinh\theta\tau) + 8\eta^4\lambda^2 e^{-\eta\tau}(2\sinh\theta\tau) - 4\eta\lambda^3\theta^2 e^{-\eta\tau}(2\sinh\theta\tau) \\
&- \eta^3\lambda\theta^2 e^{-\eta\tau}(2\sinh\theta\tau) - 4\eta^2\lambda^2\theta^2 e^{-\eta\tau}(2\sinh\theta\tau) + 4\beta^2\eta^2\gamma^2 e^{-\eta\tau}(2\sinh\theta\tau) \\
&+ \beta\eta^4\gamma e^{-\eta\tau}(2\sinh\theta\tau) + 4\beta^2\eta\gamma^2\theta e^{-\eta\tau}(2\cosh\theta\tau) + 24\beta\eta\gamma\lambda^3 e^{-\eta\tau}(2\sinh\theta\tau) \\
&+ 10\beta\eta^3\gamma\lambda e^{-\eta\tau}(2\sinh\theta\tau) - \beta\eta^2\gamma\theta^2 e^{-\eta\tau}(2\sinh\theta\tau) + 28\beta\eta^2\gamma\lambda^2 e^{-\eta\tau}(2\sinh\theta\tau) \\
&+ 8\beta^2\eta\gamma^2\lambda e^{-\eta\tau}(2\sinh\theta\tau) + 4\beta\eta\gamma\lambda^2\theta e^{-\eta\tau}(2\cosh\theta\tau) + 2\beta\eta^2\gamma\lambda\theta e^{-\eta\tau}(2\cosh\theta\tau) \\
&- 4\beta\eta\gamma\lambda\theta^2 e^{-\eta\tau}(2\sinh\theta\tau) + 16\beta^2\gamma^2\lambda\theta + 16\beta\gamma\lambda^3\theta + 16\beta\eta\gamma\lambda^2\theta + 4\beta\eta^2\gamma\lambda\theta \\
&- 16\beta\gamma\lambda^3\theta e^{-\eta\tau} - 8\beta^2\eta\gamma^2\theta e^{-\eta\tau} - 16\beta^2\gamma^2\lambda\theta e^{-\eta\tau} - 24\beta\eta\gamma\lambda^2\theta e^{-\eta\tau} - 8\beta\eta^2\gamma\lambda\theta e^{-\eta\tau}) \\
&/(8\eta\gamma\theta^3(\lambda^2 + \eta\lambda + \beta\gamma)
\end{aligned} \tag{D.2.15}$$

$$
\begin{aligned}
&M(4,6) = -(\beta\eta^5 e^{-\eta\tau-\tau\theta} - \beta\eta^5 e^{\tau\theta-\eta\tau} + 6\beta\eta^4\theta - 32\beta\lambda^4\theta - 32\beta^3\gamma^2\theta + \beta\eta^3 e^{\tau\theta-\eta\tau}\theta^2 \\
&- \beta\eta^3 e^{-\eta\tau-\tau\theta}\theta^2 - 4\beta^2\eta^3\gamma e^{\tau\theta-\eta\tau} + 4\beta^2\eta^3\gamma e^{-\eta\tau-\tau\theta} + 16\beta\eta^2\lambda^3 e^{\tau\theta-\eta\tau} \\
&- 16\beta\eta^2\lambda^3 e^{-\eta\tau-\tau\theta} - 3\beta\eta^4 e^{\eta\tau}\theta - 3\beta\eta^4 e^{-\eta\tau}\theta + 16\beta\lambda^4 e^{\eta\tau}\theta + 16\beta\lambda^4 e^{-\eta\tau}\theta \\
&+ 16\beta^2\eta^2\gamma\theta - 16\beta\eta^2\lambda^2\theta - 64\beta^2\gamma\lambda^2\theta + 32\beta^3\gamma^2 e^{\eta\tau}\theta + 16\beta\eta\lambda^4 e^{\tau\theta-\eta\tau} - 4\beta\eta^4\lambda e^{\tau\theta-\eta\tau} \\
&- 16\beta\eta\lambda^4 e^{-\eta\tau-\tau\theta} + 4\beta\eta^4\lambda e^{-\eta\tau-\tau\theta} - 64\beta\eta\lambda^3\theta + 16\beta\eta^3\lambda\theta - 8\beta^2\eta^2\gamma e^{\tau\theta-\eta\tau}\theta \\
&- 8\beta^2\eta^2\gamma e^{-\eta\tau-\tau\theta}\theta - 64\beta^2\eta\gamma\lambda\theta - 4\beta^2\eta\gamma e^{\tau\theta-\eta\tau}\theta^2 + 4\beta^2\eta\gamma e^{-\eta\tau-\tau\theta}\theta^2 \\
&- 4\beta\eta\lambda^2 e^{\tau\theta-\eta\tau}\theta^2 + 4\beta\eta\lambda^2 e^{-\eta\tau-\tau\theta}\theta^2 + 16\beta^2\eta\gamma\lambda^2 e^{\tau\theta-\eta\tau} - 16\beta^2\eta\gamma\lambda^2 e^{-\eta\tau-\tau\theta} \\
&+ 32\beta\eta\lambda^3 e^{\eta\tau}\theta - 8\beta\eta^3\lambda e^{\eta\tau}\theta + 32\beta\eta\lambda^3 e^{-\eta\tau}\theta - 8\beta\eta^3\lambda e^{-\eta\tau}\theta - 4\beta^2\eta^2\gamma e^{\eta\tau}\theta \\
&+ 4\beta^2\eta^2\gamma e^{-\eta\tau}\theta + 8\beta\eta^2\lambda^2 e^{\eta\tau}\theta + 8\beta\eta^2\lambda^2 e^{-\eta\tau}\theta + 48\beta^2\gamma\lambda^2 e^{\eta\tau}\theta + 16\beta^2\gamma\lambda^2 e^{-\eta\tau}\theta \\
&+ 48\beta^2\eta\gamma\lambda e^{\eta\tau}\theta + 16\beta^2\eta\gamma\lambda e^{-\eta\tau}\theta) \\
&/(2\eta(-3\theta^2)(4\beta\gamma + 4\eta\lambda + \eta^2 + 4\lambda^2)^{3/2})
\end{aligned}
\tag{D.2.16}
$$

$$
\begin{aligned}
&M(6,1) = (\eta^3\gamma^2 e^{-\eta\tau}\,(2\sinh\theta\tau) + 4\eta\gamma^2\lambda^2 e^{-\eta\tau}\,(2\sinh\theta\tau) + 4\eta^2\gamma^2\lambda e^{-\eta\tau}\,(2\sinh\theta\tau) \\
&+ 4\beta\eta\gamma^3 e^{-\eta\tau}\,(2\sinh\theta\tau) + \eta^2\gamma^2\theta e^{-\eta\tau}\,(2\cosh\theta\tau) - 8\beta\gamma^3\theta - 2\eta^2\gamma^2\theta - 8\gamma^2\lambda^2\theta \\
&- 8\eta\gamma^2\lambda\theta + 8\beta\gamma^3 e^{-\eta\tau}\theta + 8\gamma^2\lambda^2 e^{-\eta\tau}\theta + 8\eta\gamma^2\lambda e^{-\eta\tau}\theta)/(4\eta\theta^3(\lambda^2 + \eta\lambda + \beta\gamma))
\end{aligned}
\tag{D.2.17}
$$

$$
\begin{aligned}
&M(6,2) = (\gamma * (\eta^4\gamma e^{\tau\theta-\eta\tau} - \eta^4\gamma e^{-\eta\tau-\tau\theta} + 4\beta\eta^2\gamma^2 e^{\tau\theta-\eta\tau} \\
&- 4\beta\eta^2\gamma^2 e^{-\eta\tau-\tau\theta} - 4\eta^2\gamma\lambda^2 e^{\tau\theta-\eta\tau} + 4\eta^2\gamma\lambda^2 e^{-\eta\tau-\tau\theta} \\
&- \eta^3\gamma e^{\eta\tau}\theta + 3\eta^3\gamma e^{-\eta\tau}\theta + 8\gamma\lambda^3 e^{\eta\tau}\theta - 8\gamma\lambda^3 e^{-\eta\tau}\theta \\
&- \eta^3\gamma e^{\tau\theta-\eta\tau}\theta - \eta^3\gamma e^{-\eta\tau-\tau\theta}\theta - 8\eta\gamma\lambda^3 e^{\tau\theta-\eta\tau} \\
&+ 2\eta^3\gamma\lambda e^{\tau\theta-\eta\tau} + 8\eta\gamma\lambda^3 e^{-\eta\tau-\tau\theta} - 2\eta^3\gamma\lambda e^{-\eta\tau-\tau\theta} \\
&- 8\beta\eta\gamma^2\lambda e^{\tau\theta-\eta\tau} + 8\beta\eta\gamma^2\lambda e^{-\eta\tau-\tau\theta} - 4\beta\eta\gamma^2 e^{\eta\tau}\theta \\
&- 4\beta\eta\gamma^2 e^{-\eta\tau}\theta + 8\beta\gamma^2\lambda e^{\eta\tau}\theta - 8\beta\gamma^2\lambda e^{-\eta\tau}\theta + 4\eta\gamma\lambda^2 e^{\eta\tau}\theta \\
&- 2\eta^2\gamma\lambda e^{\eta\tau}\theta - 12\eta\gamma\lambda^2 e^{-\eta\tau}\theta + 2\eta^2\gamma\lambda e^{-\eta\tau}\theta \\
&+ 4\beta\eta\gamma^2 e^{\tau\theta-\eta\tau}\theta + 4\beta\eta\gamma^2 e^{-\eta\tau-\tau\theta}\theta + 4\eta\gamma\lambda^2 e^{\tau\theta-\eta\tau}\theta \\
&+ 4\eta\gamma\lambda^2 e^{-\eta\tau-\tau\theta}\theta)) \\
&/(\eta * (-3\theta^2) * (4\beta\gamma + 4\eta\lambda + \eta^2 + 4\lambda^2)^{3/2})
\end{aligned}
\tag{D.2.18}
$$

$$
\begin{aligned}
&M(6,3) = -(6\eta^4\gamma\lambda\theta - 64\eta\gamma\lambda^4\theta - 32\gamma\lambda^5\theta + 2\beta\eta^4\gamma^2 e^{\tau\theta-\eta\tau} - 2\beta\eta^4\gamma^2 e^{-\eta\tau-\tau\theta} \\
&+ 8\eta^2\gamma\lambda^4 e^{\tau\theta-\eta\tau} + 4\eta^3\gamma\lambda^3 e^{\tau\theta-\eta\tau} - 2\eta^4\gamma\lambda^2 e^{\tau\theta-\eta\tau} - 8\eta^2\gamma\lambda^4 e^{-\eta\tau-\tau\theta} \\
&- 4\eta^3\gamma\lambda^3 e^{-\eta\tau-\tau\theta} + 2\eta^4\gamma\lambda^2 e^{-\eta\tau-\tau\theta} + 16\gamma\lambda^5 e^{\eta\tau}\theta + 16\gamma\lambda^5 e^{-\eta\tau}\theta - 64\beta\gamma^2\lambda^3\theta \\
&- 32\beta^2\gamma^3\lambda\theta - 16\eta^2\gamma\lambda^3\theta + 16\eta^3\gamma\lambda^2\theta + 8\beta^2\eta^2\gamma^3 e^{\tau\theta-\eta\tau} - 8\beta^2\eta^2\gamma^3 e^{-\eta\tau-\tau\theta} \\
&- \eta^5\gamma\lambda e^{\tau\theta-\eta\tau} + \eta^5\gamma\lambda e^{-\eta\tau-\tau\theta} + 4\beta\eta^3\gamma^2 e^{\tau\theta-\eta\tau}\theta + 4\beta\eta^3\gamma^2 e^{-\eta\tau-\tau\theta}\theta \\
&- 4\eta^2\gamma\lambda^3 e^{\tau\theta-\eta\tau}\theta - 4\eta^2\gamma\lambda^3 e^{-\eta\tau-\tau\theta}\theta + 4\beta\eta^3\gamma^2\lambda e^{\tau\theta-\eta\tau} \\
&- 4\beta\eta^3\gamma^2\lambda e^{-\eta\tau-\tau\theta} + 24\eta\gamma\lambda^4 e^{\eta\tau}\theta - 2\eta^4\gamma\lambda e^{\eta\tau}\theta + 40\eta\gamma\lambda^4 e^{-\eta\tau}\theta \\
&- 6\eta^4\gamma\lambda e^{-\eta\tau}\theta - 64\beta\eta\gamma^2\lambda^2\theta + 16\beta\eta^2\gamma^2\lambda\theta + \eta^4\gamma\lambda e^{\tau\theta-\eta\tau}\theta \\
&+ \eta^4\gamma\lambda e^{-\eta\tau-\tau\theta}\theta + 16\beta\eta^2\gamma^2\lambda^2 e^{\tau\theta-\eta\tau} - 16\beta\eta^2\gamma^2\lambda^2 e^{-\eta\tau-\tau\theta} - 2\beta\eta^3\gamma^2 e^{\eta\tau}\theta \\
&- 8\beta^2\eta\gamma^3 e^{\eta\tau}\theta - 6\beta\eta^3\gamma^2 e^{-\eta\tau}\theta + 8\beta^2\eta\gamma^3 e^{-\eta\tau}\theta + 32\beta\gamma^2\lambda^3 e^{\eta\tau}\theta + 16\beta^2\gamma^3\lambda e^{\eta\tau}\theta \\
&+ 32\beta\gamma^2\lambda^3 e^{-\eta\tau}\theta + 16\beta^2\gamma^3\lambda e^{-\eta\tau}\theta + 4\eta^2\gamma\lambda^3 e^{\eta\tau}\theta - 6\eta^3\gamma\lambda^2 e^{\eta\tau}\theta \\
&+ 20\eta^2\gamma\lambda^3 e^{-\eta\tau}\theta - 10\eta^3\gamma\lambda^2 e^{-\eta\tau}\theta + 16\beta\eta\gamma^2\lambda^2 e^{\eta\tau}\theta - 12\beta\eta^2\gamma^2\lambda e^{\eta\tau}\theta \\
&+ 48\beta\eta\gamma^2\lambda^2 e^{-\eta\tau}\theta + 4\beta\eta^2\gamma^2\lambda e^{-\eta\tau}\theta - 4\beta\eta^2\gamma^2\lambda e^{\tau\theta-\eta\tau}\theta - 4\beta\eta^2\gamma^2\lambda e^{-\eta\tau-\tau\theta}\theta) \\
&/(2\eta * (\lambda^2 + \eta\lambda + \beta\gamma) * (-3\theta^2) * (4\beta\gamma + 4\eta\lambda + \eta^2 + 4\lambda^2)^{3/2})
\end{aligned}
\tag{D.2.19}
$$

$$
\begin{aligned}
&M(6,4) = (32\gamma\lambda^5 e^{-\eta\tau} - 3\eta^5\gamma e^{-\eta\tau} + \eta^3\gamma e^{\tau\theta-\eta\tau}\theta^2 + \eta^3\gamma e^{-\eta\tau-\tau\theta}\theta^2 - \eta^4\gamma e^{\tau\theta-\eta\tau}\theta \\
&+ \eta^4\gamma e^{-\eta\tau-\tau\theta}\theta + 80\eta\gamma\lambda^4 e^{-\eta\tau} - 14\eta^4\gamma\lambda e^{-\eta\tau} + \eta^3\gamma e^{\eta\tau}\theta^2 - 8\gamma\lambda^3 e^{\eta\tau}\theta^2 \\
&- 8\beta\eta^3\gamma^2 e^{-\eta\tau} + 16\beta^2\eta\gamma^3 e^{-\eta\tau} + 64\beta\gamma^2\lambda^3 e^{-\eta\tau} + 32\beta^2\gamma^3\lambda e^{-\eta\tau} + 48\eta^2\gamma\lambda^3 e^{-\eta\tau} \\
&- 8\eta^3\gamma\lambda^2 e^{-\eta\tau} - 4\beta\eta^2\gamma^2 e^{\tau\theta-\eta\tau}\theta + 4\beta\eta^2\gamma^2 e^{-\eta\tau-\tau\theta}\theta + 4\beta\eta\gamma^2 e^{\eta\tau}\theta^2 \\
&+ 4\eta^2\gamma\lambda^2 e^{\tau\theta-\eta\tau}\theta - 4\eta^2\gamma\lambda^2 e^{-\eta\tau-\tau\theta}\theta - 8\beta\gamma^2\lambda e^{\eta\tau}\theta^2 - 4\eta\gamma\lambda^2 e^{\eta\tau}\theta^2 \\
&+ 2\eta^2\gamma\lambda e^{\eta\tau}\theta^2 + 96\beta\eta\gamma^2\lambda^2 e^{-\eta\tau} + 16\beta\eta^2\gamma^2\lambda e^{-\eta\tau} - 4\beta\eta\gamma^2 e^{\tau\theta-\eta\tau}\theta^2 \\
&- 4\beta\eta\gamma^2 e^{-\eta\tau-\tau\theta}\theta^2 - 4\eta\gamma\lambda^2 e^{\tau\theta-\eta\tau}\theta^2 - 4\eta\gamma\lambda^2 e^{-\eta\tau-\tau\theta}\theta^2 + 8\eta\gamma\lambda^3 e^{\tau\theta-\eta\tau}\theta \\
&- 2\eta^3\gamma\lambda e^{\tau\theta-\eta\tau}\theta - 8\eta\gamma\lambda^3 e^{-\eta\tau-\tau\theta}\theta + 2\eta^3\gamma\lambda e^{-\eta\tau-\tau\theta}\theta + 8\beta\eta\gamma^2\lambda e^{\tau\theta-\eta\tau}\theta \\
&- 8\beta\eta\gamma^2\lambda e^{-\eta\tau-\tau\theta}\theta)/\big((-3\theta^2)(16\beta^2\gamma^2 + 8\beta\eta^2\gamma + 32\beta\eta\gamma\lambda \\
&+32\beta\gamma\lambda^2 + \eta^4 + 8\eta^3\lambda + 24\eta^2\lambda^2 + 32\eta\lambda^3 + 16\lambda^4)\big)
\end{aligned}
\tag{D.2.20}
$$

$$\begin{aligned}
M(6,5) = &-(-8\eta\lambda^4 e^{-\eta\tau}\left(2\sinh\theta\tau\right) - \eta^4\lambda e^{-\eta\tau}\left(2\sinh\theta\tau\right) - 12\eta^2\lambda^3 e^{-\eta\tau}\left(2\sinh\theta\tau\right)\\
&- 6\eta^3\lambda^2 e^{-\eta\tau}\left(2\sinh\theta\tau\right) - 4\beta^2\eta\gamma^2 e^{-\eta\tau}\left(2\sinh\theta\tau\right) + 4\eta\lambda^3\theta e^{-\eta\tau}\left(2\cosh\theta\tau\right)\\
&+ \eta^3\lambda\theta e^{-\eta\tau}\left(2\cosh\theta\tau\right) - \beta\eta^3\gamma e^{-\eta\tau}\left(2\sinh\theta\tau\right) + 4\eta^2\lambda^2\theta e^{-\eta\tau}\left(2\cosh\theta\tau\right)\\
&- 12\beta\eta\gamma\lambda^2 e^{-\eta\tau}\left(2\sinh\theta\tau\right) - 8\beta\eta^2\gamma\lambda e^{-\eta\tau}\left(2\sinh\theta\tau\right) + \beta\eta^2\gamma\theta e^{-\eta\tau}\left(2\cosh\theta\tau\right)\\
&+ 4\beta\eta\gamma\lambda\theta e^{-\eta\tau}\left(2\cosh\theta\tau\right) - 8\eta\lambda^3\theta - 2\eta^3\lambda\theta - 8\beta^2\gamma^2\theta - 8\eta^2\lambda^2\theta + 8\beta^2\gamma^2\theta e^{-\eta\tau}\\
&- 2\beta\eta^2\gamma\theta - 8\beta\gamma\lambda^2\theta - 16\beta\eta\gamma\lambda\theta + 8\beta\gamma\lambda^2\theta e^{-\eta\tau} + 8\beta\eta\gamma\lambda\theta e^{-\eta\tau})\\
&/(4\eta\theta^3(\lambda^2 + \eta\lambda + \beta\gamma))
\end{aligned} \tag{D.2.21}$$

$$\begin{aligned}
M(6,6) = &(16\eta\lambda^4\theta - 3\eta^5\theta - 8\eta^4\lambda\theta + 32\eta^2\lambda^3\theta + 8\eta^3\lambda^2\theta + 16\beta^2\eta\gamma^2\theta\\
&+ 4\beta^2\eta^2\gamma^2 e^{\tau\theta-\eta\tau} - 4\beta^2\eta^2\gamma^2 e^{-\eta\tau-\tau\theta} + \beta\eta^4\gamma e^{\tau\theta-\eta\tau} - \beta\eta^4\gamma e^{-\eta\tau-\tau\theta} - 8\beta\eta^3\gamma\theta\\
&+ 4\beta^2\eta\gamma^2 e^{\tau\theta-\eta\tau}\theta + 4\beta^2\eta\gamma^2 e^{-\eta\tau-\tau\theta}\theta - 8\beta\eta\gamma\lambda^3 e^{\tau\theta-\eta\tau} + 2\beta\eta^3\gamma\lambda e^{\tau\theta-\eta\tau}\\
&+ 8\beta\eta\gamma\lambda^3 e^{-\eta\tau-\tau\theta} - 2\beta\eta^3\gamma\lambda e^{-\eta\tau-\tau\theta} + 32\beta\eta\gamma\lambda^2\theta + 32\beta\eta^2\gamma\lambda\theta\\
&- 4\beta\eta^2\gamma\lambda^2 e^{\tau\theta-\eta\tau} - 8\beta^2\eta\gamma^2\lambda e^{\tau\theta-\eta\tau} + 4\beta\eta^2\gamma\lambda^2 e^{-\eta\tau-\tau\theta}\\
&+ 8\beta^2\eta\gamma^2\lambda e^{-\eta\tau-\tau\theta} - \beta\eta^3\gamma e^{\eta\tau}\theta + 3\beta\eta^3\gamma e^{-\eta\tau}\theta + 8\beta\gamma\lambda^3 e^{\eta\tau}\theta\\
&- 8\beta\gamma\lambda^3 e^{-\eta\tau}\theta - \beta\eta^3\gamma e^{\tau\theta-\eta\tau}\theta - \beta\eta^3\gamma e^{-\eta\tau-\tau\theta}\theta - 4\beta^2\eta\gamma^2 e^{\eta\tau}\theta\\
&- 4\beta^2\eta\gamma^2 e^{-\eta\tau}\theta + 8\beta^2\gamma^2\lambda e^{\eta\tau}\theta - 8\beta^2\gamma^2\lambda e^{-\eta\tau}\theta + 4\beta\eta\gamma\lambda^2 e^{\eta\tau}\theta\\
&- 2\beta\eta^2\gamma\lambda e^{\eta\tau}\theta - 12\beta\eta\gamma\lambda^2 e^{-\eta\tau}\theta + 2\beta\eta^2\gamma\lambda e^{-\eta\tau}\theta + 4\beta\eta\gamma\lambda^2 e^{\tau\theta-\eta\tau}\theta\\
&+ 4\beta\eta\gamma\lambda^2 e^{-\eta\tau-\tau\theta}\theta)/(\eta(-3\theta^2)(4\beta\gamma + 4\eta\lambda + \eta^2 + 4\lambda^2)^{3/2})
\end{aligned} \tag{D.2.22}$$

Further, assuming a delta-function type initial condition, the initial vector becomes $z(0) = \begin{bmatrix} 2\kappa & 0 & 0 & 0 & 2\kappa & 0 \end{bmatrix}^T$, the second-order moments are simply found by a combination of the first and fifth elements of their respective rows. The second-order moments can then be seen as:

$$\begin{aligned}
\mathbb{E}[X^2] = &\frac{\kappa e^{-\eta\tau}}{\theta^2(\lambda^2+\eta\lambda+\beta\gamma)}\Big(\theta\sinh\theta\tau\left(\left(\eta+\lambda\right)\left(\eta+2\lambda\right)+\beta\gamma+\beta^2\right)\Big)\\
&+ \frac{\kappa e^{-\eta\tau}}{\theta^2(\lambda^2+\eta\lambda+\beta\gamma)}\cosh\theta\tau\left(\theta^2\left(\eta+\lambda\right)+\beta\eta\left(\beta-\gamma\right)\right)\\
&- \frac{\kappa\left(\eta+\lambda\right)}{(\lambda^2+\eta\lambda+\beta\gamma)} - \frac{\kappa\beta\left(\beta-\gamma\right)\eta}{\theta^2(\lambda^2+\eta\lambda+\beta\gamma)} - \frac{4\kappa\beta\left(\beta-\gamma\right)}{\theta^2\eta}\left(1-e^{-\eta\tau}\right)
\end{aligned} \tag{D.2.23}$$

$$\begin{aligned}
\mathbb{E}[XY] = &\frac{\kappa e^{-\eta\tau}}{\theta^2(\lambda^2+\eta\lambda+\beta\gamma)}\theta\sinh\theta\tau\left(\gamma\left(\eta+\lambda\right)-\beta\lambda\right)\\
&+ \frac{\kappa e^{-\eta\tau}\left(\cosh\theta\tau-1\right)}{\theta^2(\lambda^2+\eta\lambda+\beta\gamma)}\Big(\left(\beta+\gamma\right)\left(\lambda\left(\eta+2\lambda\right)+2\beta\gamma\right)+\gamma\eta\left(\eta+2\lambda\right)\Big)\\
&+ \frac{\kappa\lambda}{\eta(\lambda^2+\eta\lambda+\beta\gamma)}\left(\beta-\gamma\right)\left(1-e^{-\eta\tau}\right) - \frac{\gamma\kappa}{(\lambda^2+\eta\lambda+\beta\gamma)}\left(1-e^{-\eta\tau}\right)
\end{aligned} \tag{D.2.24}$$

$$\begin{aligned}\mathbb{E}[Y^2] = {} & \frac{\kappa e^{-\eta\tau}}{\theta^2(\lambda^2+\eta\lambda+\beta\gamma)}\Big(\theta \sinh\theta\tau\left(\lambda\left(\eta+2\lambda\right)+\gamma\left(\gamma+\beta\right)\right)\Big) \\ & + \frac{\kappa e^{-\eta\tau}}{\theta^2(\lambda^2+\eta\lambda+\beta\gamma)}\cosh\theta\tau\left(\eta\gamma\left(\gamma-\beta\right)-\lambda\theta^2\right) \\ & + \frac{\kappa\lambda}{(\lambda^2+\eta\lambda+\beta\gamma)} + \frac{\kappa\gamma\left(\beta-\gamma\right)\eta}{\theta^2(\lambda^2+\eta\lambda+\beta\gamma)} + \frac{4\kappa\gamma\left(\beta-\gamma\right)}{\theta^2\eta}\left(1-e^{-\eta\tau}\right)\end{aligned} \tag{D.2.25}$$

Convergence to 2D moments

In the limit as $\eta \to 0$ the second-order moments are given as:

$$\begin{aligned}\mathbb{E}[X^2] &= \frac{\kappa}{2\alpha^3}\left(\lambda^2+\alpha^2+\beta^2\right)\sinh\theta\tau + \frac{\kappa\lambda}{\alpha^2}\left(\cosh\theta\tau-1\right) - \frac{\beta\kappa\left(\beta-\gamma\right)\tau}{\alpha^2} \\ \mathbb{E}[XY] &= \frac{\kappa(\gamma+\beta)}{2\alpha^2}\Big(\cosh(2\alpha\tau)-1\Big) + \frac{\kappa\lambda(\gamma-\beta)}{2\alpha^3}\sinh(2\alpha\tau) - \frac{\kappa\left(\gamma-\beta\right)\lambda\tau}{\alpha^2} \\ \mathbb{E}[Y^2] &= \frac{\kappa}{2\alpha^3}\Big(\left(\lambda^2+\alpha^2+\gamma^2\right)\sinh(2\alpha\tau)\Big) - \frac{\kappa\lambda}{\alpha^2}\Big(\cosh(2\alpha\tau)-1\Big) + \frac{\gamma\kappa\left(\beta-\gamma\right)\tau}{\alpha^2}\end{aligned} \tag{D.2.26}$$

These expressions for the second-order moments are seen to be the same as the results found for the 2D case.

APPENDIX E

MATRIX EXPONENTIAL

General

The matrix exponential can be expressed as,

$$e^{At} = \sum_{k=0}^{n-1} s_k A^k, \tag{E.1.1}$$

where A is an n-dimensional matrix, and the functions s_k come from the following relation:

$$e^{\lambda_i t} = \sum_{k=0}^{n-1} s_k \lambda_i^k, \tag{E.1.2}$$

where λ_i are the roots of the characteristic polynomial.

2D Case

Looking at the 2D case, the above expressions become,

$$e^{At} = s_0 \mathbf{I} + s_1 A, \tag{E.2.1}$$

where $s_0 = \frac{\alpha e^{\beta t} - \beta e^{\eta t}}{\alpha - \beta}$ and $s_1 = \frac{e^{\alpha t} - e^{\beta t}}{\alpha - \beta}$. Here α and β represent the two solutions to the characteristic equation. Further, by defining $s := \frac{\alpha+\beta}{2}$ and $q := \frac{\alpha-\beta}{2}$, the expressions for $s_{0,1}$ become:

$$\begin{aligned} s_0(t) &= e^{st}\left(\cosh qt - s\frac{\sinh qt}{q}\right) \\ s_1(t) &= e^{st}\frac{\sinh qt}{q}. \end{aligned} \tag{E.2.2}$$

Example

For the 2D linear incompressible flow given by $A = \begin{bmatrix} \lambda & \beta \\ \gamma & -\lambda \end{bmatrix}$ the values of s and q are found to be 0 and α, respectively. The resulting matrix exponential is given as follows:

$$e^{At} = \cosh \alpha t \mathbf{I} + \frac{\sinh \alpha t}{\alpha} A = \begin{bmatrix} \cosh \alpha t + \frac{\lambda \sinh \alpha t}{\alpha} & \frac{\beta \sinh \alpha t}{\alpha} \\ \frac{\gamma \sinh \alpha t}{\alpha} & \cosh \alpha t - \frac{\lambda \sinh \alpha t}{\alpha} \end{bmatrix}. \tag{E.2.3}$$

The result is equivalent to (6.1.18).

APPENDIX F

SECOND-ORDER MOMENTS FOR THE INERTIAL-GRAVITY-WAVE FLOW

The expressions for the second-order moments of the IGW flow are given in Tang *et al.* (2010), and are restated here. Since the second-order moments are seen to been dependent on the first-order moments, these are presented here as well for completeness. The mean values are given as follows:

$$\begin{aligned}
\bar{X} &= E_X + \frac{UE_2}{2\pi}\frac{\pi D - e^{-2\pi^2 D\tau}(\pi D\cos 2\pi\tau - \sin 2\pi\tau)}{1+\pi^2 D^2} \\
&+ \frac{UE_1}{2\pi}\frac{1 - e^{-2\pi^2 D\tau}(\cos 2\pi\tau + \pi D\sin 2\pi\tau)}{1+\pi^2 D^2}, \\
\bar{Y} &= E_Y - \frac{UE_2}{2\pi}\frac{1 - e^{-2\pi^2 D\tau}(\cos 2\pi\tau + \pi D\sin 2\pi\tau)}{1+\pi^2 D^2} \\
&+ \frac{UE_1}{2\pi}\frac{\pi D - e^{-2\pi^2 D\tau}(\pi D\cos 2\pi\tau - \sin 2\pi\tau)}{1+\pi^2 D^2}, \\
\bar{Z} &= E_Z - \frac{UE_2}{2\pi}\frac{\pi D - e^{-2\pi^2 D\tau}(\pi D\cos 2\pi\tau - \sin 2\pi\tau)}{1+\pi^2 D^2} \\
&- \frac{UE_1}{2\pi}\frac{1 - e^{-2\pi^2 D\tau}(\cos 2\pi\tau + \pi D\sin 2\pi\tau)}{1+\pi^2 D^2},
\end{aligned} \tag{F.1.1}$$

where $D = D_h + D_v$, $E_1 = \mathbb{E}\left\{\sin \Phi_0\right\}$, and $E_2 = \mathbb{E}\left\{\cos \Phi_0\right\}$. E_X, E_Y, and E_Z denote the means of the initial coordinates of the tracer.

$$\begin{aligned}
\mathbb{E}[Xe^{i\Phi}] &= E_{Xi\Phi}e^{\mu\tau} - \frac{U}{2\mu}\left(1 - e^{\mu\tau} - \frac{\mu E_{2i\Phi}}{(\mu' - \mu)}\left(e^{\mu'\tau} - e^{\mu\tau}\right)\right) + 2\pi i D_h E_{i\Phi}\tau e^{\mu\tau} \\
\mathbb{E}[Ye^{i\Phi}] &= E_{Yi\Phi}e^{\mu\tau} - \frac{Ui}{2\mu}\left(1 - e^{\mu\tau} + \frac{\mu E_{2i\Phi}}{(\mu' - \mu)}\left(e^{\mu'\tau} - e^{\mu\tau}\right)\right) \\
\mathbb{E}[Ze^{i\Phi}] &= E_{Zi\Phi}e^{\mu\tau} + \frac{U}{2\mu}\left(1 - e^{\mu\tau} - \frac{\mu E_{2i\Phi}}{(\mu' - \mu)}\left(e^{\mu'\tau} - e^{\mu\tau}\right)\right) + 2\pi i D_v E_{i\Phi}\tau e^{\mu\tau}
\end{aligned} \tag{F.1.2}$$

Given F.1.1 the second-order moments are written as:

$$
\begin{aligned}
Var(X) &= E_{X^2} - \bar{X}^2 + D_h\tau + U\Re\left\{\frac{2E_{Xi\Phi}}{\mu}(e^{\mu\tau}-1) - \frac{U\tau}{\mu} + \frac{U}{\mu^2}(e^{\mu\tau}-1)\right.\\
&\quad \left. + \frac{UE_{2i\Phi}}{\mu'-\mu}\left(\frac{e^{\mu'\tau}-1}{\mu'} - \frac{e^{\mu\tau}-1}{\mu}\right) + 4\pi i D_h E_{i\Phi}\left(\frac{\tau e^{\mu\tau}}{\mu} - \frac{e^{\mu\tau}}{\mu^2} + \frac{1}{\mu^2}\right)\right\},\\
Var(Y) &= E_{Y^2} - \bar{Y}^2 + D_h\tau + U\Im\left\{\frac{2E_{Yi\Phi}}{\mu}(e^{\mu\tau}-1) - \frac{Ui\tau}{\mu} + \frac{Ui}{\mu^2}(e^{\mu\tau}-1)\right.\\
&\quad \left. - \frac{UiE_{2i\Phi}}{\mu'-\mu}\left(\frac{e^{\mu'\tau}-1}{\mu'} - \frac{e^{\mu\tau}-1}{\mu}\right)\right\},\\
Var(Z) &= E_{Z^2} - \bar{Z}^2 + D_v\tau + U\Re\left\{-\frac{2E_{Zi\Phi}}{\mu}(e^{\mu\tau}-1) - \frac{U\tau}{\mu} + \frac{U}{\mu^2}(e^{\mu\tau}-1)\right.\\
&\quad \left. + \frac{UE_{2i\Phi}}{\mu'-\mu}\left(\frac{e^{\mu'\tau}-1}{\mu'} - \frac{e^{\mu\tau}-1}{\mu}\right) - 4\pi i D_v E_{i\Phi}\left(\frac{\tau e^{\mu\tau}}{\mu} - \frac{e^{\mu\tau}}{\mu^2} + \frac{1}{\mu^2}\right)\right\},\\
Cov(X,Y) &= E_{XY} - \bar{X}\bar{Y} + U\Re\left\{\frac{E_{Yi\Phi}}{\mu}(e^{\mu\tau}-1)\right\} + U\Im\left\{\frac{E_{Xi\Phi}}{\mu}(e^{\mu\tau}-1)\right\}\\
&\quad + U\Im\left\{\frac{UE_{2i\Phi}}{\mu'-\mu}\left(\frac{e^{\mu'\tau}-1}{\mu'} - \frac{e^{\mu\tau}-1}{\mu}\right) + 2\pi i D_h E_{i\Phi}\left(\frac{\tau e^{\mu\tau}}{\mu} - \frac{e^{\mu\tau}}{\mu^2} + \frac{1}{\mu^2}\right)\right\},\\
Cov(X,Z) &= E_{XZ} - \bar{X}\bar{Z} + U\Re\left\{\frac{E_{Zi\Phi}-E_{Xi\Phi}}{\mu}(e^{\mu\tau}-1)\right\} + U\Re\left\{\frac{U\tau}{\mu} - \frac{U}{\mu^2}(e^{\mu\tau}-1)\right.\\
&\quad \left. - \frac{UE_{2i\Phi}}{\mu'-\mu}\left(\frac{e^{\mu'\tau}-1}{\mu'} - \frac{e^{\mu\tau}-1}{\mu}\right) + 2\pi i (D_v - D_h) E_{i\Phi}\left(\frac{\tau e^{\mu\tau}}{\mu} - \frac{e^{\mu\tau}}{\mu^2} + \frac{1}{\mu^2}\right)\right\},\\
Cov(Y,Z) &= E_{YZ} - \bar{Y}\bar{Z} + U\Im\left\{\frac{E_{Zi\Phi}}{\mu}(e^{\mu\tau}-1)\right\} - U\Re\left\{\frac{E_{Yi\Phi}}{\mu}(e^{\mu\tau}-1)\right\}\\
&\quad + U\Im\left\{-\frac{UE_{2i\Phi}}{\mu'-\mu}\left(\frac{e^{\mu'\tau}-1}{\mu'} - \frac{e^{\mu\tau}-1}{\mu}\right) + 2\pi i D_v E_{i\Phi}\left(\frac{\tau e^{\mu\tau}}{\mu} - \frac{e^{\mu\tau}}{\mu^2} + \frac{1}{\mu^2}\right)\right\},
\end{aligned}
\tag{F.1.3}
$$

where $\mu = -(2\pi^2 D + 2\pi i)$, and $\mu' = -(8\pi^2 D + 4\pi i)$. All the definitions for the parameters are same as in Tang *et al.* (2010), this includes that: E_{X^2}, E_{Y^2}, E_{Z^2}, E_{XY}, E_{XZ}, E_{YZ}, $E_{Xi\Phi}$, $E_{Yi\Phi}$, and $E_{Zi\Phi}$ are the expectations of X^2, Y^2, Z^2, XY, XZ, YZ, $Xe^{i\Phi}$, $Ye^{i\Phi}$, and $Ze^{i\Phi}$, at time $\tau = 0$, respectively. Further, $E_{i\Phi}$ and $E_{2i\Phi}$ are given by: $E_{i\Phi} = E_1 + iE_2$, and $E_{2i\Phi} = \mathbb{E}\left\{\sin 2\Phi_0\right\} + i\mathbb{E}\left\{\cos 2\Phi_0\right\}$.

APPENDIX G

3D SECOND-ORDER MOMENTS FOR PURE-SHEAR SUBSYSTEM

The 2D shear-flow is given as:

$$A = \begin{bmatrix} \lambda & \beta \\ 0 & -\lambda \end{bmatrix}. \tag{G.1.1}$$

For this system, the second-order generators are given by:

$$\begin{aligned} A[X^2] &= 2\lambda X^2 + 2\beta XY + 2\kappa \\ A[XY] &= \beta Y^2 \\ A[Y^2] &= -2\lambda Y^2 + 2\kappa \end{aligned} \tag{G.1.2}$$

The resulting second-order moments are obtained as:

$$\begin{aligned} \mathbb{E}[Y^2] &= E_{y^2} e^{-2\lambda\tau} + \frac{\kappa}{\lambda}\left(1 - e^{-2\lambda\tau}\right) \\ \mathbb{E}[XY] &= E_{xy} + \frac{\beta\kappa\tau}{\lambda} + \frac{\beta\kappa}{2\lambda^2}\left(e^{-2\lambda\tau} - 1\right) + \frac{\beta E_{y^2}}{2\lambda}\left(1 - e^{-2\lambda\tau}\right) \\ \mathbb{E}[X^2] &= E_{x^2} e^{2\lambda\tau} + \left(\frac{\kappa}{\lambda} + \frac{\beta E_{xy}}{\lambda}\right)\left(e^{2\lambda\tau} - 1\right) + \frac{\beta^2 E_{y^2}}{2\lambda^2}\left(\cosh 2\lambda\tau - 1\right) \\ &\quad + \frac{\beta^2\kappa}{2\lambda^3}\sinh 2\lambda\tau - \frac{\beta^2\kappa\tau}{\lambda^2} \end{aligned} \tag{G.1.3}$$

The introduction of drift terms is seen in the $\mathbb{E}[XY]$ and $\mathbb{E}[X^2]$ expressions. It is seen that when $\beta = 0$, the above moments converge to those obtained in Appendix A.

$$A = \begin{bmatrix} \lambda & \beta & 0 \\ 0 & -(\lambda + \eta) & 0 \\ 0 & 0 & \eta \end{bmatrix} \tag{G.1.4}$$

The second-order moments are defined as:

$$\begin{aligned} \mathbb{E}[\dot{X^2}] &= 2\lambda \mathbb{E}[X^2] + 2\beta \mathbb{E}[XY] + 2\kappa \\ \mathbb{E}[\dot{XY}] &= \beta \mathbb{E}[Y^2] - \eta \mathbb{E}[XY] \\ \mathbb{E}[\dot{Y^2}] &= -2\left(\lambda + \eta\right)\mathbb{E}[Y^2] + 2\kappa \\ \mathbb{E}[\dot{XZ}] &= \left(\lambda + \eta\right)\mathbb{E}[XZ] + \beta \mathbb{E}[YZ] \\ \mathbb{E}[\dot{YZ}] &= -\lambda \mathbb{E}[YZ] \\ \mathbb{E}[\dot{Z^2}] &= 2\eta \mathbb{E}[Z^2] + 2\kappa \end{aligned} \tag{G.1.5}$$

The first 3 full moments are then given by:

$$
\begin{aligned}
\mathbb{E}[Y^2] &= E_{y^2} e^{-2(\lambda+\eta)\tau} + \frac{\kappa}{\lambda+\eta}\left(1 - e^{-2(\lambda+\eta)\tau}\right) \\
\mathbb{E}[XY] &= E_{xy} e^{-\eta\tau} + \frac{\beta E_{y^2}}{2\lambda+\eta}\left(e^{-\eta\tau} - e^{-2(\lambda+\eta)\tau}\right) + \frac{\kappa\beta}{\eta\left(\lambda+\eta\right)}\left(1 - e^{-\eta\tau}\right) \\
&\quad + \frac{\kappa\beta}{\left(\lambda+\eta\right)\left(\eta+2\lambda\right)}\left(e^{-2(\eta+\lambda)\tau} - e^{-\eta\tau}\right) \\
\mathbb{E}[X^2] &= E_{x^2} e^{2\lambda\tau} - \frac{2\beta E_{xy}}{\eta+2\lambda}\left(e^{-\eta\tau} - e^{2\lambda\tau}\right) + \frac{\beta^2 E_{y^2}}{\left(\eta+2\lambda\right)^2}\left(e^{-2(\eta+\lambda)\tau} - e^{2\lambda\tau}\right) \\
&\quad - \frac{2\beta^2 E_{y^2}}{\left(\eta+2\lambda\right)^2}\left(e^{-\eta\tau} - e^{2\lambda\tau}\right) - \frac{\beta^2\kappa}{\eta\lambda\left(\eta+\lambda\right)}\left(1 - e^{2\lambda\tau}\right) \\
&\quad + \frac{2\beta^2\kappa}{\eta\left(\lambda+\eta\right)\left(\eta+2\lambda\right)}\left(e^{-\eta\tau} - e^{2\lambda\tau}\right) - \frac{\beta^2\kappa}{\left(\lambda+\eta\right)\left(\eta+2\lambda\right)^2}\left(e^{-2(\eta+\lambda)\tau} - e^{2\lambda\tau}\right) \\
&\quad + \frac{2\beta^2\kappa}{\left(\lambda+\eta\right)\left(\eta+2\lambda\right)^2}\left(e^{-\eta\tau} - e^{2\lambda\tau}\right) - \frac{\kappa}{\lambda}\left(1 - e^{2\lambda\tau}\right)
\end{aligned}
\tag{G.1.6}
$$

Taking the limit as η goes to 0, it is seen that the moments converge to the following expressions.

$$
\begin{aligned}
\mathbb{E}[Y^2] &= E_{y^2} e^{-2\lambda\tau} + \frac{\kappa}{\lambda}\left(1 - e^{-2\lambda\tau}\right) \\
\mathbb{E}[XY] &= E_{xy} + \frac{\beta E_{y^2}}{2\lambda}\left(1 - e^{-2\lambda\tau}\right) + \frac{\kappa\beta}{2\lambda^2}\left(e^{-2\lambda\tau} - 1\right) + \frac{\beta\kappa\tau}{\lambda} \\
\mathbb{E}[X^2] &= E_{x^2} e^{2\lambda\tau} + \left(\frac{\kappa}{\lambda} + \frac{\beta E_{xy}}{\lambda}\right)\left(e^{2\lambda\tau} - 1\right) + \frac{\beta^2 E_{y^2}}{2\lambda^2}\left(\cosh 2\lambda\tau - 1\right) \\
&\quad + \frac{\beta^2\kappa}{2\lambda^3}\sinh 2\lambda\tau - \frac{\beta^2\kappa\tau}{\lambda^2}
\end{aligned}
\tag{G.1.7}
$$

Using the series expansion of the exponential function in the following term in the $\mathbb{E}[XY]$ equation $\frac{\kappa\beta}{\eta(\lambda+\eta)}\left(1 - e^{-\eta\tau}\right)$, and similar terms in the $\mathbb{E}[X^2]$ eqaution, leads to the same moments obtained for the 2D shear system.

Assuming a delta-function type initial condition, the above equations reduce to the following:

$$
\begin{aligned}
\mathbb{E}[Y^2] &= \frac{\kappa}{\lambda}\left(1 - e^{-2\lambda\tau}\right) \\
\mathbb{E}[XY] &= \frac{\kappa\beta}{2\lambda^2}\left(e^{-2\lambda\tau} - 1\right) \\
\mathbb{E}[X^2] &= \frac{\kappa}{\lambda}\left(e^{2\lambda\tau} - 1\right) + \frac{\beta^2\kappa}{2\lambda^3}\sinh 2\lambda\tau - \frac{\beta^2\kappa\tau}{\lambda^2}
\end{aligned}
\tag{G.1.8}
$$

APPENDIX H

PERMISSION FORM

04/19/2018

Phillip Walker has my permission to include the following paper, of which I was a co-author, in his doctoral dissertation.

“Finite-time statistics of scalar diffusion in Lagrangian coherent structures” (2012) Tang, W. & Walker, P., Phys. Rev. E, 86, 045201(R). DOI: 10.1103/PhysRevE.86.045201

Wenbo Tang